# Laser Polarized $^3$He Target Used for a Precision Measurement of the Neutron Spin Structure

Mikhail V. Romalis

A DISSERTATION
PRESENTED TO THE FACULTY
OF PRINCETON UNIVERSITY
IN CANDIDACY FOR THE DEGREE
OF DOCTOR OF PHILOSOPHY

RECOMMENDED FOR ACCEPTANCE
BY THE DEPARTMENT OF
PHYSICS

June 1997

© Copyright 1997 by Mikhail V. Romalis.
All rights reserved.

# Abstract

This thesis describes a precision measurement of the deep inelastic neutron spin structure function $g_1^n(x)$. The main motivation for the experiment is a test of the Bjorken sum rule. Because of smaller statistical errors and broader kinematic coverage than in previous experiments, we are able to study in detail the behavior of the spin structure function $g_1^n(x)$ for low values of the Bjorken scaling variable $x$. We find that it has a strongly divergent behavior, in contradiction to the naive predictions of the Regge theory. This calls into question the methods commonly used for extrapolation of $g_1^n(x)$ to $x = 0$. The difference between the proton and the neutron spin structure functions is less divergent at low $x$, so a test of the Bjorken sum rule is possible. We confirm the sum rule with an accuracy of 8%.

The experiment was performed at SLAC using a 50 GeV polarized electron beam and a polarized $^3$He target. In this thesis the polarized target is described in detail. We used the technique of Rb optical pumping and Rb-He spin exchange to polarize the $^3$He. Because of a novel mechanical design our target had the smallest dilution ever achieved for a high density gas target. Since this is a precision measurement, particular efforts were made to reduce the systematic errors due to the uncertainty in the target parameters. Most important parameters were measured by more than one method. We implemented novel techniques for measuring the thickness of the glass windows of the target, the $^3$He density, and the polarization. In particular, one of the methods for measuring the gas density relied on the broadening of the Rb optical absorption lines by collisions with $^3$He atoms. The calibration of this technique resulted in the most precise measurements of the pressure broadening parameters for $^3$He as well as several other gases, which are described in an Appendix. The polarization of the $^3$He was also measured by two methods, one relying on traditional NMR techniques and the other on the shift of the Rb Zeeman resonance frequency due to the $^3$He polarization. To calibrate the frequency shift polarimetry, we performed an accurate measurement of a Rb-$^3$He spin exchange parameter, significantly improving on previous results.

A part of the thesis is devoted to the analysis of the high energy data. We present an algorithm for electron-pion discrimination based on the lateral shape of their shower in the electromagnetic calorimeter. The calculation of the radiative corrections to the deep inelastic scattering and, especially, their effect on the experimental errors is also discussed. The last chapter is devoted to the interpretation of

our results in the framework of perturbative QCD. We present a physically intuitive description of the ambiguities arising in Next to Leading Order (NLO) analysis of the spin structure functions. Using such analysis we describe the implications of our data.

# Acknowledgements

First of all, I would like to thank my advisor, Gordon Cates, for providing invaluable advice, support, and encouragement in all aspects of my thesis work. I also want to thank Will Happer for answering with patience my numerous, and sometimes misguided, questions about atomic physics, Krishna Kumar for teaching me high energy physics and politics, and Albert Young for stimulating discussions on a variety of topics.

Working on a large experiment, I had the opportunity to interact with many people, all of whom I cannot mention here. I'd like to thank our spokesman, Emlyn Hughes, for his talent in making decisions when a limited amount of information is available. I also had a good fortune of working with Paul Souder and Zein-Eddine Meziani. From the polarized target group I would like to acknowledge Jim Johnson for his very concrete contribution to many parts of the target and the Michigan group: Tim Chupp, Todd Smith, Kevin Coulter and Robert Welsh. Hopefully, any arguments we may have had resulted only in better understanding of the physics issues and each other. In addition to myself, ten other graduate thesis students made the experiment work. They are Todd Smith, Yury Kolomensky, Piotr Zyla, Michael Olson, Greg Mitchel, Sebastien Incerti, Jason Wang, Frank Sabatie, David Reyna and Steve Churchwell.

The experiment would also be impossible without the help from a large number of staff members at SLAC, Princeton and elsewhere. Among all of them, undoubtedly, the most indispensable and dedicated person is our Princeton glassblower, Mike Souza. Who else can make cells with windows that are both concave and convex (i.e. have the topology of a 4-D sphere) and should be ready two days ago?

I would like to thank my labmates at Princeton for creating an atmosphere that I looked forward coming back to after long stays at SLAC and Caltech. When I was starting in the lab, the help of Hunter Middleton, Bastiaan Driehuys and Brian Saam was invaluable. I especially would like to thank Paul Bogorad, with whom we went through the whole cell-making, shift-taking marathon during the run at SLAC. Being a post-doc, not once did he avoid some of the more tedious work, sparkling it instead with a great sense of humor. I'd like to thank Karen Sauer for being a caring friend and reacting with excitement to everyday lab "news". In the last two years I had a fortune to interact with many people who created a vibrant and stimulating atmosphere. They are Stephan Appelt, Rich Fitzgerald, Stan Anderson,

Chris Erickson, Dan Walter, Andrei Baranga, Eli Miron, Ioannis Kominis, John Son, Ben Lev, and Pereclis Tsekeris. Hopefully, I learned something from each of them. I would like particularly to thank Stephan Appelt for telling me about physics I never knew existed, Dan Walter for his willingness to tackle new problems, Chris Erickson for his witty jokes, Iannis Kominis for his inspiring enthusiasm for any and all physics, and Stan Anderson for providing support from thesis writers anonymous.

Among the members of my class, I would like particularly to thank Anthony Rizzi with whom we shared as many jokes as physics ideas.

Finally, I would like to thank my parents and grandparents for guiding me to science in such a natural way, that I can't even imagine doing anything else.

*Polarization data has often been the graveyard of fashionable theories. If theorists had their way they might well ban such measurements altogether out of self-protection.*

J.D. Bjorken

Proc. Adv. Workshop on QCD Hadronic Processes, 1987

# Contents

**Abstract** iii

**Acknowledgements** v

**1 Introduction** 1

**2 Polarized Deep Inelastic Scattering** 4
- 2.1 Kinematics . . . 4
- 2.2 The Scattering Cross-Section . . . 6
- 2.3 Scaling . . . 8
- 2.4 Sum Rules . . . 9
- 2.5 Experimental Observables . . . 12
- 2.6 Past Experiments . . . 17

**3 The E-154 Experiment** 25
- 3.1 Polarized Electron Beam . . . 25
- 3.2 Møller Polarimeter . . . 28
- 3.3 Spectrometers . . . 31
- 3.4 Data Analysis . . . 39
- 3.5 Asymmetry . . . 43
- 3.6 Radiative Corrections . . . 47
  - 3.6.1 The Structure of the Radiative Corrections . . . 47
  - 3.6.2 Error Analysis . . . 49
  - 3.6.3 Input Models and their Errors . . . 52
  - 3.6.4 Results of the Radiative Corrections . . . 56

**4 Polarized $^3$He Target** 63
- 4.1 Optical Pumping and Spin Exchange . . . 63
- 4.2 Target Cells . . . 70
  - 4.2.1 Cell Dimensions . . . 74
  - 4.2.2 Window Thicknesses . . . 76
  - 4.2.3 Cell Volumes . . . 81

4.2.4 Cell Densities . . . 84
4.3 Target Setup . . . 88
4.4 Cell Temperatures . . . 90
4.5 The Dilution Factor . . . 96
4.6 Target Performance . . . 100
4.6.1 Spin Maser . . . 104

**5 $^3$He Polarimetry 119**
5.1 NMR Polarimetry . . . 119
5.1.1 Adiabatic Fast Passage . . . 119
5.1.2 Coil Modeling . . . 123
5.1.3 Water Signal Analysis . . . 125
5.1.4 Other Signal Shaping Effects . . . 131
5.1.5 Coil Gain and Other Quantities . . . 132
5.1.6 Absolute Calibration . . . 132
5.1.7 Calculation of the Calibration Constant . . . 133
5.2 EPR Polarimetry . . . 134
5.2.1 Basic Principle . . . 134
5.2.2 Detection of EPR Resonance . . . 136
5.2.3 Measurement of $\kappa_0$ . . . 139
5.2.4 Polarization Gradient . . . 145
5.2.5 Temperature Distribution in the Pumping Cell . . . 148
5.2.6 The EPR Shift in the Cells . . . 148
5.2.7 Spin Exchange Effects . . . 150
5.2.8 EPR Results . . . 154
5.3 Comparison of Two Methods of Polarimetry . . . 156
5.4 Polarization Direction . . . 158

**6 Results and QCD Analysis 164**
6.1 Traditional Analysis . . . 164
6.2 The Interpretation of QPM within QCD . . . 170
6.3 Analysis of the Data within QCD . . . 180
6.4 Conclusion and Outlook . . . 185

**A Shower Analysis 191**
A.1 Introduction . . . 191
A.2 Clustering algorithm . . . 193
A.2.1 $5 \times 5$ clusters . . . 193
A.2.2 Energy sharing . . . 194
A.2.3 Cluster time and position . . . 194
A.2.4 Shower shape . . . 198

A.2.5 Iterating the cluster shape . . . . . 201
A.2.6 Energy measurement . . . . . 203
A.3 Shape cut . . . . . 204

**B Pressure Broadening** **213**
B.1 Introduction. . . . . 213
B.2 Experimental Technique. . . . . 215
B.3 Data Analysis . . . . . 217
B.4 Results and Discussion. . . . . 220
B.4.1 $^3$He and $^4$He data. . . . . 220
B.4.2 $N_2$ and Xe data. . . . . 224
B.4.3 Oscillator Strength. . . . . 230
B.5 Conclusion . . . . . 232

**List of Figures** **236**

**List of Tables** **241**

# Chapter 1

# Introduction

At present, all experimental observations in high energy and nuclear physics are in agreement with a theory of elementary particles and interactions known as the Standard model. This is a combination of the gauge theory of electromagnetic interactions based on a U(1) group, the weak interactions based on an $SU(2)_L$ group, and the strong interactions based on a non-Abelian $SU(3)_C$ group. While each of these theories has been studied in numerous experiments and is commonly accepted, the precision with which they are tested is drastically different. For example, the electromagnetic coupling constant is known to 0.045 ppm [1]: $\alpha_{em} = 1/137.0359895(61)$, the weak coupling constant at low energy is known to 20 ppm: $G_F = 1.16639(2) \times 10^{-5}$ GeV$^{-2}$, while the strong coupling constant is only known to 3%: $\alpha_s\,(M_Z) = 0.118(3)$. Clearly, precision tests of the theory of strong interactions are called for.

This thesis describes an experiment whose goal is to precisely test one of the predictions of QCD. Because the fundamental objects in QCD, quarks and gluons, are never observed directly, it is difficult to find precisely testable predictions. The QCD sum rules give predictions about the integrals of the deep inelastic structure functions which are free from uncertainties associated with non-perturbative quark interactions at low energies. Several sum rules exist in QCD. The testable sum rules for unpolarized deep inelastic structure functions involve only neutrino scattering. Nevertheless, one such rule, the Gross – Llewellyn Smith sum rule, has been tested to 3%. The other fundamental sum rule that can be accurately tested is the Bjorken sum rule, which involves integrals of the proton and neutron *spin* structure functions.

The measurement of the spin structure functions requires the use of both a polarized beam and a polarized target. The experiment was conducted at Stanford Linear Accelerator Center (SLAC), using a 50 GeV electron beam polarized to 80%. We used a $^3$He polarized target to measure the spin structure function of the neutron. Because of the Pauli exclusion principle, the spins of the two protons in $^3$He are oppositely polarized and most of the spin is due to the neutron. The polarized $^3$He gas target relies on several atomic physics techniques. We used optical pumping of Rb vapor and Rb-He spin exchange to polarize the $^3$He. This experiment benefited

from the experience of the previous SLAC $^3$He experiment [2], which used a similar target. About half of the improvement in the statistical precision compared with the previous experiment came from the improvements in the target, especially its dilution factor. In addition, we placed a special emphasis on reducing the systematic errors originating from the target parameters.

The results of the early measurements of the proton spin structure function by EMC at CERN [3] were quite unexpected, as they seemed to imply that the fraction of the proton spin carried by the quarks was very small. This interpretation sparked considerable theoretical and experimental interest in the area, and it is still developing at a rapid pace. For reviews written in the last two years see [4, 5, 6, 7, 8, 9, 10, 11]. A relative consensus on the interpretation of the EMC result developed only recently.

This thesis is organized as follows. In Chapter 2 I introduce polarized deep inelastic scattering and spin sum rules. A brief overview of past polarized DIS experiments is given. Chapter 3 focuses on our experiment and discusses all aspects of the setup and analysis unrelated to the polarized target. In particular, we discuss the physical properties of the electromagnetic shower which can be used for discrimination between electrons and pions in our calorimeter. A full description of the analysis is given in Appendix A. We also describe the calculation of the radiative corrections to the deep inelastic scattering, in particular, their effect on the experimental errors. Chapters 4 and 5 focus on the polarized target. Chapter 4 describes the technique of optical pumping and spin exchange, fabrication of the target cells, measurements of their physical parameters and the target dilution factor. The performance of the polarized target during the run is also discussed. In Chapter 5 I describe the two techniques used for $^3$He polarimetry. A detailed analysis of the systematic errors in each technique is given. Finally, in Chapter 6 I present the results of our experiment and their interpretation within QCD. I give a physically intuitive description of the ambiguities present in QCD analysis due to the axial anomaly, and discuss the implications of the data.

# Bibliography


[1] R.M. Barnett *et al.*, (Particle Data Group), Phys. Rev. D **54**, (1996).

[2] P.L. Anthony *et al*, (the E-142 Collaboration), Phys. Rev. Lett. **71**, 959 (1993); Phys. Rev. D **54**, 6620 (1996).

[3] J. Ashman *et al.* (the EMC Collaboration), Phys. Lett. B **206**, 364 (1988); Nucl. Phys. B **328**, 1 (1989).

[4] U. Stiegler, Phys. Rep. **277**, 1 (1996).

[5] M. Anselmino, A. Efremov, and E. Leader, Phys. Rep. **261**, 1 (1995).

[6] H. Y. Cheng, Int. J. Mod. Phys. A **11**, 5109, (1996) (also hep-ph/9607254).

[7] G. Ramsey, hep-ph/9702227, submitted to Prog. Part. Nucl. Phys.

[8] I. Hinchliffe and A. Kwiatkowski, Ann. Rev. Nucl. Part. Sci. **46**, 609 (1996).

[9] B. L. Ioffe, hep-ph/9511401

[10] J. Ellis and M Karliner, hep-ph/9601280

[11] B. Frois, Prog. Part. Nucl. Phys. **34**, 87 (1995).

# Chapter 2

# Polarized Deep Inelastic Scattering

Deep Inelastic Scattering (DIS) has been a major tool in the study of hadron structure and QCD. The initial evidence for the existence of elementary particles inside the nucleon came from DIS experiments conducted at SLAC in the 60's [1]. The study of the nucleon structure using DIS has continued at SLAC, CERN and DESY, providing some of the most stringent tests of QCD. In DIS one uses a lepton probe ($e$, $\mu$, or $\nu$) whose interactions are well understood to study the properties of the nucleons (protons or neutrons). By controlling the polarization degrees of freedom one can obtain significant additional information about the structure of the nucleon.

## 2.1 Kinematics

Most DIS experiments use a high energy lepton beam scattering from a fixed nuclear target[1]. The definition of the kinematic variables for our experiment is shown in Figure 2.1. In other experiments $\mu$, or $\nu$ beams are used instead of the electrons.

All kinematic variables are defined in the lab frame. The initial electron has an energy $E$, four momentum $k^\mu$, and spin $s^\mu$, while the neutron at rest in the lab frame has $p^\mu = (M, 0, 0, 0)$ and spin $S^\mu$. The electron scatters electromagnetically from the constituents inside the neutron. Interactions through a $Z^0$ exchange are also possible, but for our experiment $Q^2 \ll M_Z^2$ and the exchange of the weak boson is strongly suppressed. It results, however, in a non-negligible correction which is applied to the data. The scattered electron is detected by the spectrometer, and its energy $E'$ and momentum $k'^\mu$ are measured. The (virtual) photon energy is $\nu = E - E'$ and its momentum transfer is $Q^2 = -q^2 = (k^\mu - k'^\mu)^2$. After the scattering, the neutron breaks up into many hadronic products. Their total invariant energy is given by $W^2 = (p^\mu + q^\mu)^2 = M^2 + 2M\nu - Q^2$. We do not detect any of the hadrons, but measure an inclusive cross-section. The scattering is called deep inelastic because $W^2 \gg M^2$. In contrast, for elastic scattering the neutron remains intact and $W^2 = M^2$.

[1] Recent DIS experiments at HERA use colliding positron-proton beams.

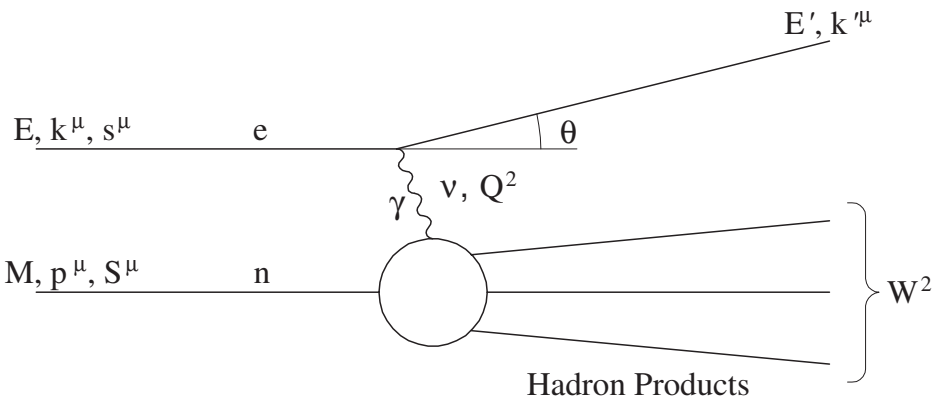


Figure 2.1: Kinematic variables used in deep inelastic scattering.

It is convenient to parametrize the scattering by two dimensionless variables, whose values range from 0 to 1. One defines:

$$x = \frac{Q^2}{2p\cdot q} = \frac{Q^2}{2M\nu} \tag{2.1}$$

$$y = \frac{p\cdot q}{p\cdot k} = \frac{\nu}{E} \tag{2.2}$$

where the first equality gives a Lorentz invariant definition and the second is true only in the Lab frame. As we will see, $x$ plays a very special role in deep inelastic processes, while $y$ is the fractional energy loss of the scattered electron. Several useful relations between the kinematic variables are given below:

$$Q^2 = 4EE'\sin^2(\theta/2) = 2EMxy \tag{2.3}$$

$$W^2 = M^2 + Q^2(1-x)/x \tag{2.4}$$

Thus, the deep inelastic limit $W^2 \gg M^2$ is also equivalent to the Bjorken scaling limit $Q^2 \gg M^2$ at constant $x$. From equation (2.3) one can see that the minimum $x$ accessible to an experiment is $x_{\min} \sim Q^2/2EM$ (for $y \sim 1$). For deep inelastic scattering one would like to have $Q^2 \gg 1$ GeV$^2$. However, experiments show that the results approach the deep inelastic limit even for $Q^2 \sim 1$ GeV$^2$. Therefore, partly by convention, the deep inelastic region is defined as $Q^2 > 1$ GeV$^2$, $W^2 > 4$ GeV$^2$. This gives $x_{\min} \sim 1/2E(\text{GeV})$. So, with a 48 GeV beam at SLAC we can reach to $x \approx 0.01$. At CERN, using 190 GeV muon beam, the DIS measurements can be done down to $x = 0.003$.

## 2.2 The Scattering Cross-Section

Using the usual rules of relativistic scattering theory, we can write the electron scattering cross-section in the following form [2, 3]:

$$d\sigma = \left|\left\langle f\left|\mathcal{M}\right|i\right\rangle\right|^2 \frac{(2\pi)^4}{4EM}\delta^4\left(p+q-\sum_{i=1}^{N}p_i\right)\frac{d^3k'}{2E'(2\pi)^3}\prod_{i=1}^{N}\frac{d^3p_i}{(2p_i^0)(2\pi)^3} \tag{2.5}$$

where $p_i$, $i = 1 \ldots N$ are the momenta of the hadron products in the final state, and the scattering matrix is given by:

$$i\mathcal{M} = \left(-ie^2\right)\left(\frac{-g_{\mu\nu}}{q^2}\right)\left\langle k', s'\left|j^\mu(0)\right|k, s\right\rangle\left\langle X, S'\left|J^\nu(0)\right|n, S\right\rangle \tag{2.6}$$

Here $X$ denotes the final hadronic state produced by the collision, $j^\mu(0)$ and $J^\nu(0)$ are the leptonic and hadronic electromagnetic currents respectively. One can separate the square of the matrix element into a product of purely leptonic and hadronic tensors, which are usually defined by:

$$\left|\left\langle f\left|\mathcal{M}\right|i\right\rangle\right|^2 = \frac{e^4}{q^4}L^{\mu\nu}W_{\mu\nu} \tag{2.7}$$

The leptonic part is given by:

$$L^{\mu\nu} = \sum_{s'}\left\langle k', s'\left|j^\mu(0)\right|k, s\right\rangle\left\langle k, s\left|j^\nu(0)\right|k', s'\right\rangle \tag{2.8}$$

where we sum over the final electron spin states, since they are not distinguished in the detector.

In the rest frame of a spin 1/2 particle[2] the spin vector can be defined as follows:

$$2\vec{s} = u^\dagger(k,s)\,\vec{\sigma}u(k,s) = \overline{u}(k,s)\,\vec{\gamma}\gamma^5 u(k,s) \tag{2.9}$$

We use a normalization of the Dirac spinors $u^\dagger u = 2E$. In the rest frame of the particle of mass $m$ polarized in the $\hat{z}$ direction $\vec{s} = m\hat{z}$. Thus, the polarization vector has units of mass. This expression is generalized to a Lorentz invariant form:

$$2s^\mu = \overline{u}(k,s)\,\gamma^\mu\gamma^5 u(k,s) \tag{2.10}$$

For an ultrarelativistic particle polarized along is momentum (definite helicity) one gets $s^\mu = \lambda k^\mu$, where $\lambda = \pm 1$ is the helicity.

[2]Some polarized DIS experiments are done with a spin-1 D target. In this case the expressions are slightly modified.

The main advantage of deep inelastic scattering is that the lepton electromagnetic current has a well known Dirac form:

$$\langle k', s' \left| j^{\mu}(0) \right| k, s \rangle = \overline{u}(k', s') \gamma^{\mu} u(k, s) \tag{2.11}$$

Summing the leptonic tensor (2.8) over the final electron spin $s'$ we get:

$$L^{\mu\nu} = 2\left(k'^{\mu}k^{\nu} + k'^{\nu}k^{\mu} - \left(k \cdot k' - m^2\right) g^{\mu\nu} - i\varepsilon^{\mu\nu\rho\sigma} q_{\rho} s_{\sigma}\right) \tag{2.12}$$

From now on we will neglect the electron mass $m$. Note that the electron spin contributes only to the anti-symmetric part of the lepton tensor.

The hadronic tensor is given by:

$$W_{\mu\nu} = \frac{1}{4\pi} \sum_{X,S'} (2\pi)^4 \delta^4 (p + q - p_X) \langle X, S' \left| J_{\mu}(0) \right| n, S \rangle \langle n, S \left| J_{\mu}(0) \right| X, S' \rangle \tag{2.13}$$

where we sum over all possible final states $X$ and final spin directions $S'$. Since the proton and the final state are not elementary Dirac particles, we do not know the electromagnetic current. However, we can greatly restrict the possible form of the current by using symmetry and invariance properties. Lorentz invariance implies that $W_{\mu\nu}$ should transform as a rank 2 tensor, so it can be formed only from available four vectors: $p_{\mu}$, $q_{\mu}$, $S_{\mu}$ and tensors $g_{\mu\nu}$, $\varepsilon_{\mu\nu\rho\sigma}$. The conservation of the hadronic electromagnetic current, time reversal invariance and parity invariance[3] allows one to specify the hadronic tensor in terms of 4 independent scalar functions of the two independent Lorentz invariant scalars, chosen to be $x$ and $Q^2$ [3]:

$$\begin{aligned} W_{\mu\nu} &= F_1\left(x, Q^2\right)\left(-g_{\mu\nu} + \frac{q_{\mu}q_{\nu}}{q^2}\right) + \frac{F_2(x, Q^2)}{p \cdot q}\left(p_{\mu} - \frac{p \cdot q}{q^2} q_{\mu}\right)\left(p_{\nu} - \frac{p \cdot q}{q^2} q_{\nu}\right) \\ &+ i\frac{g_1(x, Q^2)}{p \cdot q} \varepsilon_{\mu\nu\rho\sigma} q^{\rho} S^{\sigma} \\ &+ \frac{i}{(p \cdot q)^2} g_2\left(x, Q^2\right) \varepsilon_{\mu\nu\rho\sigma} q^{\rho} \left[(p \cdot q) S^{\sigma} - (S \cdot q) p^{\sigma}\right] \end{aligned} \tag{2.14}$$

In this way the hadronic interactions are completely parametrized by four functions: $F_1$, $F_2$, $g_1$, and $g_2$, which are called the structure functions. $g_1$ and $g_2$, in particular, are called the spin structure functions. Note that $g_1$ and $g_2$ contribute only to the antisymmetric part of the hadronic tensor. When $W_{\mu\nu}$ is contracted with $L^{\mu\nu}$, the spin structure functions contribute to the cross-section only if both the electron and the neutron are polarized[4].

[3] For neutrino scattering parity is violated which results in additional terms in the hadronic tensor.

[4] For spin-1 targets there is a contribution for an unpolarized beam, but it is difficult to measure.

It is instructive to calculate the structure functions for a target which is an elementary Dirac spinor. In this case the scattering is elastic at the tree level. $W_{\mu\nu}$ is given by the same formula (2.8) as for the leptons and we get:

$$F_1 = \frac{1}{2}\delta\left(1-\frac{Q^2}{2M\nu}\right) \tag{2.15}$$

$$F_2 = \frac{Q^2}{2M\nu}\delta\left(1-\frac{Q^2}{2M\nu}\right) \tag{2.16}$$

$$g_1 = \frac{1}{2}\delta\left(1-\frac{Q^2}{2M\nu}\right) \tag{2.17}$$

$$g_2 = 0 \tag{2.18}$$

The delta function comes from momentum conservation for elastic scattering (i.e. $W^2 = M^2$).

## 2.3 Scaling

The first deep inelastic scattering experiments found, of course, large deviations from the simple Dirac form of the structure functions. However, they found a very interesting behavior that for high momentum transfer $Q^2 > 1$ GeV$^2$ the structure functions depend only on one variable $x = Q^2/2M\nu$, and are independent of $Q^2$ at constant $x$. This behavior, known as *scaling* [4, 5] was interpreted as evidence that the nucleons are made of elementary, weakly interacting particles, which were called partons.

In this approximations one assumes that the electron scatters from one of the partons, which is assumed to be "free" during the interaction. The scattering is an incoherent sum of the contributions from different partons. We assume that each parton carries a fraction $\alpha$ of the nucleon momentum and introduce parton distribution functions $q(\alpha) = dP/d\alpha$ equal to the probability of finding a parton inside the nucleon carrying momentum fraction between $\alpha$ and $\alpha + d\alpha$. In QCD, the partons which carry electric charge and contribute to the scattering are quarks. They are elementary Dirac particles and should have elementary form factors.

Since the partons have momentum $p_q = \alpha p$, we should replace $\nu = p\cdot q/M$ by $\alpha\nu$. This results in the replacement of $\delta(1 - Q^2/2M\nu)$ by $\delta(\alpha - Q^2/2M\nu) = \delta(\alpha - x)$ in equations (2.15-2.18). Thus, an electron with kinematic variable $x$ can scatter only from a parton carrying a fraction $x$ of the momentum of the nucleon. If the partons are non-interacting, then $q(x)$ is a probability distribution that depends only on the properties of the nucleon, not on the details of the scattering. Therefore, the scattering cross-section should depend only on $x$ and not on $Q^2$ or $\nu$ separately. The

structure functions can be written in terms of the parton distributions as follows:

$$F_1\left(x,Q^2\right) = \frac{1}{2}\sum_i e_i^2 q_i\left(x\right) \quad (2.19)$$

$$F_2\left(x,Q^2\right) = x\sum_i e_i^2 q_i\left(x\right) \quad (2.20)$$

$$g_1\left(x,Q^2\right) = \frac{1}{2}\sum_i e_i^2\left(q_i^{\uparrow}\left(x\right) - q_i^{\downarrow}\left(x\right)\right) \quad (2.21)$$

$$g_2\left(x,Q^2\right) = 0 \quad (2.22)$$

where the sum runs over all partons in the nucleon weighted by the square of their electric charge $e_i$ (in units of the electron charge), and the polarized distributions are defined as the probability of finding the parton with the same $q_i^{\uparrow}\left(x\right)$ or opposite $q_i^{\downarrow}\left(x\right)$ helicity as the parent nucleon.

In QCD the partons in the nucleon are quarks and gluons. The gluons are not charged, while the quarks carry fractional charges: $e_u = 2/3$, $e_d = -1/3$, $e_s = -1/3$. The neutron is made from 2 d quarks and 1 u quark, while the proton from 2 u quarks and 1 d quark. Actually, the quarks scheme with specific charges and masses was proposed by Gell-Mann and Zweig before the creation of QCD or the discovery of scaling [6] to explain the abundance of hadrons and mesons. QCD also predicts the existence of "sea" quarks, created out of the vacuum by gluon interactions.

## 2.4 Sum Rules

One of the most fruitful and robust consequences of the quark parton model (QPM) are the sum rules for structure functions. They give a prediction for the integral over $x$ of various combinations of the structure functions. Most of them are modified only by calculable radiative corrections when full interactions of QCD are taken into account. Thus, they allow a model independent test of the QPM and its QCD modifications. For unpolarized structure functions the only testable sum rules involve neutrino scattering. They are [7]:

$$Gross - Llewellyn\ Smith\ (baryon) \ : \quad \int_0^1 dx\left(F_3^{\nu p}\left(x\right) + F_3^{\nu n}\left(x\right)\right)/2 = 3 \quad (2.23)$$

$$Adler \ : \quad \int_0^1 dx\left(F_2^{\nu n}\left(x\right) - F_2^{\nu p}\left(x\right)\right)/x = 2 \quad (2.24)$$

Here $F_3$ is an additional structure function, which is present because of parity violation in neutrino interactions. Presently, the baryon sum rule is tested to 3% (with 2 $\sigma$ deviation from the theoretical prediction), and the Adler sum rule is tested to 20% [7]. For polarized structure functions two more sum rules exist: the Bjorken sum rule

[8] and the Ellis-Jaffe [9] sum rule, which are discussed in detail below. With the data from our experiment the Bjorken sum rule can be tested to 8%.

In the parton model we can express the average helicity of each quark using our definition of the polarized quark momentum distributions:

$$\Delta q_i = \int_0^1 \left( q_i^{\uparrow}(x) - q_i^{\downarrow}(x) + \bar{q}_i^{\uparrow}(x) - \bar{q}_i^{\downarrow}(x) \right) dx \tag{2.25}$$

where $\bar{q}_i(x)$ denotes the momentum distribution of the anti-quarks. The integral of the spin structure function $g_1$ gives us a linear combination of the helicities carried by each quark flavor:

$$\Gamma_1 = \int_0^1 g_1(x)\, dx = \frac{1}{2}\left( \frac{4}{9}\Delta u + \frac{1}{9}\Delta d + \frac{1}{9}\Delta s \right) \tag{2.26}$$

which follows from equation (2.21). On the other hand, using equation (2.10) the helicity carried by each quark can be calculated from the following matrix element:

$$2\Delta q_i s^{\mu} = \left\langle N \left| \bar{q}_i \gamma^{\mu} \gamma^5 q_i \right| N \right\rangle \tag{2.27}$$

If the nucleon were a Dirac particle made of one quark then $\Delta q = 1$. In the quark parton model the two expressions for quark helicity, (2.25) and (2.27), are identified with each other. We will come back to the validity of this assumption later.

We can now derive the Bjorken sum rule. Recall from the theory of weak interactions that the weak current matrix element for the neutron decay is defined as [10]:

$$\langle \bar{p} | J_w | n \rangle = \left\langle \bar{p} \left| \tau^{+} \gamma^{\mu} \left( 1 - \gamma^5 \right) \right| n \right\rangle = \bar{U} \gamma^{\mu} \left( 1 - \frac{g_A}{g_V} \gamma^5 \right) U = 2 \left( p^{\mu} - \frac{g_A}{g_V} s^{\mu} \right) \tag{2.28}$$

where $U$ stands for a Dirac spinor and $\tau$ is a Pauli matrix acting in the isospin space. $g_A/g_V$ is an empirical quantity that parametrizes the deviation of the neutron weak axial coupling from that of a Dirac particle. Experimentally, $g_A/g_V = 1.2601 \pm 0.0025$ [11]. Using properties of the isospin operators $[\tau^{+}, \tau^{-}] = \tau^3$ and $\tau^{-} |p\rangle = |n\rangle$, the axial current can be converted to a matrix element between proton states:

$$\left\langle \bar{p} \left| \tau^{+} \gamma^{\mu} \gamma^5 \right| n \right\rangle = \left\langle \bar{p} \left| \tau^3 \gamma^{\mu} \gamma^5 \right| p \right\rangle \tag{2.29}$$

With the isospin assignments for the quarks: $\tau^3 u = u$, $\tau^3 d = -d$, and $\tau^3 s = 0$ we get:

$$\left\langle \bar{p} \left| \tau^3 \gamma^{\mu} \gamma^5 \right| p \right\rangle = \left\langle \bar{p} \left| \bar{u} \gamma^{\mu} \gamma^5 u - \bar{d} \gamma^{\mu} \gamma^5 d \right| p \right\rangle = 2 s^{\mu} \left( \Delta u_p - \Delta d_p \right) \tag{2.30}$$

Thus

$$\left\langle \bar{p} \left| \tau^{+} \gamma^{\mu} \gamma^5 \right| n \right\rangle = 2 s^{\mu} \frac{g_A}{g_V} = 2 s^{\mu} \left( \Delta u_p - \Delta d_p \right) \tag{2.31}$$

To extract the appropriate combination of the quark helicities from DIS measurements we form the difference between the integrals of $g_1$ for the proton and the neutron and use isospin invariance to set $\Delta u_p = \Delta d_n$, $\Delta d_p = \Delta u_n$, and $\Delta s_p = \Delta s_n$. By convention, the quark momentum distributions refer to the distributions in the proton: $\Delta u = \Delta u_p$. The neutron momentum distributions can be obtained by isospin invariance. This gives us

$$\Gamma_1^p - \Gamma_1^n = \frac{1}{6}(\Delta u - \Delta d) = \frac{1}{6}\frac{g_A}{g_V} \tag{2.32}$$

which is the Bjorken sum rule, derived by Bjorken in 1966 and, at that time, called a "worthless equation" [8] because of inaccessibility of the spin degrees of freedom.

In this derivation we only used the assignment of electric and isospin charges to the quarks, the isospin symmetry, and the identification of the quark helicity matrix element (2.27) with the integral of the quark momentum distribution. The assignment of the charges is fundamental to the parton model and QCD, and isospin symmetry violations due to finite quark mass and electromagnetic interactions are expected to be very small. The last assumption, however, requires further justification. The quark momentum distributions are measured in DIS at high $Q^2$, while the quark helicity matrix elements are related to weak decay constants measured at $Q^2 = 0$. In the non-interacting quark parton model the scaling is exact and the structure functions do not depend on $Q^2$. Thus the two expressions for the quark helicities are identical. This is not true in QCD, where there are scaling violations which become large and incalculable at low $Q^2$. However, it turns out that the particular combination of quark helicities $a_3 = \Delta u - \Delta d$ is independent of $Q^2$ because of axial flavor current conservation, and the relationship remains valid to zeroth order in $\alpha_s$. The only modification from QCD is due to radiative corrections for the photon-quark interactions. They can be calculated using, for example, the techniques of operator product expansion [3]. Thus, the Bjorken sum rule which rests on a small number of very fundamental assumptions, remains valid in QCD. This has led Feynman to conclude that "its verification or failure [the Bjorken Sum Rule] would have a most decisive effect on the direction of future high energy theoretical physics" [12].

One can carry this analysis further and consider the implications of the full $SU(3)_f$ symmetry of u, d and s quarks. This neglects the mass of the s quark, which is significant, and, therefore, on somewhat theoretically weaker grounds. Using SU(3) symmetry one can show that:

$$a_8 = \Delta u + \Delta d - 2\Delta s = 3F - D \tag{2.33}$$

where $F$ and $D$ are two constants that parametrize the deviation of the axial current from its Dirac form in the baryon octet [10]. $a_8$ is the second diagonal element of the axial flavor current in SU(3) and is independent of $Q^2$ due to the conservation of the current. From the data on the semileptonic weak decays of baryons one can

determine $F$ and $D$. Further, it can be argued that the polarization of the s quarks should be small on the basis of the OZI rule [9] or helicity conservation of the gluon-quark interactions [13]. If one assumes that $\Delta s = 0$, the values for $\Gamma_1^p$ and $\Gamma_1^n$ can be predicted separately:

$$\Gamma_1^p = \frac{1}{18}(9F - D) \tag{2.34}$$

$$\Gamma_1^n = \frac{1}{18}(6F - 4D) \tag{2.35}$$

which is known as the Ellis-Jaffe sum rule [9]. The status of this rule is much less solid in QCD because the assumption that $\Delta s = 0$ is not well justified and not even well defined. Recent experiments observed violations of the Ellis-Jaffe sum rule for both the neutron and the proton.

Thus, there are several predictions for the integrals of the spin structure functions of varying degree of reliability. To test these predictions one has to measure $g_1$ over a large kinematic range and calculate the integral for both the neutron and the proton.

## 2.5 Experimental Observables

To access the spin structure functions experimentally, one has to measure the cross-section for the scattering of a polarized lepton on a polarized nucleon. Using the equations for the hadronic and leptonic tensors we can easily calculate the differential cross-section of deep inelastic scattering [14]:

$$\begin{aligned}\frac{d^2\sigma}{dxdQ^2} &= \frac{4\pi\alpha^2}{Q^4 x}\left[\frac{Q^4}{4M^2E^2x}F_1\left(x,Q^2\right) + \left(1 - \frac{Q^2}{2MEx} - \frac{Q^2}{4E^2}\right)F_2\left(x,Q^2\right)\right] \\ &+ \frac{P_b P_t 4\pi\alpha^2}{Q^2 MEx}\left[\left(2 - \frac{Q^2}{2MEx} - \frac{Q^2}{2E^2}\right)g_1\left(x,Q^2\right) - \frac{2Mx}{E}g_2\left(x,Q^2\right)\right]\end{aligned} \tag{2.36}$$

for longitudinally polarized beam with polarization $P_b$ and target with polarization $P_t$. Experimentally, it is easier to measure an asymmetry between the cross-section with $P_b P_t > 0$ and $P_b P_t < 0$. The relative asymmetry is defined assuming 100% beam and target polarizations:

$$A_{\parallel} = \frac{d\sigma^{\uparrow\downarrow} - d\sigma^{\uparrow\uparrow}}{d\sigma^{\uparrow\uparrow} + d\sigma^{\uparrow\downarrow}} \tag{2.37}$$

and is given by the ratio of the polarized to the unpolarized cross-sections. One can also measure an asymmetry with the target polarization transverse to the beam:

$$A_{\perp} = \frac{d\sigma^{\downarrow\leftarrow} - d\sigma^{\uparrow\leftarrow}}{d\sigma^{\downarrow\leftarrow} + d\sigma^{\uparrow\leftarrow}} \tag{2.38}$$

Sometimes it is convenient to think about the scattering cross-section for a virtual photon shown in Figure 2.1. In this case we replace the lepton electromagnetic tensor $L^{\mu\nu}$ by the virtual photon polarization vector $\varepsilon_\lambda^\mu$ for the external photon line and remove the photon propagator:

$$\left|\langle f\left|\mathcal{M}\right|i\rangle\right|^2 = \varepsilon_\lambda^{\mu *}\varepsilon_\lambda^\nu W_{\mu\nu} \tag{2.39}$$

Also the flux factor $1/2E$ in the expression for the cross-section (2.5) should be replaced by $1/2K$, where $K = \left(W^2 - M^2\right)/2M = \nu + q^2/2M$ is a Lorentz invariant. For a real photon $q^2 = 0$ and $K = \nu$. The index $\lambda$ labels different initial polarizations of the photon. One usually defines [3]:

$$\varepsilon_\pm^\mu = \left(0, \mp 1, -i, 0\right)/\sqrt{2} \tag{2.40}$$

$$\varepsilon_0^\mu = 1/Q\left(\sqrt{\nu^2 + Q^2}, 0, 0, \nu\right) \tag{2.41}$$

which satisfy the condition $\varepsilon^\mu q_\mu = 0$. $\varepsilon_0$ corresponds to a longitudinally polarized photon and is allowed because the photon is virtual. One can define four cross-sections corresponding to different initial polarization states [14, 15]:

$$\sigma_{1/2} = \sigma\left(+1, -1/2\right) = \frac{4\pi^2\alpha}{MK}\left(F_1 + g_1 - \gamma^2 g_2\right) \tag{2.42}$$

$$\sigma_{3/2} = \sigma\left(+1, +1/2\right) = \frac{4\pi^2\alpha}{MK}\left(F_1 - g_1 + \gamma^2 g_2\right) \tag{2.43}$$

$$\sigma_L = \sigma\left(0, +1/2\right) = \frac{4\pi^2\alpha}{MK}\left(-F_1 + F_2\left(1 + \gamma^2\right)/2x\right) \tag{2.44}$$

$$\sigma_{TL} = \sigma\left(\left|+1, -1/2\right\rangle, \left|0, +1/2\right\rangle\right) = \frac{4\pi^2\alpha}{MK}\sqrt{2}\gamma\left(g_1 + g_2\right) \tag{2.45}$$

where $\sigma\left(\lambda_i, S_i\right)$ denotes the cross-section with initial photon helicity $\lambda_i$ and initial proton spin $S_i$ along the $\hat{z}$ axis. $\sigma_{TL}$ is the contribution of the interference term between the $\left|+1, -1/2\right\rangle$ and $\left|0, +1/2\right\rangle$ states. Here $\gamma = \sqrt{Q^2/\nu^2} = 2x\sqrt{M^2/Q^2} \to 0$ as $Q^2 \to \infty$ with constant $x$.

It is interesting to consider this result in terms of helicity conservation at high energy. For an ultrarelativistic fermion $\left(1 \pm \gamma^5\right)$ projects out the helicity states [2]:

$$\frac{1}{2}\left(1 - \gamma^5\right)u \approx u_L \tag{2.46}$$

$$\frac{1}{2}\left(1 + \gamma^5\right)u \approx u_R \tag{2.47}$$

Using the properties of the $\gamma$ matrixes one can show that the electromagnetic current conserves helicity: $\bar{u}\gamma^\mu u = \bar{u}_L\gamma^\mu u_L + \bar{u}_R\gamma^\mu u_R$. Figure 2.2 shows an electromagnetic

interaction between an electron and a quark. It is assumed that both the quark and the electron scatter backwards in the center of mass frame. Other cases can be expressed by using rotation properties of the angular momentum operators. Both the electron and the quark are ultrarelativistic. Using the conservation of helicity we can see that the electron is more likely to emit a longitudinally polarized photon and preserve its helicity. The quark is more likely to absorb the photon if its initial spin is opposite to the photon spin, so it can preserve its helicity as well.

It is interesting to see what happens if we use the elementary particle form of the structure functions (2.19-2.22). In the limit of deep inelastic scattering $\gamma \to 0$ and to zeroth order in $\gamma$ we get:

$$\sigma_{1/2} = \frac{4\pi^2\alpha}{MK}\delta(1-x) \tag{2.48}$$

$$\sigma_{3/2} = \sigma_L = \sigma_{TL} = 0 \tag{2.49}$$

Thus, only the dominant helicity process, shown in Figure 2.2 contributes to scattering.

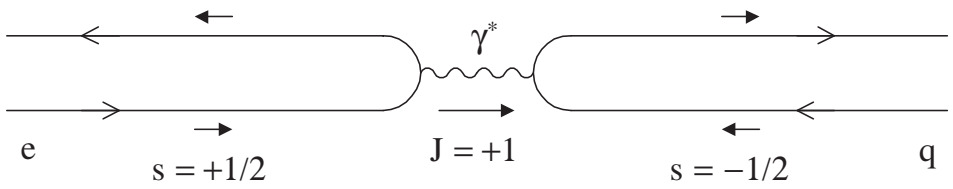


Figure 2.2: The dominant spin scattering cross-section due to the helicity conservation.

Since the nucleon is more complicated than a single quark, all of the cross-sections contribute. It is natural to define virtual photon asymmetries $A_1$ and $A_2$ as follows:

$$A_1 = \frac{\sigma_{1/2} - \sigma_{3/2}}{\sigma_{1/2} + \sigma_{3/2}} \tag{2.50}$$

$$A_2 = \frac{2\sigma_{TL}}{\sigma_{1/2} + \sigma_{3/2}} \tag{2.51}$$

In addition one defines $R = 2\sigma_L / \left(\sigma_{1/2} + \sigma_{3/2}\right)$ which measures the deviation of the unpolarized structure functions from the Callan-Gross identity $2xF_1 = F_2$ [16].

Several simple predictions can be made for $A_1$ based on the quark-parton model. For $x \to 1$ we expect that only one quark carries all of the momentum and spin of the nucleon. Therefore, the cross-section is given by equation (2.48) and $A_1 = 1$ [17]. If we assume the SU(6) model for the flavor and spin wavefunction of the quarks inside

the nucleon, then $\Delta u = 4/9$, $\Delta d = -1/9$ and using:

$$A_1 = \frac{\sum e_i^2 \Delta q_i}{\sum e_i^2 q_i} \tag{2.52}$$

we get $A_1^p = 5/9$ and $A_1^n = 0$ independent of $x$. Thus, the proton asymmetry is expected to be large and positive, while the neutron asymmetry is close to zero.

Since we cannot create a multi-GeV beam of virtual photons, we use polarized electrons (or muons) to create the photons with known polarization properties. Then $A_1$ and $A_2$ are related to the measured asymmetries $A_{\|}$ and $A_{\perp}$ by the following kinematic factors [14]:

$$A_{\|} = D\left(A_1 + \eta A_2\right) \tag{2.53}$$
$$A_{\perp} = d\left(A_2 - \zeta A_1\right) \tag{2.54}$$

where

$$D = \frac{1 - \varepsilon E'/E}{1 + \varepsilon R} \tag{2.55}$$
$$\eta = \varepsilon \frac{\sqrt{Q^2}}{E - \varepsilon E'} \tag{2.56}$$
$$d = D\sqrt{\frac{2\varepsilon}{1+\varepsilon}} \tag{2.57}$$
$$\zeta = \eta \frac{(1+\varepsilon)}{2\varepsilon} \tag{2.58}$$
$$\varepsilon = \frac{1}{1 + 2\left(1 + \nu^2/Q^2\right)\tan^2\left(\theta/2\right)} \tag{2.59}$$

$D$ can be thought of as a depolarization factor of the photon due to the fact it is not emitted parallel to the initial nucleon spin. The factors $D$ and $\eta$ are plotted vs. $x$ for the 2.75° spectrometer in Figure 2.3.

Using equations (2.42-2.45) and (2.55-2.59) we get:

$$g_1 = \frac{F_1}{1+\gamma^2}\left(A_1 + \gamma A_2\right) = \frac{F_1}{D'}\left(A_{\|} + \tan\left(\theta/2\right) A_{\perp}\right) \tag{2.60}$$
$$g_2 = \frac{F_1}{1+\gamma^2}\left(A_2/\gamma - A_1\right) = \frac{F_1}{D'}\frac{y}{2\sin\left(\theta\right)}\left(\frac{E + E'\cos\left(\theta\right)}{E'} A_{\perp} - \sin\left(\theta\right) A_{\|}\right) \tag{2.61}$$

where

$$D' = \frac{(1-\varepsilon)(2-y)}{y\left(1+\varepsilon R\right)} \tag{2.62}$$
$$F_1 = F_2 \frac{1+\gamma^2}{2x\left(1+R\right)} \tag{2.63}$$

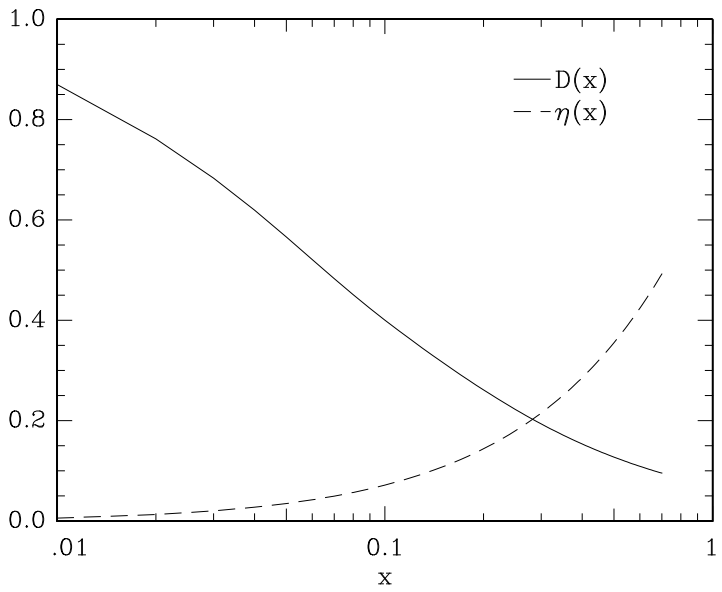


Figure 2.3: The kinematic factors $D$ and $\eta$ as a function of $x$ for the 2.75° spectrometer.

Equations (2.60-2.61) can also be obtained directly from the expression for the lepton cross-section (2.36).

So, to extract $g_1$ one has to measure both $A_{\parallel}$ and $A_{\perp}$. However, because $\tan(\theta/2)$ is small in our experiment, $A_{\perp}$ gives only a very small contribution. One also needs to know $F_2$ and $R$, which have been measured with sufficient accuracy in unpolarized deep inelastic scattering experiments [18, 19].

Experiments cannot measure $g_1(x)$ over the entire range of 0 to 1, which is needed to test the sum rules. At low $x$ the range is limited by the $Q^2 > 1$ GeV$^2$ Bjorken scaling cut, and at high $x$ by the $W^2 > 4$ GeV$^2$ deep inelastic cut and limited statistics due to very small DIS cross-section. Therefore, theoretical input is needed to extrapolate the data to $x = 0$ and $x = 1$. For extrapolation to $x = 1$ one usually assumes that $A_1 \to 1$ based on helicity conservation, as described on page 14. The contribution to the integral of $g_1$ is small, because $F_1 \to 0$ as $x \to 1$. The uncertainty due to high $x$ extrapolation is usually very small.

The extrapolation to low $x$ is more uncertain. This is one of the main reasons that the polarized DIS experiments have been conducted at increasingly higher energy to access a lower $x$ region. One historically has used Regge theory for low $x$ extrapolation, which predicts that [20, 21]:

$$g_1(x) \sim x^{-\alpha_1}, \; x \to 0 \tag{2.64}$$

where $\alpha_1$ is constrained between $-0.5 < \alpha_1 < 0$. This implies that $g_1$ goes to zero or stays constant as $x \to 0$. The validity of this assumption is questionable. Several other models exist [22, 23, 24], which predict various forms for the low $x$ behavior of $g_1$ diverging at $x = 0$ with various degrees of severity. In most experimental papers the Regge theory with $\alpha_1 = 0$ has been used for extrapolation.

Another issue that has to be addressed in interpreting experimental results is the dependence of $g_1$ on $Q^2$. Although in QPM the scaling is exact, QCD introduces scaling violations which depend of $\log Q^2$. The sum rules derived in Section 2.4 have to be evaluated at constant $Q^2$. However, because of kinematic constraints, $g_1$ is measured over a range of $Q^2$ correlated with $x$. In addition, different experiments measure $g_1$ at different $Q^2$. It is observed experimentally that $A_1 \sim g_1/F_1$ has no $Q^2$ dependence within errors. In QCD this is explained by the fact that $F_1$ and $g_1$ have very similar $Q^2$ evolution. Experimental analyses usually assume that $A_1$ is independent of $Q^2$. Since $F_1$ has been measured over a wide range of $x$ and $Q^2$, this allows one to calculate the $Q^2$ dependence of $g_1$. The questions of low $x$ behavior and $Q^2$ dependence will be considered in more detail in Chapter 6.

## 2.6 Past Experiments

The first polarized deep inelastic scattering experiments were carried out at SLAC in the 70's - early 80's. The first experiment E-80 [25] was also the first high energy experiment ever to use a polarized electron beam. The electron energy was 6-13 GeV. Polarized electrons were produced by photo-ionization of Li atoms polarized by Stern-Gerlach technique. The electron polarization was 50–80%, however the beam current was limited to $10^8$ electrons per pulse. The polarization of the electron beam was measured at the source by Mott scattering and at the target by Møller scattering. E-80 used a butanol solid target polarized by the dynamic nuclear polarization technique (DNP) [26]. The only significant non-zero spin element in butanol is hydrogen, so it is equivalent to a proton target with a dilution factor of 0.11. Polarizations up to 50% were achieved. However, the radiation resistance of the material was low, and, in fact, was a limiting factor for the beam current. The experiment collected data in the range $0.1 < x < 0.5$ at an average $Q^2$ of 2 GeV$^2$. The virtual photon asymmetry $A_1$ was found to be close to the SU(6) prediction of 5/9 in the range $0.3 < x < 0.5$ and falling down at lower $x$.

The next experiment E-130 [27] was done using a higher beam energy of 22 GeV to measure the asymmetry at higher $Q^2$. The beam and target polarizations were 85% and 50% respectively and a dedicated spectrometer was built at $\theta = 11°$. The measurements were performed in the range $0.2 < x < 0.65$ and 2 GeV$^2$ $< Q^2 <$ 6 GeV$^2$. The results were in good agreement with E-80 and confirmed the predictions of the SU(6) model.

Although the first SLAC experiments were very successful in confirming the basic picture of the proton spin structure, they lacked data at sufficiently low $x$ to calculate the first moment of $g_1$ and check the Ellis-Jaffe sum rule. The next polarized deep inelastic experiment was carried out at CERN by the European Muon Collaboration (EMC) [28]. This and subsequent CERN experiments used a muon beam with an energy of 100-200 GeV to access very low $x$ at high $Q^2$. The muon beam is produced at CERN from the decay of pions and kaons generated by stopping a proton beam in a tungsten target. The muons are naturally polarized due to the V-A structure of the weak decays. The average muon polarization during the run was 80%. An ammonia solid state target was used in the experiment, polarized by DNP to 80%. The target consisted of two sections, each 36 cm long, polarized in opposite directions. The resolution of the spectrometer was sufficient to trace the scattered electron to one of the two target halves. The direction of the target polarization was periodically reversed to reduce uncertainties due to variations in the spectrometer acceptance. However, the time drifts of the acceptance were the dominant source of the systematic error. The main limitation of the experiment was low statistics due to low intensity of the secondary muon beam. The data were collected in the range $0.01 < x < 0.7$ at $3.5\ \mathrm{GeV}^2 < Q^2 < 30\ \mathrm{GeV}^2$. Based on these data EMC calculated $\Gamma_1^p = 0.126 \pm 0.010$ (stat.) $\pm$ 0.015 (syst.) The Ellis-Jaffer sum rule, which assumes $\mathrm{SU}(3)_f$ symmetry and negligible polarization of the strange quarks, predicts $\Gamma_1^p(EJ) = 0.189 \pm 0.005$ based on the numbers for $F$ and $D$ available at that time. Thus, the experimental result disagreed by 3 $\sigma$ with the Ellis-Jaffe sum rule. If the constraint $\Delta s = 0$ is removed, then one finds using equations (2.26, 2.32, 2.33):

$$\Delta u = 0.78 \pm 0.06 \tag{2.65}$$

$$\Delta d = -0.47 \pm 0.06 \tag{2.66}$$

$$\Delta s = -0.19 \pm 0.06 \tag{2.67}$$

$$\Delta\Sigma = \Delta u + \Delta d + \Delta s = 0.12 \pm 0.17 \tag{2.68}$$

The EMC result was particularly surprising since it gave a value for $\Delta\Sigma$ consistent with zero. In contract, in the naive quark-parton model the quarks carry most of the proton spin and $\Delta\Sigma \simeq 1$. This situation was called "the proton spin crisis" and sparked a lot of interest in the study of spin structure among both theorists and experimentalists.

At this point it is appropriate to briefly review the theoretical progress in this area, which has been quite active since the release of the EMC result. For reviews written in the last two years see [7, 15, 30, 31, 32, 33, 34, 35]. Soon after the results were released, it was realized (see, however, [29]) that QCD significantly modifies the QPM interpretation of $\Delta\Sigma$ due to non-conservation of the singlet axial current and the axial anomaly, which will be discussed in detail in Chapter 6 . In addition, gluons can contribute to $g_1$ to first order in $\alpha_s$. While one expects that $\Delta\Sigma \simeq 1$ as measured

at low $Q^2$, the connection to the DIS measurements is not unique. We will defer the detailed discussion of the QCD analysis to Chapter 6. It suffices to say here that a relative consensus on this issue developed only recently.

The next experimental challenge was to measure the spin structure of the neutron to test the Bjorken sum rule. Since a free neutron target is not feasible, two alternative approaches were pursued. At CERN a Spin Muon collaboration (SMC) was formed to specifically study the nucleon spin structure. To obtain data on the neutron [36] they used a deuterated butanol target. The deuteron is equivalent to a sum of the neutron and the proton up to small nuclear corrections. A deuterated solid target can be as thick as a proton target, which is very important for statistics limited muon experiments. On the other hand, the proton asymmetry is large, while the neutron asymmetry is small. So, to extract the neutron data from measurements on the deuteron, one has to subtract a large proton asymmetry from a large deuteron asymmetry to get a small neutron asymmetry. In the process of this subtraction both the statistical and the systematic errors are amplified. The experiment used a new target similar in design to the EMC target, and the muon polarization was measured directly by looking at the asymmetry of the muon decays, whereas the EMC experiment determined the muon polarization based on a Monte Carlo.

At approximately the same time a new spin structure program was started at SLAC. To obtain the data on the neutron the E-142 collaboration used a $^3$He gas target [37]. In $^3$He the two protons are combined in a spin-0 state because of the Pauli exclusion principle, and the spin of $^3$He is mostly due to a single neutron. Thus, one is sensitive directly to the neutron asymmetry. The thickness of the gas target is much smaller than a solid target, but this is not a problem for a high intensity electron beam at SLAC. The $^3$He was polarized by spin exchange with optically pumped Rb atoms. In many aspects the polarized target [38] was similar to the target used for this experiment. The target polarization was on average 33% during the run. The polarized electron beam was produced by photoemission from an unstrained GaAs crystal. This technique has a theoretical polarization limit of 50%, and the average polarization during the run was 36%. Its main advantage is a larger beam current. The number of electrons per pulse was $3 \times 10^{11}$, 3 orders of magnitude higher than in E80/E130. Despite lower target and beam polarizations, the results of E-142 had much smaller statistical errors than SMC because of a much larger event sample.

Following the neutron experiments, both SLAC (E-143) [39] and CERN (SMC) [40] conducted the second round of experiments with proton targets. They also used a deuterium solid target to obtain another measurement of the neutron spin structure [41, 42]. A new experimental program (HERMES) to study the nucleon spin structure recently started at DESY. During their first run a $^3$He target was used to make a measurement on the neutron [43]. For the HERMES experiment polarized $^3$He was injected directly into the beam line of a positron storage ring at DESY, providing an

"internal target". While the target thickness is very small, it is compensated by a very large current in the storage ring. Such a target is also free from any dilution due to scattering from unpolarized material. HERMES used the technique of metastability-exchange pumping to polarize $^3$He. They achieved an average 50% target polarization and 60% beam polarization. Their first results were released concurrently with our data.

Thus, at present there is a relatively large number of polarized spin structure measurements, whose results are shown in Figure 2.4 for the proton and Figure 2.5 for the neutron.

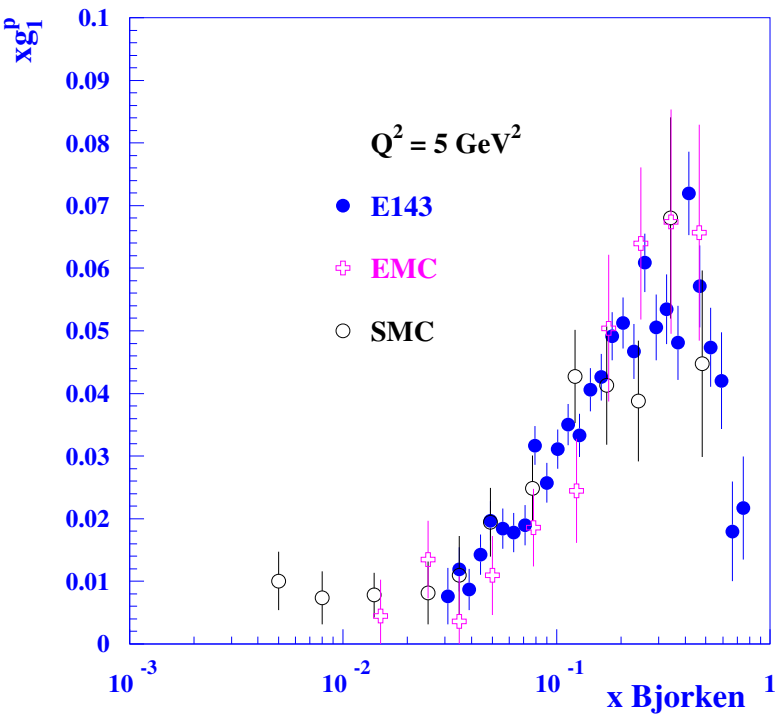


Figure 2.4: World data on the proton spin structure function $g_1^p$. Note that $xg_1^p$ is plotted on the vertical axis.

As can be seen, there is a substantial amount of data, which are consistent with each other. However, the errors of the structure function $g_1$ are much larger than, for example, unpolarized structure function $F_2$. There is clearly room for more accurate measurements. This is particularly true in the low $x$ region, where only SMC data are available. The low $x$ region is very important for extrapolation to $x = 0$, which is necessary to test the sum rules. Therefore, our experiment was designed to achieve substantially higher accuracy than any previous measurements, and also to extend the precision data down to $x = 0.014$, below previous SLAC experiments.

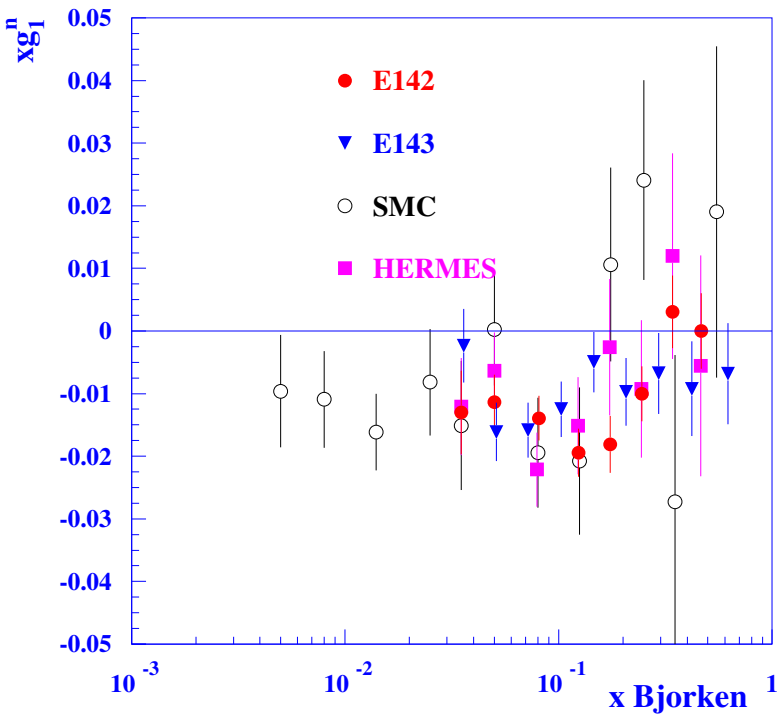


Figure 2.5: World data on the neutron spin structure function $g_1^n$. Note that $xg_1^n$ is plotted on the vertical axis.

# Bibliography


[1] E.D. Bloom *et al*, Phys. Rev. Lett. **23**, 930 (1969); J.I. Friedman and H.W. Kendall, Annu. Rev. Nucl. Part. Sci. **22**, 203 (1972).

[2] F. Halzen and A. Martin, *Quarks and Leptons* (John Willey and So., New York, 1984).

[3] A.V. Monohar in *Symmetry and Spin in the Standard Model*, B.A. Campbell *et al.* ed. (World Scientific, Singapore,1992).

[4] J.D. Bjorken and E.A. Paschos, Phys. Rev. **185**, 1975 (1969).

[5] R.P. Feynman, Phys. Rev. Lett. **23**, 1415 (1969).

[6] M. Gell-Mann, Phys. Lett. **8**, 214 (1964); G. Zweig, CERN preprint TH401, 412 (1964).

[7] I. Hinchliffe and A. Kwiatkowski, Annu. Rev. Nucl. Part. Sci. **46**, 609 (1996).

[8] J.D. Bjorken, Phys. Rev. **148**, 1467 (1966).

[9] J. Ellis and R.L. Jaffe, Phys. Rev. D **9**, 1444 (1974); Erratum, D **10**, 1669 (1974).

[10] E.D. Commins and P.H. Bucksbaum, *Weak Interactions of Leptons and Quarks*, (Cambridge Univ. Press, Cambridge, 1983).

[11] R.M. Barnett *et al.*, (Particle Data Group), Phys. Rev. D **54**, (1996).

[12] R.P. Feynman, *Photon-Hadron Interactions*, p. 159 (W.A. Benjamin, Inc., Reading, Mass., 1972)

[13] H. Y. Cheng, Int. J. Mod. Phys. **11**, 5109 (1996).

[14] T. Pussieux and R. Windmolders in *Internal Spin Structure of the Nucleon*, V. Hughes and C. Cavata ed. (World Scientific, Singapore, 1995).

[15] U. Stiegler, Phys. Rep. **277**, 1 (1996).

[16] C. Callan and D.J. Gross, Phys. Rev. Lett. **22**, 156 (1969).

[17] G.R. Farrar and D.R. Jackson, Phys. Rev. Lett. **35**, 1416 (1975).

[18] M. Arneodo *et al.*, (the NMC Collaboration), Phys. Lett. B **B364**, 107 (1995).

[19] L.W. Whitlow *et al.*, Phys. Lett B **250**, 193 (1990).

[20] R. L. Heinmann, Nucl. Phys. B **64**, 429 (1973).

[21] J. Ellis and M. Karliner, Phys. Lett. B **213**, 73 (1988).

[22] F.E. Close and R. G. Roberts, Phys. Rev. Lett. **60**, 1471 (1988).

[23] S.D. Bass and P.V. Landshoff, Phys. Lett. B **336**, 537 (1994).

[24] J. Bartels, B. I. Ermolaev, and M.G. Ryskin, Z. Phys. C **70**, 273 (1996).

[25] M.J. Alguard *et al*, Phys. Rev. Lett. **37**, 1261 (1976); Phys. Rev. Lett. **41**, 70 (1978).

[26] C.D. Jeffries, *Dynamical Nuclear Orientation*, (Interscience Publishers, New York, 1963).

[27] G. Baum *et al*, Phys. Rev. Lett. **51**, 1135 (1983).

[28] J. Ashman *et al.* (the EMC Collaboration), Phys. Lett. B **206**, 364 (1988); Nucl. Phys. B **328**, 1 (1989).

[29] R.L. Jaffe, Phys. Lett. B **193**, 101 (1987).

[30] M. Anselmino, A. Efremov, and E. Leader, Phys. Rep. **261**, 1 (1995).

[31] H. Y. Cheng, Int. J. Mod. Phys. A **11**, 5109, (1996) (also hep-ph/9607254).

[32] G. Ramsey, hep-ph/9702227, submitted to Prog. Part. Nucl. Phys.

[33] B. L. Ioffe, hep-ph/9511401

[34] J. Ellis and M Karliner, hep-ph/9601280

[35] B. Frois, Prog. Part. Nucl. Phys. **34**, 87 (1995).

[36] B. Adeva *et al.*, (the SMC Collaboration), Phys. Lett. B **302**, 533 (1993).

[37] P.L. Anthony *et al.*, (the E-142 Collaboration), Phys. Rev. Lett. **71**, 959 (1993); Phys. Rev. D **54**, 6620 (1996).

[38] H. Middleton, Ph.D. Dissertation, Princeton University, (1994).

[39] K. Abe *et al.*, (the E-143 Collaboration), Phys. Rev. Lett. **74**, 346, (1995).

[40] D. Adams *et al.*, (the SMC Collaboration), Phys. Lett. B **329**, 399, (1994).

[41] K. Abe *et al.*, (the E-143 Collaboration), Phys. Rev. Lett. **75**, 25, (1995).

[42] D. Adams *et al.*, (the SMC Collaboration), Phys. Lett. B **357**, 248, (1995).

[43] K. Ackerstaff *et al.*, (the HERMES Collaboration), hep-ex/9703005 (1997).

# Chapter 3

# The E-154 Experiment

The experiment was conducted at Stanford Linear Accelerator Center[1] in Menlo Park, California. The accelerator provides a polarized electron beam with energy up to 50 GeV. A new beam line was constructed to direct the electrons into the End Station A (ESA), were the experiment was conducted. The polarization of the electrons was measured in the ESA using a single arm Møller polarimeter. The electrons were scattered from a polarized $^3$He target and detected in two spectrometers, one located at approximately 2.75° and the other at 5.5°. Each spectrometer consisted of 2 Cherenkov tanks, several hodoscope planes and a shower counter. In this experiment no hardware trigger was used. All data collected during a beam pulse were digitized and stored on tape for later off-line analysis. The data were collected during a 2 month run in October and November of 1995. In this chapter I describe the experimental setup and data analysis unrelated to the polarized target.

## 3.1 Polarized Electron Beam

The polarized electrons at SLAC are produced by photoemission from a strained GaAs cathode. For a review of polarized electron sources see [1] and references therein. The SLAC source, in particular, is described in [2]. The level diagram of the conduction and valence bands in strained GaAs crystal is shown in Figure 3.1 [2]. The valence band consists of $P_{3/2}$ and $P_{1/2}$ levels which are split by spin-orbit interaction $\Delta_{SO}$. By introducing a uniaxial strain in the crystal one can also split the $P_{3/2}$ level into sublevels with different values of $|m_j|$ (light holes and heavy holes). In effect, the strain induces a quadrupole splitting. The amount of splitting $\delta$ is approximately proportional to the strain. A circularly polarized laser beam is used to excite the electrons from the valence band to the conduction band. If the laser is tuned to have an energy between $E_g$ and $E_g + \delta$, then only electrons from the $P_{3/2}$, $m_j = -3/2$ state

[1] The accelerator is operated by the U.S. Department of Energy.

can be excited to the $S_{1/2}$, $m_j = -1/2$ state for right circularly polarized light. Thus, the polarization of the electrons in the conduction band can theoretically reach 100%. If the crystal is not strained, the $P_{3/2}$ state is four-fold degenerate and the maximum polarization is limited to $(3-1)/(3+1) = 50\%$. To achieve high polarization the splitting $\delta$ should be larger than the width of the levels due to crystal defects and thermal smearing.

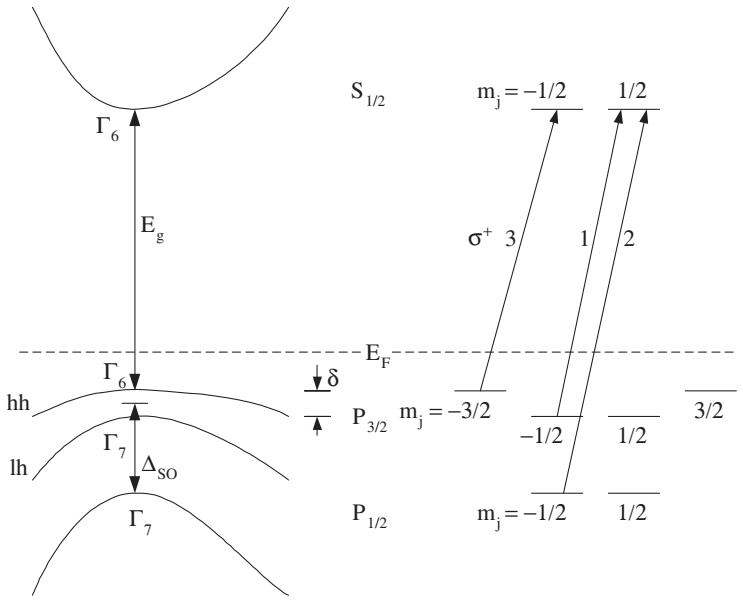


Figure 3.1: The energy level diagram for strained GaAs crystal. The numbers next to the transition lines indicate relative transition strength.

The strain is achieved by growing GaAs on a substrate of $GaAs_{0.72}P_{0.28}$ as shown in Figure 3.2. $GaAs_{0.72}P_{0.28}$ has a lattice spacing smaller by about 1% than the spacing in pure GaAs and therefore results in tensile stress of the GaAs active layer [3, 4]. The active layer is sufficiently thin to prevent relaxation of the strain. Finally, a critical feature of a photoemission cathode is its negative electron affinity (NEA). The behavior of the energy levels near the surface of the cathode is shown in Figure 3.3. A very thin film of Cs-F lowers the energy of the conduction band below the vacuum energy, which allows the excited electrons to escape from the crystal. The cathode is maintained at a negative voltage of 60-120 kV which gives the electrons an initial acceleration. Then they are magnetically focused, accelerated by RF fields and injected into the linear accelerator.

To achieve NEA it is extremely important to have a very clean cathode surface and very high vacuum when the Cs-F film is formed. The overall probability for the electron to diffuse to the surface of the crystal and escape, before decaying back to the

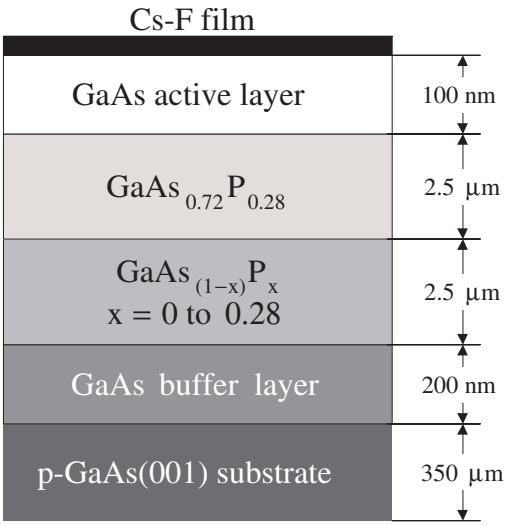


Figure 3.2: The layered structure of the strained GaAs cathode.

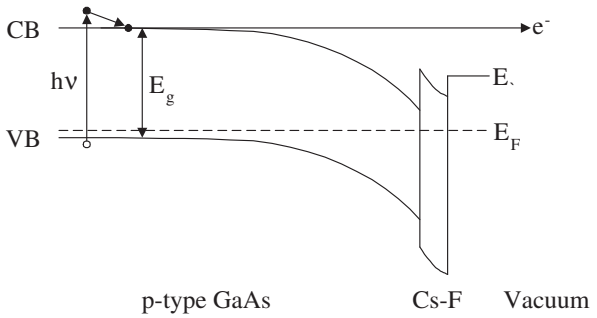


Figure 3.3: Deposition of a Cs-F film on the surface results in a negative workfunction for the electrons in the conduction band.

valence band is called the quantum efficiency (QE) of the cathode. For the cathodes used at SLAC over the last several years the QE varied from 0.007 to 10%. This indicates how sensitive the cathodes are to the preparation process. The combination of high vacuum and high voltage requirements make the polarized source an extremely complicated and delicate device. The SLAC source operates with ultrahigh vacuum at $10^{-11}$ torr and 40 kV/cm electric field gradient with a leakage current of 10nA. A special system is implemented that allows to install the cathode without breaking the vacuum. The Cs film on the surface of the cathode is periodically replenished (a process called cesiation) by an automated system. The overall reliability of the source is over 95%.

The cathode is pumped by a flashlamp-pumped Ti:Sapphire laser which delivers

~200 ns pulses with an energy of 80 $\mu$J. The circular polarization of the light is controlled by fast Pockel cells. For each pulse the polarization is chosen by a pseudo-random number generator. This information is sent via several channels (polarization bits) to the data acquisition system. Feedback systems control the intensity of the laser pulses to minimize the charge asymmetry between the left and right handed electron pulses.

The electrons from the source are accelerated to about 48 GeV by 240 klystrons in a 2-mile long linear accelerator. A new beam-line was constructed to deflect the electrons to the End Station through a 24.5° angle. When an electron is deflected, its spin processes due to the anomalous magnetic moment $a_e = (g-2)/2$. The amount of the precession is related to the deflection angle [5, 6]:

$$\theta_{prec} = \gamma \frac{g-2}{2} \theta_{bend} \tag{3.1}$$

The factor of $\gamma$ can be thought of as due to the time dilation in the rest frame of the electron. Longitudinally polarized electrons remain longitudinally polarized if $\theta_{prec}$ is a multiple of $\pi$. This implies that full polarization can only be achieved at a discrete set of energies, and also allows one to measure the energy of the beam very precisely by measuring its polarization. In our experiment $\theta_{bend} = 24.5°$ and $\theta_{prec} = 15\pi$ for electron energy of 48.35 GeV in the ESA (about 400 MeV are lost due to synchrotron radiation in the bend).

## 3.2 Møller Polarimeter

The beam polarization was measured in the ESA using a single arm Møller polarimeter [7, 8]. Møller scattering is elastic scattering of electrons on electrons. The scattering cross-section is strongly spin dependent due to helicity conservation (see Chapter 2). To calculate the cross-section we can virtually carry over the results from Chapter 2 for an elementary Dirac particle. The only modification is due to the fact that the electrons are indistinguishable particles, which results in a contribution from an additional diagram with initial and final particles interchanged. The result, written in the center of mass frame, is [8]:

$$\frac{d\sigma}{d\Omega} = \frac{\alpha^2}{s} \frac{\left(3+\cos^2\theta\right)^2}{\sin^4\theta} \left(1 - P_B P_T A(\theta)\right) \tag{3.2}$$

$$A(\theta) = \frac{\left(7+\cos^2\theta\right)\sin^2\theta}{\left(3+\cos^2\theta\right)^2} \tag{3.3}$$

The asymmetry is maximum for the center of mass scattering angle of $\theta_{CM} = 90°$ and is equal to $A(90°) = 7/9$. For $\theta_{CM} = 90°$ scattering in the lab frame both

electrons have the same energy ($E_{beam}/2$) and scatter by an equal, but opposite angle $\theta_{LAB} = 0.26°$.

The measured asymmetry

$$A_m = \frac{\sigma^{\uparrow\downarrow} - \sigma^{\uparrow\uparrow}}{\sigma^{\uparrow\downarrow} + \sigma^{\uparrow\uparrow}} = P_B P_T A\left(\theta_{CM}\right) \tag{3.4}$$

is proportional to the beam and target polarizations and can be used to measure the beam polarization if the target polarization is known.

A ferromagnetic material is usually used as a target of polarized electrons. In our case the target was a foil made of 49% Fe, 49% Co and 2% Va. This is a soft ferromagnetic material, and it is driven to saturation by placing the foil in an 100 G magnetic field. Only 2 electrons in Fe and Va are polarized, so the average electron polarization is about 8%. The foils are 3 cm wide, 35 cm long and range in thickness from 20 $\mu m$ to 154 $\mu m$, although the bulk of the data was collected with a 40 $\mu m$ foil. Because the foil is very thin, it can only be magnetized along its plane. This follows from the boundary conditions on $B$ and $H$ fields [5]:

$$B_1 \cdot n = B_2 \cdot n \tag{3.5}$$

$$B_1 \times n = \frac{\mu_1}{\mu_2} B_2 \times n \tag{3.6}$$

$$H_1 \cdot n = \frac{\mu_2}{\mu_1} H_2 \cdot n \tag{3.7}$$

$$H_1 \times n = H_2 \times n \tag{3.8}$$

Thus, the normal component of the magnetic field $B$ has to be continues across the boundary, while the parallel component increases by the ratio of the magnetic permeabilities. Therefore, for maximum asymmetry the foil should be placed parallel to the beam. However, the electron beam cannot travel along the foil. The solution is to place the plane of the foil at an angle, so the electron polarization along the direction of the beam is equal to $P_T \cos\theta_f$. In our case the angle was 20.7°, decreasing the target polarization by a factor of 0.935 and increasing the target thickness by a factor of 2.83.

To determine the polarization of the foil we use a pick-up coil to measure the amount of flux in the foil [9]. The coil has $N_c = 500$ turns and is wrapped around the foil. The flux through the coil is given by $\Phi = A_c B$, where $A_c$ is the cross-sectional area of the coil and $B = H + 4\pi M$. By sweeping the magnetic field from 100 G to -100 G one can reverse the direction of the magnetization. The voltage across the coil is given by $V = -d\Phi/dt$. An integrating voltmeter is used to measure

$$I_f = \int V\left(t\right) dt = \Phi_{fin} - \Phi_{in} = 2N_c \left(HA_c + 4\pi M A_f\right) \tag{3.9}$$

where $A_f$ is the cross-sectional area of the foil. The measurement is repeated without the foil in place. In the absence of the foil $B = H$. Because the foil is very thin, the $H$ field is not affected by the presence of the foil. This follows from the fact that the component of $H$ parallel to the foil is continues across the boundary. By subtracting the result of the second measurement we cancel the contribution from the $H$ field and get:

$$I_f - I_0 = 2A_f N_e 4\pi M \tag{3.10}$$

The cross-sectional area is determined by measuring the length and the mass of the foil and using the known density of the material.

To convert the foil magnetization into a value for the electron spin polarization one has to correct for the contribution of the orbital angular momentum. For the spin contribution one has $M_s = g_e \mu_B S$, where $g_e \simeq 2$ is the gyromagnetic ratio of a free electron, while for the orbital angular momentum $M_o = \mu_B L$. The magnetomechanical ratio of a material is defined by [10]: $M = g'\mu_B (L + S)$. It was measured for an alloy consisting of 50% Fe and 50% Co to be $g' = 1.916 \pm 0.002$ [11]. We assume that it is not affected by the presence of 2% of Va, however, the error is increased to 0.02 to allow for a small effect. One can show that the fraction of the angular momentum carried by the spin is $(g' - 1) / (g_e - 1)$, and the electron spin polarization is:

$$P_T = 2\frac{M}{n_e \mu_B g'} \left( \frac{g' - 1}{g_e - 1} \right) \tag{3.11}$$

The polarizations of the foils were measured several times and were reproducible to about 1%. The average polarization was 8.2% with slight differences between the foils.

The Møller electrons were deflected by a dipole magnet and detected by a silicon strip detector. A mask was put in front of the magnet to define the angular acceptance. A septum placed inside the magnet shielded unscattered electrons from the magnetic field. Two sets of silicon strip detectors were used. The top detector was finely segmented, so the elastic Møller peak was about 6 channels wide. The scattering angle in the CM frame was 94°. Five bottom detectors usually contained the peak in just one channel and covered CM angle from 93° to 104°. The raw asymmetry was about 5%.

The signals were fit to a lineshape expected for Møller scatters plus a quadratic background. The theoretical lineshapes included the effect of the correlation between the atomic motion of the electrons and their polarization. This effect, first identified by Levchuk [12], is due to the fact that the two polarized electrons in Fe and Co are in the 3D shell, while the inner shells are unpolarized. The electrons in the inner shells have a relatively larger momentum than the polarized electrons due to atomic motion. Although the momentum of the electrons is only about 100 keV, much smaller than the beam energy, it is not negligible compared with the electron

rest mass, and can alter the scattering angle by up to 10%. As a result, the elastic peak from the unpolarized inner electrons is significantly wider than the peak from the polarized electrons. This effect needs to be taken into account to extract the Møller asymmetry, otherwise it can result in errors up to 15% [13].

After the data are fitted to the appropriate lineshape, the background is subtracted, which increases the asymmetry by about 20%. This number is insensitive to particular ways of estimating the background and the lineshape. The final error in the measurement of the polarization is 2.8%, dominated by the uncertainty in the foil polarization (1.9%) and background subtraction (2%).

A number of diagnostic tests was performed with the Møller polarimeter in the beginning of the run. The frequency of the Ti-Sapphire laser pumping the cathode was scanned from 840 nm to 850 nm which changed the polarization from 76% to 80% with a maximum near 850 nm. The energy of the beam was scanned, mapping out one half of the oscillation cycle due to the anomalous magnetic moment (see equation 3.1). The polarization was observed to change sign when the energy was reduced from 48.3 to 46.5 GeV. Based on the fit to these data the energy of the beam was determined independently of the magnetic field measurements in the bend line. After these tests the beam polarization was very stable at an average value of 82.4%. It was found to increase slightly when the beam current was reduced from $9\times10^{10}$ to $(3 - 5)\times10^{10}$ electrons per pulse. A plot of the polarization vs. run number for the experiment is shown in Figure 3.4.

## 3.3 Spectrometers

The overall spectrometer layout is shown in Figure 3.5. The experiment utilized two separate spectrometers which detected the electrons scattered by approximately 2.75° and 5.5° degrees. Each spectrometer consisted of a set of magnets, used for momentum determination and elimination of neutral backgrounds, and a detector package to track the scattered particles.

The spectrometers were designed to have a broad kinematic coverage from 10 to 44 GeV. To eliminate the background from neutral particles the spectrometers had a "double bounce" geometry, which means that the neutral particles had to scatter at least twice from the magnets or the collimators to reach the detectors [14, 15]. The two dipole magnets in each spectrometer bent the electrons in the vertical plane in opposite directions, while the quadrupole in the 2.75° spectrometer defocused the electrons to reduce rates per detector element. Collimators were used to define the acceptance of the spectrometer. The position of the collimators in the 2.75° spectrometer was adjusted during the run to provide a constant rate as the beam current and target thickness were changed. Figure 3.6 shows the kinematic coverage in the $x - Q^2$ plane by the spectrometers. The field of the magnets was mapped prior

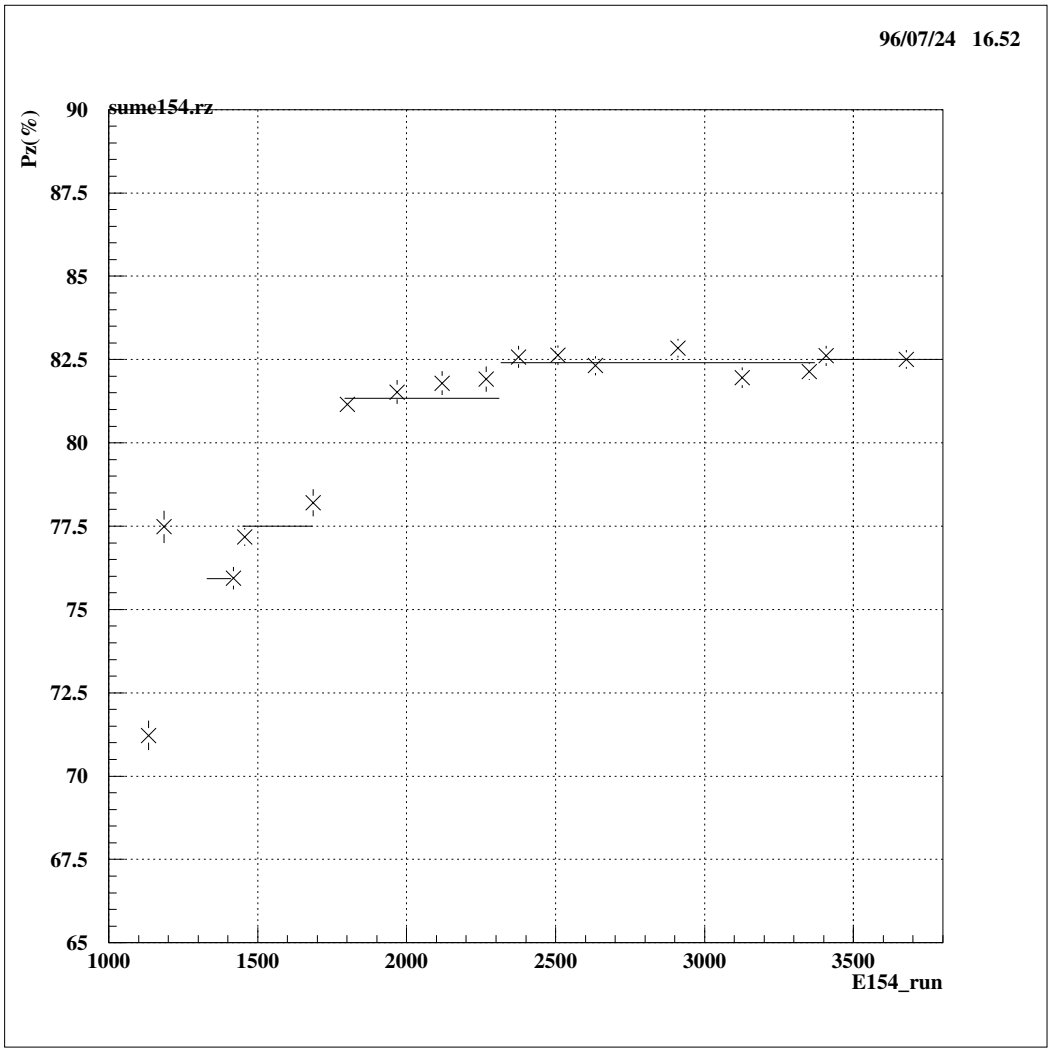


Figure 3.4: The polarization of the electron beam vs. run number.

to the experiment. They were monitored during the experiment by NMR probes. An optics model was constructed which provided a mapping between the position and direction of a track in the spectrometer and the initial momentum and angle of the scattered electron [16]. The calibration of the spectrometer was checked by a special 8 GeV run in which the energy of the proton elastic peak was measured.

The detector system in each spectrometer consisted of 2 Cherenkov tanks, 2 banks of hodoscopes and a shower counter. It was designed to identify the scattered electrons and measure their momentum and scattering angle in the presence of a large background of pions and neutral particles.

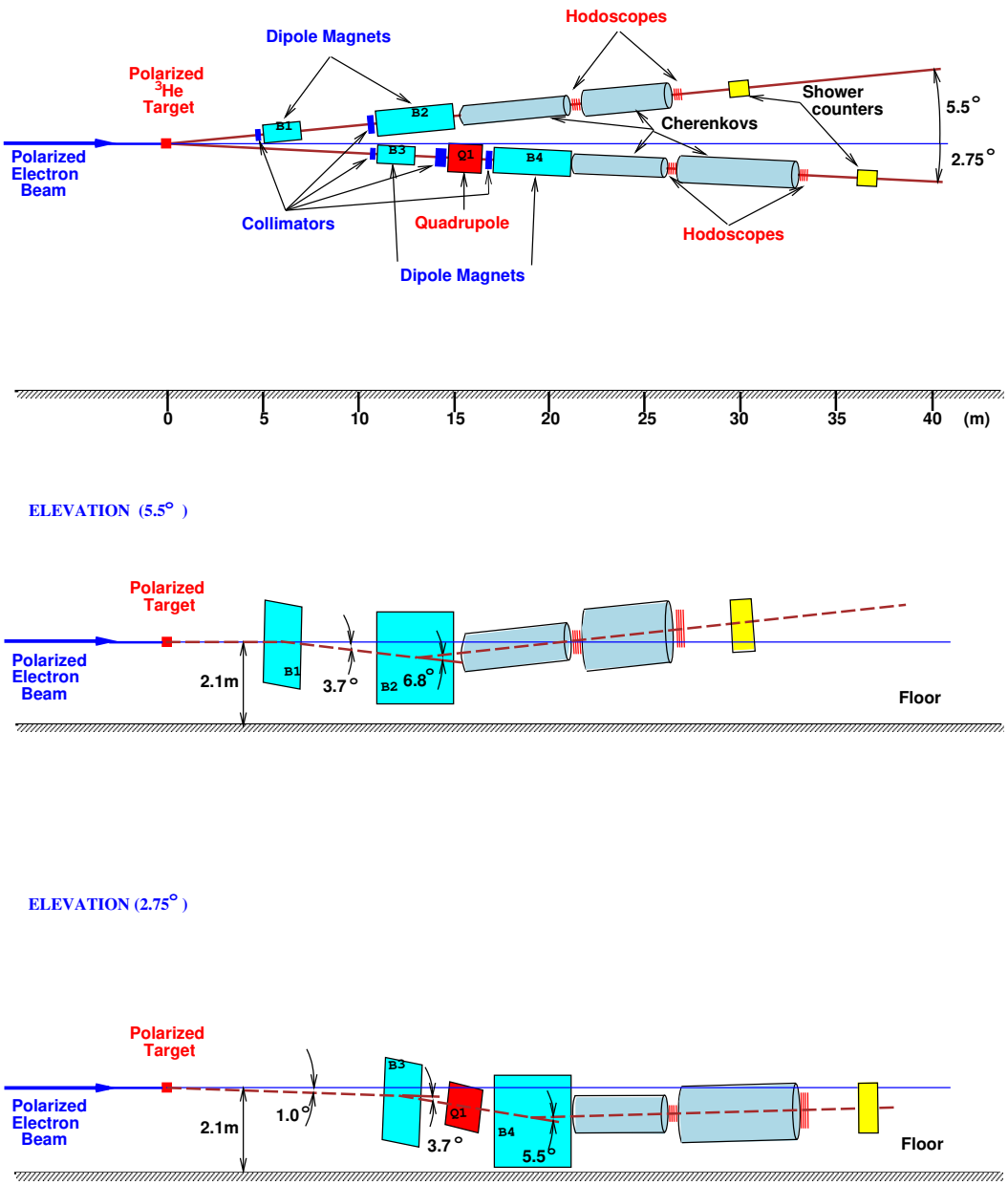


Figure 3.5: Layout of the E-154 spectrometers.

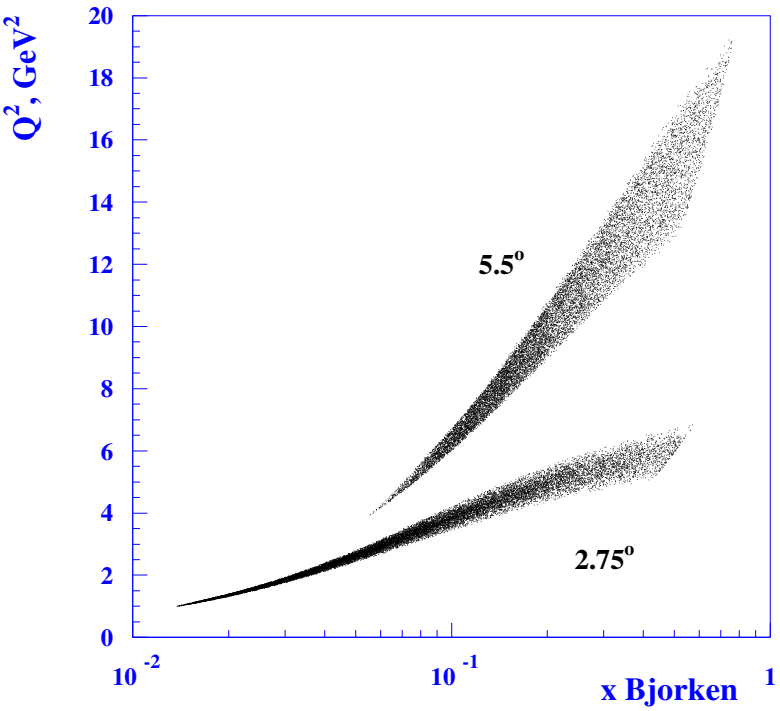


Figure 3.6: The kinematic coverage of the E-154 spectrometers.

The Cherenkov counters were used in the threshold regime to discriminate between electrons and pions. Cherenkov radiation is created by a particle traveling through a medium with a velocity greater than the velocity of light in the medium. The threshold for production of Cherenkov light is:

$$\beta = \frac{p}{\sqrt{p^2 + m^2}} > 1/n \tag{3.12}$$

where $n$ is the index of refraction of the medium. The momentum threshold for pions is $p_{th} = m_\pi \left(\Delta\varepsilon\right)^{-1/2}$, where $\Delta\varepsilon$ is the deviation of the dielectric constant from unity, $n = \sqrt{1 + \Delta\varepsilon}$. $\Delta\varepsilon$ for a gas is proportional to its density and can be easily adjusted.

The number of Cherenkov photons emitted by the electron per unit length and wavelength is given by [5, 17]:

$$\frac{d^2N}{dxd\lambda} = \frac{2\pi\alpha}{\lambda^2}\left(1 - \frac{1}{\beta^2 n^2}\right) = \frac{2\pi\alpha}{\lambda^2}\Delta\varepsilon \tag{3.13}$$

In the last expression we used the fact that for electrons $\beta$ is very close to unity. For pions above the threshold the number of photons is suppressed by an additional factor of $(1 - p_{th}^2/p^2)$. The photons are focused by a mirror onto a Photo-Multiplier Tube (PMT). The number of photoelectrons produced in the PMT is a Poisson distribution

with a mean given by:

$$N_{pe} = 2\pi\alpha L \int d\lambda QE\left(\lambda\right)\Delta\varepsilon\left(\lambda\right)/\lambda^2 \tag{3.14}$$

where $L$ is length of the tank and $QE\left(\lambda\right)$ is the quantum efficiency for collecting the photons and converting them to photoelectrons on the PMT cathode. We would like $N_{pe}$ to be sufficiently large so the probability of detecting zero photoelectrons $P(0) = e^{-N_{pe}}$ is small. For $P\left(0\right) < 1\%$ we need $N_{pe} > 4.6$. The pion production cross-section in deep inelastic scattering drops very fast with energy and becomes small for energies higher than 20 GeV. We would like to set the pion threshold to approximately that energy, while keeping the electron detection inefficiency $P\left(0\right)$ sufficiently small. To satisfy both requirements the length of the tank has to be rather large.

We choose $N_2$ gas as the media for two reasons. It has a low scintillation rate, which is important because pions can produce light by scintillation even below the Cherenkov threshold. The average number of photoelectrons due to scintillation was estimated to be 0.1 per particle [18]. In addition, $N_2$ gas has high UV transmission down to 140 nm and the Cherenkov light spectrum is weighted toward short wavelength by a factor of $1/\lambda^2$.

The parameters of the Cherenkov tanks are shown in Table 3.1. For 2C1 tank, for example, $\Delta\varepsilon = 5.2 \times 10^{-5}$ for $N_2$ pressure of 1.4 psia [19] giving a threshold for $\pi^-$ of 19.3 GeV. The photons are emitted at an angle of $0.41^\circ$ to the electron track. They are collected by spherical mirrors and imaged onto a Hamamatsu R1584 photomultiplier tube. The mirrors use an Al film and have reflectivity higher than 75% up to 160 nm [20]. The phototubes have a spectral range from 200 to 640 nm with 15-20% quantum efficiency. To detect the photons in the UV an organic wavelength shifter is deposited on the front face of the photomultiplier tubes. It absorbs photons in the range 115-310 nm and reemits them at 370 nm. Based on the manufacturer's specifications for the quantum efficiency of the PMT and the wavelength shifter and measured reflectivity of the mirrors as a function of wavelength, the predicted number of photoelectrons is about $6 - 8$ [21], which is very close to the observed number of 5.7. In contrast, according to the Particle Data Group [17] rule of thumb, the number of photoelectrons for our system is expected to be about 2.5.

The output of the PMTs was recorded by a 256 bit Flash Analog-to-Digital Converter (FADC) in 1 ns. intervals over the entire duration of the beam pulse (250 ns). The FADC consisted of 4 channels running at clock speed of 250 MHz which were interleaved, giving an effective 1 ns. resolution. The digitized waveform was stored on tape for later analysis. In addition, the last dynode of the PMT was connected to a Time-to Digital Converter (TDC) which recorded the time of the pulses whose height exceeded a preset threshold.

| Tank | Pion Threshold (GeV) | Effective Legth (m) | Mirror Curvature (m) | Pressure (psia) | Observed $N_{pe}$ |
|---|---|---|---|---|---|
| 2C1 | 19 | 5.3 | 1.2 | 1.4 | 5.7 |
| 2C2 | 19 | 6.1 | 1.6 | 1.4 | 5.1 |
| 5C1 | 16 | 5.6 | 1.2 | 2.0 | 6.2 |
| 5C2 | 16 | 4.0 | 1.6 | 2.0 | 5.0 |

Table 3.1: Parameters of the Cherenkov detectors

The hodoscope system used for tracking consisted of a number of finely segmented plastic scintillation counters. Passage of charged particles though the plastic causes scintillation in the UV region. By adding a small amount of organic wavelength shifter, this radiation is converted to visible photons, in our case at 408 nm. Approximately 10-15 photons were emitted for each particle [22]. The photons propagate down the plastic scintillator by total internal reflection and reflection from aluminum foil which is wrapped around each finger. A PMT mounted on one end of the finger is used to detect the photons. Its output is connected to a multihit TDC which records the time(s) of particle passage. Because of a large pion background, it was critical to have a very finely segmented hodoscope to reduce the rate per detector element and the dead time. A total of 10 (8) planes of hodoscopes were used in 2.75°(5.5°) degree spectrometer with a total of 784 channels. For better coverage, the fingers in each hodoscope plane overlapped by about 1/3 of their width.

An electromagnetic calorimeter at the end of the spectrometer was used to measure the energy of the electrons and provide additional discrimination between electrons and pions. Each of the two calorimeters consisted of 200 blocks of lead glass arranged in 20 rows of 10 blocks each. The blocks were made of F2 lead glass (about 42% lead) and were 6.2 cm×6.2 cm in cross-section and 75 cm long [23].

High energy electrons lose energy in the shower counter by emitting high energy bremsstrahlung photons which in turn produce $e^+e^-$ pairs. This results in a cascade effect and a large number of photons and electrons/positrons is created. The radiation length $X_0$ is defined as the length over which the initial electron losses all but $1/e$ of its energy to bremsstrahlung. The characteristic pair production length for a high energy photon is $(7/9)\,X_0$. Thus, the length scale of the shower is governed by $X_0$. For our glass $X_0 = 3.17$ cm [24]. As the energy of the electrons decreases, the loss by ionization starts to dominate over bremsstrahlung. This energy is called the critical energy $E_c$. In our material $E_c \simeq 13.9$ MeV. The electrons and positrons created by the shower emit Cherenkov radiation in the lead glass, which has an index of refraction $n = 1.58$. A PMT is mounted at the end of each block to detect the Cherenkov light. The number of Cherenkov photons is proportional to the total track length of all electrons/positrons created by the shower, which is proportional to the

shower energy. Therefore, the integrated PMT signal is proportional to the energy deposited in each block. An Analog-to-Digital Converter (ADC) is used to measure the integral of the PMT signal over the pulse length. In addition, multihit TDCs record the time(s) of the pulses that exceeded a preset threshold.

The longitudinal profile of the shower is approximately given by [25]:

$$\frac{dE}{dz} \sim \left(\frac{z}{X_0}\right)^{\alpha} e^{-z/\lambda X_o} \tag{3.15}$$

where $\lambda \approx 1.9$, and $\alpha = \ln\left(E/E_c\right)/\lambda$. The peak energy deposition occurs at (7 - 8) $X_0$. The total length of our lead blocks is 23.6 radiation length and the electromagnetic shower is entirely contained within the calorimeter.

The transverse shower profile is due to Coulomb scattering of the electrons and positrons during the initial stages of the shower development [25]. It is usually parameterized by a Møller radius, given by $R_M = X_0 E_s/E_c$, where $E_s = m_e c^2\sqrt{4\pi/\alpha} =$ 21.2 MeV. For our glass $R_M \approx 4.8$ cm. The transverse energy profile is approximately given by an exponential:

$$\frac{dE}{dr} \sim e^{-4r/R_m} \tag{3.16}$$

In our experiment the energy of the electron shower was contained almost entirely in 9 adjacent block, the central block containing a large fraction of the energy. At later stages of shower development the photon absorption length becomes longer and the divergence of the photons starts to contribute the shower width. This gives a broader profile in the back of the shower, so the total shape is often parameterized by two exponentials [26, 27]:

$$\frac{dE}{dr} \sim \left(e^{-r/R_1} + Ae^{-r/R_2}\right) \tag{3.17}$$

Because the number of particles in an electromagnetic shower is very large (roughly equal to $E/E_c \sim 1000$), the shower has a symmetric shape and is not affected by fluctuations.

Hadronic showers are characterized by a nuclear interaction length $\lambda_I = 35$ g/cm$^2 A^{1/3}$ [17]. For our lead glass $\lambda_I = 34$ cm, so the total shower length is only about $2\lambda_I$. Therefore, only a fraction of pion energy is deposited in the glass. Engelmann *et al.* [28] studied the energy deposition for a monoenergetic pion beam in a 24.2 radiation length calorimeter made of similar F2 lead glass ($X_0 = 3.22$ cm). They found that about 17% of the pions do not shower, leaving only a minimum ionizing track of 0.5 GeV. The rest form a broad peak centered at 38% of their energy. The fraction of pions that deposit between 80 and 100% of their energy is only about 3%. In contrast, all electrons deposit more than 99% of their energy in the calorimeter. This allows one to use the shower counter for pion discrimination by putting a cut on the ratio of $E/p$, where $E$ is the energy deposited in the calorimeter and $p$ is the

momentum measured by tracking. For electrons it should be equal to 1. In fact, the gain of the PMTs in the shower counter was calibrated so that the $E/p$ ratio for the electrons was close to 1 and then a low $E/p$ cut was used for pion discrimination. Figure 3.7 shows the histogram of $E/p$ ratios for electrons and pions in our calorimeter. The electrons and pions were selected by applying a cut on the Cherenkov pulses (large pulses in both tanks for the electrons, no pulses for pions). As can be seen, the separation between electrons and pions is very clean.

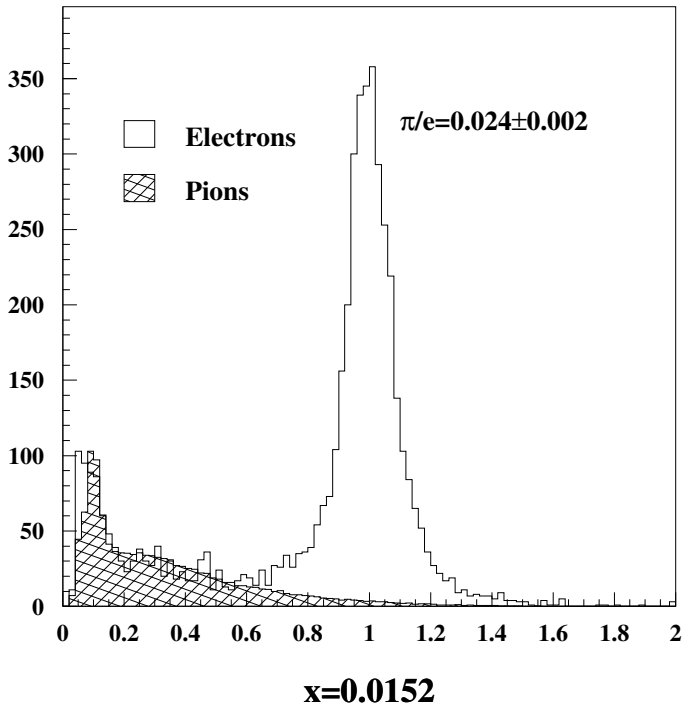


Figure 3.7: The $E/p$ ratio for electrons (open) and pions (hatched).

The transverse shape of the shower (i.e. the relative amount of energy deposited in adjacent blocks) can be used for additional pion discrimination [28]. The shape of the electron shower is highly regular and is described by equation (3.17). For pions, the shower is broader because of a larger nuclear interaction length $\lambda_I$. In addition, because a small number of particles is produced in the shower, there are large fluctuations. Some of the energy can be converted to $\pi^0$ (for example, via charge exchange $\pi^- p \to \pi^0 n$) which decays into $2\gamma$ and produces an EM cascade. If a $\pi^-$ converts to $\pi^0$ in the very front of the calorimeter, it will deposit most of its energy, and the shape of its shower will be indistinguishable from that of an electron shower. In other cases, a $\pi^0$ is produced later during the shower development and the transverse profile of the shower is highly asymmetric.

Several other hardware elements were used in the experiment. The beam current was monitored by two toroids, which detected the voltage induced in a toroidal coil placed around the beam as the an electron pulse went through. The beam position was monitored by a wire array, which consisted of a grid of wires spaced by about 1 mm. As the beam went through the wires, it induced a voltage proportional to the beam intensity. This allowed measurements of the beam position and width in both dimensions. In addition, traveling wave beam position monitors (TWBPM) were used to determine the beam position. The quality of the beam was monitored by a set of two scintillation counters, called the "Good spill" and "Bad spill". The good spill counter was placed in the ESA downstream of the target. It was a large area scintillator that essentially measured an average particle flux scattered from the target. The shape of the signal provided direct information about the time structure of the beam and was used by accelerator operators for tuning. The "Bad spill" monitor was placed upstream of the target. Any signal in this counter indicated that the beam was scattering from the walls of the beam pipe or had a large halo. This information was also used by the operators and gave the shift crew a concrete reason to complain about the quality of the beam. The rate in various detector elements was monitored by scalers, which counted the number of pulses per spill. This information was used for quick diagnostic. Various operating parameters (i.e high voltages, magnet currents, Cherenkov pressures) were recorded periodically. An automated program monitored their status and set off an alarm if their values deviated from a specified range.

The data acquisition system was based on CAMAC modules, which interfaced with detector electronics, and VME processors, which controlled the writing of data to tape. The electronics were located in the 2.75° spectrometer hut, and were not accessible while the beam was on. However, they were quite reliable and required little maintaince. The data were recorded directly to an automated SLAC tape silo without operator intervention. The throughput of the data acquisition system was about 0.7-0.8 Mbytes/s. A total of 1.4 Tbytes of data were collected during the experiment. A control program, run on a local workstation, was used for menu-driven control of the data acquisition program. On-line analysis programs ran on dedicated workstations for monitoring of the detector performance.

## 3.4 Data Analysis

The data analysis was done independently by two groups, one based at SLAC and the other at Caltech. Although the basic steps of the analysis were the same, some algorithms differed between the groups. The results of the two analyses were in excellent agreement and were averaged for the final result. The following description will be based on the Caltech algorithm.

Because of the amount of data collected during the experiment, the data analysis

was done in 2 steps. First, the raw data were searched for particle tracks satisfying minimum requirements for an electron. The list of found tracks and associated detector hits was written to Data Summary Tapes (DST). This step of the analysis took 7 weeks running on four DEC Alpha 64 bit, 266 MHz workstations and reduced the amount of data by a factor of 6. Then, DSTs were analyzed, applying additional cuts and grouping the events according to their $x$ and $Q^2$ values. Resulting summary files were used in calculation of the asymmetry.

The Cherenkov data contained the digitized form of the PMT output for the entire spill. The analysis proceeded in the following steps. Pulses were detected in the waveform by looking for jumps in the derivative of the signal. The height and area of the pulse were determined. Before proceeding to the next pulse, an average pulse shape, scaled by the height of the current pulse, was subtracted from the waveform. This removed small oscillations present in the tail of the pulse. The effective dead time of the detector and the algorithm was about 5 nsec.

It was found that the time resolution can be significantly improved by using TDC information collected from the last dynode of the PMT [29]. Although the time resolution of the FADC is 1 nsec, it is achieved by interleaving 4 channels running at 250 MHz each. When the beam trigger is received, the FADC clock waits for the next tick (up to 4 nsec) before starting the data acquisition. This results in jitter of the overall time of the FADC waveform. The TDC, on the other hand, has a true 1 nsec resolution. Therefore, the TDC time of a clean pulse can be used to shift the time of the entire FADC waveform. This improved the time resolution from 1.4 to 0.8 nsec, increasing the tracking efficiency.

The analysis of the shower counter data required a more sophisticated algorithm because of the limited amount of data available. For each block of the shower counter the ADC signal gave an integral of the PMT output over the entire spill. In addition, the TDC signal gave the time of the pulse (or pulses, if they were separated by more than 20 nsec). Because of high instantaneous rate in the spectrometer, often more than one particle deposited its energy in the block during the spill. Such situation was called an overlap. It was necessary to divide the energy recorded by the ADC between the particles (energy sharing). The TDC information was used for this purpose. For the shower counter the TDCs recorded both the leading edge time (when the PMT output exceeded the threshold) and the trailing edge time (when the output dropped below the threshold). The difference between the time of the leading and the trailing edge is correlated to the height of the pulse and can be used to estimate its area. The top half of the 2.75° calorimeter, most affected by the overlaps, was equipped with three TDC's set at different thresholds to provide more information for energy sharing. The relationship between the TDC pulse width and the energy of the pulse was determined empirically from a sample of events not affected by overlaps.

The analysis proceeded in the following steps [16] (see also Appendix A). First,

local maxima in energy deposition were identified among the blocks. They formed the central blocks of "clusters". Additional blocks were assigned to the clusters based on their proximity in space and/or in time of the TDC hits. The clusters were considered for further analysis only if their total energy exceeded a minimum possible energy for an electron. This cut rejected many pions, which often deposit very little energy, at the initial step of the analysis. If any of the blocks had multiple TDC hits, their energy was shared among different hits ("cells"). The sharing was done by doing a least $\chi^2$ fit using the energy estimate and error determined from the TDC information constrained to the total ADC signal.

Further useful information can be extracted from the data by using particular physical properties of the electromagnetic shower [30], Appendix A. The transverse profile of the shower, given by equation (3.17), can be used to estimate the energy deposited in each block of the cluster based on the position of the electron hit. This can be done by integrating the shower profile over the size of the block. Using 1-dimensional version of equation (3.17) one can show that the energy deposited in the central block of width $2d$ by an electron of energy $E_0$ is:

$$E_C(x) = E_0\left[\left(1-\exp\left(-\frac{d}{R_1}\right)\cosh\left(\frac{x}{R_1}\right)\right)+A\left(1-\exp\left(-\frac{d}{R_2}\right)\cosh\left(\frac{x}{R_2}\right)\right)\right] \tag{3.18}$$

where $x$ is the distance of the electron hit from the center of the central block. The energy deposited in the side block is:

$$E_S(x) = E_0\left[\exp\left(-\frac{x}{R_1}\right)\sinh\left(\frac{d}{R_1}\right)+A\exp\left(-\frac{x}{R_2}\right)\sinh\left(\frac{d}{R_2}\right)\right] \tag{3.19}$$

Figure 3.8 shows the fraction of the electron energy deposited in a block as a function of the distance of the electron hit from the block center. If the distance is less than $d$, it is the central block, if it's greater than $d$ it is the side block. The constants in equation (3.18) are adjusted to fit the data. As can be seen, the transverse profile of the shower has a regular shape with little fluctuations and can be used to extract useful information.

The applications of the transverse shower profile in the analysis are discussed in [30], which is reproduced in Appendix A. Here we only enumerate its uses.

1. The position of the electron track can be calculated by considering the ratio of the energy deposited in the side block and the central block $E_S/E_C$. This provides a better position determination than a simple center of gravity method [26, 27]. The position determined from the shower is important because it is used as a starting point for the tracking algorithm.

2. The shower shape can be used to estimate the electron energy based on information from only a few blocks, rather then by adding the energy of all blocks

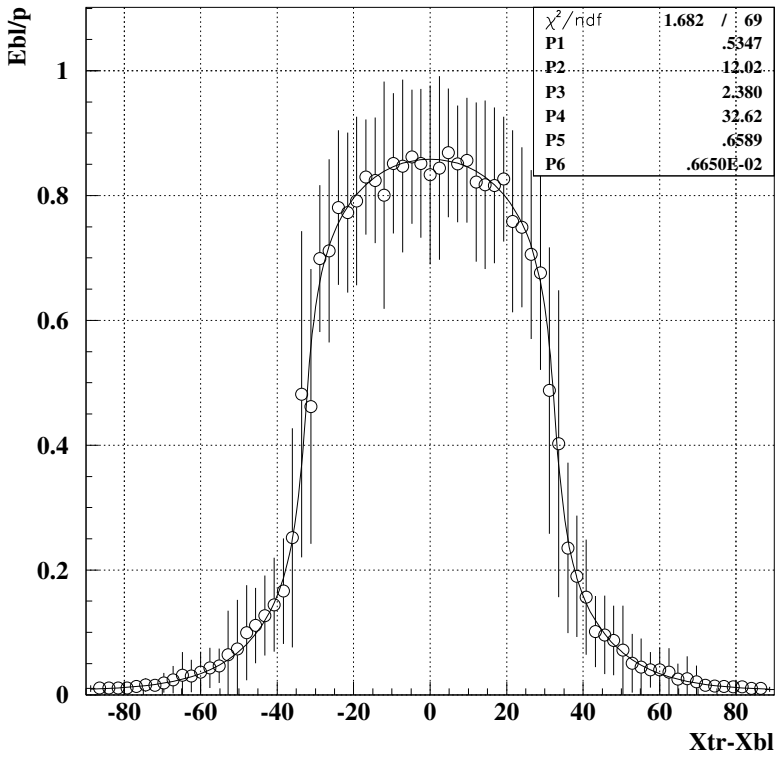


Figure 3.8: The energy deposited in a shower block as a function of the track distance from the center of the block. The error bars indicate the RMS of the distribution.

in the cluster (9 or more). This method is less affected by overlaps, since the probability of an overlap is smaller for a smaller number of blocks.

3. The energy sharing can be improved by fitting the shape of the shower to the actual energy deposition in the blocks of the cluster. The energies of the blocks affected by the overlap are adjusted to better fit the shape.

4. The shape of the shower can provide additional discrimination between the electrons and pions, since the pion shower is wider and more asymmetric than the electron shower. One can put a cut on the $\chi^2$ of the electron shower shape fit to reject the pions [28].

The SLAC analysis group used different algorithms to analyze the shower data [31, 32, 33]. For comparison of the performance of the two approaches see Appendix A.

The tracking algorithm mainly relies on the timing information from the hodoscope TDC's. The process starts by collecting information from the shower counter and the Cherenkovs to determine an initial position and time of a track candidate.

Then hodoscope elements are identified, which have hits in time and within certain kinematic cuts. These hits are grouped into miniclusters when several fingers intersect in time and space. A fitting routine is then used to minimize the $\chi^2$ of the track by varying its time and coordinates. Since there is no magnetic field inside the spectrometer, the track trajectory is a straight line. Hits in the hodoscope which give inappropriately large contribution to the $\chi^2$ are dropped as accidental. Corrections are applied for the time of light propagation in the hodoscope fingers and the Cherenkov counters (1-2 ns). The momentum of the electron can be determined from the track based on the knowledge of the field of the magnets in front of the spectrometer.

During the analysis of the DSTs, additional cuts were applied. Since all DSTs could be analyzed in three days, one could experiment with different cuts. Cuts were used to eliminate data taken under poor electron beam conditions, as determined by several beam diagnostic devices (wire arrays, TWBPM, bad and good spill). Entire runs were eliminated if the polarization of the target was too small, the hardware was malfunctioning, or the electron beam had a large charge asymmetry. Electrons were selected by making cuts on the height of the Cherenkov pulses, the $\chi^2$ of the shower shape fit and the $E/p$ ratio. The process of such selection is shown in Figure 3.9. The first plot shows the $E/p$ spectrum for all particles in the detector. A large number of pions can be eliminated simply by applying a cut on the energy of the cluster, since no electrons can have a cluster with an energy less than 10 GeV. In the Caltech analysis such cut was applied at the initial stage of the analysis, significantly reducing the amount of data. Next we apply a cut on the Cherenkov signals, which eliminates most of the pions. As a compromise between pion contamination and electron inefficiency, we require a pulse in both tanks, one of which should exceed 2.5 photoelectrons. Then we apply a cut on the $\chi^2$ of the shower shape fit, further reducing the pion background. The $E/p > 0.8$ cut is applied last.

## 3.5 Asymmetry

The asymmetry in each $x$ bin can be calculated from the data using the following formula:

$$A_{\parallel} = \frac{1}{P_b P_t f} \frac{N^{\uparrow\downarrow} - N^{\uparrow\uparrow}}{N^{\uparrow\downarrow} + N^{\uparrow\uparrow}} \tag{3.20}$$

where $N^{\uparrow\downarrow}$ ($N^{\uparrow\uparrow}$) is the number of electrons detected in that $x$ bin for the target and electron spins anti-parallel (parallel). $P_b$ and $P_t$ are the beam and target polarizations respectively and $f$ is the target dilution factor defined as:

$$f = \frac{N_{He}}{N_{He} + N_u} \tag{3.21}$$

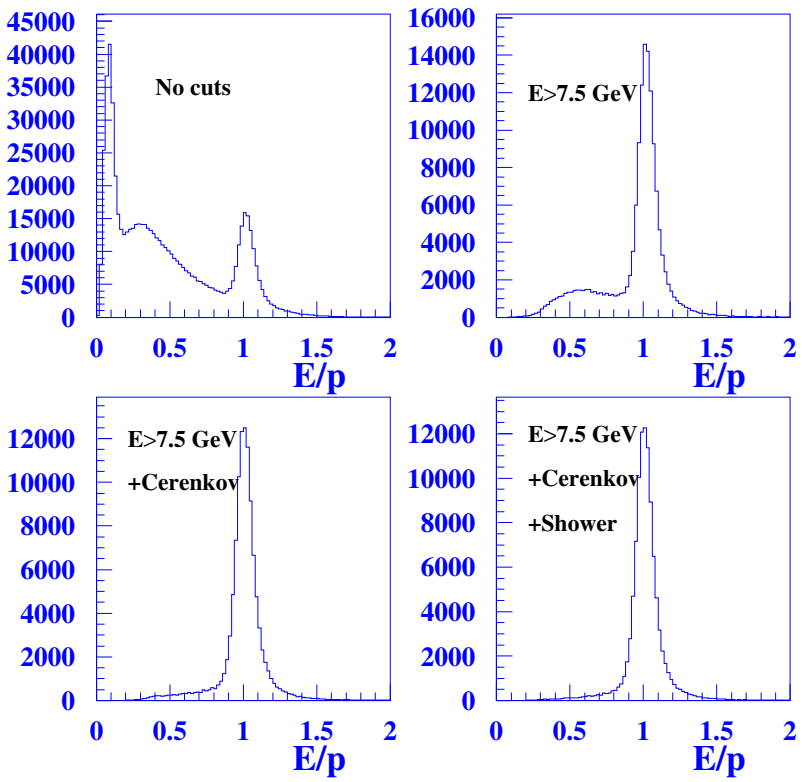


Figure 3.9: Electron selection by a series of cuts, shown from top left to bottom right

where $N_{He}$ is the number of counts from $^3$He and $N_u$ is the number of counts from the unpolarized material of the target, like the glass windows and the nitrogen gas. The target dilution factor will be discussed in Chapter 4 and the polarization in Chapter 5.

Several important corrections have to be applied to the asymmetry. One has to take into account the contamination of the electron sample by pions which were misidentified as electrons due to detector inefficiencies. Also, some electrons are produced by pair creation and do not come from deep inelastic scattering. Their contribution should be subtracted. To correct the measured asymmetry we need to know both the size of the background and its asymmetry (*c.f.* equation (3.37)):

$$A_{corr} = A_{meas}\left(1 + \frac{N_{Back}}{N_{DIS}}\right) - A_{Back}\frac{N_{Back}}{N_{DIS}} \tag{3.22}$$

The pion contamination is about $(N_{\pi^-}/N_{DIS}) = 3\%$ at low $x$, as determined by estimating the pion background under the electron $E/p$ peak (see Figure 3.7). The pion asymmetry is determined from our data by selecting a pion sample with a veto on both Cherenkovs. The asymmetry is negative and is about three times smaller than the electron asymmetry, but is not consistent with zero. The contamination by

electrons produced by pair creation (i.e. $\gamma \rightarrow e^+e^-$, $\pi^0 \rightarrow e^+e^-\gamma$) is measured in dedicated positron runs with the magnet polarity reversed. It is assumed that the number of positrons and electrons created in such processes is equal. The contamination is significant, reaching 10% in the lowest $x$ bin. The asymmetry of the positrons is consistent with zero, however the errors are large due to limited statistics. The positron asymmetry is the largest source of systematic error for our lowest $x$ bin.

Detector inefficiencies can bias the measured asymmetry (known as the rate dependence). If the efficiency of the detector $\varepsilon$ decreases with the electron rate $R$:

$$\varepsilon = \varepsilon_0 \left(1 - \beta_1 R - \beta_2 R^2 \ldots\right) \tag{3.23}$$

then the detected asymmetry is reduced compared with its true value:

$$A_{\rm det} = A \left(1 - \beta_1 R - \beta_2 R^2 \ldots\right) \tag{3.24}$$

where $\beta_1$ and $\beta_2$ are some coefficients which depend on the hardware and software performance. The experiment was designed to minimize the rate dependence. To study this effect we simulated a double rate in the spectrometer by combining the raw data from two pulses and taking into account the electronics dead time [34]. By this method we determined that $\alpha$:

$$\alpha = \frac{\varepsilon\left(R\right)}{\varepsilon\left(2R\right)} - 1 = \beta_1 R + 3\beta_2 R^2 \tag{3.25}$$

is in the range of 4-8%. Since we expect that both $\beta_1$ and $\beta_2$ are positive, but do not know their relative size, we correct the asymmetry by one half of the observed rate dependence:

$$A = \frac{A_{\rm det}}{1 - \alpha/2} \tag{3.26}$$

and include the whole size of $\alpha$ as a error.

We also apply a correction to take into account the neutral current interaction by $Z^0$ exchange. This is a parity-violating interaction which would be present even if the target were unpolarized. Thus, the sign of the electroweak asymmetry $A_W$ does not change when the target polarization is reversed, while the sign of the electromagnetic asymmetry changes. The target polarization was reversed several times during the experiment[2], and we observed a non-zero parity violating asymmetry at $4\sigma$ level.

In Chapter 2 we only considered the electron vertex shown in Figure 2.1 at the tree level. In reality, the vertex is modified by the electromagnetic radiative corrections. The effect of these corrections (known as the internal radiative corrections) should be

[2] We rely on electron polarization reversal, which is done randomly every pulse, to eliminate the systematic errors due to acceptance drifts, etc.

subtracted from the data to come back to the simple picture described in Chapter 2. In addition, the electrons can bremsstrahlung before or after deep inelastic scattering, which is taken into account by applying the external radiative corrections. The radiative corrections are discussed in detail in the next section, based on [35].

To extract the neutron spin structure function from a measurement on $^3$He one has to apply corrections due to nuclear effects. Naively, only neutron contributes to the spin asymmetry in $^3$He because the spins of the two protons are opposite to each other due to the Pauli exclusion principle. However, this naive picture is modified because the spacial wavefunction of $^3$He is not a pure S state. It has contributions from S$'$ and D states. In the S$'$ state the nucleons have a relative angular momentum with respect to each other, although the total angular momentum is zero. The spin originates from one of the protons, while the other is coupled with the neutron to a zero spin. In the D state the three nucleons have a total spin of 3/2, which is combined with 2 units of angular momentum to give a spin 1/2 nucleus. The probability of the P state is strongly suppressed because it has opposite parity. Ignoring the collective nuclear effects, one can write:

$$g_1^{He}(x) = p_n g_1^n(x) + 2p_p g_1^p(x) \tag{3.27}$$

where $p_n$ and $p_p$ are the polarizations of neutron and proton respectively in the $^3$He wavefunction. The polarizations have been calculated in [36]: $p_n = 0.87 \pm 0.02$ and $p_p = -0.028 \pm 0.004$. To subtract the proton contribution we use the world data on $g_1^p(x)$ and include their uncertainty in our systematic error. The collective nuclear effects for scattering from $^3$He are negligible in the deep inelastic region [37].

To calculate $g_1$ from the asymmetry one also needs to include a small contribution from $A_\perp$ (see equation (2.60)). We measured $A_\perp$ in a series of dedicated runs by rotating the $^3$He polarization perpendicular to the beam direction. The laser system was not setup to pump in this direction, so $^3$He polarization was decaying during these measurements. In addition to using these data for the calculation of $g_1$, we also extracted $g_2$ using equation (2.61). Our $g_2$ data [38] are consistent with zero (see equation 2.22). For more details see [38].

Finally, one should also be aware of the *higher twist effects*, which appear if $Q^2$ is not sufficiently large. They are due to the breakdown of the assumption of independent scattering from individual quarks. Their contribution is expressed as an expansion in powers of $1/Q^2$. The calculation of these corrections is difficult and their size and even sign is uncertain, but they are quite small for our values of $Q^2$ [39]. We do not apply any correction due to this effect.

## 3.6 Radiative Corrections

The radiative corrections can be split into two distinct parts. The internal corrections are due to the radiation emitted by the electrons immediately before or after the nuclear scattering. The electrons are off-shell ($q^2 \neq m^2$) between the emission of the photon and the nuclear scattering. The external corrections are due to Bremsstrahlung of the electrons in the material of the target. The electrons are on-shell between the emission of the photon and the nuclear scattering. To calculate the internal corrections we used a program POLRAD 1.5 [40], written by Shumeiko and coworkers, the same group that developed the theory of polarized radiative corrections [41, 42, 43]. The external corrections were calculated based on the technique of Tsai [44, 45].

There are two main difficulties in calculating the radiative corrections. The first is the treatment of the errors. The radiative corrections work as a non-linear and non-local transformation between the measured asymmetries and the Born asymmetry. So, they affect non-trivially not only the central values, but also the errors of the asymmetry. The second is the use various input models. Calculations of the radiative corrections require knowledge of the polarized and unpolarized structure functions for a large kinematic range, and $^3$He quasi-elastic and elastic form factors. Some of them are well known, others are more controversial.

### 3.6.1 The Structure of the Radiative Corrections

In general, the cross-section for polarized scattering can be written as:

$$\sigma = \sigma_u + \sigma_p P_b P_T \tag{3.28}$$

where $\sigma_u$ and $\sigma_p$ are the unpolarized and polarized cross-sections respectively. The asymmetry is given by $A = \sigma_p/\sigma_u$, after the polarization factors are divided out. The internal radiative corrections consist of the vertex correction and the radiative tail and can be written as:

$$\sigma_I = \sigma^B(x)\, V + \int\int_x^1 I\left(x, x', Q^2\right) \sigma^B\left(x', Q^2\right) dx' dQ^2 \tag{3.29}$$

The tail is divergent as $x' \to x$, and so is the vertex correction $V$ [43]. Their sum, however, is finite. The regularization can be done in different ways. In POLRAD, an infinite term is subtracted from the vertex correction and added to the tail. That makes both the tail and the vertex correction finite. One drawback of this procedure is that the tail now depends not only on the value of $\sigma^B(x')$ for $x' > x$, but also on $\sigma^B(x)$. Although this procedure is mathematically exact, it is difficult to interpret physically. The physical tail should depend only on the value of $\sigma^B(x')$ for $x' > x$. For a finite bin size the part of the tail that falls within the same bin should not be

treated as a radiative correction. Therefore, to facilitate the discussion about error propagation we will separate the tail into the contribution from the same bin and the contribution from other bins. This separation is purely formal and does not affect the calculation of the central values of the radiative corrections. The sum of the vertex correction and the tail from same the bin is finite. With the internal corrections, the asymmetry can be written in the following form:

$$A_I(x) = \frac{\sigma_p^I(x)}{\sigma_u^I(x)} = \frac{\sigma_p^B(x)\left(V + \int\int_x^{x_1} I_p(x,x',Q^2)\,dx'dQ^2\right) + \sigma_p^T}{\sigma_u^B(x)\left(V + \int\int_x^{x_1} I_u(x,x',Q^2)\,dx'dQ^2\right) + \sigma_u^T} \quad (3.30)$$

$$\sigma_p^T(x) = \int\int_{x_1}^1 I_p\left(x,x',Q^2\right)\sigma_p^B\left(x',Q^2\right)dx'dQ^2 + \sigma_p^{El}(x) + \sigma_p^{QE}(x) \quad (3.31)$$

$$\sigma_u^T(x) = \int\int_{x_1}^1 I_u\left(x,x',Q^2\right)\sigma_u^B\left(x',Q^2\right)dx'dQ^2 + \sigma_u^{El}(x) + \sigma_u^{QE}(x) \quad (3.32)$$

where $I_{p,u}(x,x',Q'^2)$ represent the contribution from other regions in $x$ and $Q^2$ due to inelastic scattering, $\sigma_{p,u}^I$ are the internally radiated cross-sections, $\sigma_{p,u}^B$ are the Born cross-sections, $\sigma_{p,u}^{El}$ and $\sigma_{p,u}^{QE}$ are the contributions from the elastic (i. e. scattering from the whole $^3$He nucleus, no nuclear break-up) and quasi-elastic (elastic scattering from a proton or neutron) tails respectively. $x_1$ is the edge of the bin, and we factored out the cross-sections in (3.30) assuming that they do not vary appreciable from $x$ to $x_1$. The inelastic part can be broken further into the deep inelastic contribution from the kinematic region measured by our experiment and the resonance contribution.

The external corrections can be divided into contributions from Bremsstrahlung before nuclear scattering and after nuclear scattering. Since the glass windows for E-154 are very thin, the contribution of the external corrections before scattering is very small (it's effect is less than 1%). After scattering, some electrons go through a much thicker glass wall (made even thicker by the oblique angle), and the external corrections are not negligible. They can be included, after the internal corrections have been applied, in the following fashion:

$$\sigma_{u,p}^E(x) = \int_x^1 E(x,x')\sigma_{u,p}^I(x')dx' \quad (3.33)$$

$E(x,x')$ is given explicitly in [45].

The measured asymmetry is given by the ratio of the external (i. e. fully radiated) cross-sections:

$$A_m(x) = \frac{\sigma_p^E(x)}{\sigma_u^E(x)} \quad (3.34)$$

Our goal is to invert equations (3.30-3.34) and calculate $A_B(x) = \sigma_p^B(x)/\sigma_u^B(x)$, given $A_m(x)$. The main difficulty arises from terms that include $\sigma_p^B(x',Q^2)$, making the problem non-local in $x$ and $Q^2$. Therefore, we use an iteration technique, adjusting the value of $A_B(x)$ until $A_m(x)$ is reproduced.

Following historical convention, we present the final result in the form $A_B(x) = A_m(x) + A_{RC}(x)$. This, however, is only a convenient way of characterizing the size of the corrections. It can not be used for error analysis, because $A_{RC}$ depends on $A_m$.

### 3.6.2 Error Analysis

The error analysis is also complicated by the presence of $\sigma_p^B(x', Q^2)$ terms. However, for a given $x$ bin we only need to know the cross-section at higher $x$. To simplify the discussion, assume that we made a measurement only in the lowest $x$ bin, and already know the value $\sigma_p^B$ (i. e. $g_1$) for all higher $x$. (One could actually use the data from E-142 and E-143 at higher $x$ instead of our data. It would cause some increase in the size of the errors, but make the analysis simpler.) To simplify the notation, we also ignore, for the moment, the external corrections. Then we can write:

$$A_m = \frac{\sigma_p^B\left(V + \int\int_x^{x_1} I_p\left(x, x', Q^2\right) dx' dQ^2\right) + \sigma_p^T}{\sigma_u^B\left(V + \int\int_x^{x_1} I_u\left(x, x', Q^2\right) dx' dQ^2\right) + \sigma_u^T} \tag{3.35}$$

$\sigma_{p,u}^T$ include the inelastic, quasi-elastic and elastic tails, all of them come from measurements unrelated to our experiment. One can show that as $x_1 \to x$ the polarized and unpolarized inelastic tails become the same: $I_p\left(x, x', Q^2\right) \to I_u\left(x, x', Q^2\right)$. This is because the emitted photons have very low energy and do not depolarize the electron. To simplify the notation, we introduce a new vertex correction factor:

$$V'(x_1) = \left(V + \int\int_x^{x_1} I_p\left(x, x', Q^2\right) dx' dQ^2\right) = \left(V + \int\int_x^{x_1} I_u\left(x, x', Q^2\right) dx' dQ^2\right) \tag{3.36}$$

Then, by trivial algebra, we get:

$$A_B = \frac{\sigma_p^B}{\sigma_u^B} = A_m \frac{\sigma_u^B V'(x_1) + \sigma_u^T}{\sigma_u^B V'(x_1)} - \frac{\sigma_p^T}{\sigma_u^B V'(x_1)} = A_m + \left(A_m \frac{\sigma_u^T}{\sigma_u^B V'(x_1)} - \frac{\sigma_p^T}{\sigma_u^B V'(x_1)}\right) \tag{3.37}$$

This shows that $A_{RC}$ (the term in parenthesis) depends explicitly on $A_m$ at the measured point, and has errors correlated with it. Now, it is simple to calculate the effect of the radiative corrections on the errors. Equation (3.37) represents a linear transformation applied to the measured asymmetry, and should be treated in the same way as other linear transformations we apply to our data (*cf.* $A_m = (A_{raw} - A_{weak} P_b) / (P_t P_b f_t)$). One should increase the statistical and systematic error of $A_m$ by:

$$\frac{1}{f} = \frac{\sigma_u^B V'(x_1) + \sigma_u^T}{\sigma_u^B V'(x_1)} \tag{3.38}$$

The factor $f$ can be thought of as a dilution factor due to the radiative corrections. In addition, one should add to the systematic error any uncertainty due to the fits

and models used in the calculations of $\sigma_u^T$, $\sigma_u^B$, and $\sigma_p^T$. A similar procedure was implemented by SMC in their most recent analysis of the radiative corrections [46].

The value of the dilution factor depends on $x_1$. This dependence has the following physical interpretation. The effect of the radiative corrections is similar to the effect of a finite energy resolution, which smears events from neighboring bins. The smearing can be deconvolved, but that causes an increase in the errors. For example, suppose there are two bins which are so smeared that only 1% of their event sample is not common. If the measured asymmetry is different by 1% between the two bins, we would have to conclude that the Born asymmetry changes by 100% from one bin to the next. The error on the asymmetry extracted in such a way would be huge. On the other hand, if we ignored the possible variation of the Born asymmetry between the two bins, we would not need to apply any correction at all. By binning our data into a certain number of bins we are already setting a minimum scale for possible variation of $g_1$. Furthermore, the real physical meaning of our data is not in the values of $g_1(x)$ in individual bins, but in the long range trends of the data. We want to extract, for example, the low $x$ power of the data, the integral over the measured range or other quantities that involve several bins. Therefore, it is not necessary to set $x_1$ equal to the edge of the bin. It can be moved further, which results in a larger dilution factor and a smaller error increase. This is similar to binning the data into bins which are comparable with the energy resolution without doing a deconvolution procedure.

We now come back to the more complicated case, when $\sigma_p^B$ for all $x$ is determined from the measured data, and include the external corrections. We can convert the integrals in equations (3.30-3.33) to sums over $x$ bins.

$$A_m(x_i) = \frac{\sigma_p^B(x_i)\,V'(x_1)}{\sigma_u^E(x_i)} + \frac{\sum_{j=i+1}^{N}\left[I(i,j)+E(i,j)\right]\sigma_p^B(x_j) + \tilde{\sigma}_p^R(x_i) + \tilde{\sigma}_p^{El}(x_i) + \tilde{\sigma}_p^{QE}(x_i)}{\sigma_u^E(x_i)} \quad (3.39)$$

Only the unknown contribution of $\sigma_p^B(x)$ needs to be written explicitly. Here $I(i,j)$ and $E(i,j)$ represent non-local contributions from internal and external corrections respectively, $\sigma_p^R$ is the resonance contribution, and the tilde means that the external corrections are already taken into account. Equation (3.39) can be written in a matrix form:

$$A_{mi} = M_{ij}A_{Bj} + A_{Ti} \quad (3.40)$$

$$A_{Bi} = M_{ij}^{-1}\left(A_{mj} - A_{Ti}\right) \quad (3.41)$$

where

$$M_{ii} = \sigma_u^B(x_i)\,V'(x_1)/\sigma_u^E(x_i) \quad (3.42)$$

$$M_{ij} = \left[I\left(i,j\right) + E\left(i,j\right)\right]\sigma_u^B\left(x_j\right)/\sigma_u^E(x_i) \quad (3.43)$$

$$A_{Ti} = \left[\tilde{\sigma}_p^R\left(x_i\right) + \tilde{\sigma}_p^{El}\left(x_i\right) + \tilde{\sigma}_p^{QE}\left(x_i\right)\right]/\sigma_u^E(x_i) \quad (3.44)$$

In this form the quantities measured in the experiment ($A_{mi}$) are explicitly separated from the quantities measured in other experiments ($M_{ij}$ and $A_{Ti}$). We also assumed that $Q^2$ evolution is known, so if we measured $A_m$ at one $Q^2$ , we can calculate it at all $Q^2$. Equation (3.41) is a linear transformation, so the errors can be handled in a straight forward fashion. The error of $A_{Bi}$ is due to the error in $A_{mi}$, and also the errors in $A_{mj}\,(j > i)$. The diagonal term $M_{ii} = f$ is the same as in the previous discussion. Therefore, the statistical and systematic errors should be increased by a factor of $1/f$.

In addition, the non-diagonal terms of $M$ induce correlations between different bins. Since the statistical errors are usually assumed totally uncorrelated, the error due to $A_{mj}\,(j > i)$ does not really belong to the statistical error. The systematic error is assumed to be 100% correlated, so it is also not appropriate. Fortunately, the effect of correlations is small, and by adding them in quadrature to the systematic error we are making the most conservative approximation.

In reality, it is difficult to calculate the components of the matrix, as it requires splitting the integration of the inelastic tail into many separate bins. It is easier to calculate the errors using:

$$\sigma^2\left(A_{Bi}\right) = \sum_{j=i+1}^{N}\left(\frac{\partial A_{Bi}}{\partial A_{mj}}\right)^2\sigma^2\left(A_{mj}\right) \quad (3.45)$$

where we use the fact that the statistical errors $\sigma\left(A_{mj}\right)$ are uncorrelated. To evaluate the derivatives we calculate the variation of $A_{Bi}$ as the input values $A_{mj}$ are changed. The effect of the correlations is very small and increases the systematic error by about 1%.

To calculate the central values of the corrections we are using a fit to the data. The measured asymmetries have statistical errors and are randomly distributed around their "true" values. The fit, hopefully, lies closer to the "true" result. For radiative corrections we need to know the size of the Born polarized cross-section relative to other cross-sections. So, it is best to use the results of the fit $A_m^f(x)$. One has to choose which particular fit to use in calculating the central values, since many functional forms give acceptable $\chi^2$. They differ from one another by an amount comparable with the statistical errors of the data. Varying the form of the fit is equivalent to varying the input values $A_{mj}$ by some fraction of their statistical errors. So, the variation of the radiative corrections due to different fits is already taken into account by multiplying the statistical error by the dilution factor. One should just choose one "best" fit and use it to calculate the central values.

In addition to increasing the statistical and systematic error by the dilution factor, the radiative corrections introduce additional systematic errors due to the uncertainty in the input models unrelated to our experiment. To estimate these errors, we vary the input models within amounts constrained by the existing experimental data.

### 3.6.3 Input Models and their Errors

Calculation of the radiative corrections require the knowledge of the unpolarized deep inelastic structure functions, polarized and unpolarized structure functions in the resonance region, quasi-elastic form factors and elastic form factors. They also depend on the $Q^2$ evolution of $g_1$. In choosing appropriate models it is important to know what region of the kinematic space has the biggest contribution to each tail.

The inelastic tail corresponds to electron scattering resulting in the excitation or break-up of one of the nucleons in $^3$He. Since the final state does not have a definite invariant mass, the contribution of the inelastic tail is calculated by a two-dimensional integration in $Q^2$ and $x$. Part of it comes from the measured $x$ region and part from the resonance region. In both cases one needs to know the structure functions for a range of $Q^2$. Figure 3.10 shows the contribution to the integral as a function of $x$ and $Q^2$ for the unpolarized inelastic tail for $x = 0.015$. The line on the plot separates the resonance region ($W^2 < 4$ GeV$^2$, high $x$, low $Q^2$) from the deep inelastic region. To clearly show a large range of heights the square root of the integrand is plotted. The contribution for $Q^2 < 1$ GeV$^2$ ($> 1$ GeV$^2$) comes from electrons which lost energy before (after) scattering. A large contribution comes from $Q^2 \sim 0.25$ GeV$^2$. It corresponds to electrons losing most of their energy by emitting a photon before scattering, since $Q^2 = 0.23$ GeV$^2$ for $E = E' = 10$ GeV, $\theta = 2.75°$. For $F_2(x, Q^2)$ we used the NMC-95 fit [47] in the deep inelastic region. The error was estimated by changing the parameters of the fit within the errors given by the parameterization (typically, $2-3\%$ for both proton and deuteron structure functions which are assumed uncorrelated), as well as by changing to an older fit NMC-92 [48]. In the resonance region, we used the parameterization of Bodek *et al.* [49] and varied it by 5% which is the maximum error quoted in [49] for the relevant kinematic range.

The contribution to the polarized tail from various $x$ and $Q^2$ is shown in Figure 3.11. Again, we plot the square root of the integrand to show a greater range of heights. The dominant contribution comes from the resonance region, which has a large asymmetry. The data of E-143 [50] were used in this region. The uncertainty was estimated by varying the asymmetries within experimental errors of E-143. The dependence on the value of $g_2$ was estimated by varying E-154 $g_2$ data within their experimental errors.

The quasi-elastic tail results from elastic electron scattering from one of the nucleons in $^3$He. Since the nuclear binding energy is much smaller than the electron energy

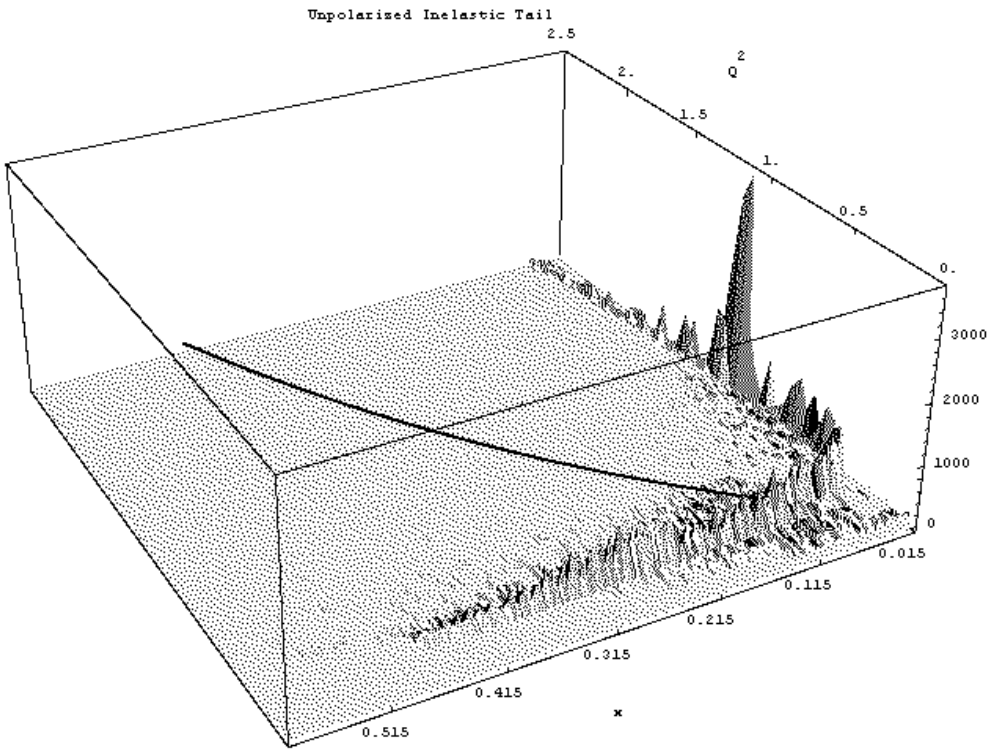


Figure 3.10: Contribution to the unpolarized inelastic tail vs. $x$ and $Q^2$.

or the bin width, one can reduce the integration to one dimension, using $W(\nu, Q^2) = W(Q^2)\,\delta\left(\nu - \frac{Q^2}{2M}\right)$. However, one has to include the Pauli suppression effect for small $Q^2$, since not all of the nucleons can participate in the scattering due to the exclusion principle. One usually uses the Fermi model for the nucleus, which is in good agreement with experiment [51]. The suppression factor is given in [52, 53]. To determine the Fermi momentum for $^3$He we used a calculation of the quasi-elastic cross-section by Atti *et al.* [54] compared with the Fermi model [55, 56]. It gives $k_F = 125 \pm 10$ MeV. Figure 3.12 shows the contribution to the unpolarized quasi-elastic tail vs. $Q^2$, as well as the value of the Pauli suppression factor for $x = 0.015$. The peak at $Q^2 = 0.23$ GeV$^2$ corresponds to electrons losing most of their energy before nuclear scattering. The polarized tail has a similar $Q^2$ dependence.

One also needs to know the neutron and proton elastic form factors for $Q^2 < 1$ GeV$^2$. A lot of measurements have been done in this region. Most of the data for the proton electric and magnetic form factors and the neutron magnetic form factor are

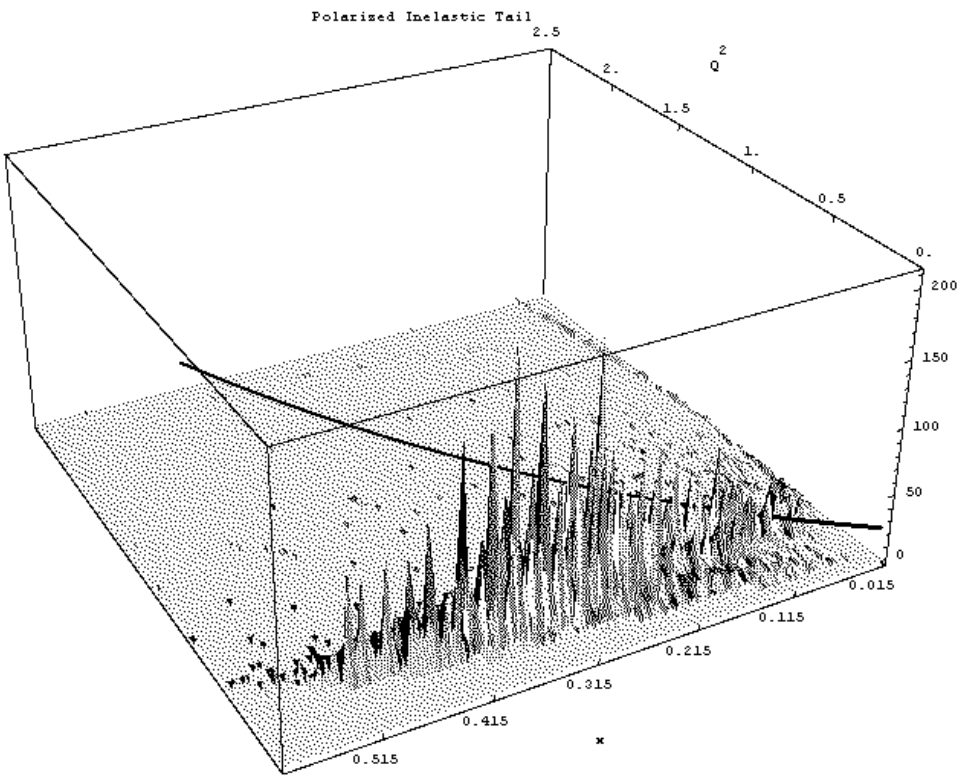


Figure 3.11: Contribution to the polarized inelastic tail vs. $x$ and $Q^2$.

consistent with the simple dipole fit: $G_E^p = G_M^p/\mu_p = G_M^n/\mu_n = \left(1 + Q^2/0.71GeV^2\right)^{-2}$. The models given in [57, 58], which predict small variations from the dipole fit (5%), are also consistent with the data. The neutron electric form factor was taken from [59], also consistent with measurements summarized in [57]. The differences among these models were used to estimate the errors.

The elastic tail arises from electron scattering elastically from the whole $^3$He nucleus. The contribution from the elastic peak vs. $Q^2$ is shown in Figure 3.13. All of it comes from very low $Q^2$. It occurs when the electron emits a hard photon at a large angle, deflects by about 2.75° and then scatters elastically by a small angle (or, first scatters elastically and then emits a photon). The polarized tail has a similar $Q^2$ dependence. Since the form factors are constrained to go to 1 at $Q^2 = 0$, the contribution is not very sensitive to the shape of the form factors. We used the data from McCarthy *et al.*[60] which cover the appropriate $Q^2$ range. The error was estimated by varying the parameterization within the errors given in the paper.

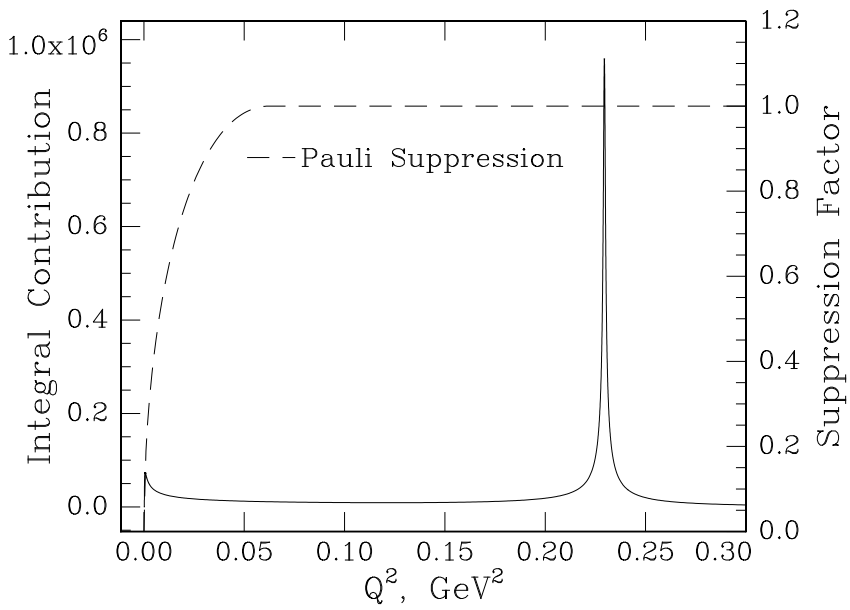


Figure 3.12: Contribution to the unpolarized quasi-elastic tail vs. $Q^2$ and the Pauli suppression factor.

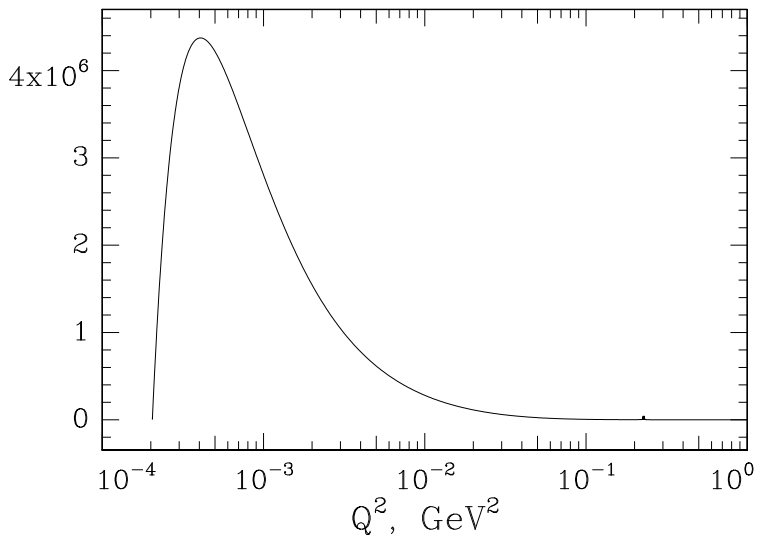


Figure 3.13: Contribution to the unpolarized elastic tail vs. $Q^2$.

### 3.6.4 Results of the Radiative Corrections

The measured (uncorrected) asymmetries of $^3$He were parameterized by:

$$g_1(x)/F_1(x) = -0.058x^{0.32}(1-x)^{2.31} \tag{3.46}$$

for the $x$ range of the data. We assumed that $g_1/F_1$ is independent of $Q^2$, consistent with the rest of the analysis.

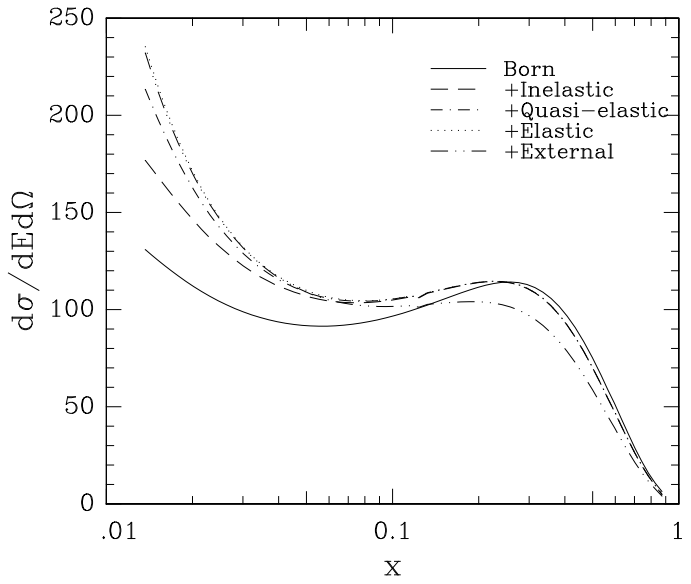


Figure 3.14: The unpolarized Born cross-section and tails in the 2.75° spectrometer.

Figure 3.14 shows the unpolarized cross-section vs. $x$ and various tail contributions for the 2.75° spectrometer. The corrections to the unpolarized cross-section are dominated by the inelastic and quasi-elastic tail at low $x$, while at high $x$ the external corrections become significant. The total cross-section is increased by almost a factor of two at low $x$. Figure 3.15 shows the polarized tails. The polarized Born cross-section is ten times bigger than the largest tail. Elastic tail makes a large contribution at low $x$ because it has a large asymmetry. Tables 3.2 shows the values of the radiative corrections, the enhancement factor for both the statistical and the systematic errors, and the systematic error due to the corrections themselves. We present the results graphically for the 2.75° spectrometer in Figure 3.16. The smaller error bars on the asymmetry are the uncorrected statistical errors, the larger error bars show the enhancement by the radiative corrections. The error bars on the radiative corrections themselves indicate their uncertainty due to the input models.

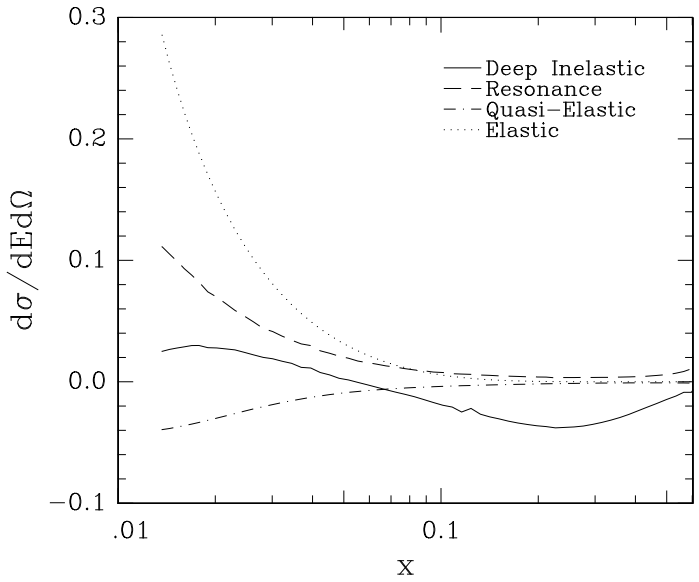


Figure 3.15: The polarized tails in the 2.75° spectrometer.

The corrections reach one third of the asymmetry at low $x$, however, they are always comparable to the statistical errors of the data. Their primary effect on the errors is to increase the statistical and systematic errors from other sources. The systematic errors due to the corrections themselves are relatively small.

The radiative corrections were also calculated independently by the SLAC analysis group [61]. They used a different computer program, developed at SLAC on the basis of formalism given in [42]. The results of the two calculations for the individual contributions and the total radiative corrections are in good agreement. Any differences are mostly due to the use of a different functional form to parametrize the asymmetry for the calculation. Different fits to the asymmetry with a good $\chi^2$ can differ from each other by a substantial fraction of the statistical errors. As a result, the radiative corrections can differ by as much the increase of the statistical error (i.e. 68.6% of the statistical error for the lowest $x$ point). The errors due to this variation are taken into account by the radiative corrections dilution factor.

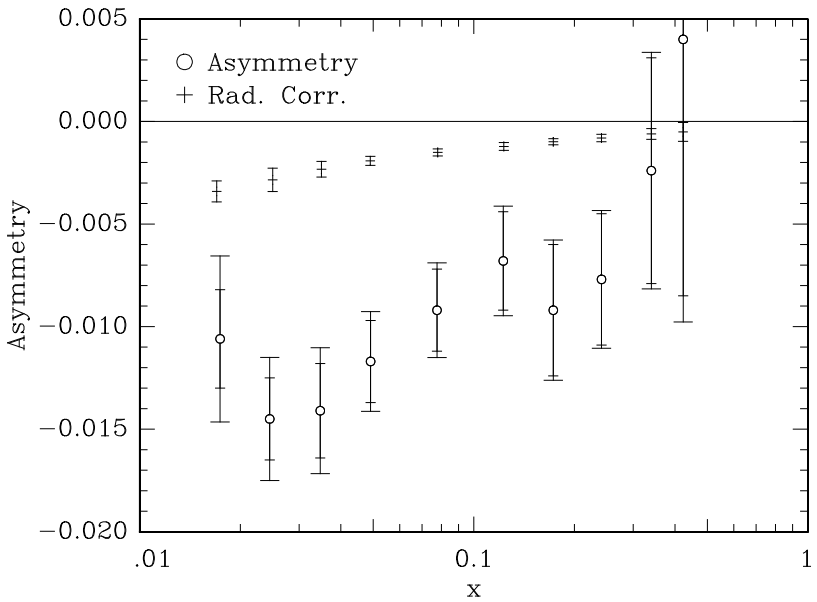


Figure 3.16: Uncorrected asymmetry $A_{||}$ for $^3$He and the radiative corrections. The error bars are explained in the text.

| $x$ bin | $\Delta A^{RC}$ | $\sigma\left(A^{Born}\right)/\sigma\left(A^{meas}\right)$ | Syst. |
|---|---|---|---|
| 2.75° spectrometer | | | |
| 0.017 | -0.00341 | 1.686 | 0.00051 |
| 0.025 | -0.00285 | 1.500 | 0.00057 |
| 0.035 | -0.00233 | 1.334 | 0.00038 |
| 0.049 | -0.00192 | 1.216 | 0.00022 |
| 0.078 | -0.00151 | 1.154 | 0.00017 |
| 0.123 | -0.00122 | 1.113 | 0.00019 |
| 0.173 | -0.00099 | 1.068 | 0.00015 |
| 0.241 | -0.00081 | 1.049 | 0.00018 |
| 0.340 | -0.00061 | 1.048 | 0.00026 |
| 0.423 | -0.00051 | 1.102 | 0.00046 |
| 5.5° spectrometer | | | |
| 0.0573 | -0.00290 | 1.319 | 0.00070 |
| 0.0837 | -0.00251 | 1.202 | 0.00053 |
| 0.1231 | -0.00227 | 1.123 | 0.00037 |
| 0.1725 | -0.00210 | 1.066 | 0.00035 |
| 0.2420 | -0.00185 | 1.039 | 0.00022 |
| 0.3424 | -0.00152 | 1.022 | 0.00020 |
| 0.4423 | -0.00124 | 1.009 | 0.00030 |
| 0.5643 | -0.00102 | 1.028 | 0.00063 |

Table 3.2: The radiative corrections to $A_{||}^{^3He}$ and their effect on the errors.

# Bibliography


[1] R. Prepost and T. Maruyama, Ann. Rev. Nucl. Part. Sci. **45**, 41 (1995)

[2] R. Alley *et al.*, Nucl. Instr. Meth. A **365**, 1 (1995).

[3] T. Maruyama, E.L. Garwin, R. Prepost, G.H. Zapalac, J.S. Smith, J.D. Walker, Phys. Rev. Lett. **66**, 2376 (1991).

[4] R. Prepost in *Spin Structrure in High Energy Processes*, Proceeding of XXI SLAC Summer Institute, (1993).

[5] J. D. Jackson, *Classical Electrodynamics*, (John Wiley and So., New York, 1975).

[6] L. Stuart, E-154 Technical Note #6, (1995).

[7] H. R. Band, G. Mitchell, R. Prepost, and T. Wright, E-154 Technical Note #40, (1996).

[8] J. Arrington *et al.*, Nucl. Instr. Meth. A **311**, 39 (1992).

[9] H.R. Band and R. Prepost, E-143 Technical Note #110, (1996)

[10] C. Kittel, *Introduction to Solid State Physics*, (John Willey & So., New York, 1956).

[11] G.G. Scott and H.W. Sturner, Phys. Rev. **184**, 184 (1969).

[12] L.G. Levchuk, Nucl. Instr. Meth. A **345**, 496 (1994).

[13] M. Swartz *et al.*, Nucl. Instr. Meth. A **363**, 526 (1995).

[14] G.G. Petratos, SLAC-ESA Technical Note, (1993).

[15] R. Arnold *et al.*, SLAC-ESA Technical Note, (1993).

[16] Y. Kolomensky, Ph.D. Thesis, Univ. of Massachusetts, (1997).

[17] R.M. Barnett *et al.*, (Particle Data Group), Phys. Rev. D **54**, (1996).

[18] M. Buenerd, E-154 Technical Note #32, (1996).

[19] Handbook of Chemistry and Physics, D.R. Lide ed., p.6-156 (CRC Press, Boca Raton, 1993).

[20] P. Zyla, private communication, (1997)

[21] M. Buenerd, E-154 Technical Note #41, (1996)

[22] J. Wang, private communication, (1997).

[23] H. Borel *et al.*, IEEE Tran. Nucl. Sci. **42**, 529 (1996).

[24] G. T. Bartha *et al.*, Nucl. Inst. Meth. A **275**, 59 (1989).

[25] N.V. Rabin, Instr. Exp. Tech. **35**, 1 (1992).

[26] G. A. Akopdjanov *et al.*, Nucl. Instr. Meth. **140**, 441 (1977).

[27] F. Bianchi *et al.*, Nucl. Instr. Meth. A **279**, 473 (1989).

[28] R. Engelmann *et al.*, Nucl. Instr. Meth. **216**, 45 (1983).

[29] J. Wang, E-154 collaboration meeting, May 1996.

[30] Y. Kolomensky and M. Romalis, E-154 Technical Note #48, (1996).

[31] V. Breton, H. Fonvieille, P. Grenier, C. Guicheney, J. Jousset, Y. Roblin, F. Tamin, Nucl. Instr. Meth. A **362**, 478 (1995).

[32] S. Incerti, E-154 Technical Note #30, (1996); E-154 Technical Note #31, (1996).

[33] S. Incerti and Y. Terrien, E-154 Technical Note #22, (1995).

[34] P. Zyla, E-154 Collaboration Meeting, May 1996.

[35] M. Romalis and Y. Kolomensky, E-154 Technical Note # 54 (1997).

[36] J.L. Friar, B.F. Gibson, G.L. Payne, A.M. Bernstein, T.E. Chupp, Phys. Rev. C **42**, 2310 (1990).

[37] C.C.D. Atti, S. Scopetta, E. Pace, G. Salme, Phys. Rev. C **48**, 968 (1993).

[38] K. Abe *et al.* (the E-154 Collaboration), submitted to Phys. Lett. B.

[39] J. Ellis and M. Karliner, Phys. Lett. B **341**, 397 (1995).

[40] I.V. Akushevich, N.M. Shumeiko, and A.E. Tolkachev, (unpublished notes).

[41] I.V. Akushevich and N.M. Shumeiko, J. Phys. G **20**, 513 (1994).

[42] T.V. Kuchto and N.M. Shumeiko, Nucl. Phys. B **219**, 412 (1983).

[43] D.Y. Bardin and N.M. Shumeiko, Nucl. Phys. B **127**, 242 (1977).

[44] L.W. Mo and Y.S. Tsai, Rev. Mod. Phys. **41**, 205 (1969).

[45] Y.S. Tsai, SLAC-PUB 848 (1971).

[46] B. Badelek, hep-ph/9612274.

[47] M. Arneodo *et al.*, Phys. Lett. B **364**, 107 (1995).

[48] P. Amaudruz *et al.*, Nucl. Phys. B **371**, 3 (1992).

[49] A. Bodek *et al.*, Phys. Rev. D **20**, 1471 (1979).

[50] P. Raines, Ph.D. Thesis, University of Pennsylvania, 1996 (unpublished).

[51] E.J. Moniz *et al.*, Phys. Rev. Lett. **26,** 445 (1971).

[52] T. DeForest, J.D. Walecka, Adv. Phys. **15**, 1 (1966).

[53] Y.S. Tsai, Rev. Mod. Phys. **46**, 815 (1974).

[54] C.C. Atti, E.Pace, G. Salme, Phys. Rev. C **51**, 1108 (1995).

[55] E. J. Moniz, Phys. Rev. **184**, 1154 (1969).

[56] Van Orden program for calculation of quasi-elastic cross-section.

[57] S. Blatnik, N. Zovko, Acta Phys. Austriaca **39**, 62 (1974).

[58] F. Iachello, A.D. Jackson, and A. Lande, Phys. Lett. B **43**, 191 (1973).

[59] S. Galster *et al.*, Nucl. Phys. B **32**, 221 (1971).

[60] J.S. McCarthy, I. Sick, R.R. Whitney, Phys. Rev. C **15**, 1396 (1977).

[61] D. Reyna, E-154 Technical Note, (1997).

# Chapter 4

# Polarized $^3$He Target

Our experiment used a polarized $^3$He target as a source of polarized neutrons. To polarize the $^3$He we used spin exchange with optically pumped Rb vapor. In this chapter I describe the techniques used for polarizing large quantities of $^3$He and constructing a high quality nuclear target. Measurements of the dimensions, densities, and temperatures of the target cells are described in detail. These numbers are important for determining the polarization and the dilution factor of $^3$He. The later is described in this chapter, while Chapter 5 will be devoted to the former. The target performance during the run is also discussed.

## 4.1 Optical Pumping and Spin Exchange

There are two techniques commonly used for polarizing $^3$He. One technique uses direct optical pumping of the metastable 2 $^3S_1$ state of $^3$He [1]. The metastable state is produced by RF discharge in a few torrs of $^3$He. The electron spin in the 2 $^3S_1$ state is polarized by optically pumping the 2 $^3S_1 \rightarrow$ 2 $^3P_0$ transition with 1.08 $\mu m$ circularly polarized light. The polarization is transferred to the nucleus by the hyperfine interaction. While high nuclear polarization can be obtained, the use of this technique for high density targets is difficult because the $^3$He density has to be very low to maintain the RF discharge. However, it is well suited for internal targets, which do not require high density gas. It was used recently for a measurement of the neutron spin structure function at DESY [2]. Compressors have been developed to produce high density gas without destroying the polarization [3]. With the compressors the technique has been used recently for a measurement of the $^3$He electric form factor [4].

In our experiment, we use the second technique, which can be more easily applied for high density targets [5]. In this technique $^3$He is polarized by a two step process. First, Rb vapor is polarized by optical pumping with circularly polarized light. Second, the Rb electron polarization is transferred to the $^3$He nucleus by spin-exchange

interaction.

Optical pumping of alkali metals [6] relies on the angular momentum selection rules in the optical excitation process. A simplified level diagram, ignoring the effect of the Rb nuclear spin, is shown in Figure 4.1. The modifications due to the nuclear spin will be discussed later. When pumping with right circularly polarized light, the electrons can only be excited from the $m = -1/2$ level. They decay back with equal probabilities to both levels, but can't be excited again from the $m = +1/2$ state. Thus, in the absence of any relaxation processes, all spins will accumulate in the $m = +1/2$ state. Several important conditions have to be met for this scheme to work. First, one has to apply a magnetic field, parallel to the direction of the light propagation, to split the Zeeman levels. Second, when the electrons decay radiatively back to the ground state, they emit photons almost isotropically and with varying degree of polarization. In our conditions the cell is optically thick and most of the photons are reabsorbed before exiting the cell. Since these photons do not have, in general, the same polarization and direction of propagation as the pumping light, they severely limit the efficiency of the pumping process. To avoid this effect, about 60 torr of $N_2$ buffer gas is added to the cell, which radiationlessly quenches the excited electrons back to the ground state. Although in our targets the optical pumping takes place in the presence of 10 atm. of $^3$He gas, $N_2$ is still necessary. The quenching cross-section for $N_2$ and other diatomic gases is several orders of magnitude larger than for $^3$He because the energy of the electron can be transferred to the vibrational and rotational motion of the $N_2$ molecule. The quenching cross-sections have been measured in [7]. Using their results we estimate that the quenching time of the excited state is about 1.3 ns, compared with radiative decay time of 28 ns. Therefore, only about 5% of the atoms decay by emitting a photon. The $N_2$ pressure is chosen by a compromise between the quenching rate and the contribution of $N_2$ to the dilution factor. In addition, there is a large collisional relaxation of the electron spin in the excited state due to both $N_2$ and $^3$He. Therefore, electrons decay to the ground state with equal probability. In the absence of spin relaxation in the ground state, two photons are required to polarize one Rb atom.

Due to the non-zero Rb nuclear spin the energy levels displayed in Figure 4.1 are modified by hyperfine interaction. The hyperfine splitting is much larger than the Zeeman splitting in a typical holding field of 20 G, so the electrons are in the eigenstates of the total spin $F = I + S$, where $I$ is the nuclear spin ($I = 5/2$ for $^{85}$Rb and $I = 3/2$ for $^{87}$Rb) and $S$ is the electron spin. The level structure of the ground state is shown in Figure 4.2. There is still a level ($F = 3, m = 3$) from which the atoms cannot be excited by right circularly light, but now it takes many more excitation cycles to transfer the electrons to this state. However, most sources of spin relaxation and spin exchange affect only the electron spin and do not relax the nuclear spin. An electron from the $F = 3, m = 3$ state after going through a spin

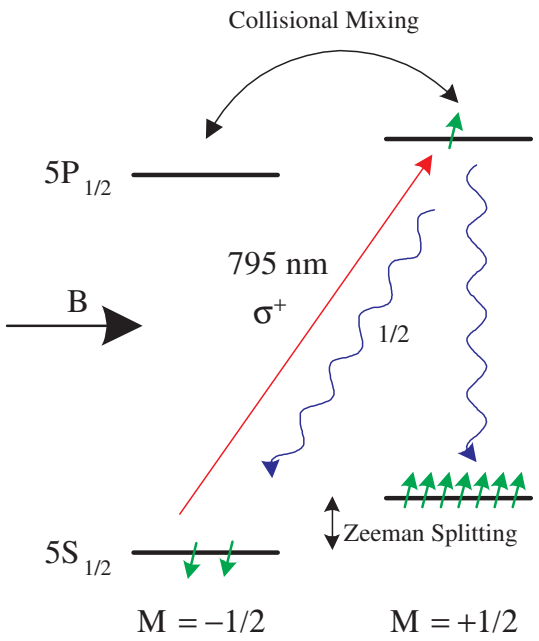


Figure 4.1: Optical pumping by circularly polarized light.

relaxation or exchange process is most likely to end up in one of the $m = 2$ states. It will need to go through, on average, only two excitation cycles to be pumped back to the $m = 3$ state. Therefore, the nuclear spin acts only as a "reservoir" of the angular momentum, without affecting the efficiency of optical pumping.

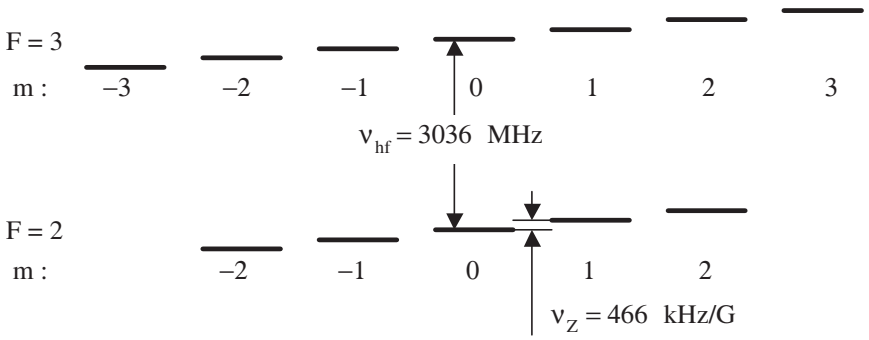


Figure 4.2: Ground state energy levels for $^{85}$Rb.

In our conditions the absorption lines are pressure broadened by $^3$He to about 160 GHz FWHM. Therefore, the hyperfine structure of the optical lines is not resolved and the atoms from both hyperfine states are equally likely to absorb the light Under

these conditions it can be shown [8, 9] that the relative population of the Zeeman levels obeys a spin temperature distribution [10]:

$$\langle F, m \left| \rho \right| F, m \rangle = \frac{1}{Z} e^{\beta m} \tag{4.1}$$

where $\rho$ is the Rb spin density matrix and $\beta$ is the inverse spin temperature, related to the average electron polarization by $P_{Rb} = \tanh(\beta/2)$. The spin temperature distribution has been shown to hold experimentally [11] with high degree of accuracy.

The average polarization is determined by the ratio of the optical pumping and electron spin destruction rates

$$P_{Rb} = \frac{R}{R + \Gamma_{SD}} \tag{4.2}$$

The optical pumping rate is defined as:

$$R = \int \Phi(\nu)\, \sigma(\nu)\, d\nu \tag{4.3}$$

where $\Phi(\nu)$ is the laser photon flux per unit frequency and $\sigma(\nu)$ is the light absorption cross-section. The electron spin destruction rate $\Gamma_{SD}$ is mostly due to the spin-rotation interaction during collisions of the Rb atom with other atoms [12]:

$$\mathcal{H}_{SR} = \gamma N \cdot S \tag{4.4}$$

which can couple the spin angular momentum to the rotational angular momentum $N$ of the colliding pair. The spin destruction rate due to collisions with gas species $i$ is proportional to the density of that species, so we can write

$$\Gamma_{SD} = k_{Rb-He} \left[^3He\right] + k_{Rb-N_2} \left[N_2\right] + k_{Rb-Rb} \left[Rb\right] \tag{4.5}$$

introducing spin destruction rate constants $k_{Rb-i} = \langle v \sigma_{Rb-i} \rangle$. The constants have been measured by Wagshul and Chupp [13]:

$$k_{Rb-He} \leq 2 \times 10^{-18} cm^3/s \tag{4.6}$$

$$k_{Rb-N_2} = 8 \times 10^{-18} cm^3/s \tag{4.7}$$

$$k_{Rb-Rb} = 8 \times 10^{-13} cm^3/s \tag{4.8}$$

Recent experiments at Princeton [9] found strong temperature dependence of these rates, which was not taken into account in [13], so the numbers should be treated only as a "factor of 2" estimates.

In our operating conditions ($[^3He] = 2 \times 10^{20}$ cm$^{-3}$, $[N_2] = 1.8 \times 10^{18}$ cm$^{-3}$, $[Rb] = 4 \times 10^{14}$ cm$^{-3}$) this gives the following contributions to the spin destruction rate:

$$\Gamma_{SD} = 400_{Rb-He} + 14_{Rb-N_2} + 320_{Rb-Rb} = 734\, s^{-1} \tag{4.9}$$

Thus, Rb-Rb and Rb-$^3$He collisions contribute in approximately equal amounts to the relaxation of the Rb spin. Its important to realize that Rb-Rb spin-exchange process, which happens at a rate of $2.7 \times 10^5$ s$^{-1}$ does not contribute to the spin relaxation. In addition to spin rotation interaction, Rb spin can relax due to collisions with the walls. This effect has been studied in [13]. Because of high $^3$He pressure, the Rb diffusion constant is very small $D_{Rb-He} = 0.15$ cm$^2$/s at 150°C [13], so relaxation due to wall collisions is only significant within $\sqrt{D_{Rb-He}/\Gamma_{SD}} \sim 0.1$ mm. of the wall.

Finally, there is the relaxation due to the spin exchange with $^3$He, responsible for transferring Rb electron polarization to $^3$He [14]. The spin-exchange is due to hyperfine interaction between the Rb electron and the $^3$He nucleus [15]:

$$\mathcal{H}_{SE} = \alpha K \cdot S \tag{4.10}$$

where $K$ is the $^3$He nuclear spin. This interaction gives rise to both a transfer of the polarization to $^3$He and a shift of the Rb Zeeman frequency due to the $^3$He polarization. The frequency shift is used for $^3$He polarimetry, as described in Chapter 5. The spin exchange rate constant has been measured in two experiments with results different by a factor of 2. Coulter *et al.* [16] get $k_{SE} = \langle v\sigma_{SE}\rangle = (1.2 \pm 0.2) \times 10^{-19}$ cm$^3$/s, while Larson *et al.* [17] report $k_{SE} = (6.1 \pm 0.2) \times 10^{-20}$ cm$^3$/s using a similar experimental technique. Clearly, more measurements of this number are required. Spin exchange with $^3$He contributes about $\Gamma_{SE} = k_{SE}[^3He] = 24$ s$^{-1}$ to the relaxation of the Rb spin[1]. Therefore, approximately 3% of the Rb atoms transfer their spin to $^3$He, while the rest lose it in spin destruction processes.

The $^3$He nuclear polarization increases with time due to spin exchange according to the following equation:

$$P_{He}(t) = \langle P_{Rb}\rangle \frac{\gamma_{SE}}{\gamma_{SE} + \Gamma}\left\{1 - \exp\left[-\left(\gamma_{SE} + \Gamma\right)t\right]\right\} \tag{4.11}$$

where $\gamma_{SE} = k_{SE}[Rb]$, $\Gamma$ is $^3$He nuclear spin relaxation rate, and $\langle P_{Rb}\rangle$ is the average Rb polarization in the cell. Compared to the Rb spin exchange rate (rate per Rb atom), the $^3$He spin exchange rate (rate per $^3$He atom) is slower by the ratio of Rb to He number densities. So, the $^3$He spin exchange rate is very small $\gamma_{SE} = 4.8 \times 10^{-5}$ s$^{-1}$ = 1/(5.8 hrs.). Fortunately, the nuclear relaxation rate of $^3$He can also be quite small. The limiting factor is the $^3$He–$^3$He magnetic dipole relaxation, which was calculated by Newbury *et al.* [18]:

$$\Gamma_D = \frac{[^3He]}{744} hrs^{-1} \tag{4.12}$$

where $[^3He]$ is in amagats. All $^3$He relaxation rates measured in our lab are larger or equal to this limit. For E-154 cells the limit from this source of relaxation is

[1] Here and in other calculations, the result of Coulter *et al.* [16] is used, unless stated otherwise.

$1/\Gamma_D = 84$ hrs. Therefore, provided that all other sources of relaxation are eliminated, one can achieve high $^3$He polarization.

In addition to the dipole-dipole relaxation there are several other sources of relaxation which are small or can be made small. Relaxation due to magnetic field gradients [19, 20] is given by:

$$\Gamma_G = D_{He} \frac{|\nabla B_x|^2 + |\nabla B_y|^2}{B_z^2} \tag{4.13}$$

Because of high $^3$He density in our cells, the self-diffusion constant is small $D_{He} = 0.28$ cm$^2$/s. To achieve negligible relaxation $1/\Gamma_G = 1000$ hrs., we need $|\nabla B_x|/B_z < 0.001$ cm$^{-1}$. We used Helmholtz coils with a diameter of 150 cm, much larger than our cell dimensions $\sim 30$ cm, and a holding field $B_z$ of 10-20 G. Precautions were taken to remove all ferromagnetic material from the vicinity of the target. Under these conditions we found that it was not difficult to satisfy the inhomogeneity condition.

The relaxation due to beam ionization has been studied in [21, 22, 23]. The relaxation can be written as:

$$\Gamma_B = (n_a + n_m)\,\Gamma_I \tag{4.14}$$

where $\Gamma_I$ is the rate of production of $^3$He ions by the electron beam. $n_a$ describes the contribution from single $^3$He$^+$ ions, which is due to hyperfine interaction between the single electron and the nucleus. $n_a$ can range from 0 to 1 [22] and in our conditions is close to 1 [24]. $n_m$ describes the contribution from the formation of $^3$He$_2^+$ molecules, which can relax the nuclear spin by spin-rotation interaction (4.4). $n_m$ can be quite large, but in our cell the molecules are quickly broken up by collisions with $^3$He and neutralized by collisions with $N_2$, so $n_m \ll 1$. For our experimental conditions we calculate the relaxation time due to beam ionization from 400 to 1100 hrs. depending on the beam current. No significant depolarization due to the beam was observed (see Figure 4.21).

Even in the absence of the two relaxation sources described above, which are dependent on the environment, the $^3$He relaxation rate is usually larger than the dipole-dipole contribution. In most cases the relaxation rate is constant for a given cell and is not affected by heating cycles, measurement conditions, etc. The relaxation can be due to paramagnetic impurities in the walls or in the gas phase, which cause a large magnetic dipole relaxation rate. Or, it can be due to $^3$He sticking to the surface of the cell for a long time and relaxing by exchange with other nuclear spins [25]. Since most common paramagnetic gases ($O_2$, NO) are reactive with Rb, they probably are gettered by Rb when the cell is hot. On the other hand, the measurements of the relaxation rate are always done at room temperature to remove the contribution of Rb spin exchange. Therefore, the possibility of outgassing of paramagnetic gases cannot

be excluded. The sources of relaxation on the surface are even more uncertain. It can be ferromagnetic elements in the composition of the glass or contaminants on the surface. $RbO_2$ is also paramagnetic. It is unlikely that $^3$He can stick to the wall for a long time, because it has very low polarizability and no wall coatings are used. However, it can diffuse and get trapped in micro-fissures, if they are present. It was found [24] that the nuclear relaxation rate can be significantly reduced by using only glass surfaces which are freshly formed during glass blowing. Freshly reblown glass probably has much less micro-fissures than stock tubing.

For our best cell, called Picard, the nuclear relaxation time was measured after the run to be $1/\Gamma = 84 \pm 5$ hrs. So, the relaxation due to sources other then $^3$He dipole-dipole interaction was longer than 1300 hrs! Using the ratio of surface to volume, one can calculate that an average atom strikes the surface about $2\times10^{11}$ times before relaxing. Even for the worst cells, which have a nuclear relaxation time of 30 hrs, this number is equal to $7 \times 10^9$. We also measured the nuclear relaxation time of Picard during the run, in the presence of the electron beam. This measurement was performed during $A_\perp$ running, when the cell was at room temperature. During the measurement the polarization was directed perpendicular to the electron beam using an additional set of Helmholtz coils. The relaxation time was $55 \pm 3$ hrs, significantly shorter than the lifetime measured before or after the run. This indicates that an additional source of relaxation with a time constant of 160 hrs. was present. It may be due to beam depolarization larger than calculated (we calculate $1/\Gamma_B = 1100$ hrs. for Picard), relaxation due to magnetic field gradients created by the spectrometer magnets, or some other effect associated with operation of all experimental equipment at once. With time constants from the spin-up of Picard, one can estimate that this decrease in the lifetime reduced the equilibrium $^3$He polarization by 3%. It would have even smaller effect on other cells with shorter intrinsic lifetimes.

For optimization of the target design and operating parameters, it is convenient to rewrite the equation for equilibrium $^3$He polarization as follows:

$$P_{He} = \left(\frac{R}{R+\Gamma_{SD}}\right)\left(\frac{\gamma_{SE}}{\gamma_{SE}+\Gamma}\right) \tag{4.15}$$

from which it is obvious that for high polarization we need $\gamma_{SE} \gg \Gamma$ and $R \gg \Gamma_{SD}$. To satisfy the first condition, we need to have very high quality cells with $\Gamma \sim \Gamma_D$ and high Rb number density since $\gamma_{SE} = k_{SE}\,[Rb]$. The second condition is also not trivial to satisfy, because $\Gamma_{SD}$ has components which are proportional to the Rb and He density, both of which are quite large. So, we need to have a large pumping rate, i.e. high laser intensity.

This experiment relied on laser diode arrays for most of optical pumping. Laser diode arrays have many advantages over Ti-Sapphire lasers, which were used in E-142 and also supplemented diode lasers in this experiment. They are much cheaper per

watt of power, more compact, require less power, and almost no operator attention. Their main disadvantages are a very broad spectral profile, on the order of 2-4 nm, and, for some models, large non-uniformity of the laser beam. The spectral width problem is partly alleviated by very large pressure broadening of the Rb absorption lines. In our cells the absorption line FWHM is about 0.34 nm, and we are usually able to absorb about half of the light. The propagation of the light through the cell is governed by a set of non-linear integro-differential equations:

$$R(z) = \int \Phi(\nu, z)\,\sigma(\nu)\,d\nu \tag{4.16}$$

$$\frac{\partial \Phi(\nu, z)}{\partial z} = -n_{Rb}\sigma(\nu)\,\Phi(\nu, z)\left(1 - \frac{R(z)}{R(z) + \Gamma_{SD}}\right) \tag{4.17}$$

These equations do not take into account variations of the light intensity in the transverse direction, which can be significant for diode lasers, and the depolarizing surface layer. Solving equation (4.16, 4.17) one can calculate the average Rb polarization:

$$\langle P_{Rb} \rangle = \int_V \frac{R(z)}{R(z) + \Gamma_{SD}} dz dA \tag{4.18}$$

and, using equation (4.11), the $^3$He polarization for a given laser power, Rb number density, etc. However, even the basic spin destruction rates in equation (4.9) are uncertain by as much as a factor of 2. The Rb number density, another critical parameter, is also uncertain by a factor of 2 because of the temperature uncertainty due to the heating by laser light. Although one can model the performance of the cells, the predictions are usually rather unreliable and the optimization is often done at the experimental stage.

## 4.2 Target Cells

The two main goals in the construction of the target cells were a long nuclear relaxation time and a large dilution factor. For an experiment limited by the count rate in the spectrometer, such as ours, the running time required to achieve a given statistical error is proportional to the square of both the polarization and the dilution factor. The dilution factor, defined in Chapter 3, is the ratio of the number of electrons scattered from $^3$He compared with the total number of scattered electrons:

$$f(x) = \frac{L_{He}\,[He]\,\sigma_{He}(x)}{L_{He}\,[He]\,\sigma_{He}(x) + L_{N_2}\,[N_2]\,\sigma_{N_2}(x) + L_{gl} n_{gl} \sigma_{gl}(x)} \tag{4.19}$$

where $L_i$ is the length of the material and $\sigma_i(x)$ is the deep inelastic scattering cross-section (not to be confused with the optical cross-section $\sigma(\nu)$). For glass

$n_{gl}\sigma_{gl}(x) = \sum_c n_c\sigma_c(x)$ is the sum over different chemical elements in the glass. While the use of diode lasers allowed us to increase the average $^3$He polarization from 33% in E-142 to 38%, and reach polarizations up to 48%, the bulk of the improvement in the target came from a smaller dilution (a larger value of the dilution factor). The $^3$He dilution factor for E-142 was about 0.35, while for this experiment it was 0.56 on average and as high as 0.65 for some cells. Thus, the improvement from the dilution factor was much more significant than from the target polarization.

From equation (4.19) it is clear that we need to reduce the glass thickness seen by the electron beam. At the same time, the dilution factor can be increased by increasing the density of $^3$He. These are mutually conflicting requirements, as the glass cell with very thin windows cannot withstand large $^3$He pressure. To achieve a larger dilution factor, we designed special concave windows [26], which can withstand much higher pressure than usual convex windows used in E-142. The windows were made by Princeton Glassblower Mike Souza. A detailed schematic of the windows is shown in Figure 4.3.

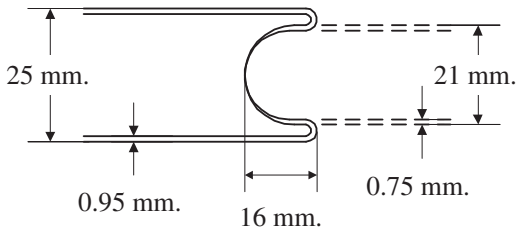


Figure 4.3: The schematic of the inverted window design. Dashed lines show the tube from which the window is originally blown.

The procedure for cell fabrication was as follows. First, simple, non-inverted convex windows were produced. Their thickness was determined by either a mechanical measurement or X-ray absorption, as described later in the text. The windows which fell within the desired range from 2 to 3 mils were sealed in the inverted configuration. The rest of the windows were resized and measured again. The inverted configuration was made by sealing the window to a tube of a larger diameter, as shown in Figure 4.3. It was very important not to have a sharp edge at the joint of the two tubes. All inverted windows were pressure tested. For pressure testing we filled the windows with water to reduced the amount of energy stored during the test. It is known that water has corrosive effects on glass [27], therefore, the test was limited to 10 min. in duration. Deionized water was used. The cells were tested to 19 atm. overpressure, while the operating pressure in the cells did not exceed 12 atm. The yield of the windows was highly variable and mostly dependent on the quality of the seal between the window and the outer tube. Overall, approximately 1 in 4 windows survived the

test and were used in cell construction.

In other ways the geometry of the cells was similar to the E-142 cells. They consisted of two chambers, the target cell and the pumping cell, connected by a transfer tube. Figure 4.4 shows the dimensions of the target cell Picard. During operation the pumping cell was heated to $\sim 180°$C to get sufficient Rb density for optical pumping and spin exchange. The Rb vapor density in the target cell was negligible. $^3$He polarization was transferred to the target cell by diffusion. By using two chambers we avoided problems associated with simultaneous access for laser and electron beams and the depolarizing effects of the electron beam on the Rb vapor. Because only part of the cell is used for optical pumping, equation (4.11) for $^3$He polarization is modified. One can show [24] that the only modification is a replacement of the spin exchange rate $\gamma_{SE} = k_{SE}\,[Rb]$ by the volume averaged rate:

$$\overline{\gamma_{SE}} = \gamma_{SE}\frac{N_p}{N_p + N_t} \tag{4.20}$$

where $N_p$ and $N_T$ are the number of $^3$He atoms in pumping and target cells respectively. Thus, the effective spin exchange rate is a factor of 3 smaller than the rate in the pumping cell. This makes it only more important to have a very long nuclear relaxation time.

The cells were constructed using the techniques developed for E-142 [24]. We used 1720 Corning glass, primarily because of its low permeability to $^3$He. Using permeability data from [28] we estimate that the cell losses 10% of $^3$He in about 100 years, compared to about 2 month for Pyrex. In addition, Corning 1720 is highly resistant to alkali metals and does not react with them even at high temperature. Finally, the surface properties of Corning 1720 have been shown to allow very long nuclear relaxation times, although other glasses are not necessarily worse. On the other hand, Corning 1720 is one of the most difficult glasses to work with, and this experiment would have been impossible without the great skill of our glassblower Mike Souza.

The glass was rinsed in nitric acid, deionized water and spectroscopic grade methanol. One of the most important steps in the procedure was resizing, during which the stock tubing was mounted on a lathe and its diameter increased by slowly melting the glass and blowing into the tube. The purpose of the procedure is to ensure that the surface of the glass is freshly formed, without microfissures and impurities usually present on tubing from stock. This prevented $^3$He from diffusing into the micro-fissures and depolarizing. All parts of the cell were resized from tubing several millimeters smaller than the required size. A complete cell was annealed to relieve any stress created during assembly.

The gas filling procedure was also similar to E-142. The cell was attached to a high purity vacuum system. A broken Rb ampule was sealed into the glass manifold.

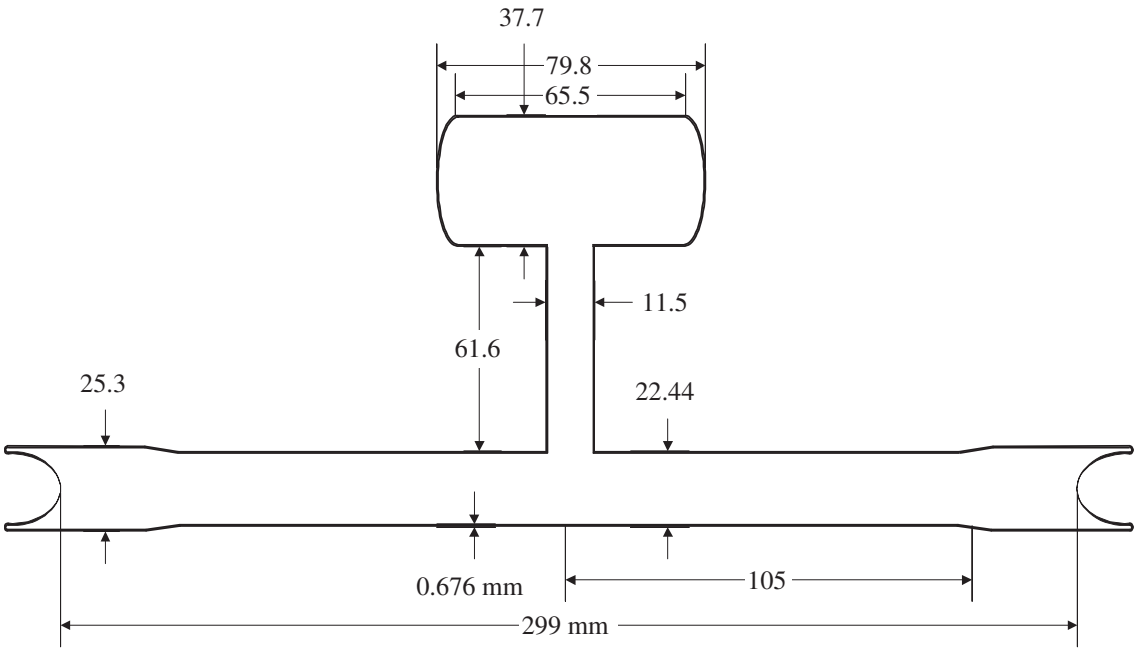


Figure 4.4: Dimensions of the target cell Picard, mm.

The vacuum system used a Varian diffusion pump and a cold $N_2$ trap. Pressures of $1\times10^{-8}$ torr were routinely achieved. The cell was baked under vacuum for several days at 450°C to drive the water vapor off the walls. Rb was distilled several times prior to introduction into the cell. The cell was filled with ultra-pure gases ($N_2$ grade 6 and $^3$He grade 5.5). The gases were additionally cleaned by Ultra-Pure getters [29] operated at 350°C. To fill the cell to 10 amg. it was cooled by liquid He, so the pressure in the cell was less than 1 atm when it was being removed from the manifold by melting of a thin glass tube. Liquid He was flowing through a specially constructed dewar which fit over the target chamber of the cell. After the cells were filled, they were baked at 140° overnight. This procedure is believed to improve the lifetime of the cell by allowing Rb to cover the surface and getter any impurities in the gas phase.

The nuclear relaxation lifetimes of the cells measured before the run are shown in Table 4.2. All cells had lifetime in excess of 30 hrs. Two cells had a lifetime within errors of the bulk limit and another 2 cells in excess of 50 hrs.

The physical parameters of the cells, i.e. dimensions, volumes, densities, are very important in calculating the polarization and the dilution factor of the target.

Because of the increased statistical precision of our experiment, it was very important to reduce the errors in these quantities. Therefore, we pay particular attention to their measurement, as described in the next 4 sub-sections.

### 4.2.1 Cell Dimensions

The dimensions of the cells enter into the polarimetry analysis in various ways. The size and shape of the target cell and the pumping cell determine the size of the AFP signal used for $^3$He polarimetry. By far, the most important dimension for determining this signal is the diameter of the target cell, since it determines the volume of polarized material between the pick-up coils. The dimensions of the transfer tube determine the diffusion time for polarized $^3$He between the pumping and the target cells, and hence, the difference between the pumping cell and target cell polarizations which is needed for EPR polarimetry. The care taken to measure each of the dimensions was roughly proportional to the sensitivity of the final result to that number. All dimensions of the cells are listed in Table 4.1. The missing numbers for Riker are quantities which could not be measured after the run due to the violent explosion which destroyed the cell. Riker was the only cell for which both the pumping cell and the target cell were destroyed when one of the windows failed.

| Cell | Target Cell | | | Flare | | Transfer Tube | | Pumping Cell | | |
|---|---|---|---|---|---|---|---|---|---|---|
| Name | OD | $\sigma_{OD}$ | Wall | Start | OD | OD | Length | OD | L. 1 | L. 2 |
| Dave | 20.75 | 0.02 | 0.730 | 110 | 26.7 | 12.4 | 61.5 | 36.3 | 84.0 | 95.1 |
| Riker | 21.72 | ? | 0.697 | 105 | 25.7 | 11.8 | ? | 37.2 | 70.6 | 82.3 |
| Bob | 20.80 | 0.03 | 0.728 | 115 | 26.6 | 12.3 | 61.2 | 36.1 | 79.0 | 94.6 |
| SMC | 20.66 | 0.05 | 0.733 | 110 | 26.3 | 12.2 | 63.5 | 37.8 | 77.7 | 90.7 |
| Generals | 21.62 | 0.13 | 0.700 | 110 | 25.9 | 12.9 | 59.2 | 36.0 | 66.8 | 80.0 |
| Hermes | 20.53 | 0.03 | 0.737 | 110 | 26.7 | 11.9 | 62.9 | 37.7 | 74.8 | 89.4 |
| Prelims | 21.24 | 0.04 | 0.713 | 110 | 26.0 | 12.9 | 59.4 | 36.1 | 68.3 | 80.5 |
| Chance | 21.33 | 0.05 | 0.710 | 118 | 25.4 | 13.5 | 67.0 | 35.8 | 79.0 | 93.0 |
| Picard | 22.40 | 0.09 | 0.676 | 105 | 25.3 | 11.5 | 61.6 | 37.7 | 65.5 | 79.8 |
| Water I | 20.55 | 0.03 | 0.737 | 102 | 24.8 | 14.0 | 59.7 | 36.8 | 74.9 | 88.9 |
| Water II | 22.62 | 0.07 | 0.669 | 112 | 25.4 | 13.2 | 72.6 | 36.8 | 73.7 | 94.5 |

Table 4.1: Cell Dimensions in mm.

The target cell diameters were measured with a caliper at 8 different points near the middle of the cell, where the pick-up coils are placed. Since the cells are made from reblown glass, they are not exactly cylindrical and there is a small variation of the diameter along the cell. The amount of the variation is indicated by $\sigma_{OD}$ which is simply the standard deviation of the data set. Although the simple average of the

| Cell Name | Length, mm | Nuclear Lifetime, hrs | $N_2$ Density, amg. |
|---|---|---|---|
| Dave | 291 | 45 | 0.075 |
| Riker | 300 | 67 | 0.047 |
| Bob | 299 | 58 | 0.075 |
| SMC | 302 | 50 | 0.079 |
| Generals | 297 | 45 | 0.079 |
| Hermes | 295 | 44 | 0.079 |
| Prelims | 300 | 30 | 0.078 |
| Chance | 299 | 41 | 0.078 |
| Picard | 299 | 68 | 0.078 |
| Water I | 302 | | |
| Water II | 297 | | |
| Ref. Cell 1 | 303.5 | | |
| Ref. Cell 2 | 297.4 | | |
| Ref. Cell 3 | 304.3 | | |
| Ref. Cell 4 | 302.3 | | |

Table 4.2: Miscellaneous cell parameters: the length, the nuclear relaxation time measured before the run, and the density of $N_2$ gas.

measurements does not take into account the scaling of the area with the square of the diameter, it is different from the true value only in second order (i.e. $\Delta A/A = (\sigma_{OD}/OD)^2/3 = 10^{-5}$ for the worst case). The error of individual measurements is about 0.025 mm. Assuming that different positions along the cell were sampled randomly (in reality, measurements were made at roughly regular intervals, but the dependence of the diameter on the position may be non-monotonic, so it is more conservative to assume random sampling), the OD spread should be divided by the square root of the number of measurements. This gives an error of 0.05 mm in the worst case. The caliper may also have a systematic error of up to 0.05 mm. To be conservative, an error of 0.5% (0.1 mm) is used for the OD of the target cell.

The thickness of the glass walls of the target chamber was measured for several cells using laser interferometry, described in the next section, or a caliper, with the results given in Table 4.3. Again, the measurements were made at several points near the middle of the cell. The results are fitted to a function $t_w = A/D_{cell}$ where $A = 15.14$ mm$^2$ is a common constant for all cells. It assumes that when the glass is reblown to a bigger diameter it is not stretched, and the wall thickness is inversely proportional the diameter due to volume conservation. Using the spread divided by the square root of the number of measurements as the error, the data give a fit with $\chi^2 \ll 1$. This confirms the dependence of the wall thickness on the diameter and

| Cell Name | Wall Thickness | Spread |
|---|---|---|
| Riker | 0.691[c] | 0.028 |
| Generals | 0.710[l] | 0.040 |
| Hermes | 0.734[l] | 0.045 |
| Prelims | 0.702[c] | 0.055 |
| Picard | 0.682[l] | 0.068 |
| Water I | 0.732[l] | 0.045 |

Table 4.3: Wall Thickness, mm. (c - caliper, l -laser)

implies that the errors are very conservative. In Table 4.1 the results of the fit are used to generate the numbers for the wall thicknesses. The error in the wall thickness is 0.02 mm.

The rest of the numbers in Table 4.1 come from direct measurements with a caliper. For the pumping cell, Length 1 is the distance between the points where the cylinder starts to round off and Length 2 is the total outside length of the cell. The errors range from 1% for the pumping cell OD to 5% for not very well defined dimensions (like position of the flare). The wall thicknesses are: flare - 0.95 mm, pumping cell - 1.03 mm, transfer tube - 1.18 mm, all with an error of 0.1 mm. They were determined by measuring tube samples which were reblown in the same way as the cells, as well as by measuring the wall thicknesses of broken cells. For calculation of the dilution factor, one also needs the lengths of the cells, which are given in Table 4.2. They are accurate to 1%.

### 4.2.2 Window Thicknesses

The thicknesses of the cell windows were measured by three methods. Initially, we measured the thickness mechanically, with a displacement micrometer, which had a resolution of 0.05 mils and an accuracy of 0.1 mil. However, some of the windows would break under the pressure of the tip and others might be scratched. Therefore, we started to use an X-ray absorption method to measure the thicknesses. We used a $^{55}$Fe source, which emits X-rays due to K electron capture. The energies and relative intensities of the lines are given in Table 4.4 [30]. The X-ray spectrum is shown in Figure 4.5. We used a germanium detector to detect the X-rays. To determine the total X-ray count we always integrated under the area of both peaks, since the detector resolution was not sufficient to cleanly separate the two. At this low energy the X-rays are absorbed only by the photoelectric effect, since the cross-section for Compton scattering is 1500 times smaller. Since the photons are absorbed in one interaction process, there are no problems due to back-scattering or deflection. The absorption length of the $^{55}$Fe X-rays in glass is approximately 1.6 mils. This is almost ideal for our windows of 2-3 mils, as one can show that the optimal ratio of the

| Energy, keV | Relative Intensity |
|---|---|
| 5.899 | 100 |
| 5.888 | 50 |
| 6.492 | 20.2 |

Table 4.4: X-rays emitted by the $^{55}$Fe source.

window thickness to the absorption length is 2:1. A collimator with a circular hole 3 mm. in diameter was used to restrict the detector acceptance. Thus, the measured thickness was an average over a 3 mm. area in the center of the window. For each set of measurements we determined the incident intensity by counting X-rays with no windows. We also measured a small background rate by blocking the hole in the collimator, and subtracted it from the other intensities.

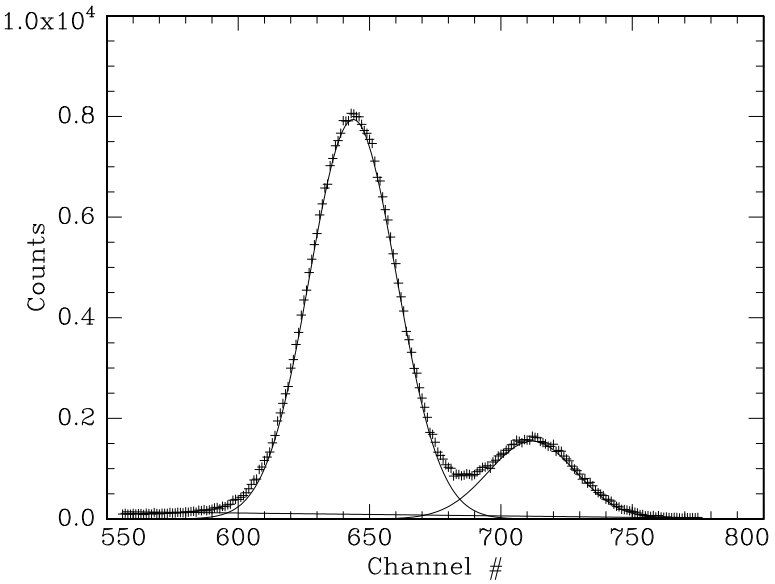


Figure 4.5: X-ray spectrum from $^{55}$Fe source recorded by a germanium detector. The spectrum is fit well by a sum of two gaussians plus a small linear background.

The absorption cross-section is inversely proportional to the third power of the energy [30]:

$$\sigma_x \sim E^{-3} \tag{4.21}$$

Since there are two lines of different energy, we approximate the absorption by a sum of two exponentials:

$$I(x) = I_0 \left( e^{-\alpha_1 x} + r e^{-\alpha_2 x} \right) \tag{4.22}$$

The parameters in equation (4.22) are measured as follows. To calculate $r$ we fit the spectrum shown in Figure 4.5, which was obtained with no windows in the path of the X-rays, to two gaussians and determine the ratio of their areas. We obtain $r = 0.195$. Note that this number is different from the naive estimate using the data in Table 4.4: $r_0 = 0.134$, because the X-rays are partly absorbed in the air between the source and the detector. The more energetic X-ray is absorbed less, so its relative intensity is higher. To determine $\alpha_2/\alpha_1$ we use the photoelectric cross-sections given as a function of energy in [31] and the known composition of glass (see Table 4.12). We obtain $\alpha_2/\alpha_1 = 0.761$. Again, this number is slightly different from a naive estimate $\alpha_2/\alpha_1 = (E_1/E_2)^3 = 0.749$ because equation (4.21) is only approximate. To check this ratio, we also recorded the X-ray spectrum and separately measured the absorption of the two lines for several windows. In this way we obtained $\alpha_2/\alpha_1 = 0.760 \pm 0.003$. To determine the last constant $\alpha_1$ we measured the X-ray absorption for a number of windows whose thickness was known from a different method. Initially, we used mechanical measurements for this calibration, but later we recalibrated with interferometric measurements, described later in the text. The data used for calibration are shown in Figure 4.6 with a fit to equation (4.22). From the fit we obtain $\alpha_1 = (41.5 \pm 0.7\,\mu m)^{-1}$. This number can be compared with a theoretical estimate based on known cross-sections [31] and the composition of the glass: $\alpha_1^{th} = (42.7 \pm 1.4\,\mu m)^{-1}$, where the error is dominated by the uncertainty in composition of the glass.

With this calibration we can now calculate the thickness of all windows measured by X-rays. The error is dominated by the statistical uncertainty. The windows were measured for 100–200 sec., which gave about 1000 counts in the detector and a error of about 3%.

After the run we implemented an interferometric method for measuring the thickness, which is much more accurate. In addition, the measurements could be performed on windows already sealed in cells, which is impossible with the other two methods. This allowed us to remeasure all of the surviving windows of the cells used in the run. The schematic of the setup is shown in Figure 4.7. It is easy to show that the reflection coefficient is given by [32]:

$$\begin{aligned} R &= \frac{K}{1+K} \\ K &= \left[\frac{n^2-1}{2n}\sin\left(\frac{2\pi}{c}n\nu d\right)\right] \end{aligned} \tag{4.23}$$

where $n$ is the index of refraction of the glass and $d$ is the thickness of the window. Therefore, the reflection coefficient oscillates as the frequency of the light is scanned. Figure 4.8 shows such a signal recorded by the photodiode. In fitting the data we also allowed for a background due to smearing of the interference fringes. The frequency of

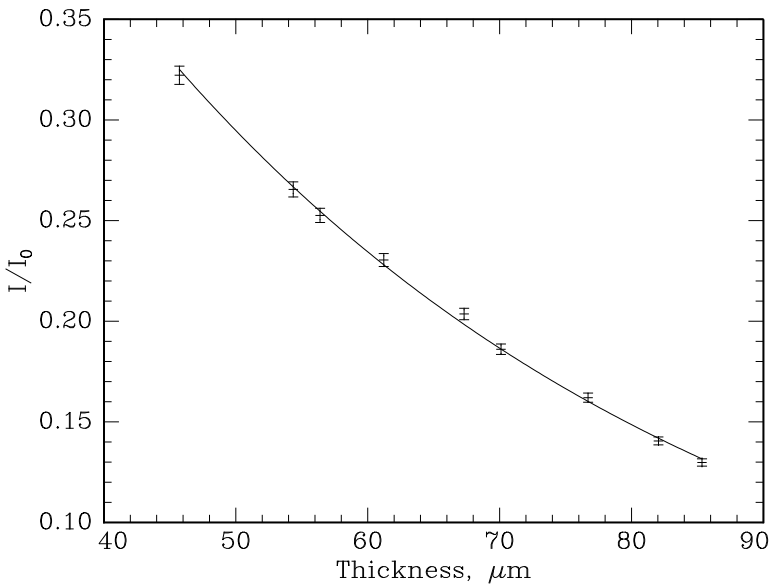


Figure 4.6: Absorption of X-rays in windows as a function of their thickness. The errors are statisitical. The thickness is measured by the interferometric method.

the oscillations can be determined very precisely. The correction due to the deviation of the beam from the normal direction is proportional to $\cos 4^\circ = 0.998$, and is negligible. So, we only need to know the index of refraction of 1720 glass to determine the window thickness. The index of refraction is known at the Na D line [33, 34] $n = 1.530$. Using approximate wavelength dependence from [35] we estimate that $n = 1.523$ at 780 nm. In addition, we determined this number by a measurement of the Brewster angle at 780 nm: $\tan\theta_B = n = 1.519 \pm 0.01$. The windows measured after the run suffered substantial radiation damage (they were brown). To check that the radiation damage did not affect the index of refraction, we measured the thickness of two pieces of glass from the wall of a cell. They were sufficiently thick (1 mm) to be also measured accurately with a micrometer. In this way we found $n = 1.528 \pm 0.01$. So, we know $n$ to better than a percent.

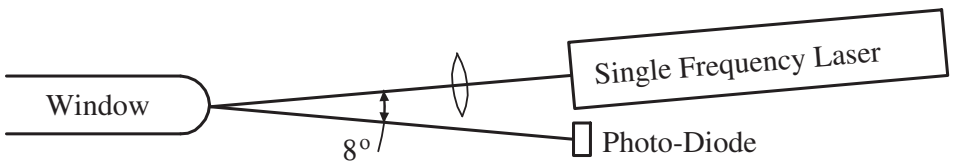


Figure 4.7: Setup for interferometric thickness measurements.

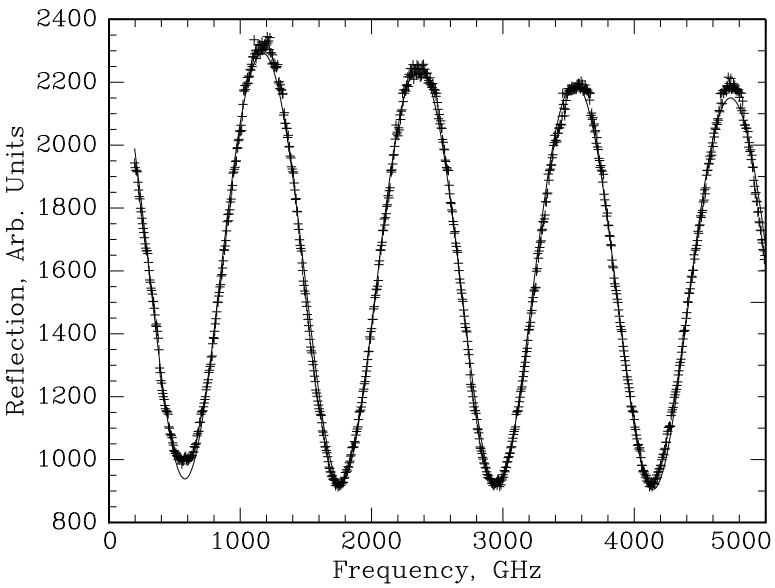


Figure 4.8: Reflection coefficient as a function of the laser frequency.

The optical method was used to measure the thickness of the windows used for calibration of the X-ray absorption. We also compared it with mechanical measurements, with results shown in Figure 4.9. As can be seen, the two independent methods for measuring the thickness are in good agreement. Since the optical method is more precise, a small correction described by the fit shown in Figure 4.9 is applied to the mechanical measurements. Finally, the optical method allows one to study the variations in the thickness of the window with position. The optical beam is focused to much less then a millimeter in diameter and is easily positioned anywhere on the window (the beam is also visible with an IR viewer, which makes alignment much easier). The measurements were performed for Picard, displacing the beam by about 2 mm from the center in different directions, which is somewhat larger than the expected alignment error of $\sim$1 mm. Compared to the thickness in the center, the thickness changes ranged from –2.2% to +7.7%, with an average of +2% and a standard deviation of 3%. The results of the window measurements for all cells are shown in Table 4.5. The difference column indicates the difference between methods, if more than one was used. It shows that the mechanical and X-ray methods have comparable accuracy on the order of 5%. For the windows measured with the optical method we use a error of 3% due to the non-uniformity of the windows. For X-ray measurements the error is probably somewhat larger than the statistical error because of thickness variations. We use a 5% error for those windows which have not been measured optically.

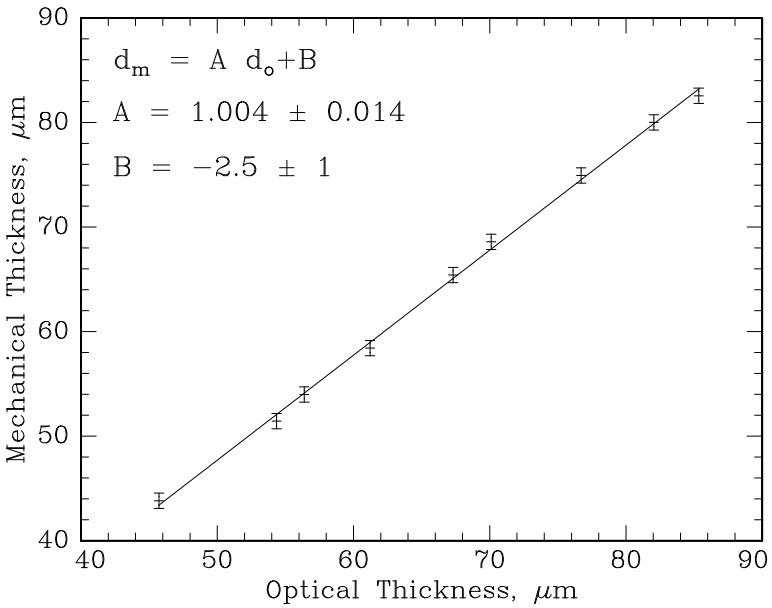


Figure 4.9: Comparison of the mechanical and optical measurements of the window thicknesses. The errors are estimated based on repeatablity of the mechanical measurements.

### 4.2.3 Cell Volumes

For the analysis, it is important to know both the total volume of the cell and the partial volumes of the pumping cell, the target cell, and the transfer tube. The total volume of the cell is used in calculating the gas density from the gas filling data. The partial volumes are needed for corrections to the density due to different temperatures in different parts of the cell. We know the volumes from three different sources: calculations based on outside dimensions and wall thicknesses (this is the only way we know individual volumes), volume measurements on the vacuum system, and buoyancy measurements. The results of the three methods are listed in Table 4.6.

The volume measurements on the vacuum system were done using a calibrated volume and an accurate barotron [36]. First, the calibrated volume was filled to a certain pressure, and the rest of the vacuum system was pumped out. Then the calibrated volume was opened to the string containing the cell and the final pressure was recorded. After the cell was pulled off, the same procedure was repeated again. The measured reduction of the string volume is almost exactly equal to the volume of the cell, since the pull-off volume is only 0.1 $cm^3$. The uncertainties come from the volume of the valves ($\sim$0.2 $cm^3$), as well as variations in the volume of the flexible

| Cell Name | Window # | Thickness, $\mu m$ | | | Diff, % |
|---|---|---|---|---|---|
| | | Mechanical | X-ray | Optical | |
| Picard | 39 u | 65.3 | | 69.3 | 6.1 |
| | 41 d | 57.7 | | 61.6 | 6.8 |
| Riker | 40 * | 66.5 | | | |
| | 36 * | 60.0 | | | |
| Hermes | 54 u b | | 46.9 | | |
| | 50 d | | 56.6 | 59.0 | 4.2 |
| Prelims | 30 u | 45.5 | 44.7 | 45.8 | 0.7/2.5 |
| | 43 d b | 42.4 | 42.0 | | 1.0 |
| Generals | 45 u b | 52.5 | 51.9 | | 1.1 |
| | 48 d | 54.4 | 59.0 | 59.9 | 10/1.5 |
| Dave | 81 u b | | 45.0 | | |
| | 80 d | | 53.5 | 52.5 | 1.9 |
| SMC | 38 * | 67.7 | 69.5 | 68.8 | 1.6/1.0 |
| | 56 * | | 61.0 | 64.2 | 5.2 |
| Bob | 60 u b | | 70.1 | | |
| | 61 d | | 69.7 | 69.5 | 0.3 |
| Chance | $38_x$ u | | 85.1 | 83.0 | 2.5 |
| | $13_x$ d | | 81.2 | 83.0 | 2.2 |
| Ref. Cell #1 | 94 u | | 58.4 | | |
| | 91 d | | 46.5 | | |
| Ref. Cell #2 | $4_x$ u | | 73.5 | 74.2 | 1.0 |
| | $7_x$ d | | 46.3 | 45.9 | 0.9 |
| Ref. Cell #3 | D u | | 50.9 | 57.3 | 12.6 |
| | F d | | 48.5 | 48.1 | 0.8 |
| Ref. Cell #4 | E u | | 70.8 | 72.1 | 1.8 |
| | K d | | 64.0 | 61.9 | 3.3 |

Table 4.5: Window thicknesses. Notation: u – upstream. d – downstream, b – broke in beam, * – orientation not known.

bellows with pressure. The error in the volume of the cell is on the order of 0.4%, based on repeated measurements of a portion of the vacuum manifold.

The buoyancy measurements rely on Archimede's principle. First, the cell is weighed on an accurate scale. Then, the cell is attached to a metal block suspended from the scale and submerged in water. The buoyant force on the cell, which is proportional to the cell outside volume, causes a decrease in the apparent weight of

| Cell Name | Calculations | | | | Vacuum System | Buoyancy |
|---|---|---|---|---|---|---|
| | Target | Pumping | Transfer | Total | | |
| Dave | 102.0 | 83.7 | 4.5 | 190.2 | - | 186.8 |
| Riker | 114.7 | 75.5 | 3.8 | 194.0 | - | 187.8 |
| Bob | 105.1 | 80.8 | 4.3 | 190.2 | 189.0 | 189.0 |
| SMC | 107.1 | 83.9 | 4.4 | 195.4 | - | 190.0 |
| Generals | 111.4 | 67.9 | 4.7 | 184.0 | 179.6 | 180.1 |
| Hermes | 103.5 | 81.5 | 4.1 | 189.1 | 185.4 | 183.9 |
| Prelims | 106.5 | 69.1 | 4.8 | 180.4 | - | 178.6 |
| Chance | 108.6 | 73.8 | 6.0 | 188.4 | 179.6 | 180.5 |
| Picard | 116.6 | 74.1 | 3.6 | 194.3 | 190.1 | 191.5 |

Table 4.6: Cell Volumes in $cm^3$.

the block. The inside cell volume is calculated using the formula:

$$V_C = \frac{W_b - W_{bc} + m_c}{\rho_w} - \frac{m_c - m_g}{\rho_{gl}} \tag{4.24}$$

where $W_b$ is the weight of the block submerged in water, $W_{bc}$ is the weight of the block and the cell submerged together, $m_c$ is the mass of the cell, and $m_g$ is the mass of the $^3$He gas. $\rho_w$ is the density of water and $\rho_{gl}$ is the density of glass. The scale was calibrated using precision weights, so the error in the weight measurements is less than 0.2%. The density of 1720 glass is equal to 2.54 $g/cm^3$ according to [33] and 2.52 $g/cm^3$ according to [34]. This value was checked by performing the buoyancy measurement on a 1720 glass tube. The result is $2.506 \pm 0.005$ $g/cm^3$. The overall error of the volume measurements by the buoyancy method is about 0.4%

While the results of the vacuum system measurements and the buoyancy measurements agree quite well (standard deviation 0.5%), the calculations give a result $2.3 \pm 1\%$ too high. This is not surprising, since the geometrical model used for the volume calculation was very simple. For Water Cell I the volumes of individual parts were measured during filling with water, with results given in Table 4.7.

| Water Cell I | Target | Pumping | Transfer | Total |
|---|---|---|---|---|
| Calculation | 101.9 | 79.4 | 5.9 | 187.2 |
| Filling | 98.8 | 76.5 | 6.6 | 181.9 |
| Difference | +3.1% | +3.8% | -12% | +2.9% |

Table 4.7: Individual volumes of cell chambers.

So, the volumes of both the target cell and the pumping cell are overestimated by about the same amount. However, only the ratio of the volumes enters into the

analysis, so the errors will cancel to a large degree due to correlations. We always use volumes of the same origin in the analysis, not the volume of the pumping cell and the total volume from the buoyancy measurement. The small (1%) scatter in the results of the volume calculations indicate that it is very unlikely that the two volumes will fluctuate in opposite directions by a large amount. Nevertheless, a conservative 3% error is assumed in the ratio of the volumes since it makes very little difference on the final result.

### 4.2.4 Cell Densities

The density of $^3$He in the cells was measured using two independent methods. The first method used the measurements of the pressures in the vacuum system while the cell was being filled with gas. During the filling of the cell with $^3$He, the target cell was cooled by liquid He to about 10K and its temperature was quite uncertain. So, the amount of $^3$He gas was carefully measured before it was put into the cell. A certain amount of gas was introduced into a calibrated manifold volume and its pressure recorded. The calibrated volume was then opened to the cold cell and the final pressure was recorded after equilibrium was established. One can thus calculate how much gas had exited the calibrated volume and entered into the cold cell. This procedure was repeated several times until a sufficient amount of gas was introduced into the cell. The final density of $^3$He is then given by:

$$n_{He} = \frac{273.16}{T_V\ V_C} \left\{ \left[ \sum_{j=1}^{N} \left( P_f^j - P_i^j \right) V_M \right] - \left( V_S - V_C \right) P_f^N \right\} \tag{4.25}$$

where $V_M$, $V_S$, and $V_C$ are known volumes of the vacuum manifold, the string and the cell respectively. $P_i^j$ and $P_f^j$ are the pressures in the vacuum manifold for $j^{th}$ fill cycle before and after it was opened to the cell. The temperature in the room was measured before the filling procedure. However, the vacuum system temperature $T_V$ was somewhat uncertain due to the presence of very cold helium vapors exiting the dewar during filling. Although the helium stream from the dewar did not directly hit any part of the system and quickly rose to the ceiling, it might have reduced the temperature somewhat. We will assign a somewhat arbitrary error of 2°C to $T_V$. Other errors come from the uncertainties in the volumes (0.4%) and pressures (0.3%), so the total error of this method is about 0.9%.

Before the cell was filled with $^3$He gas, a known amount of $N_2$ was introduced into the cell manifold. It froze into the cell when it was cooled by liquid He before filling it with $^3$He. In this way we determined the $N_2$ densities in the cells, which are given in Table 4.2. They are accurate to about 5%.

While the fill measurements provide sufficient accuracy, they cannot be rechecked for errors and the possibility of cell leakage after filling cannot be excluded. Therefore,

the cell density was also measured using a different technique that allows the measurements to be done after the cell has been filled and sealed. It uses the broadening and shift of the Rb resonance absorption lines by $^3$He. In the presence of several atmospheres of He gas, the pressure broadening of the Rb absorption lines, $D_1$ and $D_2$, exceeds the Doppler broadening and the lines acquire a simple lorentzian shape [37]. As was first measured by Chen [38], the width and the shift of these lines is linear in He pressure to several tens of atmospheres and can serve as a good measure of the He density. Since Rb pressure broadening data for $^3$He exist only for the $D_1$ line [17], and even they are not quite of sufficient accuracy for our purposes, an experiment was performed to measure the broadening and shift of the Rb absorption lines by $^3$He. In addition, we studied pressure broadening of Rb $D_1$ and $D_2$ lines by $^4$He, $N_2$, and Xe. The data were analyzed using a line-shape for a Van der Waals interatomic potential derived in [39]. The results are presented in [40], which is reproduced in Appendix B. Here we only give a brief description of the measurement for $^3$He.

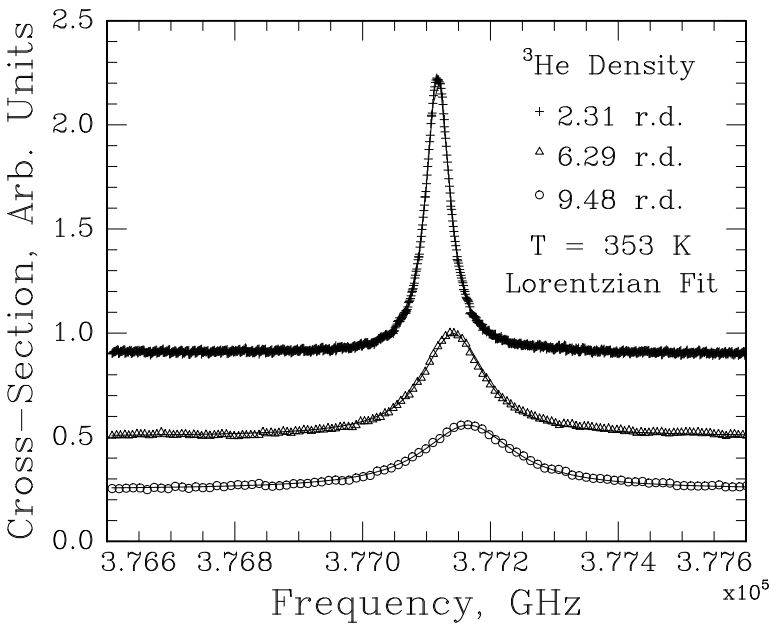


Figure 4.10: Rb $D_1$ absorption cross-section for several $^3$He densities.

A single frequency Coherent 899-29 Ring laser was used to scan across the absorption lines. The laser linewidth is much smaller than the width of the absorption lines and does not contribute to broadening. The laser also has a built-in wavemeter which was used to measure the pressure shifts of the line position. The transmission of the laser light through a 7 cm long cell was monitored with a photodiode. The cell was

heated to $80°C$, so the absorption factor $e^{-n\sigma L}$ ranged from 0.3 to 0.007 for the range of densities studied. For most measurements the power of the laser was attenuated to 3 mW to avoid saturating the transition. To check the linearity of the photodiode and the absence of atomic line saturation we also took data with the laser attenuated to 30 $\mu$W. The temperature of the cell was kept stable to 0.1°C to ensure constant Rb number density. The measurements were performed for $^3$He densities ranging from 1.5 to 9.5 amagats. The cell was attached to a pressure transducer which provided pressure measurements accurate to 0.3%. To convert the pressure to a density, one has to include the non-ideal behavior of the gas at these densities. At relatively low pressures it is usually described by the virial expansion [41]:

$$\frac{p}{kT} = n + Bn^2 + Cn^3 + \cdots \tag{4.26}$$

At the densities used in this experiment, it is only necessary to keep the first two terms. The values of $B$ for $^4$He are given in [42]. It also contains data that indicate that the difference between $^3$He and $^4$He is at most several percent. However, the CRC Handbook of Chemistry and Physics gives somewhat different numbers. We will use B=11.6±1 cm$^3$/mol. At the highest density this gives a 0.5% correction to the ideal gas law. It should be pointed out that this correction does not apply to equation (4.25), because all measurements on the vacuum system are performed at pressures below 1 atm. and at room temperature, where the ideal gas law is quite accurate. Typical absorption curves for the $D_1$ line are shown in Figure 4.10. For our purposes of comparing the absorption width in a calibration cell with the absorption width in a target cell it is sufficient to fit the lines to a simple lorentzian:

$$\sigma(\nu) = \frac{\sigma_0 \Gamma}{(\nu - \nu_c)^2 + \Gamma^2} \tag{4.27}$$

which describes the data sufficiently well. More sophisticated lineshapes are discussed in Appendix B. The dependence of the half-line width and position on $^3$He density is shown in Figure 4.11. It is well described by a linear fit $\Gamma = \Gamma_0 + a\,[^3He]$ for the width and a quadratic fit for the line center: $\nu_c = \nu_0 + b\,[^3He] + c\,[^3He]^2$. In all cases, the intercept of the fit is equal to zero within errors. The results of the fits are given in Table 4.8. The errors are given only for reference since they do not include correlations.

| | $\Gamma_0$, GHz | $a$, GHz/amg. | $\nu_0$, GHz | $b$, GHz/amg. | $c$ , GHz/amg.$^2$ |
|---|---|---|---|---|---|
| $D_1$ | 0.46±0.61 | 9.34±0.095 | 1.21±0.58 | 4.97±0.23 | 0.141±0.02 |
| $D_2$ | 0.08±0.56 | 10.38±0.087 | 0.48±0.33 | 0.583±0.14 | 0.0415±0.012 |

Table 4.8: Specific broadening and shift of Rb resonance lines in the presence of $^3$He.

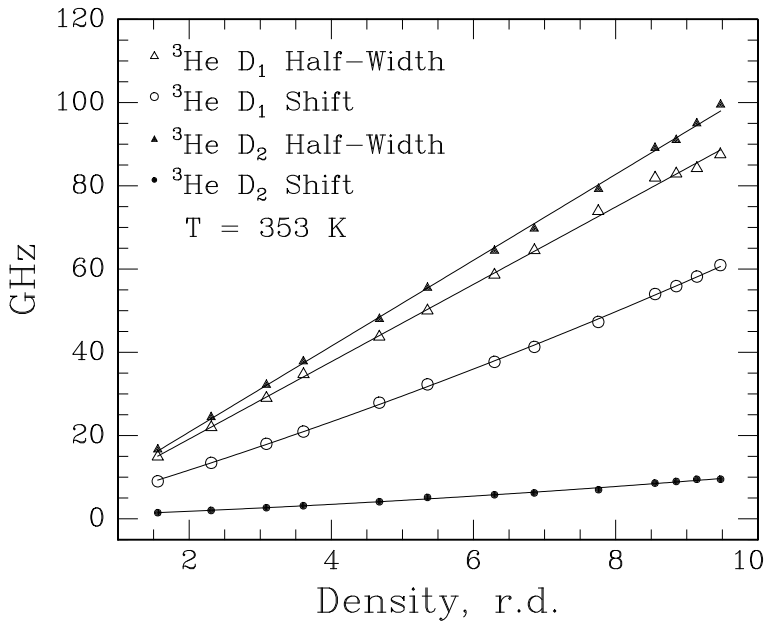


Figure 4.11: The width and shift of Rb resonance lines as a function of $^3$He density.

The Rb optical absorption curves for the SLAC-E154 $^3$He cells were measured before the run for all cells. Three quantities were used to determine the density: $D_1$ width, $D_1$ shift and $D_2$ width. Since the $D_2$ line shift is small, it was not used directly to determine the pressure but to check the absolute wavelength calibration of the laser. The specific shift and broadening of the Rb lines in the presence of $N_2$ was also measured and gave a correction to the $^3$He broadening on the order of 1%. The results of the three measurements were first averaged with equal weight and then the standard deviation from the average was calculated for each quantity. The errors of the pressure measurements are 0.13 amg. for $D_1$ width, 0.074 amg. for $D_2$ width, and 0.084 amg. for $D_1$ shift. The systematic difference between measurements did not exceed 0.04 amg. The results were then averaged using the error as the weight. The error on the final average is about 1.0%

Table 4.9 shows the results of the individual optical measurements, the combined weighted average and the results of the pressure measurements during filling. The density is in amagats, $1\ amg. = 1\ r.d. = 2.689 \times 10^{19}\ cm^{-3}$. The average deviation of the two methods is 1.3%, in very good agreement with their estimated errors of 1.0% and 0.9% respectively, and the systematic difference is 0.4%. After the run, optical measurements were performed on the three remaining cells (Picard, SMC, Chance) and no measurable reduction in density was found. We will use the average of the two methods with an error of 1% for the cell density at temperature equilibrium.

| Cell Name | Optical Measurement, amg. | | | | Fill Density | Diff. % | Average |
|---|---|---|---|---|---|---|---|
| | $D_1$ width | $D_2$ width | $D_1$ shift | W. Ave. | | | |
| Dave | 8.48 | 8.72 | 8.78 | 8.70 | 8.87 | -2.0 | 8.78 |
| Riker | 8.80 | 8.91 | 8.89 | 8.88 | 8.86 | 0.2 | 8.87 |
| Bob | 8.99 | 8.89 | 8.76 | 8.86 | 8.81 | 0.6 | 8.83 |
| SMC | 8.59 | 8.76 | 8.75 | 8.73 | 8.96 | -2.6 | 8.84 |
| Generals | 9.00 | 8.75 | 8.74 | 8.78 | 8.77 | 0.1 | 8.77 |
| Hermes | 8.67 | 8.78 | 8.62 | 8.70 | 8.77 | -0.8 | 8.74 |
| Prelims | 9.19 | 8.95 | 8.90 | 8.97 | 8.84 | 1.5 | 8.90 |
| Chance | 8.77 | 8.99 | 8.71 | 8.85 | 8.97 | -1.4 | 8.91 |
| Picard | 8.97 | 8.90 | 8.83 | 8.89 | 8.84 | 0.6 | 8.87 |

Table 4.9: $^3$He densities in amagats.

## 4.3 Target Setup

The target setup included two orthogonal sets of Helmholtz coils, a mechanical target mover, a number of sensors and coils used for polarimetry and the laser system. The target schematic with major components is shown in Figure 4.12. Two orthogonal sets of Helmholtz coils were used to control the direction of the polarization (only one shown). One set of coils created a holding fields parallel to the direction of the beam, while the second set was used to adiabatically rotate the direction of the polarization and to collect data with the polarization transverse to the beam. The coils were driven with Kepco BOP–36–12 power supplies, which allowed sweeping the magnetic field for polarization measurements, as described in Chapter 5. The $^3$He cell was installed inside a scattering chamber, which was pumped out by mechanical pumps. $^4$He cooling jets were directed at the windows of the cell to remove the heat deposited by the electron beam. In addition to the polarized $^3$He target, a reference cell was mounted inside the scattering chamber. The reference cell could be filled with varying amounts of gas remotely, and was used for measurements of the dilution factor. A mechanical mover system was used to switch between the polarized target, the reference cell and the "no target" position. The pumping chamber of the polarized $^3$He cell was enclosed in an oven. The oven was sealed around the pumping cell with RTV rubber glue. Hot air flowed through the oven to heat the pumping cell to approximately 180°C. A number of RTD sensors monitored the temperature in various parts of the cell.

The laser system consisted of 3 fiber-coupled diode arrays and 4 Ti-Sapphire lasers. The fiber-coupled arrays, a relatively new product, were manufactured by OptoPower [43]. They are based on a linear diode array mounted on a thermo-electric cooler. Each diode in the array is individually coupled to an optic fiber and the fibers are

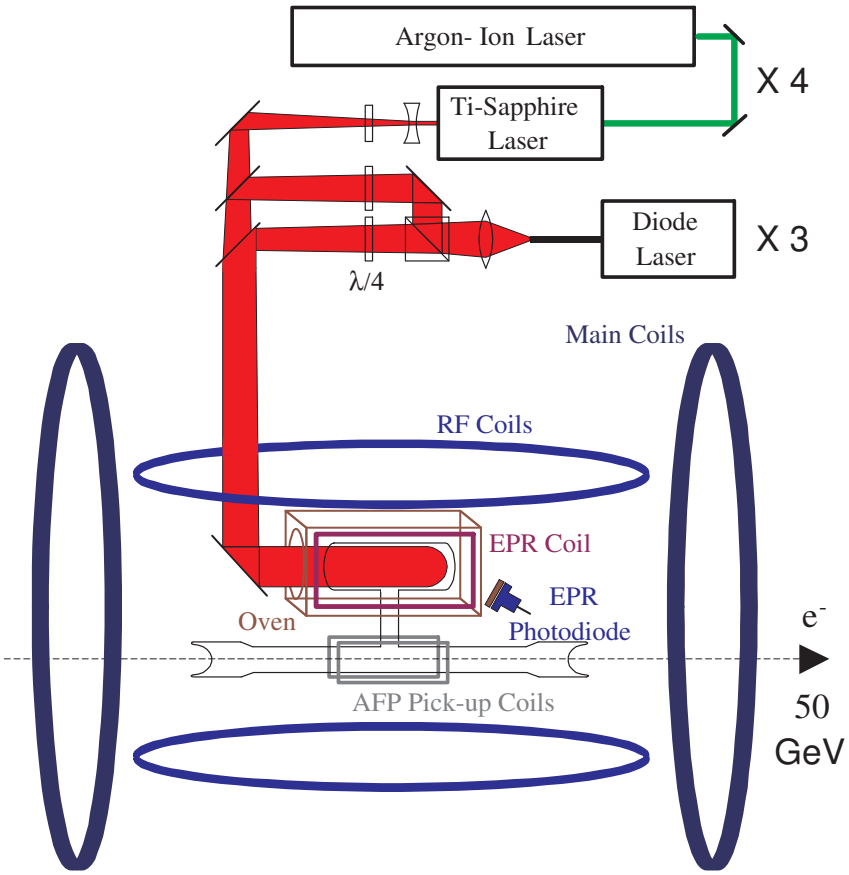


Figure 4.12: The overall setup of the $^3$He target.

combined in a bundle. The diameter of the fiber bundle is about 1.5 mm and the divergence of the beam coming from the bundle is about 10° full cone. The laser power out of the fiber is about 15-17 watts. The light is mostly unpolarized because the fibers do not preserve the direction of the polarization. The spectral width of the diode is about 2 nm FWHM. The profile is not entirely symmetric, as it depends on the wavelength distribution of the 20 individual lasers. The wavelength of the diode can be adjusted by either the temperature or the diode current. The current also controls the power of the laser. The wavelength is increased by 1 nm for every 3°C and 2 amp. One usually sets the current to obtain the desired power and then adjusts the temperature to tune the laser on wavelength. However, since temperature tuning is time consuming due to slow response, fine tuning if often done with the current. Because the diode lasers are very broad, tuning to resonance by observing the fluorescence is difficult. The lasers were tuned by measuring their wavelength with a LightWave wavemeter which had resolution of 0.01 nm. To check the absolute

calibration of the wavemeter, a Ti-Sapphire laser was tuned to Rb resonance by observing the fluorescence and its wavelength was measured and used as a reference point. Another method that can be used for tuning is to observe the EPR signal from the cell, as described in Chapter 5. The EPR signal is roughly proportional to the Rb polarization, so by maximizing it one can optimize the wavelength of the laser.

The beam coming out of the fiber optic bundle is focused by a single lens with a focal length of $f = 200$ mm and transported to the target, which is 5 m away, using 2" mirrors. Since the light from the diode lasers is unpolarized, some manipulation is required before it can be used for optical pumping. The beam is linearly polarized using a beam splitter cube. Both parts of the beam are utilized by using two quarter wave plates and appropriate mirrors. Two beams are obtained from each laser, circularly polarized in the same direction.

In addition, we used 4 Spectra Physics Ti-Sapphire lasers (Model 3900S) pumped by Argon-ion lasers (Model 2040E). Each laser system could be tuned to give about 5 W of power. However, the lasers would drift down to 3–4 W over approximately one day. Since laser tuning required access to the End Station and interruption of the data taking, we could not keep the lasers optimally tuned. In this regard the diode lasers are also much better, since they require virtually no maintenance. Over the course of two month of continues operation (1500 hrs.) the diode laser power dropped by only about 10-20%. Only one laser failed (possibly due to operator error) during the whole experiment. In contrast, 3 out of four ion tubes in the Argon lasers were replaced during the run.

The reference cell system allowed studies of the target dilution factor. The reference cell had the same geometry as the real polarized $^3$He cell and could be filled remotely with a variable amount of $^3$He. The pressure in the cell was read by a transducer gauge and a mechanical manometer.

## 4.4 Cell Temperatures

Under normal running conditions, the pumping cell was heated to achieve sufficient Rb number density, and the target cell and pumping cell had very different temperatures[2]. Although the total number of atoms in the cell did not change, the density in each of its chambers was different from the fill density. The ideal gas law will be used to describe the gas inside the cell under conditions of temperature disequilibrium. The non-ideal behavior gives a correction proportional to $Bn\left(\frac{T_P}{T_T}-1\right)$, which is only 0.1%. Using the ideal gas law, one gets the following equations for the density in the

[2]This was not true for most of the $A_\perp$ when the cell was in thermal equilibrium.

target and pumping cells:

$$n_T = \frac{n_0}{1 + \frac{V_P}{V_0}\left(\frac{T_T}{T_P} - 1\right)}; \qquad n_P = \frac{n_0}{1 + \frac{V_T}{V_0}\left(\frac{T_P}{T_T} - 1\right)} \tag{4.28}$$

where $n_0$ is the density at thermal equilibrium, $V_0$ is the total volume of the cell, and $T_T$ and $T_P$ are the average temperatures of the target and pumping cells respectively. Equation (4.28) assumes that the pressure is equal everywhere inside the cell. In the presence of convection there may be local fluctuations of the pressure. To estimate possible pressure difference between the target and the pumping cell we will consider the Poiseuille flow through the transfer tube [45]:

$$\frac{dN}{dt} = \frac{\pi R^4 p\,\Delta p}{8\eta k T L} \tag{4.29}$$

and calculate a characteristic pressure difference. Using the value of the viscosity $\eta = 35\,\mu$Pa s from [42], we get a pressure gradient $\Delta p/p = 2.4 \times 10^{-6}$ when we set the number of particles that goes through the transfer tube in one second equal to the total number of particles in the cell. So, the pressure fluctuations are negligible. The convection between the pumping cell and the target cell is also suppressed because the pumping cell with the less dense gas is above the target cell, the direction opposite to what would drive convection.

The temperature of the cell was monitored by 7 RTDs, 5 of which were mounted on the target cell or the reference cell and another 2 of which were mounted inside the pumping cell oven. One of the two RTDs inside the oven was attached to the pumping cell with heat sink compound, and connected to the Omron temperature controller. The other RTD was used to measure the temperature of the air flowing through the oven. The air was significantly cooler than the cell itself due to laser heating of the cell. After the run the RTDs were calibrated against an accurate thermometer. It was found that their readings have a constant offset. The hardware readings should be reduced by the amount shown in Table 4.10. The correction is different from [44] because the numbers there refer to the software temperature readings. The error in the temperature measurements is about 2°C after the correction has been applied.

| RTD | 1 | 2 | 3 | 4 | 5 | Omron |
|---|---|---|---|---|---|---|
| Correction, °C | 3.3 | 4.3 | 2.3 | 2.4 | 0.6 | 0.2 |

Table 4.10: RTD Corrections.

There are two effects complicating the calculation of the $^3$He density when the cell is hot. First, the pumping cell is heated by the laser light. As a result, there is a large difference between the temperature of the air flowing around the cell and

the temperature of $^3$He inside the cell. Therefore, the RTD's in the oven do not give a reliable measurement of the $^3$He temperature. Second, the heat is flowing to the target cell through the transfer tube in the center, while its ends are cooled by He jets. Therefore, there is a significant temperature gradient in the target cell. These uncertainties contribute significantly to the errors in both methods of polarimetry and have to be studied in detail.

The question has been raised as to how close the temperature measured by the RTDs mounted outside of the cell was to the gas temperature inside. The heat conductivity of the glass, equal to approximately 1 W/m K, is not as low as it seems. For example, if the pumping cell absorbs 30 W of power from the lasers, the gradient across the glass is only 2.7°C. The heat conductivity of the gas itself is, in fact, much lower. To test the accuracy of the temperature measurement in the target cell and the reference cell, an RTD was placed *inside* the reference cell which was mounted in the scattering chamber. The RTD was also wrapped in aluminum foil to reduce heating by radiation. With the reference cell filled to about 17 psi, the difference between the readings of the RTDs inside and outside of the cell was only $1.4 \pm 0.9$°C. Since the pressure in the actual cells is a factor of 10 greater, the temperature difference should be even smaller.

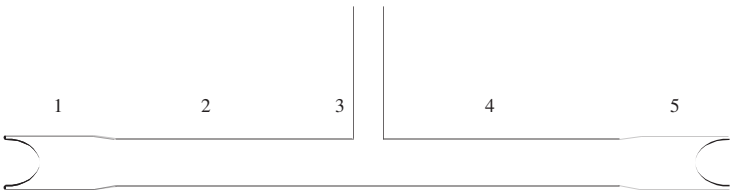


Figure 4.13: Approximate positions of the RTDs mounted on the target cell.

In the beginning of the run all 5 RTDs were mounted on the target cell. Figure 4.13 shows their approximate positions. This allows a careful study of the temperature distribution along the target cell. To better understand the temperature distribution we will construct a very simple thermal model. First, calculate the heat flux from the pumping cell into the target cell:

$$Q = \frac{\left(\lambda_{He} A_{He}^{Tr} + \lambda_{gl} A_{gl}^{Tr}\right) \Delta T}{L_{Tr}} \tag{4.30}$$

where $\lambda$ is the heat conductivity, $A^{Tr}$ is the cross-sectional area, $L_{Tr}$ is the length of the transfer tube and $\Delta T$ is the temperature gradient. Using $\lambda_{He} = 0.22$ W/m K and $\lambda_{gl} = 1$ W/m K we get $Q = 0.09$ W/s. Along the target cell the heat conductance of the glass is $A_{gl}^{Ta}\lambda_{gl} = 4.6 \times 10^{-5}$ W m/K and the heat conductance of the $^3$He gas is $A_{He}^{Ta}\lambda_{He} = 7.0 \times 10^{-5}$ W m/K. Since they are not very different, the radial temperature

gradient should be small. In any case, the radial temperature gradient is at most of the same order of magnitude as the longitudinal gradient and the temperature difference between different radial points is smaller than the temperature difference along the cell by the aspect ratio of the target cylinder. So, a one-dimensional model of heat conduction should be applicable. The data show that the temperature of the target cell does not change by more than a few degrees when the cooling jets are turned off, so most of the heat is carried away by radiation. We will assume a delta function source of heat in the middle of the target cell and a uniform heat sink along the length of the cell. The temperature then satisfies the following differential equation:

$$\frac{d^2T}{dz^2} = -\frac{Q}{\left(\lambda_{gl} A_{gl}^{Ta} + \lambda_{He} A_{He}^{Ta}\right)} \left(\delta(0) - \frac{1}{L_{Ta}}\right) \tag{4.31}$$

The solution of this equation is

$$T(z) = T_0 - \frac{Q}{\sum \lambda A} \left[\left(\Theta(z) - \frac{1}{2}\right) z - \frac{z^2 L_{Ta}}{2}\right] \tag{4.32}$$

where $\Theta(z)$ is the step function. Figure 4.14 shows this distribution along with temperature measurements for 3 cells. Only the value of $T_0$ was adjusted to fit the data. Although this model is overly simplified and should not be taken too seriously, it fits the data surprisingly well. It probably means that the temperature distribution can be described by some elaboration of the heat conduction model and that convection does not play a significant role.

One has to distinguish between two temperatures relevant to the analysis. The volume average temperature of the target cell enters into equation (4.28) and gives the average density of the target cell which is used in both the polarimetry and the dilution factor calculations. On the other hand, the pick-up coils were located in the middle of the cell (see Figure 5.1), which was at a higher temperature and therefore a lower density. So for the purpose of polarimetry, a coil average temperature of the target cell should be calculated using a weighting proportional to the amount of flux generated by the pick-up coils. It can be shown that to first order in temperature gradient, $n_C = n_T T_T / T_C$, where $n_C$ and $T_C$ are the density and the temperature in the central region between the coils. To calculate the average temperature in the central region of the cell, Simpson weighting was used, $T_C = \frac{1}{6}(T_2 + 4T_3 + T_4)$ when all 5 RTDs were mounted on the target cell. This gives a $T_C$ that is 2°C lower than the integral of the temperature distribution (4.32). On the other hand, the real heat source was not a delta function, but was spread over 1 cm. So, the temperature distribution should be rounded off on the top. To estimate the error due to the weighting method, one can look at the two extreme weighting schemes: $T_C = (T_2 + T_3 + T_4)/3$ or $T_C = T_3$. They give temperatures different from the

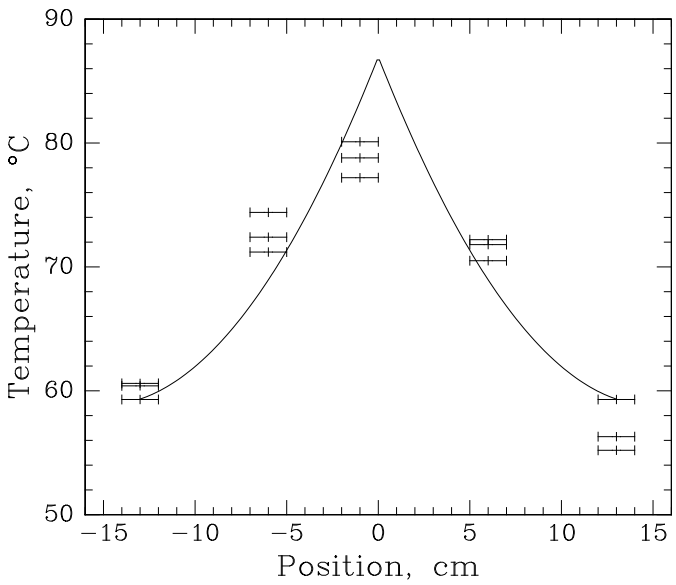


Figure 4.14: Target temperatures of 3 cells compared with the heat conduction model.

Simpson weighting by about 2°C. To find the volume average of the temperature, the following weighting was used: $T_T = 0.185\,(T_1 + T_5) + 0.21\,(T_2 + T_3 + T_4)$, which reflects the larger relative volume of the ends of the target cell. For the 3 cells which had 5 RTDs, the temperature in the center of the target cell was calculated to be $7.6 \pm 1$°C higher than the average temperature. Given the reproducibility of this temperature gradient, the temperature distribution for the cells that had only 3 RTDs can be calculated. On the basis of the above considerations, a 5°C error will be used for the values of $T_C$ and $T_T$.

To determine the amount of heating of the gas inside the pumping cell by the lasers, we studied the variation of the AFP signal when the lasers were turned on and off. Turning the lasers off reduced the temperature of the pumping cell and decreased the density of $^3$He in the target cell according to equation (4.28). The AFP signal was measured before the lasers were turned off and about 10 min. after they were turned off. With the lasers off, the pumping cell reached the temperature of the control RTD. Since the heat flux going through the transfer tube is very small, the temperature of the target cell did not change appreciably in 10 min. The AFP signal decreased by about 1%, an easily measurable amount. Additional measurements were performed to correct for the fast spin-down of the cell with the lasers turned off. Two such studies were performed for Picard and Chance at 170°C and 190°C respectively. The results indicate that the average temperature inside the pumping cell was higher than the control temperature by $14 \pm 5$°C and $7 \pm 4$°C, respectively.

A simple thermal calculation can also be done to estimate the spatial temperature distribution inside the pumping cell. We begin by calculating the temperature distribution in a spherical cell of radius $R$ with a uniform heat source throughout its volume. In spherical coordinates the heat conduction equation is:

$$\nabla^2 T = \frac{\partial^2 T}{\partial r^2} + \frac{2}{r}\frac{\partial T}{\partial r} = -\frac{Q}{\lambda} \tag{4.33}$$

where $Q$ is the power absorbed from the laser per unit volume. The solution is:

$$T(r) = T_w + \frac{Q}{6\lambda}\left(R^2 - r^2\right) \tag{4.34}$$

where $T_w$ is the temperature of the wall. Assuming that 20 W of power are absorbed in a 70 cm$^3$ pumping cell, and using $R = 2$ cm, which is slightly larger than the actual radius of the pumping cell to account for the fact that it is cylindrical, the temperature in the center of the cell is calculated to be 77°C higher than the wall temperature. The average temperature over the cell is $T_w + QR^2/15\lambda = T_w + 30°\text{C}$, a factor of 2-3 higher than what was actually measured. This implies that convection probably plays some role. There is a region in the pumping cell where the temperature drops with height - a necessary condition for convection. To determine if the gas is indeed unstable against convection, the Rayleigh number [45] is calculated:

$$\Re = \frac{\Delta T g h^3 \rho^2 c_p}{T \eta \lambda} \tag{4.35}$$

where $h$ is a characteristic dimension, $g$ is the acceleration of gravity, and $c_p$ is the heat capacity per unit mass. Assuming $h = R$ and $\Delta T = 77°\text{C}$, we get $\Re = 20000$. The critical value of $\Re$ above which the gas becomes unstable depends on the geometry. For example, for two parallel plates it is equal to 1708. So the gas is most likely unstable against convection, although not overwhelmingly. In the analysis of the EPR data, the heat conduction model will be used to establish a limit on the temperature gradient in the pumping cell.

The relevant temperatures and densities for the cells during normal running conditions are listed in Table 4.11. Based on the measurements discussed above, we assume that the pumping cell temperature is 10°C higher than the control setting and $T_C = T_T + 7.6°\text{C}$. The uncertainty in $T_T$ and $T_C$ is 5°C, and the uncertainty in $T_P$ is 10°C. This causes an error in $n_C/n_0$ of 1.6%. For some of the cells, the pumping cell temperature was changed during the run. However, these changes caused a change in the density of at most 1.0%. The pumping cell temperature was averaged over the use of the cell with approximate polarization weighting. The error due to this weighting procedure is no more than 0.5%.

| Cell | $T_T$ | $T_C$ | $T_P$ | $n_T/n_0$ | $n_C/n_0$ | $n_P/n_0$ |
|---|---|---|---|---|---|---|
| Dave | 65 | 71 | 200 | 1.144 | 1.124 | 0.824 |
| Riker | 68 | 76 | 200 | 1.121 | 1.095 | 0.814 |
| Bob | 69 | 77 | 190 | 1.125 | 1.099 | 0.836 |
| SMC | 63 | 70 | 185 | 1.129 | 1.106 | 0.834 |
| Generals | 65 | 73 | 190 | 1.111 | 1.085 | 0.817 |
| Hermes | 67 | 74 | 185 | 1.125 | 1.102 | 0.840 |
| Prelims | 67 | 75 | 200 | 1.121 | 1.095 | 0.812 |
| Chance | 66 | 74 | 195 | 1.121 | 1.095 | 0.820 |
| Picard | 65 | 73 | 180 | 1.107 | 1.081 | 0.830 |

Table 4.11: Cell Temperatures and relative densities.

The size of the density increase due to the temperature gradient can be tested by analyzing the data taken during $A_\perp$ running with Picard. The cell was heated up and cooled several times with long periods of time in between, which allows one to extract the ratio of the AFP signal when the cell is cold and hot. By fitting the polarization data with spin-up and spin-down curves, a ratio of AFP signals equal to $1.104 \pm 0.02$ was measured. Corrections should be applied to this number due to the change in the magnetic flux from the pumping cell and due to the change in the LC circuit gain. These effects are described in more detail below. The corrected ratio is 1.083, very close to $n_C/n_0 = 1.081$ for Picard.

## 4.5 The Dilution Factor

We now have all the information needed to calculate the dilution factor for the cells using equation (4.19). The gas densities of $^3$He and $N_2$ are given in Tables 4.9 and 4.2. They should be multiplied by the temperature enhancement factors $n_T/n_0$, given in Table 4.11, since we are interested in the average density over the whole target cell. Of course, for $A_\perp$ running, when the cell is at room temperature, no such correction is required. The window thicknesses are given in Table 4.5. The cross-sections $\sigma_i$ in equation (4.19) are calculated using the unpolarized DIS structure functions [46, 47, 48]:

$$\sigma_i\left(x,Q^2\right) = K\left(x,Q^2\right)\left[Z_i F_2^p\left(x,Q^2\right) + \left(A_i - Z_i\right) F_2^n\left(x,Q^2\right)\right] EMC\left(A_i,x\right) \quad (4.36)$$

where $K\left(x,Q^2\right)$ contains kinematic factors, and $EMC\left(A_i,x\right)$ is a correction factor taking into account the nuclear binding and shadowing effects, known as the "EMC effect". We also need to know the chemical composition of Corning 1720 glass, which is given in Table 4.12. The variation between different references does not cause a significant error.

| Reference | $SiO_2$ | $Na_2O$ | CaO | MgO | $B_2O_3$ | $Al_2O_3$ | $K_2O$ | $As_2O_3$ |
|---|---|---|---|---|---|---|---|---|
| [33] | 60.7 | 1.0 | 8.6 | 7.4 | 5.0 | 17.3 | 0.2 | 0.5 |
| [49] | 57 | 1.0 | 5.5 | 12 | 4.0 | 20.5 | | |
| [50] | 62 | 1 | 8 | 7 | 5 | 17 | | |
| Ave: | 59.9 | 1.0 | 7.4 | 8.8 | 4.7 | 18.2 | | |

Table 4.12: Chemical composition of Corning 1729 glass by weight.

However, equation (4.36) only takes into account the tree level diagram of the electromagnetic scattering. The cross-sections are significantly modified by the radiative corrections to the basic scattering process. We calculated the radiative corrections to the unpolarized cross-sections $\sigma_i$ using the techniques described in Chapter 3. A phase shift analysis program was used to calculate the elastic form factors of the heavier elements from their charge density distribution [51]. The radiation length for the external corrections was determined by separating the target into several regions and using a Monte Carlo to calculate the radiation length seen by each region.

By comparing the calculated unpolarized cross-sections with the rate in the spectrometer, we can obtain a very powerful check on many aspects of the experiment, such as the spectrometer acceptance, target thickness, detector efficiency, beam current, etc. The number of counts seen in the spectrometer is given by:

$$\frac{dN(x)}{dx} = N_0 \sum_i \sigma_i^{corr}(x) L_i n_i d\Omega(x) \tag{4.37}$$

where $\sigma_i^{corr}$ are the radiatively corrected cross-sections, $d\Omega(x)$ is the solid angle acceptance of the spectrometer, determined using Monte-Carlo techniques [52], and $N_0$ is the number of incident electrons. The results of such comparison are shown in Figures 4.15 – 4.17. Figure 4.15 shows the spectrum for pure $^3$He, which is obtained by subtracting the rates from a full and empty reference cell. The dot-dash curve shows the spectrum expected from a simple Born cross-section (4.36). Clearly, it does not agree with the experimental spectrum, and the radiative corrections are very important. Upon applying these corrections the agreement becomes much better. There are still a number of effects which have not been taken into account, such as the detector efficiency, pion and positron contamination. However, they are much smaller than the radiative correction. The disagreement at high $x$ may also be due to a slight miscalibration of the spectrometer momentum (5% change in the momentum would account for most of it). It is very nice to see that although our experiment was not designed to measure absolute cross-sections, it can do it with a reasonable accuracy. It also provides the only experimental verification of the program used to calculate the radiative corrections. Since the same program was used to calculate the polarized cross-sections, it gives us additional confidence in its results. Figures 4.16 and 4.17 show the comparison between absolute rates for an empty reference cell and Picard.

The agreement is satisfactory. For the empty reference cell we see a large deviation at low $x$ due to contamination by charge symmetric background. It is interesting to note that if most of the charge-symmetric background originates in the glass cell, it can not have any asymmetry. This could allow us to significantly reduce the systematic error due to this effect, which dominates our error at low $x$.

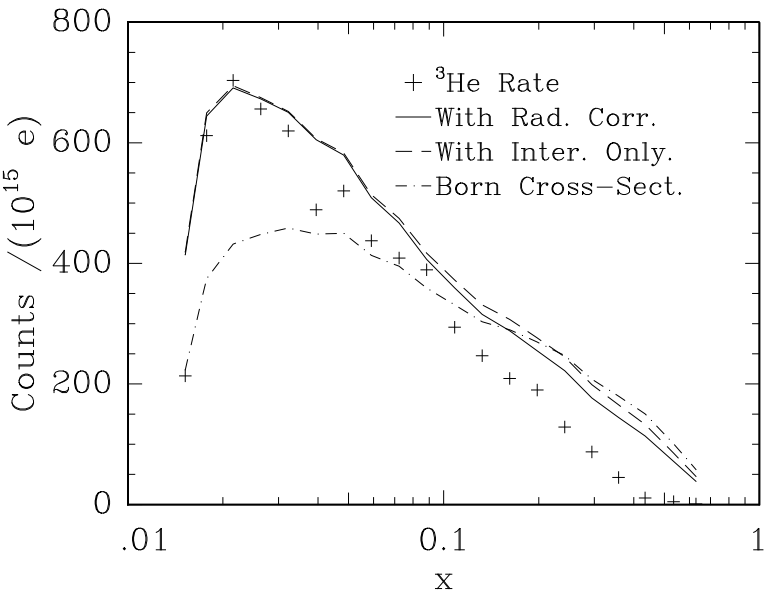


Figure 4.15: The event spectrum for $^3$He compared to the calculated cross-section with radiative corrections. There are no adjustable parameters.

For the dilution factor the effect of the radiative corrections is significantly reduced, because only the ratio of the cross-sections enters into equation (4.19). Their effect on the dilution factor of Picard is shown in Figure 4.18. A conservative 100% error is used for the radiative corrections to the dilution factor. In addition, the errors in the window thicknesses, $^3$He density, and cell lengths contribute to the uncertainty in the dilution factor.

The dilution factor can also be determined in a completely independent way by using the reference cell. Making the measurements with an empty and full reference cell one can determine the rate in the spectrometer from pure $^3$He. Let $(dN/d[He])$ be the rate in the spectrometer per unit $^3$He density. Then, the dilution factor can be written as:

$$f = \frac{(dN/d[^3He])[^3He]}{N_{tot}} \tag{4.38}$$

where $N_{tot}$ is the total rate from a given target. For this method one only needs to

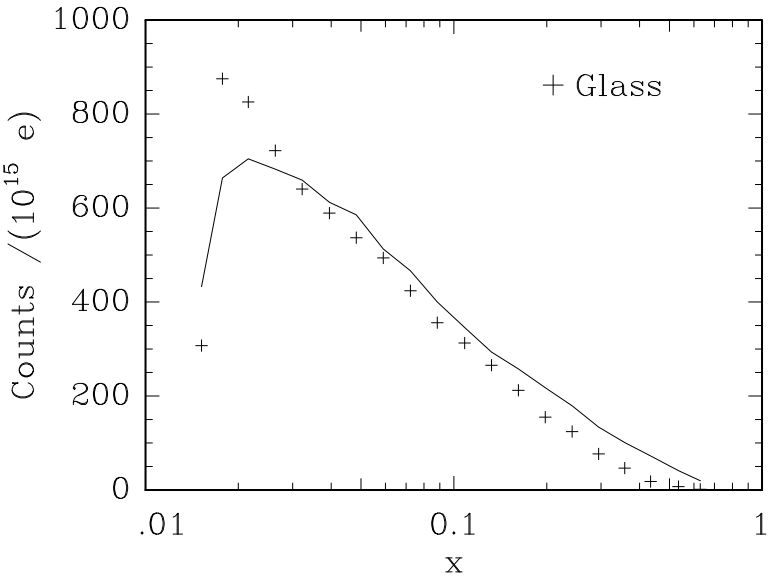


Figure 4.16: The event spectrum for an empty glass cell. The solid line includes all radiative corrections.

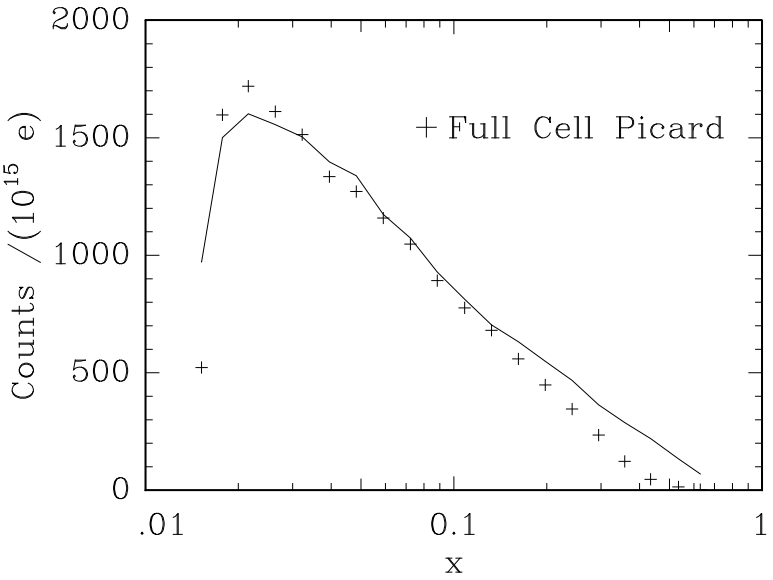


Figure 4.17: The event spectrum for a polarized $^3$He target "Picard".

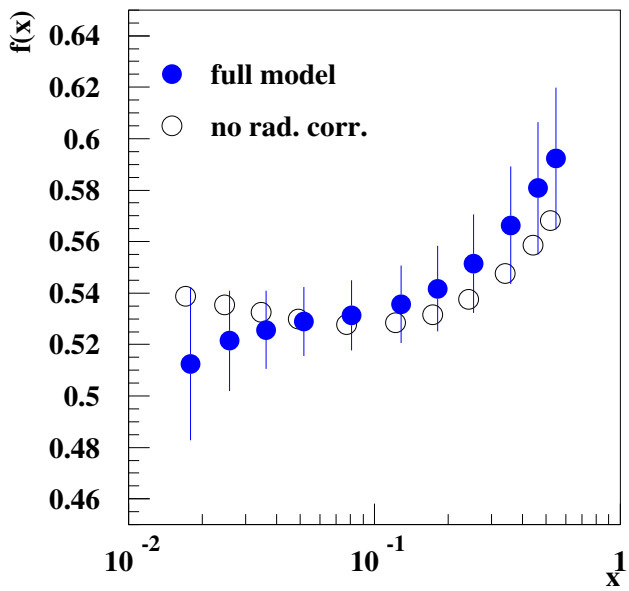


Figure 4.18: Radiative corrections to the dilution factor.

know the density of $^3$He in the target, but not the window thicknesses or the radiative corrections. A comparison between the two methods of calculating the dilution factor is shown in Figure 4.19 for Picard. The two methods are in good agreement for all cells [48]. For the final result we determined the dilution factor from equation (4.36) and the radiative corrections. The error on the dilution factor is 5%, dominated by the radiative corrections error.

## 4.6 Target Performance

The polarization of the target during the two month run is shown in Figure 4.20. The spin-up curve of the cell Picard, which achieved the highest polarization, is shown in Figure 4.21. As can be seen, some problems were encountered during the run. There were two types of problems: mechanical failures of the cells and $^3$He polarizations lower than expected. It was soon realized that the windows of the cells fail in the beam after approximately 3-6 days. The cell usage during the run is summarized in Table 4.13. The total beam charge accumulated by each cell before failure is shown in Figure 4.22. Points with upward arrows indicate that the cell had not failed, but was removed for another reason. The horizontal coordinate corresponds to the thickness of the thinner window. In all cases the thinner window failed first. In general, cells

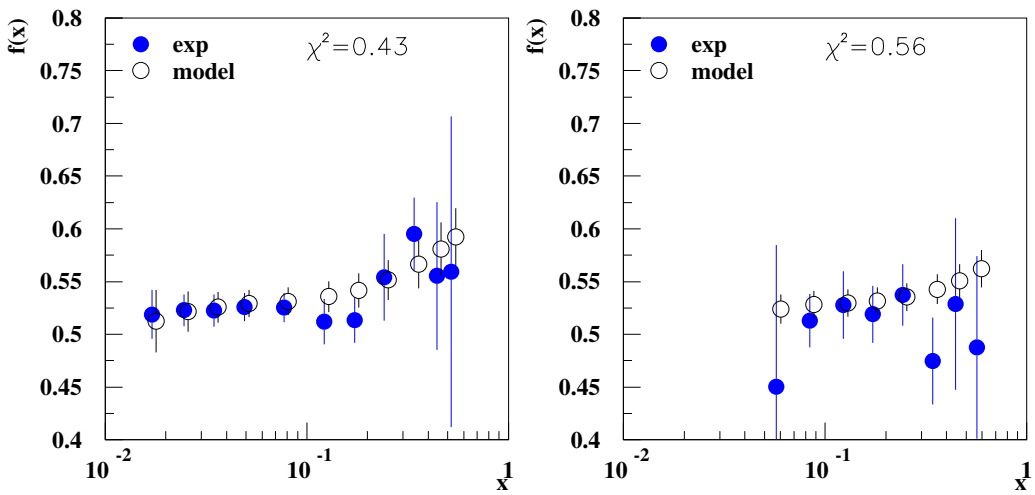


Figure 4.19: Comparison of the two methods for calculating the dilution factor for target cell Picard.

with thicker windows lasted longer. Trying to prevent cell failures, we reduced the beam current in the middle of the run from $9 \times 10^{10}$ electrons per pulse to $5 \times 10^{10}$. It is not clear if it had a significant effect. While "Prelims" and "Hermes" lasted longer than the trend suggested by the cells ran at $9 \times 10^{10}$, "Generals" did not last any longer. We further reduced the current to $3 \times 10^{10}$ for Picard, but the total charge accumulated by Picard before the end of the run is not particularly large.

If we extrapolate the trend seen in the data to the window thickness corresponding to one of the cells used in E-142, we get an expected total charge of $5 \times 10^{18}$. In contrast, the E-142 cells accumulated up to $20 \times 10^{18}$ electrons without failure. Compared with E-142 our problems are rather surprising. All windows were pressure tested to about 60% overpressure, unlike E-142, for which only some representative windows were tested. No cell has ever failed after being filled with gas without the effect of the beam. The beam current was initially equal to $9 \times 10^{10}$ electrons per pulse (1.7 $\mu$A), smaller than the current in E-142, which reached up to $20 \times 10^{10}$ electrons per pulse. We reduced the current further to $5 \times 10^{10}$, but that did not solve the problem. Finally, because the windows were thinner by a factor of 2 compared with E-142, it was expected that the amount of heating would also be smaller. The only unfavorable difference with E-142 was the duration of the pulse. While in E-142 it was about 1.4 $\mu$sec, for our experiment the beam pulse was 200 nsec long. So, the instantaneous current was higher by about a factor of 3.6 in the beginning of the experiment and 1.9 times higher after the reduction in the current. The beam size at the target was

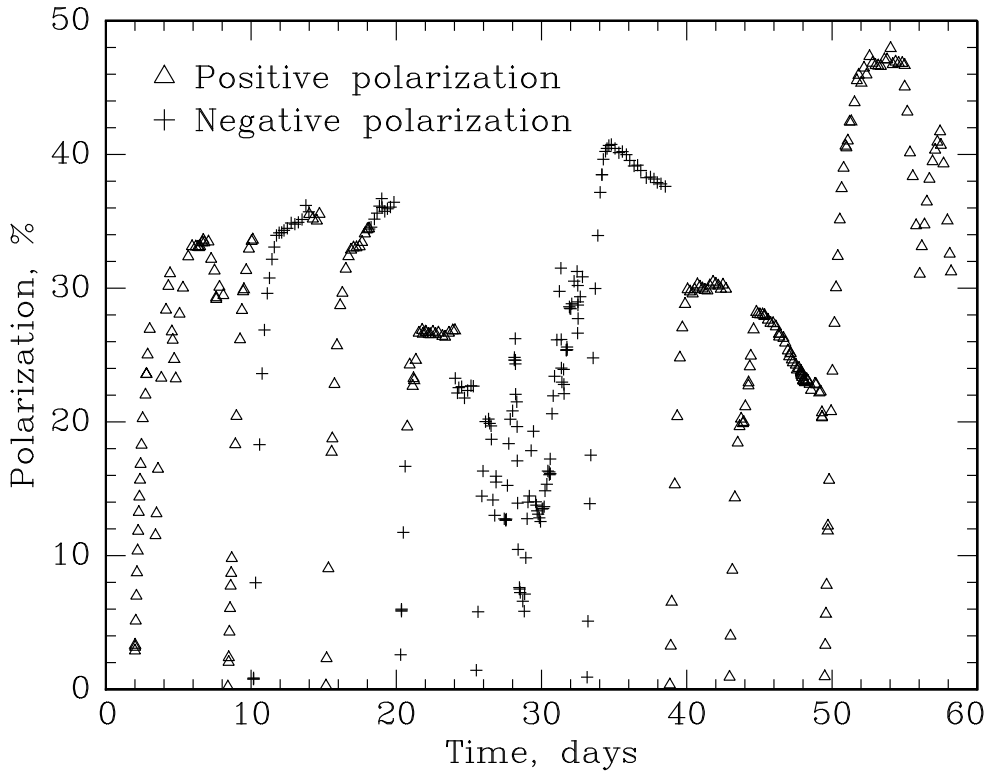


Figure 4.20: Target polarization during the run.

difficult to measure exactly because the wire array was several meters downstream of the target. The beam diameter was about 1 mm and may have been somewhat smaller than in E-142. It is believed that the failure of the windows was caused by the instantaneous heating and possibly a shock wave caused by each beam pulse [54]. For example, it takes about 160 ns for the sound to propagate the transverse dimension of the beam (1 mm). Another possibility is that the inverted windows, although initially quite strong, easily fail due to the buckling instability when damaged by the electron beam. The failures of the cells occurred on average every 6 days. It took approximately 24 hours to replace the cell and polarize it. However, the gain in the dilution factor, compared with E-142 cells, was approximately a factor of 2.6 in running time, so the down time was relatively insignificant.

The problems with $^3$He polarization that were faced during the run were also rather unexpected. Their origin is not entirely understood for all cells. However, the cells that exhibited most pronounced polarization problems are somewhat better understood. These cells are SMC (20th to 25th day in Figure 4.20), Generals (25th

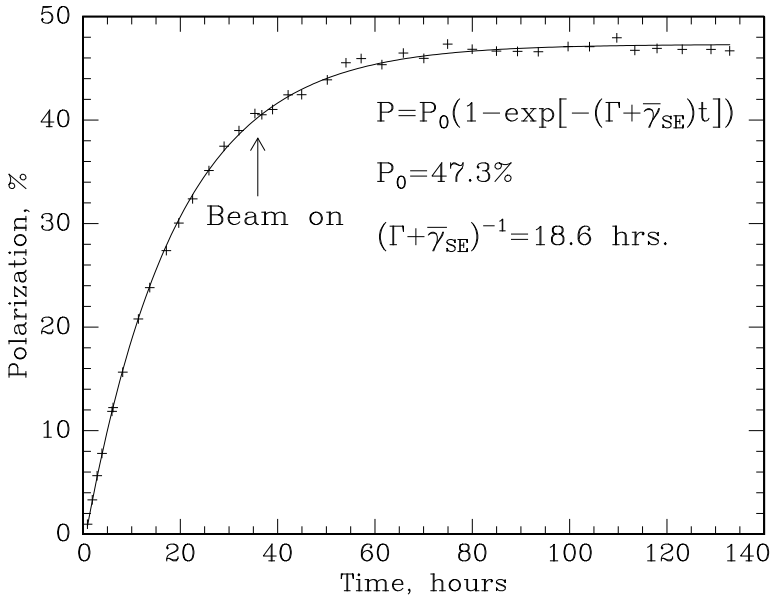


Figure 4.21: Spin-up of target cell Picard during the run.

| Cell Name | Date Installed | Date Removed | First Run | Last Run |
|---|---|---|---|---|
| Dave | 10/4 22:30 | 10/11 2:15 | 1201 | 1388 |
| Riker | 10/11 7:00 | 10/17 21:15 | 1412 | 1757 |
| Bob | 10/18 2:00 | 10/22 21:50 | 1777 | 2043 |
| SMC | 10/23 3:00 | 10/28 6:00 | 2050 | 2311 |
| Generals | 10/28 9:00 | 11/04 19:25 | 2316 | 2594 |
| Hermes | 11/05 00:30 | 11/10 13:30 | 2597 | 2902 |
| Prelims | 11/10 19:30 | 11/14 17:25 | 2903 | 3100 |
| Chance | 11/14 20:00 | 11/21 5:45 | 3101 | 3371 |
| Picard | 11/21 10:00 | 11/30 3:00 | 3377 | 3788 |
| Ref. Cell #1 | 9/18 8:00 | 10/17 21:15 | 733 | 1757 |
| Ref. Cell #2 | 10/18 2:00 | 10/23 00:06 | 1777 | 2047 |
| Ref. Cell #3 | 10/23 3:00 | 11/04 21:22 | 2050 | 2596 |
| Ref. Cell #4 | 11/05 00:30 | 11/30 3:00 | 2597 | 3788 |

Table 4.13: Cell usage during the run.

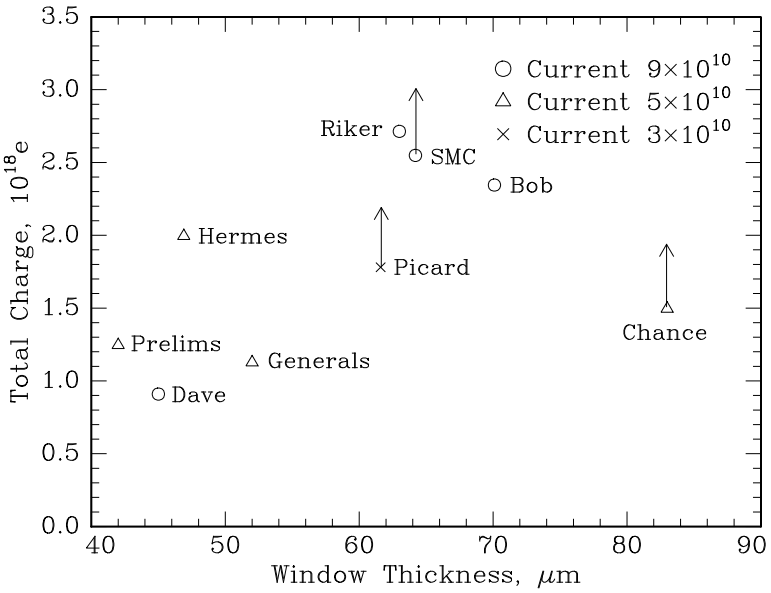


Figure 4.22: Total charge accumulated by cells before failure. The cells with upward arrows had not failed.

to 32nd day) and Chance (43rd to 49th day). In Chance the problem was most likely caused by a decaying nuclear relaxation lifetime. Before the run a measurement of the cell lifetime gave 40 hrs, but after the run we measured the lifetime and found that it was only 16 hrs. So, Chance lifetime apparently decayed in the beam. This is the only cell, to our knowledge, whose lifetime decreased during the run.

The problem with SMC and Generals is believed to be caused by an entirely different effect, associated with non-linear coupling between the polarization and the coils, called masing.

### 4.6.1 Spin Maser

During the run there were several very peculiar effects which strongly point toward the masing effect. First, the polarization of the cell SMC saturated very abruptly at 27%, as shown in Figure 4.23, and stayed remarkably constant over a period of several days, insofar of changes in cell temperature and laser power aimed at increasing the polarization. Even more unexpectedly, the polarization dropped to 23% upon reversal of the holding field direction and then stayed constant at this new value. This behavior is very difficult to explain in terms of linear relaxation rates.

The next cell, Generals, behaved in an even more bizarre fashion, as shown in Figure 4.24. The polarization failed to reach 25% and every attempt to increase the

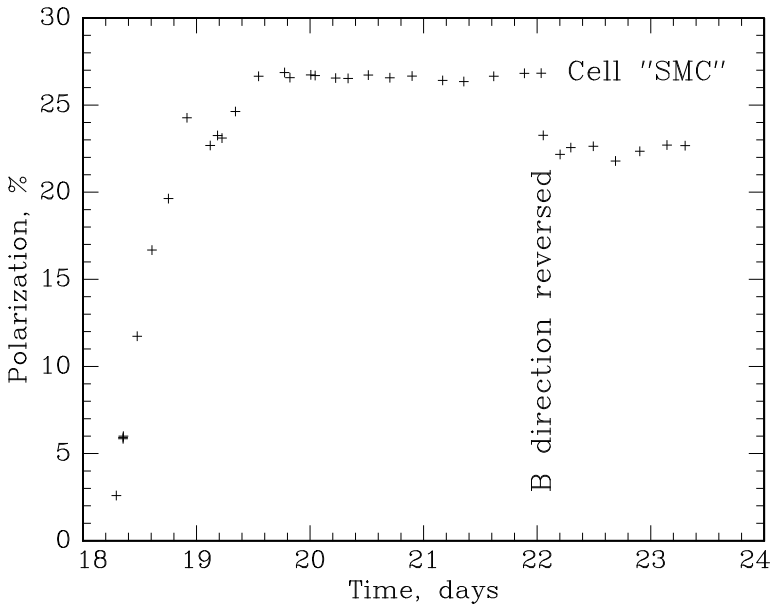


Figure 4.23: Polarization of cell "SMC" during the run.

polarization by changing the optical pumping conditions failed. Finally, it was found that the polarization of the cell rose if it was kept out of the pick-up coils and only moved in for a very short time to do the AFP measurement. This seems to imply that the coupling to the pick-up coils played a significant role in the effects being observed. Finally, it was decided to lower the value of the holding field from 19 G to 12 G. This apparently allowed the polarization to rise even while the cell was between the pick-up coils. We continued to use 12 or 9 G holding field for the rest of the experiment.

Finally, after the run we performed dedicated tests on SMC trying to confirm the basic predictions of the masing hypothesis. According to this hypothesis, the problems with polarization in SMC and Generals were caused by a non-linear coupling between the pick-up coils and the spins which resulted in sustained precession of the magnetization about the $z$ axis. The masing phenomenon has the following rather peculiar properties:

1. Masing can occur only if the spins are polarized in the high energy Zeeman state, so they can dump their energy into the coil.

2. Masing is characterized by a threshold, below which the effect is negligible (the polarization is stable) and above which the polarization is unstable and will spontaneously develope a large transverse component.

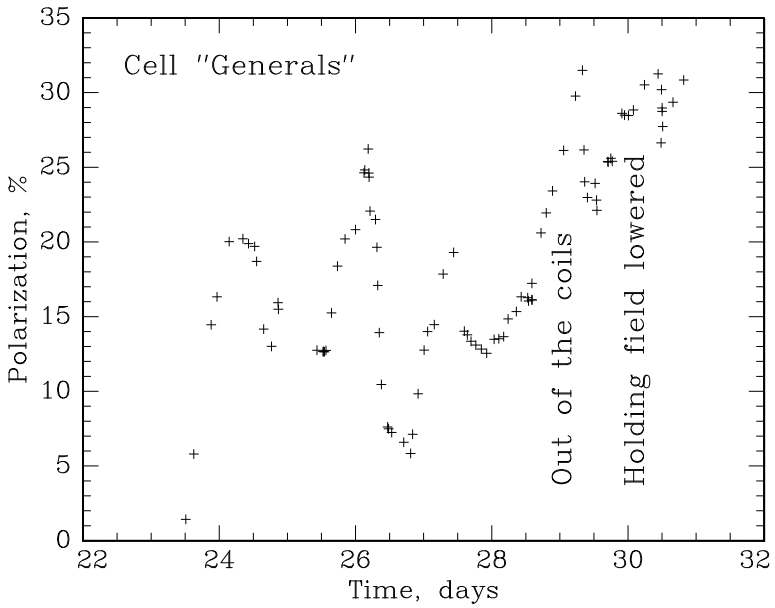


Figure 4.24: Polarization of cell "Generals" during the run.

3. The value of the threshold depends on the coupling to the coil, which is dependent on the difference between the resonance frequency of the coil and the Larmor frequency of the spins.

4. The threshold depends on the transverse nuclear relaxation time $T_2$. It becomes larger when $T_2$ is short, for example, because of a large field gradient.

With these properties in mind we conducted a series of tests shown in Figure 4.25. The polarization was seen to rise and then saturated abruptly, as it did for SMC during the run. At this point a magnetic field gradient of 5 mG/cm was applied, with the goal of shortening $T_2$ and increasing the masing threshold. It, indeed, caused the polarization to rise sharply. It should be pointed out that the more usual relaxation due to field gradients (4.13) would tend to decrease the polarization. When the gradient was turned off, the polarization dropped very abruptly, which was consistent with a masing instability, but inconsistent with an additional relaxation rate. The cycle was repeated for the second time with the same results. Then the holding field was decreased from 19 G to 9 G. Even in the absence of a field gradient the polarization started to rise. This behavior is exactly the same as what was observed for Generals during the run. It is due to a decrease of the coil coupling as the Larmor frequency is moved further from the coil resonance. Finally, the spins were stored at 19 G with no gradient, but in the low energy Zeeman states. As predicted by the

masing model, this conditions allowed the polarization to rise. So, qualitatively, the spins reacted exactly as they should for a maser. We can even explain a jump in the polarization of SMC when the magnetic field was reversed by noticing that the field gradients usually have two components, one from the imperfections of the Helmholtz coils, which is proportional to the magnetic field, and the other from the ambient field gradients. When the field is reversed, the two components add or subtract in different ways, which can lead to a slightly different value of $T_2$ and change the masing threshold.

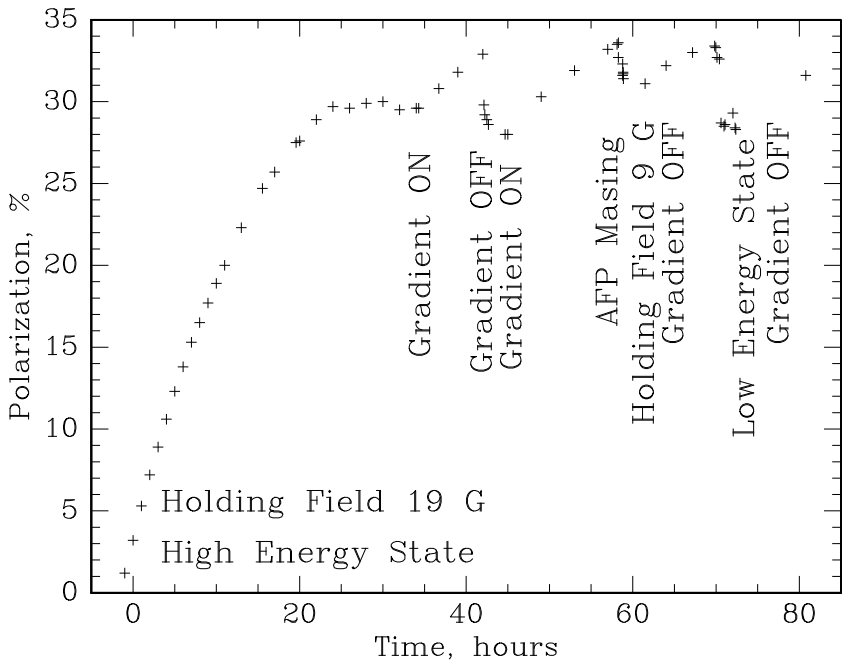


Figure 4.25: Tests done with SMC after the run.

We will now present a quantitative description of the masing effect. The basic idea is the following. Consider a polarized cell in a holding magnetic field along the $z$ direction. The cell is placed inside (or near) a coil which is part of an LC circuit. Assume that the magnetization has a small transverse component. The spins are precessing around the magnetic field. Their precession induces a voltage in the coil. The voltage induced in the coil causes a current to flow through it. This current produces a magnetic field transverse to the holding field. Under certain conditions this induced field can cause the spins to tip away from the $z$ axis and increase the voltage induced in the coil. That in turn increases the transverse field and causes a runaway situation. The longitudinal polarization of the spins will decrease while

certain conditions are met. Thereafter it will remain constant at the so-called masing threshold. A spin maser was studied in detail by Richards *et al.* [54]. It can be used for a number of interesting experiments, for example, searches for permanent Electric Dipole Moment, as described in [55, 56]. We will describe the dynamics of the spins using Bloch equations. Although the qualitative behavior of the spins is described well by these equations, numerical estimates appear to be very far off.

We start with Bloch equations with phenomenological relaxation rates:

$$\frac{d\vec{M}}{dt} = \gamma\vec{M} \times \vec{B} - \frac{M_x\hat{i} + M_y\hat{j}}{T_2} - \frac{M_z\hat{k}}{T_1} \tag{4.39}$$

The magnetic field consists of the holding field $B_0$ in the $z$ direction and a transverse magnetic field created by the coil. We will go to a frame rotating with the spins at the Larmor frequency $\omega$. Since the transverse field is induced by the spins, it has a component rotating at the same frequency.

Writing (4.39) in individual components we get:

$$\begin{aligned}
\frac{dM_z}{dt} &= \gamma(M_xB_y - M_yB_x) - \frac{M_z}{T_1} \\
\frac{dM_x}{dt} &= \gamma M_y(B_z - \frac{\omega}{\gamma}) - \gamma M_zB_y - \frac{M_x}{T_2} \\
\frac{dM_y}{dt} &= -\gamma M_x(B_z - \frac{\omega}{\gamma}) + \gamma M_zB_x - \frac{M_y}{T_2}
\end{aligned} \tag{4.40}$$

The last two equations can be combined if we use $M_T = M_x + iM_y$ and $B_T = B_x + iB_y$. The induced magnetic field is proportional to the transverse magnetization, so we can write $B_T = A(\omega)M_T$. We get the following two equations describing the behavior of the spins:

$$\begin{aligned}
\frac{dM_z}{dt} &= \gamma|M_T|^2 Im(A(\omega)) - \frac{M_z}{T_1} \\
\frac{dM_T}{dt} &= -iM_T\gamma(B_z - \frac{\omega}{\gamma}) + i\gamma A(\omega)M_TM_z - \frac{M_T}{T_2}
\end{aligned} \tag{4.41}$$

where we used $M_xB_y - M_yB_x = Im(M_T^*B_T)$.

Now we need to calculate the coupling of the spins with the coil. Let's represent the magnetic moment $\vec{m}$ of the spins by a small loop of area $\vec{a}_m$ with current $I_m$ flowing through it so that $I_m\vec{a}_m = \vec{m}$. Let the coil produce a magnetic field $\vec{B}(x) = \vec{b}(x)I_c$ when current $I_c$ is flowing through it. The flux of this magnetic field through the current loop is $\Phi_m = I_c\vec{b} \cdot \vec{a}_m = L_mI_c$, where $L_m$ is the mutual inductance of the coil and the loop. The flux of the field produced by the loop in the coil is $\Phi_c = L_mI_m = \vec{b} \cdot \vec{m}$, using the fact that the mutual inductances are equal [57].

The voltage induced in the coil is:

$$V = -\frac{d\Phi_c}{dt} = -\int_{V_{cell}} b_T(x)\frac{dM_T}{dt} \simeq i\omega V_{coil}\langle b_T\rangle M_T \tag{4.42}$$

where $\langle b_T\rangle$ is the average of the transverse component of the coil field over the volume $V_{coil}$ where the coil field is significant. We will come back to this approximation later. We also implicitly assumed that in the laboratory frame $M_T|_{lab} = M_T|_{rot}e^{-i\omega t}$

The current flowing through the coil is

$$I = \frac{V}{i\omega L + R - i/\omega C} = \frac{V}{R}\,\frac{\frac{\omega^2}{Q^2\omega_r^2} + i(1-\frac{\omega^2}{\omega_r^2})\frac{\omega}{Q\omega_r}}{\frac{\omega^2}{Q^2\omega_r^2} + (\frac{\omega^2}{\omega_r^2}-1)^2} = \frac{V}{R}(a_1(\omega) + ia_2(\omega)) \tag{4.43}$$

where $\omega_r^2 = 1/(LC)$, $Q = \omega_r L/R$. This equation defines the dimensionless circuit response functions $a_1(\omega)$, $a_2(\omega)$.

The field produced by the coil is $B(x) = b(x)I/2$. The factor of 2 accounts for the fact that we are considering only one of the two counterrotating components of $B$.

Combining equations above we get for $A(\omega)$:

$$A(\omega) = \omega V_{coil}\langle b_T\rangle^2(-a_2(\omega) + ia_1(\omega))/(2R) \tag{4.44}$$

We can see now that the coupling of the spins with the coil is proportional to the square of the magnetic field $b_T$. For the pick-up coil used for polarimetry the field is reasonably uniform over some volume and then quickly goes to zero. We can therefore divide the cell into an active region inside the coil were $M_T \neq 0$ and the rest of the cell with $M_T = 0$. We further assume that $M_T$ is constant over the active region. The average field of the coil over the active region is about 30% higher than the minimum field and 30% lower then the maximum field in that region. So this approximation is OK if we are looking for a factor of 2 estimate. It is convenient to define radiation dumping magnetization $M_{rd}$:

$$\frac{1}{M_{rd}} = \frac{\gamma V_{coil}\langle b_T\rangle^2}{2R} \tag{4.45}$$

We now have the following differential equations for the magnetization:

$$\frac{dM_z}{dt} = \frac{|M_T|^2}{M_{rd}}\omega a_1(\omega) - \frac{M_z}{T_2} \tag{4.46}$$

$$\frac{dM_T}{dt} = -iM_T(\omega_0 - \omega) - (a_1(\omega) + ia_2(\omega))\frac{M_z}{M_{rd}}\omega M_T - \frac{M_T}{T_2} \tag{4.47}$$

where $\omega_0 = \gamma B_z$. In (4.47) there is an imaginary part causing $M_T$ to rotate and a real part causing changes in its magnitude. We chose a frame rotating together with

the spins, so the imaginary part should be set to zero. This gives us an equation for the frequency $\omega$:

$$\omega_0 = \omega(1 - a_2(\omega)\frac{M_z}{M_{rd}}) \tag{4.48}$$

The frequency of the spin precession is different from the Larmor frequency, a phenomenon known as "frequency pulling".

The differential equations are non-linear and can exhibit an instability. Equation (4.47) has two terms, one tending to relax $M_T$ to zero due to $T_2$ and another tending to increase it (if $M_z < 0$) due to the coil coupling. The competition between these terms determines the onset of masing. For $M_z > 0$ both terms are negative and the spins are stable. In other words, the spins are susceptible to masing only in the high energy state.

The steady state solution of equations (4.46, 4.47) is

$$\omega_0 = \omega_m(1 + \frac{a_2(\omega_m)}{\omega_m a_1(\omega_m) T_2}) \tag{4.49}$$

$$M_{eq} = -\frac{M_{rd}}{\omega_m a_1(\omega_m) T_2} \tag{4.50}$$

This gives the value of the "masing threshold", below which the coupling with the coil has a negligible effect on the magnetization, and above which the system becomes unstable and the magnetization eventually decays to $M_{eq}$.

We now try to estimate the masing threshold for SMC. The pick-up coil consists of two square windings 2.4 cm $\times$ 9.6 cm with 150 turns each. The average field of the coil is calculated on Mathematica. We get $\langle b \rangle$ = 37 G/A. The DC resistance of the coil is 40 $\Omega$. However, from an independent measurement of $Q$ we conclude that the resistance at 100 kHz (the resonance frequency of the circuit) is 56 $\Omega$. It is somewhat lower at 60 kHz (the Larmor frequency in the holding field of 19 G), say approximately 50 $\Omega$. The volume of the active region is 30 cm$^3$. So, we get $M_{rd}$ = 1.22 G. For convenience, we convert this to polarization by dividing by the number density and the magnetic moment of $^3$He, $M_{rd}$ = 425 (dimensionless).

It is more difficult to estimate $T_2$. All experiments with masers [54, 55, 56] have been done in the regime of *motional narrowing*, when the dephasing time $T_p = (h\gamma\,|\nabla B_z|)^{-1}$ is much longer than the diffusion time $T_d = h^2/D$, where $h$ is a characteristic dimension of the cell and $D$ is the diffusion constant. In this regime the magnetization decays exponentially with a time constant given by:

$$\frac{1}{T_2} = k\frac{h^4\gamma^2\,|\nabla B_z|^2}{D} \tag{4.51}$$

where $k$ is a dimensionless constant which depends on the geometry of the sample. For example, for a sphere with $h = R$, $k = 8/175$ [19]. These results do not apply

to our situation, however, since in our case the diffusion time is much longer than the dephasing time. Their ratio $\beta = T_d/T_p$ is ranging from 300 to 7500 depending on what number we use for $h$. Before considering the relaxation under these conditions, we can try to get a rough estimate by going to the other extreme of infinitely slow diffusion.

In the static approximation there is no diffusion and the only time scale is given by the dephasing time $T_p$. The decay of the spins is not exponential and depends on the geometry of the sample. To study the effect of the gradient on the masing equilibrium we used an anti-Helmholtz coil. It was found that a gradient of approximately 3 mG/cm was necessary to establish equilibrium at 30% polarization. Then $T_p \approx 1/(h\gamma\nabla B_z) \approx 3$ ms, where $h$ is the half-length of the active region, equal to 5 cm. We assume that $T_2 = kT_p$, where $k$ is of order unity.

The masing instability is also suppressed because the Larmor frequency at the holding field (60 kHz) is very far from the resonance of the circuit (100 kHz). The frequency pulling increases the masing frequency by 5%. We get $a_1(\omega_m) = 2.9 \times 10^{-4}$. Putting everything together we get $M_{eq} = 1230$, which is a factor of 4000 higher than the observed threshold of $M_{eq} = 0.3$. So, our naive estimates seem to disagree with observations by a very large amount.

Let's for a moment close our eyes to this disagreement and study the dynamics of the spins. Equations (4.46, 4.47) need to be modified to include the effect of optical pumping and polarization transfer between different parts of the cell. We get the following set of differential equations:

$$\begin{aligned}
\frac{dM_z}{dt} &= \frac{M_T^2 \omega a_1(\omega)}{M_{rd}} + \frac{M_p - M_z}{T_t} + 2\frac{M_e - M_z}{T_e} - \frac{M_z}{T_1} \\
\frac{dM_T}{dt} &= -\frac{a_1(\omega)\omega M_T M_z}{M_{rd}} - \frac{M_T}{T_2} \\
\frac{dM_p}{dt} &= \frac{M_{Rb} - M_p}{T_{se}} - \frac{M_p}{T_1} - \frac{M_p - M_z}{T_p} \\
\frac{dM_e}{dt} &= \frac{M_z - Me}{T_e} - \frac{M_e}{T_1} \\
\frac{d\omega}{dt} &= \frac{a_2(\omega)\omega \dot{M}_z/M_{rd}}{1 - a_2(\omega)\frac{M_z}{M_{rd}} - a_2'(\omega)\omega\frac{M_z}{M_{rd}}}
\end{aligned} \tag{4.52}$$

where $M_e$, $M_p$, and $M_{Rb}$ are $^3$He polarizations in the ends of the target cell, the pumping cell, and Rb polarization respectively. Also, $T_t$, $T_p$, $T_e$, $T_{se}$, $T_1$ are diffusion times for the target cell, the pumping cell, the ends of the cell, the spin exchange time, and the longitudinal relaxation time. The constraint equation (4.48) for $\omega$ was converted to a differential equation for the numerical calculation. These equations were solved on Mathematica, the result for $M_z$ is shown in Figure 4.26. The shape

of the curve is not sensitive to exact values of $T_2$ and $M_{rd}$, they were adjusted to get saturation at ∼30%. So, the dynamical behavior is explained quite well by the theory.

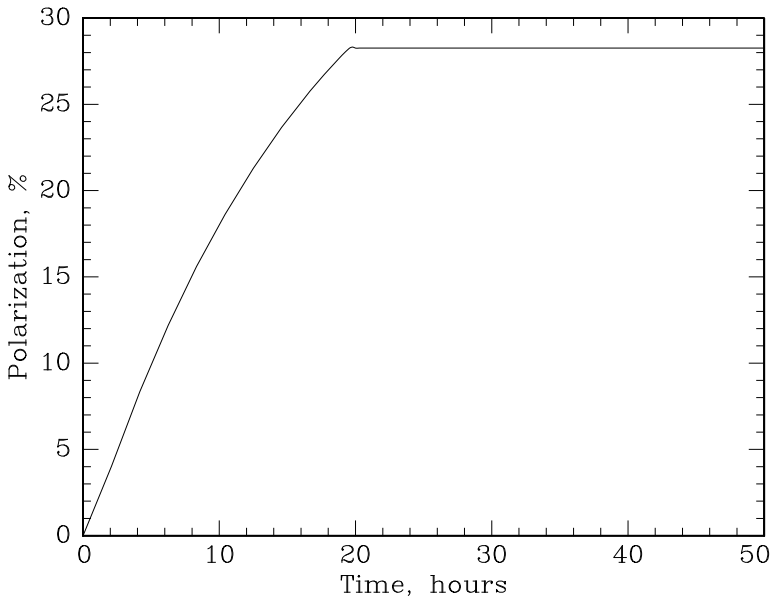


Figure 4.26: The evolution of the polarization with time predicted by the masing equations. The coil coupling is adjusted to achieve saturation at ∼30%.

All properties of the maser are in agreement with observations, except the numerical estimate of the masing threshold. The most suspicious number in our calculation is the value of the $T_2$, so we need to consider the transverse relaxation in greater detail. The relaxation is due to the magnetic field inhomogeneity in the presence of diffusion, and is governed by the following differential equation [58, 59]:

$$\frac{\partial M_T(\vec{r},t)}{\partial t} = D\nabla^2 M_T(\vec{r},t) - i\vec{g}\cdot\vec{r}M_T(\vec{r},t) \tag{4.53}$$

where $\vec{g} = \gamma\vec{\nabla}B_z$ and $D$ is the gas diffusion constant. We replace the phenomenological relaxation term in the Bloch equations by (4.53) and take into account the position dependence of the magnetization. Then the transverse magnetization obeys the following differential equation:

$$\frac{\partial M_T(\vec{r},t)}{\partial t} = i\gamma B_T M_z + D\nabla^2 M_T(\vec{r},t) - i\vec{g}\cdot\vec{r}M_T(\vec{r},t) \tag{4.54}$$

Following the methods of [58], we decompose $M_T(\vec{r},t)$ into normal modes with

exponential time dependence:

$$M_T(\vec{r},t) = \sum_i c_i m_i(\vec{r})\, e^{-E_i t} \tag{4.55}$$

Substituting this expansion into equation (4.42) we obtain

$$V = i\omega \sum_i c_i e^{-E_i t} \int_{cell} b_T(\vec{r})\, m_i(\vec{r})\, d^3r \tag{4.56}$$

We ignored the time dependence due to $E_i$, which is on the order of $gh$, much smaller than $\omega$. The magnetic field of the pick-up coils is reasonably constant inside the coils and then quickly drops to zero (see Figure 5.1). Since we are interested only in rough estimates, we will separate the integral in equation (4.56) as follows:

$$\int_{cell} b_T(\vec{r})\, m_i(\vec{r})\, d^3r = \langle b_T \rangle \int_{coil} m_i(\vec{r})\, d^3r \tag{4.57}$$

where $\langle b_T \rangle$ is the average magnetic field of the pick-up coils and the integral extends only over the volume where the field is significant. For convenience, we introduce a dimensionless mode filling factor :

$$A_i = \frac{1}{V_{coil}} \int_{coil} m_i(\vec{r})\, d^3r \tag{4.58}$$

It follows that:

$$B_T(\vec{r},t) = b_T(\vec{r})\, \omega \frac{(-a_2(\omega) + i a_1(\omega))}{2R} V_{coil} \langle b_T \rangle \sum_i c_i e^{-E_i t} A_i \tag{4.59}$$

Since we consider the case when the Larmor frequency is far away from the coil resonance, the frequency shift due to the factor $\exp(-E_i t)$ is ignored. Upon substitution into equation (4.54) we obtain a time independent equation:

$$\left(D\nabla^2 - i\vec{g}\cdot\vec{r} + E_i\right) m_i(\vec{r}) + i\gamma M_z \omega \frac{(-a_2(\omega) + i a_1(\omega))}{2R} V_{coil} \langle b_T \rangle^2 A_i = 0 \tag{4.60}$$

where we ignored the position dependence of $b_T$ and $M_z$. The normal modes $m_i(\vec{r})$ are subject to the boundary condition at the walls of the cell:

$$n \cdot \nabla m_i = 0 \tag{4.61}$$

which assumes that the walls are non-depolarizing. Although equation (4.60) is still linear in $m_i$ ($A_i$ is proportional to $m_i$), it is no longer homogeneous. There is a discrete set of eigenvalues $E_i$ which correspond to eigenstates $m_i$ satisfying the boundary conditions. It is shown in [58] that in the absence of coil coupling the real part of

$E_i$ is always positive, corresponding to decaying modes. We would like to find the value for $M_z$ when the real part of $E_i$ becomes negative, indicating an exponentially growing mode.

We study the equation in one dimension. Note that the only spacial dependence of the equation comes from the $\vec{g} \cdot \vec{r}$ term. There are no terms which depend on $z$, the direction of the magnetic field. Therefore, we can let $\vec{g}$ point in any direction, not necessarily parallel to $z$. For example, let the gradient $\vec{g}$ be in the $\hat{x}$ direction and assume that the cell is a cylinder parallel to the $\hat{x}$ axis with flat end walls located at $x = \pm h$. Following [58], we introduce dimensionless coordinate and time:

$$\zeta = x/h; \quad \tau = \frac{tD}{h^2}; \quad \alpha_i = E_i \frac{h^2}{D} \tag{4.62}$$

The dimensionless coil coupling factor is given by:

$$f = \frac{\gamma V_{coil} \langle b_T \rangle^2 \omega h^2 [He] \mu_{He}}{2RD} (a_1(\omega) + i a_2(\omega)) P_{He} \tag{4.63}$$

and the equation reduces to:

$$\left( \frac{\partial^2}{\partial \zeta^2} + i\beta\zeta + \alpha_i \right) m_i(\zeta) - f A_i = 0 \tag{4.64}$$

with

$$A_i = \frac{1}{2} \int_{-1}^{1} m_i(x)\, dx \tag{4.65}$$

Using the numbers given above we estimate for $h = 1$ cm that $\beta = 300$ and $f = -(0.3+20i)$. We tried to study this equation numerically starting with the eigenvalues given in [58] for $f = 0$. We first set $A_i$ to some value and find the eigenstates of the equation. For sufficiently large values of $f$ the eigenvalues indeed have a negative real part. Using the eigenstates, we calculate $A_i$ and then iterate the procedure. Unfortunately, the iterations failed to converge for the values of $\beta$ and $f$ in the range of interest.

In general, $A_i$ is complex, which implies that the real part of $E_i$ depends on both the real and the imaginary parts of $f$. This is different from the case of simple exponential dumping, where only the real part of $f$ determines the masing threshold. Since the imaginary part of $f$ is much larger than the real part, this may indicate that the masing threshold is lower.

To summarize, we have a lot of qualitative evidence for the masing effect. Because masing is described by non-linear equations, there are a lot of rather specific predictions about the qualitative behavior of the spin maser, all of which are in agreement with the experiment. In fact, we cannot think of any other effect which could explain even a fraction of the spin behavior explained by masing. On the other hand,

our initial numerical estimates of the threshold appear to be unsuccessful. The dependence of the masing threshold on various parameters is not entirely understood. For example, it is not clear why no masing was observed in Picard, which by naive analysis would be even more susceptible. With additional effort it should be possible to solve equation (4.64) numerically and see if the result is in better agreement with the experiment. It also would be very interesting to study the effect experimentally under more controlled conditions. If our data are indeed explained by masing, the dependence of the threshold on various parameters can be expected to be non-trivial.

# Bibliography


[1] F.D. Colgerove, L.D. Scheafer, and G.K. Walters, Phys. Rev. **132**, 2561 (1963).

[2] K. Ackerstaff *et al.*, (The HERMES Collaboration), hep-ex/9703005, (1997).

[3] J. Becker et al, Nucl. Instr. Meth. **346**, 45 (1994).

[4] M. Meyerhoff et al. (The A3 Collaboration), to be publ. in Phys. Lett. B.

[5] T.E. Chupp, M.E. Wagshul, K.P.Coulter, A.B. McDonald, and W. Happer, Phys. Rev. C **36**, 2244 (1987).

[6] W. Happer, Rev. Mod. Phys. **44**, 169 (1972).

[7] E.S. Hrycyshyn and L. Kraus, Can. J. Phys. **48**, 2761 (1970).

[8] W. Happer, private communication, (1997).

[9] S. Appelt, A. Baranga, A. Young, and W. Happer, to be published.

[10] L.W. Anderson, F.M. Pipkin, and J.C. Baird, Phys. Rev. **120**, 1279 (1960).

[11] A. Young, S. Appelt, A. Baranga, C. Erickson, and W. Happer, to be published in Appl. Phys. Lett.

[12] Z. Wu, T.G. Walker, and W. Happer, Phys. Rev. Lett. **54**, 1921 (1985).

[13] M.E. Wagshul and T.E. Chupp, Phys. Rev. A **49**, 3854 (1994).

[14] M.A. Bouchiat, T.R. Carver, and V.M. Varnum, Phys. Rev. **138**, A694 (1960); R.L. Gamblin and T.R. Carver, Phys. Rev. **138**, A964 (1965).

[15] T. Walker, Phys. Rev. A **40**, 4959, (1989).

[16] K.P. Coulter, A.B. McDonald, W. Happer, T.E. Chupp and M. E. Wagshul, Nucl. Instr. Meth. A **270**, 90 (1988).

[17] B. Larson, O. Häusser, P.P.J. Delhij, D. M. Whittal, and D. Thiessen, Phys. Rev. A **44**, 3108 (1991).

[18] N.R. Newbury, A.S. Barton, G.D. Cates, W. Happer, and H. Middleton, Phys. Rev. A **48**, 4411 (1993).

[19] G.D. Cates, S.R. Schaefer, and W. Happer, Phys. Rev. A **37**, 2877 (1988).

[20] G.D. Cates, D.J. White, T.R. Chien, S.R. Schaefer, and W. Happer, Phys. Rev. A **38**, 5092 (1988).

[21] K.D. Bonin, T.G. Walker, and W. Happer, Phys. Rev. A **37**, 3270 (1988).

[22] K.D. Bonin, D.P. Saltzberg, and W. Happer, Phys. Rev. A **38**, 4481 (1988).

[23] K.P. Coulter, A.B. McDonald, G.D. Cates, W. Happer, and T.E. Chupp, Nucl. Instr. Meth. A **276**, 29 (1989).

[24] H. Middleton, Ph.D. thesis, Princeton University, (1994).

[25] B. Driehuys, G.D. Cates, and W. Happer, Phys. Rev. Lett. **74**, 4943 (1995).

[26] M. Souza, Fusion, J. Amer. Sci. Glassblow. Soc., Nov. 1995, p 20.

[27] S. M. Wiederhorn, J. Amer. Ceram. Soc. **50**, No. 8, (1967).

[28] A. Suckow, P. Schlosser, H. Rupp, and R. Bayer, Glass Technology **31**, 160 (1990).

[29] Ultra-Pure Systems Inc., Colorado Springs, CO 80960, Tel. 719-576-3355

[30] K. Debertin, R. Helmer, *Gamma- and x-ray spectrometry with semiconductor detectors*, (Elsevier Science, Amsterdam, 1988).

[31] E. Storm and M.I. Israel, Nucl. Data Tables A **7**, 565 (1970).

[32] D. Griffiths, *Introduction into Electrodynamics*, (Prentice-Hall, Englewood Cliffs, 1989).

[33] *Handbook of Material Science*, Ed. C.T. Lynch, (CRS Press 1974).

[34] *Handbook of Glass Properties*, Ed. N.P. Bansal, R.H. Doremus, (Orlando Academic Press 1986).

[35] *Handbook of Chemistry and Physics*, D.R. Lide ed., p.6-156 (CRC Press, Boca Raton, 1993).

[36] MKS Instruments, Inc., Andover, MA 01810, Tel. (508) 975-2350.

[37] C. Ottinger, R. Scheps, G.W. York, A. Gallagher, Phys. Rev. A **11**, 1815 (1975).

[38] S.Y. Ch'en, Phys. Rev. **58**, 1051 (1940).

[39] R. Walkup, B. Stewart, and D.E. Pritchard, Phys. Rev. A **29**, 169 (1984).

[40] M.V. Romalis, E. Miron, and G.D. Cates, to be submitted to Phys. Rev. A.

[41] J.O. Hirschfelder, C.F. Curtiss, R.B. Bird, *Molecular Theory of Gases and Liquids*, (John Wiley, New York, 1954).

[42] J. Kestin, K. Knierim, E.A. Mason, B. Najafi, S. T. Ro, M. Waldman, J. Phys. Chem. Ref. Data **13**, 229 (1984).

[43] Opto Power Corporation, 3321 E. Global Loop, Tucson AZ 85706, Tel. (520) 746-1234.

[44] M. Romalis, E-154 Technical Note # 34, (1996).

[45] L.D. Landau, E.M. Lifshitz, *Fluid Mechanics*, (Pergamon Press, Oxford, 1987).

[46] M. Arneodo *et al.*, (the NMC Collaboration), Phys. Lett. B **364**, 107 (1995).

[47] G.I. Smirnov, Phys. Lett. B **364**, 87 (1995).

[48] P. Zyla and T. Averett, E-154 Technical Note # 43, (1996).

[49] J. Mara, Proc. Am. Sci. Glassblow. Soc. **10**, 68 (1965).

[50] Corning Corparation, quoted by phone (1991).

[51] R. Whithey, Phys. Rev. C **9**, 2230 (1974).

[52] Y. Kolomensky, Ph.D. thesis, University of Massachusettes, (1997).

[53] B. Richter, (private communication to E. Hughes).

[54] M.G. Richards, B.P. Cowan, M.F. Secca, and K. Machin, J. Phys. B **21**, 665 (1988).

[55] T.E. Chupp, R.J. Hoare, R.L. Walsworth, and B. Wu, Phys. Rev. Lett. **72**, 2363 (1994).

[56] R.E. Stoner, M.A. Rosenberry, J.T. Wright, T.E. Chupp, E.R. Oteiza, and R.L. Walsworth, Phys. Rev. Lett. **77**, 3971 (1996).

[57] J. D. Jackson, *Classical Electrodynamics*, (John Wiley, New York, 1975).

[58] S. D. Stoller, W. Happer, and F.J. Dyson, Phys. Rev. A **44**, 7459 (1991).

[59] T. M. de Sweet and P. N. Sen, J. Chem. Phys. **100**, 5597 (1994).

# Chapter 5

# $^3$He Polarimetry

With the reduction of the statistical errors achieved by our experiment, it becomes extremely important to reduce the systematic errors, like the uncertainty in the target polarization or the dilution factor. In fact, the target dilution factor and the polarization are the two dominant sources of the systematic error for the integral of $g_1(x)$ over the measured range. A lot of effort was put into measurements of these quantities and our errors are significantly smaller than in previous experiments. Because of this, the total systematic error of our experiment is approximately equal to the statistical error. Unlike many other experiments, the polarization of the target was measured by two totally independent methods. The agreement of the two results gives us additional confidence, since they are likely to have totally different sources of systematic errors. One method is a traditional NMR using Adiabatic Fast Passage (AFP) as was used, for example, in E-142. The second method is a rather novel technique relying on the shift of the Rb Zeeman resonance (EPR) frequency due to $^3$He polarization. The errors of the two methods are comparable. We will describe each of the two methods in turn, and then discuss their agreement. The polarization analysis is described in [1], some of the results presented in this chapter have been reported in [2].

## 5.1 NMR Polarimetry

### 5.1.1 Adiabatic Fast Passage

Adiabatic Fast Passage (AFP) NMR [5] was used to measure the $^3$He polarization regularly during the run. The NMR setup is shown in Figure 5.1. The RF coils were used to create an oscillating field of magnitude $2H_1$ perpendicular to the main magnetic field $H$ aligned along the $z$ axis. The oscillating RF field can be decomposed into two counter-rotating components, each of magnitude $H_1$. To consider the behavior of the spins under the influence of the rotating field, it is useful to go into a reference

frame rotating around the $z$ axis at $\omega$, the frequency of the $H_1$ field. In this frame, the field seen by the spins is $\vec{H}_{eff} = (H - H_0)\,\hat{z} + H_1\hat{x}'$, where $H_0 = \gamma\omega$, and $\gamma$ is the gyromagnetic ratio. The other rotating component of the field is oscillating at a frequency $2\omega$ in this frame and does not affect the spins. The size of the Bloch-Siegert frequency shift [3] due to the counter-rotating field is only $H_1^2/4H_0^2 = 2 \times 10^{-6}$. Initially, the holding field $H$ is significantly smaller than $H_0$ (i.e. $H_0 - H \gg H_1$), and the effective field is almost parallel to the $z$ axis. The magnetic field is swept through resonance until $H$ is greater than $H_0$. If the sweep is slow enough, the spins can follow the changing field adiabatically. The maximum rate of change of $\vec{H}_{eff}$ occurs near the resonance and is given by $\dot{H}/H_1$. So, the adiabatic condition is satisfied if $\dot{H}/H_1 \ll \omega$. However, the sweep cannot be too slow, because the spins relax faster near the resonance when the effective field is very small. For $^3$He, the relaxation rate in the rotating frame is given by [4]: $1/T_{1r} = D\left|\vec{\nabla}H_z\right|^2/H_1^2$, where $D$ is the $^3$He diffusion constant. The sweep rate $\dot{H}$ was optimized to minimize polarization losses during AFP sweep. Both inequalities are satisfied very well:

$$D\frac{\left|\vec{\nabla}H_z\right|^2}{H_1^2} \approx 2.3 \times 10^{-3} \ll \frac{\dot{H}}{H_1} = 15 \ll \omega = 5.8 \times 10^5 \tag{5.1}$$

The measurements showed that the AFP losses were approximately 0.1% per sweep. The NMR signal was detected by two pick-up coils which were orthogonal to both the Helmholtz coils and the RF coils. The measured signal is proportional to the transverse component of the magnetization:

$$S(t) \propto \left(\vec{M}\right)_T = M\frac{\left(\vec{H}_{eff}\right)_T}{\left|\vec{H}_{eff}\right|} = M\frac{H_1}{\sqrt{(H(t) - H_0)^2 + H_1^2}} \tag{5.2}$$

This is the basic shape of the signal, it is modified by a number of effects, as described below.

Data acquisition was controlled by a Mac Quadra computer running IgorPro$^{TM}$. The magnetic field was swept up and down through the resonance by sending a linear ramp to the Kepco power supply from the D/A output of the computer. Both outputs of the Lock-in amplifier were digitized and recorded by the computer. The phase of the lock-in was adjusted to maximize the signal in one of the channels. For the water calibration the uncertainty in the signal height due to the phase setting of the Lock-in was about 0.5%. The RF field was turned on several seconds before the sweep and turned off after the sweep. The A-$\varphi$ box was used to apply a signal of arbitrary magnitude and phase to one of the differential inputs of the Lock-in. It was necessary to cancel the direct pick-up of the RF field. Table 5.1 lists various AFP parameters. For $^3$He AFP the field was swept up and then immediately down. For the water

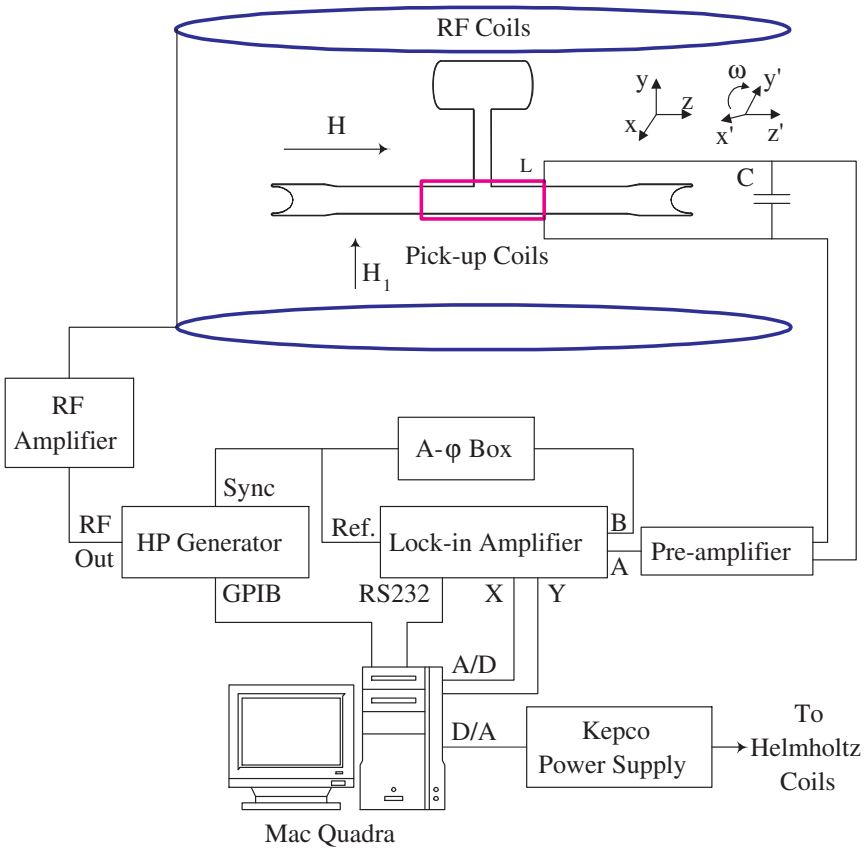


Figure 5.1: NMR equipment setup.

calibration there was a delay of 15 sec. at high field to allow the proton spins to come into thermal equilibrium at the new value of the magnetic field.

Figure 5.2 shows a typical $^3$He AFP signal, a fit to the shape (5.2), and the residuals of the fit. Five parameters were used in the fit: The height, width and center of the peak as well as a constant and linear background. The residuals of the fit are quite small, and the height of the signal can be extracted with an error of less than 0.2%. However, to extract the absolute polarization of the $^3$He, one has to calibrate the signal.

In principle, the calibration can be accomplished by a calculation of the magnetic flux captured by the pick-up coils and the knowledge of the gain of the LC circuit and various other gains in the system. Such calculation was performed and is discussed later in the text. However, it is difficult to estimate its uncertainties and one can never be sure that all effects are taken into account. Therefore, the calibration is typically performed by measuring the NMR signal from protons in water, where the

| Parameter | Value for $^3$He | Value for water calibration |
|---|---|---|
| Resonance frequency $\omega$ | 92.000 kHz | 92.000 kHz |
| Resonance field $H_0$ | 28.364 G | 21.608 G |
| Sweep starting field | 18.32, 8.80 G | 17.59 G |
| Sweep ending field | 35.92 G | 24.92 G |
| Sweep rate | 1.192 G/s | 1.192 G/s |
| RF field, $H_1$ | 72±2.1 mG | 86.4±3 mG |
| Lock-in Time Constant $\tau$ | 10 ms | 10 ms |
| Digitizing Rate | 15 ms | 15 ms |

Table 5.1: AFP Parameters.

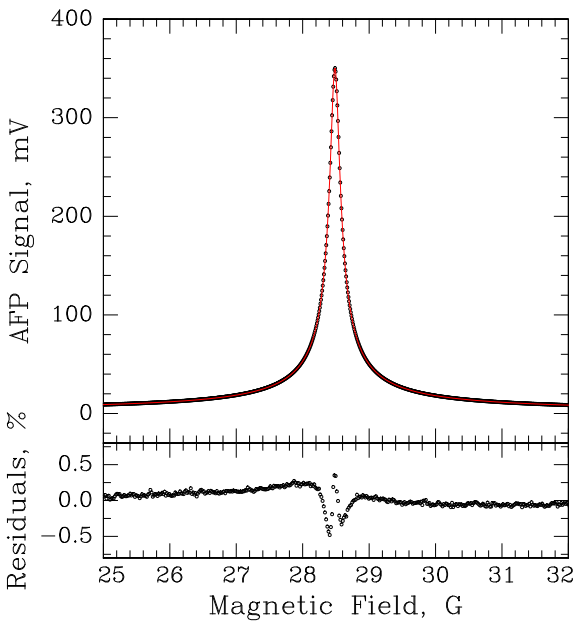


Figure 5.2: $^3$He AFP signal with a fit described in the text, bottom panel shows residuals of the fit.

absolute polarization is known from the Boltzman distribution:

$$P_w = \tanh \frac{\mu_p B}{kT} \tag{5.3}$$

Water is used because it has one of the highest concentrations of protons. The calibration procedure is complicated by several factors. First, the AFP signal from water is $10^5$ times smaller than the $^3$He signal because the thermal polarization of water is only $7.5 \times 10^{-9}$ at the magnetic field used in the experiment. It is quite

difficult to detect, and one usually has to resort to averaging many signals to get an acceptable signal to noise ratio. In our case, each set of water data consisted of about 50 sweeps. Second, we would like to measure the signal from a cell filled with water which has dimensions identical to the dimensions of the $^3$He cell. In practice, the cell used for water calibration had slightly different dimensions and position between the pick-up coils, and these differences require a correction to the signal height. Third, the relaxation processes in water are different then in $^3$He and so the signal (5.2) is significantly modified. Therefore, to properly fit the signal and accurately determine its height, we need to consider the relaxation processes in detail. Fourth, the water calibration is a time consuming procedure and consequently was done only before and after the run. So, one has to worry about changes in various quantities that might affect the signal height between the two water signal measurements. Each of these problems will be addressed below.

### 5.1.2 Coil Modeling

Careful modeling of the pick-up coils is necessary to take into account the differences in the dimensions, positions and relative densities between the $^3$He cells and the water cell. For some cells these differences lead to corrections as large as 20%. In addition, coil modeling allows one to calculate from first principles the expected size of the water signal. It provides a useful cross-check with an error comparable to other calibration methods.

Consider the coupling of the spins with the pick-up coil. We represent the magnetic moment $\vec{m}$ of the spins by a small loop of area $\vec{a}_m$ with a current $I_m$ flowing through it, so that $I_m\vec{a}_m = \vec{m}$. Let the coil produce a magnetic field $\vec{B}(x) = \vec{b}(x)I_c$ when the current $I_c$ is flowing through it. The flux of the coil magnetic field through the imaginary loop is $\Phi_m = I_c\vec{b}\cdot\vec{a}_m = L_m I_c$, where $L_m$ is the mutual inductance of the coil and the loop. The flux of the field from the loop through the pick-up coil is $\Phi_c = L_m I_m = \vec{b}\cdot\vec{m}$, using the fact that the mutual inductances are equal.

The voltage induced in the coil during the sweep is:

$$V(t) = -\frac{d\Phi_c}{dt} = -\int_{V_{cell}} n(x)\vec{b}(x)\cdot\frac{d\vec{m}}{dt}\,d^3x = -\omega m_T(t)\sin(\omega t)\int_{V_{cell}} n(x)b_T(x)\,d^3x \tag{5.4}$$

where $n$ is the density of the spins, $b_T$ is the transverse component of the coil field, and $m_T$ is the transverse component of the magnetization given by (5.2). So, the calculation of the coil response reduces to the integral of the field produced by the coil over the volume of the cell, weighted by the density of the spins. In our case the cell is well approximated by a combination of cylinders. Assume that each of the cylinders (i.e. target cell, pumping cell) has a constant density of spins (we will consider a correction due to the density gradient in the target cell later). Then

the volume integral can be converted to a surface integral of the vector potential: $\int_V \vec{B} dV = \int_V \nabla \times \vec{A} dV = \int_S \vec{n} \times \vec{A} da$. So, we need to calculate only a two-dimensional integral over the surface of the cell. Assuming that the cell is placed symmetrically between the coils it is sufficient to calculate the field from only one of the pick-up coils. The coils are modelled by a series of rectangular loops. The effect of the bend on one side of the coils can be modelled as an additional loop, whose plane is perpendicular to the axis of the cylinder. Using $\vec{A}(x) = 1/c \int \vec{J}(x')/|x - x'| \, d^3x'$, it is easy to calculate the vector potential of a rectangular loop. It has a relatively simple analytical form. The two-dimensional integral of $A$ over the surface of the cell was performed using Mathematica. To account for the finite thickness of the coils with sufficient accuracy we also integrated over two of the three coil dimensions. The dimensions were carefully measured with a caliper and checked against the mechanical drawing of the coils.

To gauge the accuracy of the model a number of systematic checks was done. The model was checked by comparing the water signals from two water cells (I and II) with widely different dimensions. The ratio of the signals, equal to 1.26 with a error of 1.7%, agrees with the model to better than 1%. Also, the amount of the signal coming from the pumping cell was checked by taking data with the pumping cell full and empty. The ratio of the signals agrees to 1.2%, while the error is 1.4%.

In addition to the dimensions of the cells we need to know their vertical position between the pick-up coils. We studied it after the run for the three surviving cells, Picard, SMC and Chance. The central position was determined by moving the cell in the target mover and measuring the AFP signal. The data can be described by a parabola near the maximum. It was found that the nominal position for all cells was too low with respect to the center of the coil by 2.7±0.3 mm. The nominal position was determined when the cell was at room temperature and the scattering chamber was open to air. The cell is mounted from the top of the scattering chamber, while the pick-up coils are mounted from the bottom. We believe that when the scattering chamber is pumped out and the cell it heated up, there is a deformation which results in the relative displacement between the pick-up coils and the cell. This displacement resulted in a reduction of the AFP signal by about 3%. Based on the reproducibility of the offset we will assume that all other cells were also 2.7 mm away from the center with a error of 0.5 mm.

The flux numbers were generated for each of the cells using dimensions and relative densities given in Chapter 4. We split the integral over the cell into integrals over several cylinders (target cell, pumping cell, transfer tube):

$$F = \int_{targ} b_T(x) \, d^3x + \frac{n_P}{n_C} \int_{pump} b_T(x) \, d^3x + \frac{1}{2}\left(\frac{n_P}{n_C} + 1\right) \int_{tran} b_T(x) \, d^3x \qquad (5.5)$$

and took into account the difference in $^3$He density of the pumping cell. $b_T$ was calculated based on the dimensions of the pick-up coils, while the boundaries of

the integrals depended on the dimensions and position of the cells. For Picard a position 3.0 mm below the center of the coils was used. This vertical displacement was measured directly after the experiment. For the water cell, which was mounted in a different way, a vertical displacement of $0\pm1$ mm was used. The numbers are given in Table 5.2. $b_T$ is in units of $\mathrm{cm}^{-1}$ (we factor our $1/c$ in CGS units or $\mu_0/4\pi$ in SI units) and $F$ is in units of $\mathrm{cm}^2$.

| Dave | Riker | Bob | SMC | Generals | Water II |
|---|---|---|---|---|---|
| 65.2 | 73.0 | 65.8 | 64.7 | 72.5 | 81.7 |
| Hermes | Prelims | Chance | Picard | Water I | |
| 63.7 | 69.5 | 70.5 | 78.0 | 64.0 | |

Table 5.2: Coil Flux $F$ in units of $\mathrm{cm}^2$.

The errors are dominated by the radius of the target cell, contributing 1% to the flux error, the uncertainty in the vertical position of the cell, contributing 1% (except for the water cell) and the uncertainty in the horizontal position, contributing 0.6%.

### 5.1.3 Water Signal Analysis

The analysis of the water signals is complicated because the thermal relaxation time for protons is comparable to the sweep time, so equation (5.2) does not describe the signal very well. Relaxation during the sweep affects both the height and the shape of the AFP signal. It also makes the signal dependent on the speed and direction of the magnetic field sweep. We use the Bloch equations to describe the time evolution of the three components of the polarization $(P_x, P_y, P_z)$ in the rotating frame [5]:

$$\begin{aligned}
\frac{dP_x}{dt} &= \gamma P_y \left(H - H_0\right) - \frac{\left(P_x - \chi H_1\right)}{T_2\left(H_1\right)} \\
\frac{dP_y}{dt} &= -\gamma P_x \left(H - H_0\right) + \gamma P_z H_1 - \frac{P_y}{T_2\left(H_1\right)} \\
\frac{dP_z}{dt} &= -\gamma P_y H_1 - \frac{\left(P_z - \chi H\right)}{T_1} \\
H &= H_0 + \alpha t
\end{aligned} \tag{5.6}$$

where $T_1$ is the longitudinal relaxation time, $T_2\left(H_1\right)$ is the transverse relaxation time in the presence of the rotating magnetic field $H_1$, and $\chi = \mu_p/k_B T$. When the RF field is off and the DC field is constant, the polarization has a value of $P = \chi H$. The resonance occurs at time $t = 0$ and a sweep begins at a negative time, $t_0 < 0$ and ends at a positive time, $t_1 > 0$.

Naively, one would expect $T_1 = T_2$ for water since the correlation time, $\tau_c$, associated with the translation and rotation of the molecules is much shorter than the Larmor frequency. However, several measurements [6, 7, 8] show that:

$$1/T_2 = 1/T_1 + 0.125\,\mathrm{sec}^{-1} \tag{5.7}$$

for neutral (i.e. pH=7.0) water. The reason for this turns out to be the presence of 0.037% of $^{17}$O isotope in natural water [7]. $^{17}$O has a spin of 5/2 and a scaler coupling to proton spins. The time that an H atom spends attached to a particular water molecule with an $^{17}$O is about $10^{-3}$ sec. The relaxation time of the $^{17}$O spin itself is about $4\times10^{-3}$ sec. Since neither of these times is shorter than the Larmor frequency $\omega$, the motional narrowing does not apply. As a result, the proton resonance is split into several lines and the transverse relaxation time is reduced compared to the longitudinal relaxation time.

The value of $T_1$ was determined from a special measurement done on the cell used for the water calibration. The computer was set to sweep the field up and then immediately down. By changing the end point of the sweep, the amount of time between the resonances on the way up and down was changed. The ratio of the two peaks was compared with the results of a numerical integration of equations (5.6). The ratio of the signal heights for the up and down sweeps is very sensitive to the value of $T_1$, and insensitive to a difference between the values of $T_1$ and $T_2$. In this way, it was found that $T_1 = 2.4 \pm 0.3$ seconds at 20±2°C. The uncertainty comes mainly from the possibility of a small delay between the up and down sweeps generated by the computer. One should be aware that $T_1$ is extremely sensitive to temperature. It changes by about 0.4 seconds when the temperature changes by 5°C. It also depends on the amount of $O_2$ dissolved in the water. The value of $T_1$ for deoxygenated water is 2.95 seconds at 20°C [9]. Our water was de-ionized but not de-oxygenated. Using the data from [10], and the solubility of $O_2$ in water, it is estimated that the concentration of $O_2$ was about 50% of the saturation value for the data taken before the run.

To apply the correction due to a $T_2$ shorter than $T_1$, it must first be checked that the relaxation due to $^{17}$O is the only process contributing to the difference between $T_1$ and $T_2$. There are certain paramagnetic ions [7, 11] which can form molecular complexes with water and reduce $T_1$ and $T_2$ by different amounts. The ions could, for example, dissolve from the glass walls of the cell. So, after the run, the water cells still containing the original water used in the calibration were shipped to Princeton, where both $T_1$ and $T_2$ were measured using a pulsed NMR spectrometer [12]. $T_1$ was measured using saturation and inversion recovery. First, either a 90° or 180° RF pulse was applied to the spins and then another 90° pulse was applied after a time $\tau$. The height of the FID after the second pulse is proportional to $M_0\left(1 - e^{-\tau/T_1}\right)$ for a 90° pulse and $M_0\left(1 - 2e^{-\tau/T_1}\right)$ for an 180° pulse. The measurement was repeated every 60 sec with different values of $\tau$ until the decay curves were mapped out.

$T_2$ was measured with the spin echo technique using the CPMG sequence [13]. First, a 90° pulse along the $x'$ axis starts the precession of the spin. The spins dephase in time $T_2^* \ll T_2$ due to magnetic field inhomogeneities. At some time $\tau > T_2^*$ an 180° pulse is applied along the $y'$ axis. It reverses the direction of all the spins and at time $2\tau$ they come into phase again, producing an FID. The 180° pulse is repeated every $2\tau$, producing a series of echoes. The envelope of the echoes decays with a time constant $1/T_2' = 1/T_2 + 1/3D\gamma^2 \left|\nabla H\right|^2 \tau^2$, where $D$ is the diffusion constant of water. In our case the relaxation due to diffusion was small for $\tau < 15$ ms. The measurements with $\tau = 15$, 10, and 5 ms all agreed within errors indicating that the imperfections of the 180° pulse did not cause a significant error. It was found that for both water cells, as well as for a control sample of freshly deionized water, $T_1 = 3.0 \pm 0.1\,\mathrm{sec}$ and $T_2 = 2.2 \pm 0.15\,\mathrm{sec}$ at 26°C. So, $1/T_2 - 1/T_1 = 0.12 \pm 0.03$ $\mathrm{sec}^{-1}$ in agreement with (5.7). The measurement also implies $T_1 = 2.5\,\mathrm{sec}$ at 20°C, in agreement with the AFP measurements taken at SLAC before the run.

In order to apply a correction due to $T_2 < T_1$, the magnitude of the $H_1$ field during the AFP sweep must be taken into account. The effect of the $H_1$ field was studied by Meiboom in [7], who used an AFP technique for measuring $T_2$. Using his treatment we calculate:

$$1/T_2\left(H_1\right) = 1/T_1 + 0.033\,\mathrm{sec}^{-1} \tag{5.8}$$

for $H_1 = 0.086$ G. Putting the values of $T_1$ and $T_2$ back into (5.6), we find that the height of both the up and down water signals is reduced by 0.4%. It should be pointed out that if one ignored the dependence of $T_2$ on $H_1$, as had been done by some authors, one would get a correction of 1.4%.

To fit the water signals we would like to find an analytic function for the signal shape which takes into account the relaxation during the sweep. Equations (5.6) were integrated numerically on Mathematica and it was found that the reduction of $T_2$ compared with $T_1$ causes a negligible correction to the shape of the signal. It only affects its height. Since we need an analytic function to fit the data, we will first assume $T_1 = T_2$ and develop an expression for the signal shape. We will then correct its height to include the fact that $T_2 < T_1$. If $T_1 = T_2$ the polarization follows the effective magnetic field $\vec{H}_{eff} = \left(H - H_0\right)\hat{z} + H_1\hat{x}$ provided that the adiabatic conditions are satisfied, and the set of equations (5.6) can be reduced to one equation for $P_{eff}$:

$$\frac{dP_{eff}}{dt} = \frac{1}{T_1}\left(P_{eq}\left(t\right) - P_{eff}\right), \quad P_{eq}\left(t\right) = \chi\left(\frac{H\left(H - H_0\right) + H_1^2}{\sqrt{H_1^2 + \left(H - H_0\right)^2}}\right) \tag{5.9}$$

The integral form of the solution is:

$$P\left(t\right) = e^{-\left(t - t_0\right)/T_1}\left(P\left(t_0\right) + \frac{1}{T_1}\int_{t_0}^{t} e^{\left(t' - t_0\right)/T_1} P_{eq}\left(t\right) dt'\right) \tag{5.10}$$

but the integral does not have an analytic representation. One can get an analytic approximation if $\alpha t \gg H_1$ by expanding $P_{eq}(t)$ in powers of $1/t$, or if $t \ll T_1$ by expanding the exponential in powers of $t/T_1$. Fortunately, $H_1/\alpha = 0.07\,\mathrm{sec} \ll T_1 = 2.4\,\mathrm{sec}$, and by switching from one approximation to the other one can cover the whole region of interest. Two terms were kept in each of the expansions and the switching time was adjusted to minimize the deviations from the result of numerical integration of (5.9). The resulting expression did not deviate from numerical results by more than 0.08% of the peak height. Since the noise of the averaged water data is about 1% of the peak height, the fit did not introduce any systematic biases. Each signal was fitted individually using Genplot© on a PC and the results averaged. The fit contained 5 parameters: the height, width and center of the peak and a constant and linear background. We used the value of $T_1$ determined in the same cell before the run. The water signals can also be averaged directly, correcting for slight drifts in the center position. The result is shown in Figure 5.3, along with a fit.

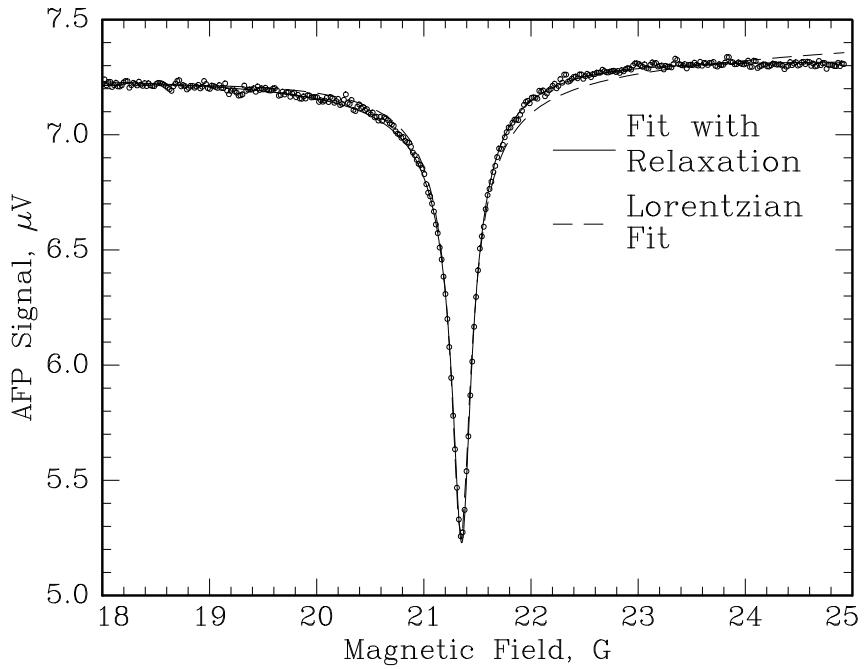


Figure 5.3: An average of 50 water signals with a fit based on the Bloch equations.

Since the relaxation during the resonance is already taken into account in equation (5.9), the heights of the up and down peaks should be the same. So, a consistency check can be performed by using the value of $T_1$ from the independent measurement

before the run and comparing the heights of the water signals. For the data taken before the run, the two heights are different by 1.8%, while the combined error is 1.6%, neglecting the error in $T_1$. For the data taken after the run the peaks are different by 3.6% which is outside the error bars. The two heights are equal if we use $T_1 = 1.95$ sec. Given the sensitivity of $T_1$ to the environment, this value is not too unreasonable. It should also be pointed out that the variation of $T_1$ causes the heights of the two peaks to move in opposite directions and has a negligible effect on their average. Another way to identify potential disagreement with the model is to study the systematic deviations in the residuals of the fit. The residuals of individual fits were added together to reduce the noise, a typical result is shown in Figure 5.4. For most data the systematic deviations were less than or equal to 1.5%, although there is one set of data (the up signal for the pre-run data) were the deviations are up to 3%. The random noise in the data is about 1%. To check if these deviations indicate a fundamental deficiency of the model, some data were taken in January under more favorable noise conditions. In these data the noise level was approximately 0.6% and systematic variations were also on the order of 0.6%, approximately the same as the He AFP residuals. Nevertheless, we will assume that the systematic error of the water signal analysis is 1.5%.

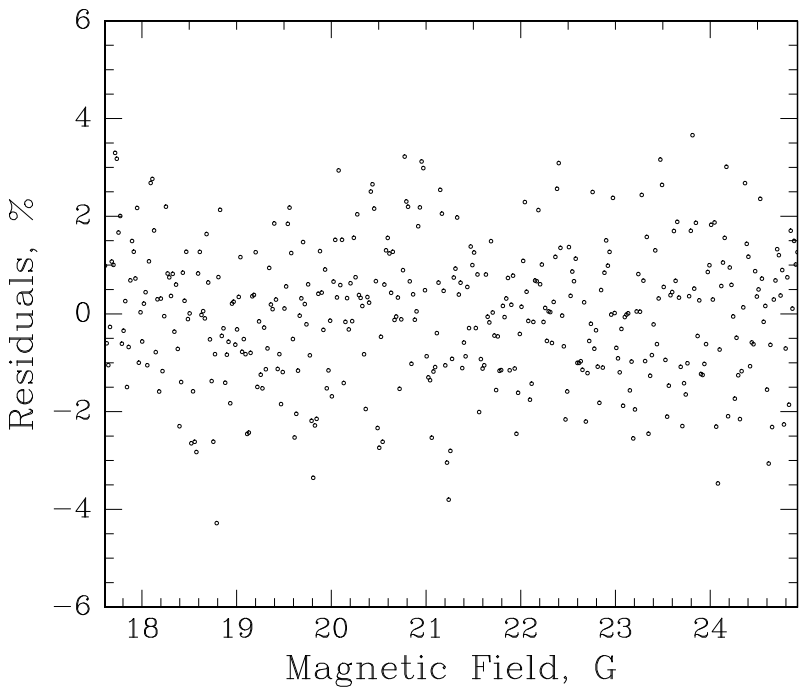


Figure 5.4: Average residual of the water signal as a percentage of the peak height.

For the final result we averaged the results of the individual fits and applied a correction (0.4%) due to $T_2 < T_1$. The height of the water signals taken before the run is $S_w = 1.502 \pm 0.015(stat)$ $\mu$V, and $S_w = 1.533 \pm 0.013(stat)$ $\mu$V after the run. Here, for definiteness, we already took into account the nominal gain of the pre-amp and the lock-in, so the voltage refers to the RMS voltage at the output of the LC circuit. The same convention applies to the $^3$He and water signals shown in Figures 5.2 and 5.3.

An alternative method to analyze the water signals is to fit them to the same analytic form as the $^3$He signals and then apply a correction to the height of the signal to take the relaxation into account. When the water signals are fit to equation (5.2), we find that the peak heights for the up and down sweeps are not equal. The ratio of up to down peak heights is equal to 0.813 for the data taken before the run and 0.849 for the data after the run. This information can be used to determine $T_1$ directly from the calibration data. With a numerical integration we generate water signals according to equations (5.6) and then fit them to a lorentzian (5.2). The value of $T_1$ is adjusted until the ratio of the up to down heights is reproduced. In this way we found that $T_1 = 2.7 \pm 0.4$ sec. for the data taken before the run and $T_1 = 1.8 \pm 0.2$ sec. for the data taken after the run. Equation (5.8) is used to calculate $T_2$.

With these values for $T_1$ and $T_2$ NMR signals are generated by numerical solution of the Bloch equations and the results are fit to a simple lorentzian. It is found that the average height of the up and down signals, as determined by the lorentzian fit, should be corrected by a factor of 1.012$\pm$0.004. To check if this number is affected by the noise in the signal, gaussian noise was added to the simulated signals generated by the solution of the Bloch equations. No significant changes were found. The calibration data are fit to the same lorentzian lineshape. After applying the correction, we find $S_w = 1.520 \pm 0.022(stat)$ $\mu$V before the run and $S_w = 1.543 \pm 0.015(stat)$ $\mu$V after the run.

The two methods give slightly different results for the height of the water signals, although the discrepancy is less than the systematic error of 1.5%. While in the first method the signals are fit to a more accurate shape and, therefore, should be less sensitive to the random distortions, the second method is more closely relying on the calibration data for extracting $T_1$. We use the average of the two methods and add the difference between them (0.9%) to the systematic error. The result is $S_w = 1.513 \pm 0.015(stat) \pm 0.025(sys)$ $\mu$V before the run and $S_w = 1.538 \pm 0.015(stat) \pm 0.025(sys)$ $\mu$V after the run. The temperatures for the two data samples were identical within errors ($22 \pm 3$°C). The difference between the two numbers before and after the run, equal to 1.7%, is approximately the same as their combined error. So, any variation of the pick-up coil sensitivity with time is seen only at $1\sigma$ level. It may be due to a slow deformation of the pick-up coils by heat or an abrupt motion of the pick-up coils during Riker explosion. We will assume that the sensitivity varied linearly with

time and apply appropriate corrections to the calibration constants of all cells.

### 5.1.4 Other Signal Shaping Effects

The shape of the signal given by (5.2) for $^3$He and by (5.6) for water is modified by two additional effects; the field inhomogeneity and the time constant of the lock-in amplifier. Ideally, these modifications should be the same for both $^3$He and water. However, the value of the $H_1$ field was different (see Table 5.1) due to problems with the switch on the HP used to turn the RF on and off. Since both effects depend on the value of $H_1$, they need to be studied in more detail. In addition, they need to be included in the comparison of the absolute signal size with the results of a calculation.

The effect of the Lock-in amplifier time constant can be accurately modelled by the following integral:

$$S(t) = e^{-(t-t_0)/\tau} \int_{t0}^{t} e^{(t'-t_0)/\tau} \frac{H_1}{\sqrt{H_1^2 + (\alpha t')^2}} dt' \tag{5.11}$$

This integral was evaluated on Mathematica for $\tau$ =10 ms. The height of the signal is reduced by 0.7% for $^3$He and by 0.5% for water. The residuals for a lorentzian fit are 0.2%.

The field inhomogeneity causes the spins in different parts of the cell to come into resonance at different times during the sweep, which broadens the signal and reduces its height. The $dB_z/dz$ component of the gradient causes the biggest effect, because the region sampled by the pick-up coils extends in that direction. The signal can be written in the form:

$$S(t) = \int \frac{H_1}{\sqrt{H_1^2 + (\alpha t - b)^2}} g(b)\, db \tag{5.12}$$

where $g(b)$ gives the relative number of the spins experiencing a gradient field $b$. For a linear gradient in the $z$ direction, a square pulse distribution extending from $-b_0$ to $b_0$ is used. $b_0$ is determined by studying the height of the AFP signals as a function of $H_1$. This was done for Picard and Chance over a range of $H_1$ from 55 to 88 mG. The data first have to be corrected for the shaping due to the lock-in time constant by evaluating the integral (5.11). The analysis of the data gives $b_0 = 18 \pm 5$ mG or roughly $dB_z/dz$ = 3.6 mG/cm. When the signals are fit to a function of the form (5.2) plus a constant and linear background, the height is reduced by 0.9% for $^3$He, but by only by 0.7% for water, because of the larger $H_1$ field. The residuals of the fit are approximately 0.4%, consistent with Figure 5.2. We will correct for this effect by reducing the water signal height by 0.2%, so that it is consistent with the conditions of $^3$He AFP.

### 5.1.5 Coil Gain and Other Quantities

To study the temperature dependence of the pick-up coils gain as well as possible coil loading, we periodically mapped out the Q curve of the pick-up coils using an excitation loop. The voltage induced in the pick-up coils as a function of frequency can be described by the following equation:

$$V(\nu) = \frac{\mathcal{E}}{\sqrt{\left(\left(\frac{\nu}{\nu_0}\right)^2 - 1\right)^2 + \frac{1}{Q^2}}} \tag{5.13}$$

where $\mathcal{E}$ is the EMF induced in the pick-up coils. The EMF is proportional to the frequency, so we can write $\mathcal{E} = A\nu$, where $A$ is a constant which depends only on the geometry. The variation of the gain of the LC circuit during the run was about 0.5%. The gain was higher by $0.9\% \pm 0.5\%$ when the coils were hot with a $^3$He cell installed than under conditions for water calibration. The absolute size of the circuit gain at 92 kHz is $G_c = V/\mathcal{E} = 5.583 \pm 0.05$.

The analysis of the water signals was done in such a way that only the thermal proton polarization at the resonance enters into the calculations. This allows the RF frequency to be used rather then the magnetic field in the calculation of the Boltzman polarization. Using the temperature of $22 \pm 3$°C we get $P_{th} = (h\nu/2kT) = 7.481 \times 10^{-9}$ with 1% error. The density of protons in water at 22°C is $n_p = 6.670\ 10^{22}$ cm$^{-3}$ and the ratio of magnetic moments of the $^3$He and $^1$H is $\mu_{He}/\mu_p = 0.7617$

### 5.1.6 Absolute Calibration

Using the model of the pick-up coils, the model of the LC circuit and other corrections described above, one can calculate the expected size of the water signal from first principles. One more effect needs to be included. The BNC cable running from the target to the Counting House was loading the output of the pre-amplifier which has an output impedance of 50Ω. At 92 kHz, the cable can be treated as a capacitor. To measure its capacitance, the cable was connected to the 600Ω output of the pre-amp, and from the reduction of the signal it was estimated that its capacitance is 8.4 nF. Assuming 30pF/ft, this corresponds to 280 ft of cable, a reasonable number. The signal is reduced by $3 \pm 1\%$ due to the loading by the cable. We also need to know the number of turns in the pick-up coils, which is equal to $N_c = 150$ [14]. The voltage detected by the lock-in is given by:

$$V = \frac{\mu_0}{4\pi}\omega\mu_p F n_p P_{th} N_c G_c G_p G_l C \tag{5.14}$$

where $G_p$ and $G_l$ are the pre-amp and lock-in gains respectively, and $C = 0.958$ is a correction factor which includes the attenuation in the cables and reduction in

the signal height due to field inhomogeneity and lock-in time constant. Putting all of the numbers together we get a value for the water signal of 1.48 $\mu$V, which is only different by 3% from the actual signal. It is difficult to estimate the error of the calculation. It is dominated by the uncertainty of the coil dimensions, and is probably about 5%. Nevertheless, this comparison is an extremely powerful check of the model calculations. Since they are able to reproduce the absolute size of the water signal, we trust them to reproduce the scaling between different cells.

### 5.1.7 Calculation of the Calibration Constant

Since the AFP signal is proportional to the spin magnetization, it is easy to scale the water signal to calculate the calibration constant between the $^3$He signal height and the polarization: $P_{He} = C_w S_{He}$, where $w$ stands for water calibration.

$$C_w = \left(\frac{P_{th}}{S_w}\right)\left(\frac{\mu_p n_p}{\mu_{He} n_0 \left(n_C/n_0\right)}\right)\left(\frac{G_{cw}G_{pw}G_{lw}}{G_{cHe}G_{pHe}G_{lHe}}\right)\left(\frac{F_w}{F_{He}}\right) \tag{5.15}$$

Each of the parameters and their errors are summarized in Tables 5.3. The errors for the lock-in and pre-amp non-linearity are determined by connecting the lock-in and pre-amp in series and changing the gain on both of them so that the product remains constant. Any changes in the output would indicate that one of the devices is non-linear. Such variations were less then 1%. The results for the water calibration constants in units of %/mV cells are given in Table 5.4. The total error on the water calibration constant is 3.4%.

| Parameter | Value | Error (%) |
|---|---|---|
| $P_{th}$ | $7.481\times10^{-9}$ | 1.0 |
| $S_w$ | 1.510 - 1.535 $\mu$V | 1.8 |
| $\mu_p/\mu_{He}$ | 1.313 | – |
| $n_p$ | 2482 amg. | 0.1 |
| $n_0$ | Table 4.9 | 1.0 |
| $n_C/n_0$ | Table 4.11 | 1.6 |
| $G_{cw}/G_{cHe}$ | 0.991 | 0.5 |
| $G_{lW}/G_{lHe}$ | 1000, (1)[1] | 0.7 |
| $G_{pW}/G_{pHe}$ | 20, (1)[1] | 0.7 |
| $F_w/F_{He}$ | Table 5.2 | 1.6 |

Table 5.3: Water Calibration Error Table.

[1]The nominal ratio of the gains is already included in the size of the water signal.

| Dave | Riker | Bob | SMC | Generals | Hermes | Prelims | Chance | Picard |
|---|---|---|---|---|---|---|---|---|
| 0.1595 | 0.1445 | 0.1603 | 0.1611 | 0.1476 | 0.1656 | 0.1496 | 0.1471 | 0.1349 |

Table 5.4: Water Calibration Constants, %/mV

## 5.2 EPR Polarimetry

### 5.2.1 Basic Principle

The EPR method of polarimetry uses the shift of the Rb Zeeman resonance due to the magnetic field created by polarized $^3$He. The EPR resonance is shifted due to two effects. The Rb-$^3$He spin exchange interaction that is responsible for polarization transfer to $^3$He also produces a shift in the Rb EPR frequency proportional to the $^3$He polarization. Also, the classical magnetic field produced by $^3$He magnetization shifts the frequency of the Rb Zeeman resonance. These shifts are quite substantial (about 20kHz out of 8MHz) and easy to measure. To isolate the shift due to $^3$He we reversed the direction of the $^3$He polarization and measured the difference in the EPR frequency between the two polarization states.

To understand the contribution from the spin exchange it is convenient to use the density matrix formalism. For binary Rb-$^3$He collisions the time evolution of the density matrix $\rho$ of Rb is given by the following equation [15, 16]:

$$\begin{aligned}\frac{d}{dt}\rho &= -2\pi i\left[A\vec{I}\cdot\vec{S},\rho\right] - i\left[\omega_e S_z - \omega_I I_z,\rho\right] + \\ &\quad \frac{1}{T_{He}}\left(4\alpha\left\langle\vec{K}\right\rangle - \vec{C}\right)\cdot\vec{S} + \frac{2iK_{He}}{T_{He}}\left[\left\langle\vec{K}\right\rangle\cdot\vec{S},\rho\right] + \frac{d^O}{dt}\rho \qquad (5.16)\end{aligned}$$

where $I$ and $S$ are the nuclear and electron spins of Rb atom, $\vec{K}$ is the $^3$He nuclear spin, $1/T_{He} = n_{He}\bar{v}\sigma_{Rb-He}$ is the Rb-He spin exchange rate per Rb atom. $K_{He}$ is a frequency shift parameter, $\alpha$ and $\vec{C}$ are operators acting on the nuclear spin of Rb. $A$ is the Rb hyperfine splitting, $\omega_e = g_e\mu_B B/\hbar$ and $\omega_I = g_I\mu_N B/\hbar$ are the electron and nuclear Zeeman frequencies. $d^O\rho/dt$ is the contribution to the time evolution from other effects which do not depend explicitly on the $^3$He nuclear spin. Their effect will be considered later. The real part of the Rb-He spin exchange term results in the spin transfer between Rb and He, while the imaginary part causes the frequency shift. Since the nuclear spin is polarized along the $z$ axis, $\left\langle\vec{K}\right\rangle = K_z\hat{z}$, the frequency shift due to $^3$He can be directly added to the Zeeman term. The real part of the spin exchange will contribute to the frequency shift only in second order, i.e. $(T_{He}\omega_e)^{-2} = 10^{-12}$ [15], and is quite negligible. We therefore are left with:

$$\frac{d}{dt}\rho = -2\pi i\left[A\vec{I}\cdot\vec{S},\rho\right] - i\left[\left(\omega_e - \frac{2K_{He}}{T_{He}}\left\langle\vec{K}\right\rangle\right)S_z - \omega_I I_z,\rho\right] \qquad (5.17)$$

This can be rewritten in the more familiar Hamiltonian formalism using $i\hbar d\rho/dt = [\mathcal{H}, \rho]$:

$$\mathcal{H} = 2\pi\hbar A\vec{I}\cdot\vec{S} + \hbar\left(\omega_e - \frac{2K_{He}}{T_{He}}\left\langle\vec{K}\right\rangle\right)S_z - \hbar\omega_I I_z \tag{5.18}$$

Since $A = 1012$ MHz $\gg \omega_e/2\pi = 8$ MHz, we should use the eigenstates of the $\vec{I}\cdot\vec{S}$ operator, which are also the eigenstates of the total angular momentum $\vec{F} = \vec{I} + \vec{S}$. Their energy is given by the Breit-Rabi formula [17]:

$$E_{F=I\pm1/2,M} = -\frac{h\nu_{HF}}{2\left(2I+1\right)} - g_I\mu_N BM \pm \frac{h\nu_{HF}}{2}\left(1 + \frac{4M}{2I+1}x + x^2\right)^{1/2} \tag{5.19}$$

where $x = \left(\omega_e + \omega_I - \left(2K_{He}/T_{He}\right)\left\langle\vec{K}\right\rangle\right)/2\pi\nu_{HF}$, and $h\nu_{HF} = A\left(I + 1/2\right)$. By applying an RF field we induce transitions between neighboring $M$ sublevels and measure the frequency of these transitions. Figure 5.5 shows the EPR frequencies of the $\Delta M = 1, \Delta F = 0$ transitions for $F = 3$ manifold of $^{85}$Rb ($I = 5/2$) as a function of $B$. At low field all transitions have the same frequency, but they split at higher field. The effect of the Rb-$^3$He spin exchange is equivalent to an additional magnetic field $\Delta B = \left(2K_{He}\hbar/T_{He}g_e\mu_B\right)\left\langle\vec{K}\right\rangle$. (The contribution from the nuclear Zeeman splitting can be ignored, since $\omega_I/\omega_e = 1.5\times10^{-4}$). The value of $\Delta B$ for our conditions is about 0.04 G, so in calculating the change of the EPR frequency due to $^3$He we can use the derivative of the EPR frequency with respect to the magnetic field, which is shown in the inset of Figure 5.5. So, the frequency shift due to the spin exchange is given by:

$$\Delta\nu_{SE} = \frac{d\nu_{EPR}\left(F,M\right)}{dB}\frac{2\hbar K_{He}n_{He}\bar{v}\sigma_{Rb-He}}{g_e\mu_B}\left\langle\vec{K}\right\rangle \tag{5.20}$$

It is proportional to the density and the polarization of $^3$He and depends on temperature, the absolute magnetic field and $F, M$ quantum numbers of the transition.

The other part of the frequency shift comes from the classical magnetic field created by polarized $^3$He. The magnetic field is proportional to the $^3$He magnetization and, therefore, the polarization and density of $^3$He:

$$\Delta\nu_B = \frac{d\nu_{EPR}\left(F,M\right)}{dB}CM_{He} = \frac{d\nu_{EPR}\left(F,M\right)}{dB}Cn_{He}\mu_{He}\left\langle\vec{K}\right\rangle/K \tag{5.21}$$

where $C$ is a dimensionless factor of order unity that depends on the geometry of the sample. We can combine the two shifts for a sample of specific shape. So, for a spherical sample we define:

$$\Delta\nu_{EPR} = \frac{8\pi}{3}\frac{d\nu_{EPR}\left(F,M\right)}{dB}\kappa_0\mu_{He}n_{He}P_{He} \tag{5.22}$$

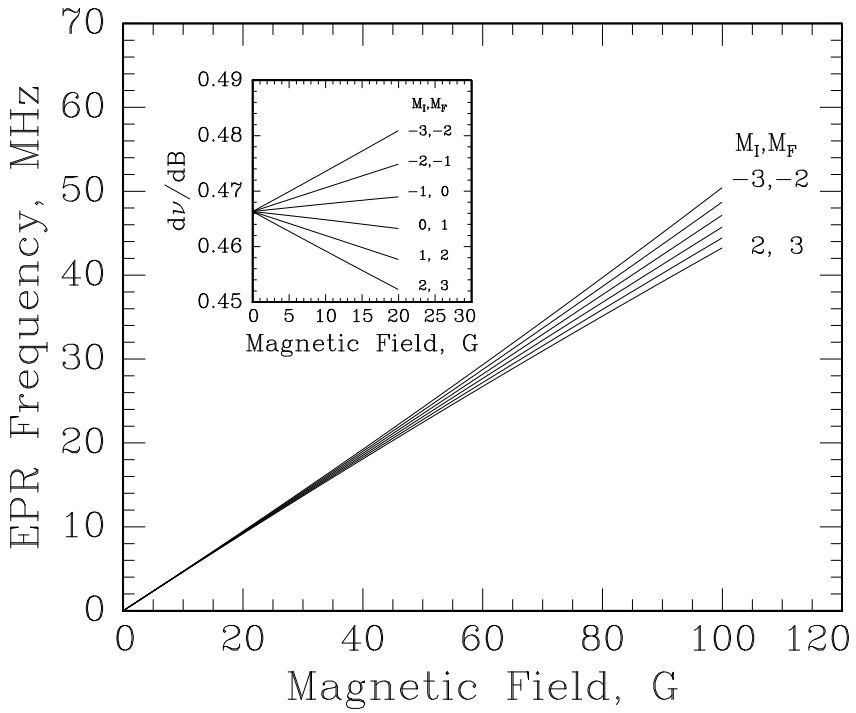


Figure 5.5: The frequency of the EPR transitions as a function of the magnetic field. The inset shows the derivative of the frequency for different levels.

where $\kappa_0$ is a constant that depends on temperature, but not on the density or polarization of $^3$He, and $P_{He} = \left\langle \vec{K} \right\rangle / K$. The shift parameter $K_{He}$ is absorbed into $\kappa_0$. At low magnetic field $d\nu_{EPR}(F,M)/dB = \mu_B g_s / h(2I+1)$, and (5.22) is identical to previous definitions in the literature [18, 19, 20]. The value of $\kappa_0$ is not known with sufficient accuracy from calculations based on interatomic potentials and has to be measured experimentally.

### 5.2.2 Detection of EPR Resonance

To detect the EPR resonance we relied on the fact that during optical pumping the polarization of Rb vapor is very high (60-90%). It means that most of the atoms are in the $F = 3, M = 3$ state (or $M = -3$ for oppositely polarized light). Although the Rb vapor is optically thick for unpolarized light, the laser light can penetrate quite far into the cell because most atoms are in the state that cannot absorb circularly polarized photons from the lasers. Among the atoms that do absorb the photons and are excited to the $P$ state most are radiationlessly quenched to the ground state by the

nitrogen in the cell. A small fraction (3-5%) decays by emitting a fluorescence photon at either $D_1$ or $D_2$ line. The fluorescence photons are observed through a $D_2$ filter to block the radiation scattered from the lasers, which are tuned to the $D_1$ transition. These photons form the picture that is usually observed with a CCD camera to monitor the optical pumping. The intensity of the fluorescence is proportional to the rate of photon absorbtion in the cell. If we apply an RF field at the EPR frequency corresponding to $M = 3 \rightarrow 2$ transition, it will tend to equalize the population of the two states. The number of atoms in the $M = 2$ state capable of absorbing laser light will increase and the intensity of the fluorescence will increase. So, by monitoring the intensity of the fluorescence as a function of the RF frequency we can detect the EPR resonance.

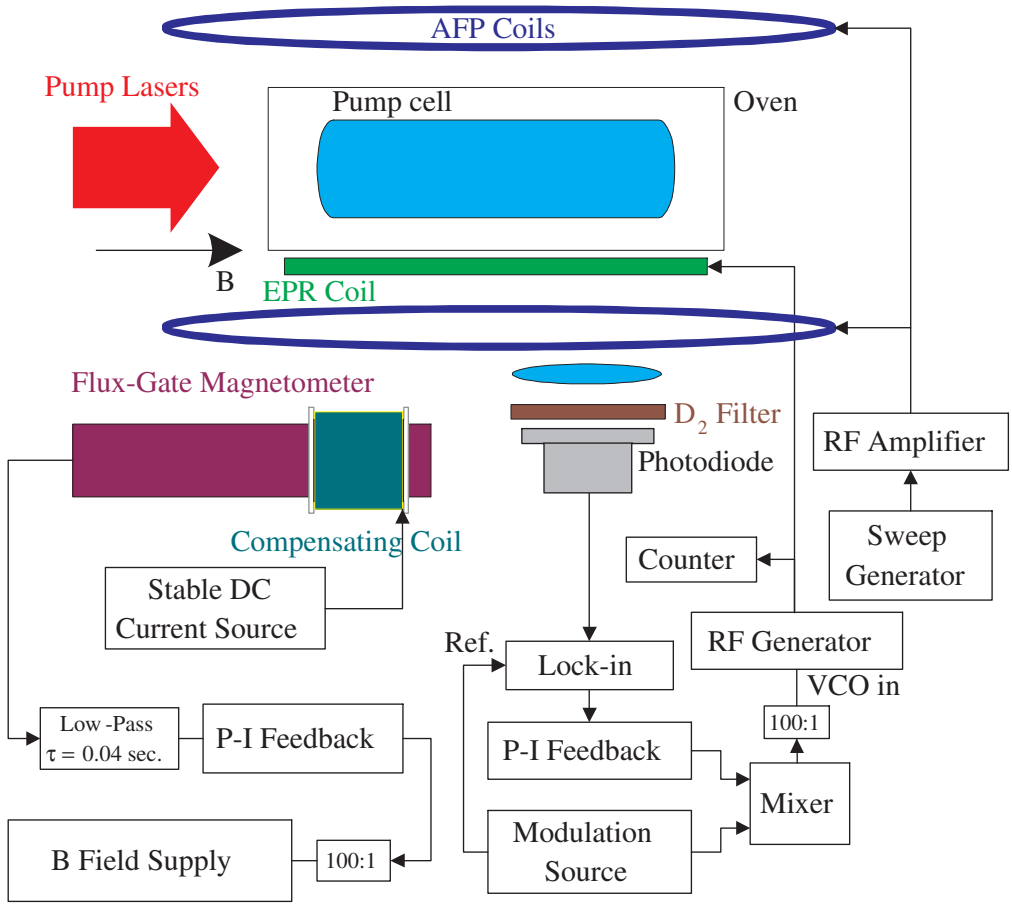


Figure 5.6: Equipment setup for EPR detection.

The equipment setup for EPR measurements is shown on Figure 5.6. The RF field

| Parameter | Value |
|---|---|
| RF Frequency | 8.5 MHz |
| RF Amplitude | 10 V p-p |
| Mod. Freq. | 210 Hz |
| Mod. Ampl. | 6 kHz |
| Lock-in time const. | 0.1 sec |
| AFP sweep start | 92 kHz |
| AFP sweep stop | 30 kHz |
| Sweep time | 10 sec |

Table 5.5: Parameters for EPR frequency shift measurements.

was created by a coil mounted on the side of the oven. The fluorescence from the cell was detected by a photodiode with a $D_2$ filter. The RF was frequency modulated using a Voltage Controlled Oscillator (VCO), Wavetek function generator model 80. The signal measured by the lock-in amplifier referenced to the modulation frequency was proportional to the derivative of the EPR line shape. A feedback circuit adjusted the DC level at the input of the VCO to keep the lock-in signal zero, i.e. locked to the center of the line [18, 19]. The operating parameters of the system are given in Table 5.5. A circuit diagram of the proportional-integral feedback circuit and the mixer is shown in Figure 5.7. The RF frequency was measured by a counter and transferred to the Mac via GPIB interface. To accurately determine a shift in the EPR frequency it was important to keep the magnetic field stable to one part in $10^5$. We used a Bartington Flux-Gate magnetometer [22] to measure the magnetic field. Since the range of the magnetometer is only $-5$ to 5 G, we canceled the holding field by a small coil wound around the magnetometer. The field and the field gradient created by the coil near the target were negligible. The coil was driven by a stable current source that served as a reference to which the field was locked. The output of the magnetometer was kept near zero by an identical feedback circuit controlling the power supply for the Helmholtz coils.

To isolate the frequency shift due to the $^3$He polarization we periodically reversed the direction of the polarization. The reversal was done by AFP, only instead of sweeping the magnetic field through the resonance we swept the RF frequency. This way we could keep the field locked during the whole measurement cycle. The behavior of the spins during the frequency sweep AFP is identical to normal AFP and the end result of the sweep is an 180° flip. We utilized the same coils, RF amplifier, and generator. The generator was programmed to sweep the frequency at the appropriate rate to satisfy the AFP conditions. The parameters of the sweep are given in Table 5.5. The measurement cycle consisted of recording the EPR frequency for about 1 min, then flipping $^3$He spins by AFP and recording the frequency for another minute. This

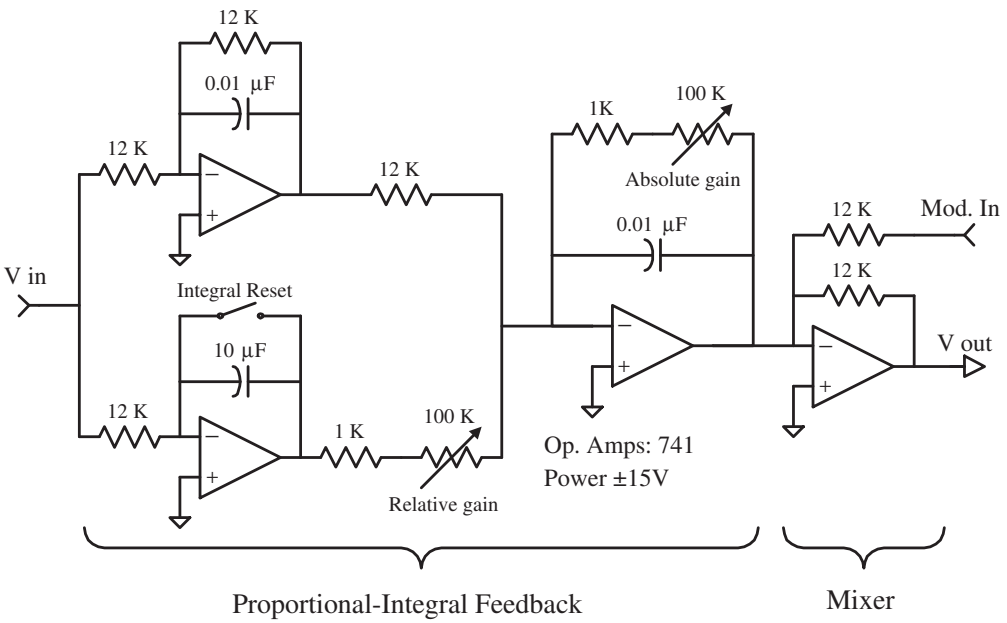


Figure 5.7: The circuit diagram of the proportional-integral feedback and the mixer.

procedure was repeated several times. A typical data set is shown in Figure 5.8. The data are fit allowing a small amount of polarization loss per cycle which is due to the AFP losses and the decay of the polarization during one half of the cycle because the lasers are pumping in the opposite direction. The quality of the data is very good and the size of the frequency shift can be extracted with a error of less than 0.5%.

### 5.2.3 Measurement of $\kappa_0$

To use the EPR frequency shift for polarimetry we need to know the value of $\kappa_0$ for Rb-$^3$He system. Although it was measured previously [19, 20, 21], there is some disagreement between the numbers, and none of the measurements were done at high temperature and Rb number density used in our experiment. Therefore, a new experiment was done at Princeton under conditions very similar to SLAC. The experiment used an interplay between the two sources of frequency shift to measure the value of $\kappa_0$ [20]. For a spherical sample the frequency shift is given by equation (5.22). For a sample of another shape we can imagine a sphere around the EPR detection region which will give the same shift plus a shift due to the remaining parts of the sample. Since the He atoms in these parts do not come into direct physical contact with the Rb atoms in the detection region, they cannot contribute to the shift through the spin exchange. They will only contribute through the classical magnetic

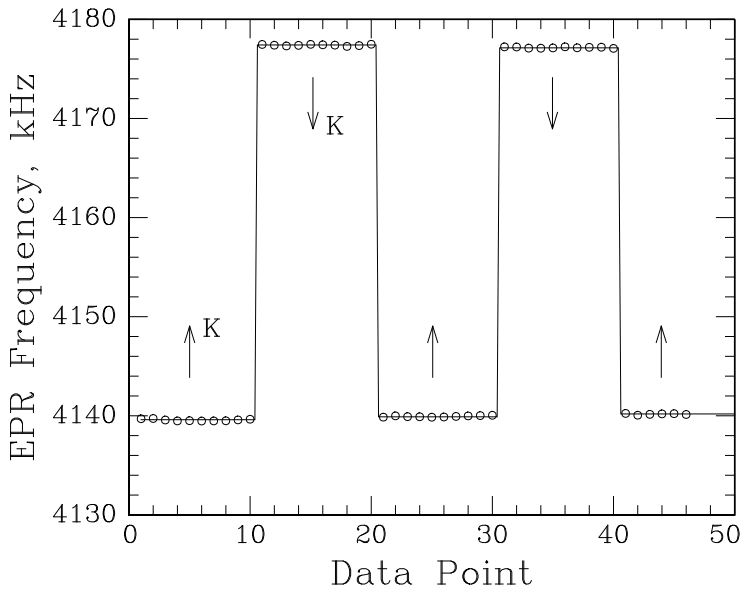


Figure 5.8: EPR polarization measurement for the target cell Picard.

field shift which can be calculated based on the geometry of the sample. Making two measurements with different geometry we can separate the magnetic field shift from the shift due to spin exchange and determine the value of $\kappa_0$.

We used a long cylinder to make the measurements as shown in Figure 5.9. The magnetic field inside a very long cylinder magnetized along its axis is $B = 4\pi M$, where $M$ is the magnetization of the cylinder. For a cylinder magnetized perpendicular to its axis the field is $B = 2\pi M$. The field inside a uniformly magnetized sphere is $B = 8\pi M/3$. Using the linearity of electromagnetism we can simply subtract the field of the sphere from the field of the cylinder to calculate the magnetic field shift of the EPR frequency. The frequency shift for the longitudinal and transverse orientations is given by:

$$\Delta\nu_L = \frac{d\nu_{EPR}(F,M)}{dB}\mu_{He}n_{He}P_{He}\left(\frac{8\pi}{3}\kappa_0 + \left(4\pi - \frac{8\pi}{3}\right)\right) \quad (5.23)$$

$$\Delta\nu_T = \frac{d\nu_{EPR}(F,M)}{dB}\mu_{He}n_{He}P_{He}\left(\frac{8\pi}{3}\kappa_0 + \left(2\pi - \frac{8\pi}{3}\right)\right) \quad (5.24)$$

Solving these equations we get $\kappa_0 = 3(\Delta\nu_L + \Delta\nu_T)/8(\Delta\nu_L - \Delta\nu_T) - 1/8$. Introducing polarization to frequency conversion constants $\Delta\nu_L = P_{He}K_L$, $\Delta\nu_T = P_{He}K_T$, we can cancel the polarization of $^3$He: $\kappa_0 = 3(K_L + K_T)/8(K_L - K_T) - 1/8$

A cylindrical cell 0.5" in diameter and 7" long was prepared for this experiment. The magnetic field produced by a uniform magnetization in the cell was calculated

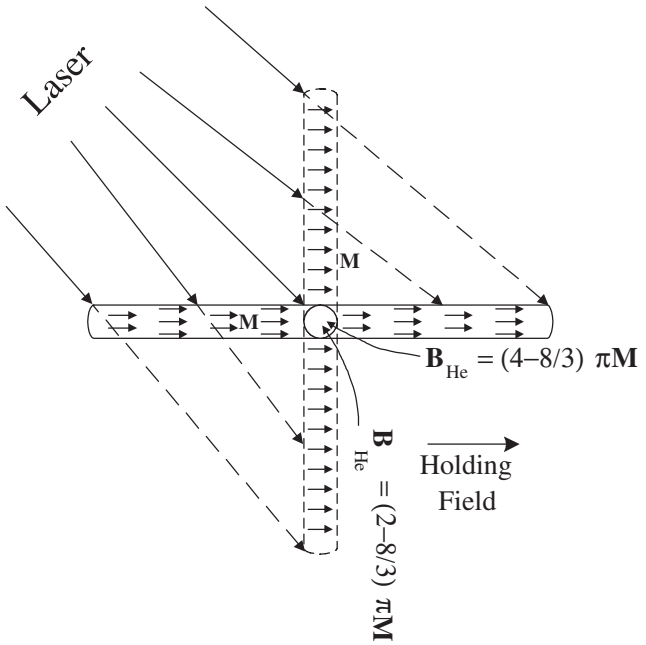


Figure 5.9: Experimantal arrangement for $\kappa_0$ measurements.

on Mathematica and differed from the field for an infinite cylinder by less than 0.6%. To change the orientation of the magnetization, the cell together with the oven was rotated with respect to the holding field as shown in Figure 5.9. The EPR detector placed at the center of the cell was very similar to what was used at SLAC. It consisted of a 3/4 in. diameter RF coil, a light collecting lens, a $D_2$ filter and a photodiode. The electronics was also similar, except for the field locking mechanism. Since the value of $\kappa_0$ depends on the difference between the EPR shifts in the two orientations, which is only 10% of the total shift, the frequency shifts has to be measured with much higher accuracy. To achieve sufficient accuracy it was necessary to keep the field stable to one part in $10^6$, which exceeds the stability of the current source. Therefore, the field was locked to a Cs magnetometer which uses an RF generator as a reference source. The principle of operation of the Cs magnetometer is also based on the EPR resonance [19, 23]. The field locking is essentially an inversion of the above mentioned feedback scheme, where the RF frequency is kept constant and the magnetic field is locked to the resonance. The RF generator was synchronized with the counter used to measure the Rb EPR frequency to avoid any relative drifts. The magnetometer was placed sufficiently far from the He cell to avoid any spurious feedback due to the magnetic field created by $^3$He. The magnitude of the frequency shift was measured by periodically flipping $^3$He polarization with AFP. During the measurement the cell was also frequently rotated by 90° from the longitudinal to the transverse orientation.

To keep the laser illumination constant during the measurement it was positioned at 45° to the magnetic field in the plane of the cell rotation.

The measurement procedure consisted of a combination of the following three actions: measuring the EPR frequency (M), flipping the spins by AFP (F), and rotating the cell (R). It was important to take into account the polarization losses due to AFP flips and the optical pumping in the opposite direction, since they were significant compared to the required accuracy. Several measurement sequences were tried and it was found that the best cycle is (MFMFMR), repeated many times during the measurement. Let's follow the polarization during a measurement cycle. For definiteness, we start in the longitudinal orientation with the $^3$He spins pointing in the direction of optical pumping, creating a negative frequency shift and having a polarization $P$. During the measurement of the EPR frequency the polarization changes due to optical pumping and spin relaxation. We will parametrize the changes by a fractional polarization loss per second, so after a time $T$ the polarization will be $P\,(1 - S_{DL}T)$. The first subscript refers to the orientation of the spins (up or down) and the second subscript refers to the orientation of the cell (longitudinal or transverse). We also introduce $S_{UL}$ for He spins against the optical pumping direction in the longitudinal orientation of the cell, $S_{DT}$ and $S_{UT}$ for the transverse orientation of the cell. Since the changes of the polarization during the whole measurement sequence are relatively small (about 5%), we will assume that the fractional loss parameters remain constant. For AFP losses we introduce a fractional loss constant $\alpha$ per flip. Then the frequency shift at various points in the cycle is given by (see Figure 5.10 for notation):

$$\begin{aligned}
f_1 &= f_L - PK_L \\
f_2 &= f_L - P\,(1 - S_{DL}T)\,K_L \\
f_3 &= f_L + P\,(1 - S_{DL}T)\,(1 - \alpha)\,K_L \\
f_4 &= f_L + P\,(1 - S_{DL}T)\,(1 - \alpha)\,(1 - S_{UL}T)\,K_L \\
f_5 &= f_L - P\,(1 - S_{DL}T)\,(1 - \alpha)^2\,(1 - S_{UL}T)\,K_L \\
f_6 &= f_L - P\,(1 - S_{DL}T)\,(1 - \alpha)^2\,(1 - S_{UL}T)\,(1 - S_{DL}T)\,K_L \\
f_7 &= f_T - P\,(1 - S_{DL}T)\,(1 - \alpha)^2\,(1 - S_{UL}T)\,(1 - S_{DL}T)\,K_T \\
f_8 &= f_T - P\,(1 - S_{DL}T)\,(1 - \alpha)^2\,(1 - S_{UL}T)\,(1 - S_{DL}T)\,(1 - S_{DT}T)\,K_T
\end{aligned} \tag{5.25}$$

where $f_L$ and $f_T$ are the baseline EPR frequencies in the longitudinal and transverse orientation. During the first cycle we directly measure three quantities: $M_1 = (f_1 + f_2)/2$, $M_2 = (f_3 + f_4)/2$, and $M_3 = (f_5 + f_6)/2$. We can extract $f_L = (M_1 + 2M_2 + M_3)/3$ if we expand everything to first order, since all losses are much less than a percent. We also calculate the frequency shift before and after the longitudinal cycle: $\Delta f_{BL} = f_L - M_1 = PK_L(1 - S_{DL}T/2)$, and $\Delta f_{AL} = f_L - M_2 = PK_L\,(1 - S_{DL}T)\,(1 - \alpha)^2\,(1 - S_{UL}T)\,(1 - S_{DL}T/2)$. We repeat the same procedure

for the next cycle, done in the transverse orientation. Now we calculate:

$$A_1 = \frac{\Delta f_{AL} - \Delta f_{BT}}{\Delta f_{AL} + \Delta f_{BT}} = \frac{K_L - K_T\,(1 - S_{DL}T/2)\,(1 - S_{DT}T/2)}{K_L + K_T\,(1 - S_{DL}T/2)\,(1 - S_{DT}T/2)} \tag{5.26}$$

where again we used first order expansion. Repeating the cycle one more time we can also form the ratio $A_2 = (\Delta f_{BL} - \Delta f_{AT})\,/\,(\Delta f_{AT} + \Delta f_{BL})$. Averaging the two asymmetries we get:

$$A = \frac{A_1 + A_2}{2} = \frac{K_L - K_T}{K_L + K_T}\left\{1 - \frac{K_L K_T}{(K_L + K_T)^2}\left(\frac{S_{DL} + S_{DT}}{2}T\right)^2\right\} \tag{5.27}$$

to the lowest non-trivial order in $(S_{DL} + S_{DT})$. The amount of losses due to $S_{DL}$ and $S_{DT}$ is very small, since the laser pumping prevents the decay of the polarization. The total loss during a complete cycle $S_{DL}T + S_{UL}T + 2\alpha$ is about 0.5%, most of it is due to spin-down in the up state and the AFP losses. Even if we use this number the correction to the asymmetry is only $6 \times 10^{-6}$, a negligible amount. We usually repeated the cycle 10-30 times to reduce the random measurement noise to about 0.5%. For an infinite cylinder we immediately get the value of $\kappa_0$: $\kappa_0 = 3/\,(8A) - 1/8$. For our cell the field was slightly different ($B_{He} = 4.1643M$ for longitudinal and $-2.0822M$ for transverse orientation), so $\kappa_0 = 0.3728/A - 0.1243$.

Various systematic checks were performed during the experiment. The biggest systematic uncertainty comes from the temperature of the cell. A 50W diode laser was used for optical pumping and EPR detection, and it caused a substantial heating of the cell. We used 4 RTDs mounted inside the oven to monitor the temperature. One was mounted near the air inlet and shadowed from the laser light. The second was mounted in front of the cell near its center. It was shadowed from the laser by a teflon screen and attached to the body of the cell with a heat sink compound. The third was mounted behind the cell near the center, and the forth was at the end of the oven opposite to the air inlet and shadowed from the laser. We used the temperature of the second RTD as the cell temperature. The temperatures of the other RTD's differed by less than 5°C. It is particularly important to study the asymmetry in temperature between the transverse and longitudinal orientations. Given the temperature dependence of $\kappa_0$, an asymmetry of 1°C will cause a error of about 1%. Therefore the temperature was carefully recorded during the measurement cycle. It was found that the asymmetry was less than 0.6°C. We also studied the dependence of $\kappa_0$ on the power of the diode laser while keeping the temperature constant. Reducing the power of the laser by about a factor of 2 changed the value of $\kappa_0$ by 0.5%. Another way to check for significant temperature asymmetry is to vary the measurement period $T$, reducing it to the point were the temperature asymmetry does not have enough time to develope. We changed $T$ from 3 to 100 sec and have not seen changes in $\kappa_0$ of more than 0.4%. The alignment of the cell with respect

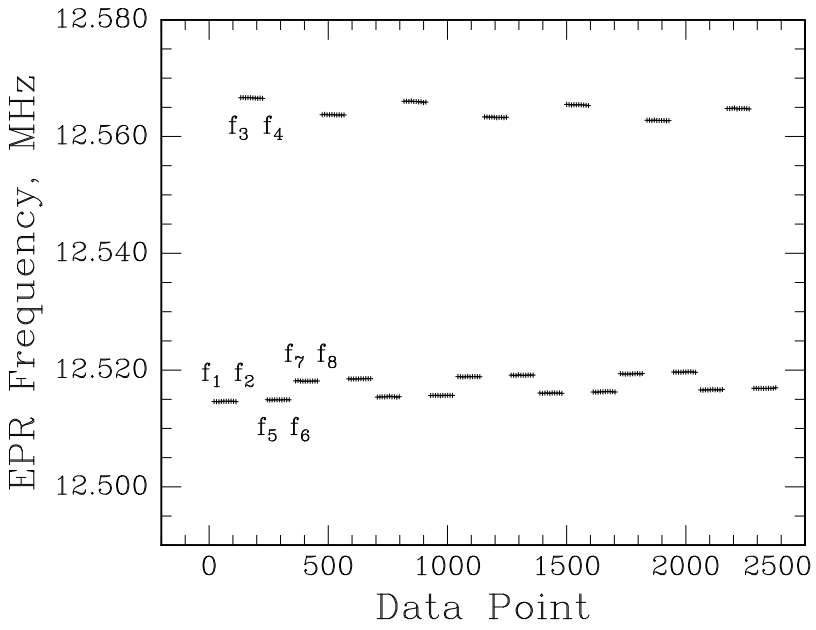


Figure 5.10: The $\kappa_0$ measurement sequence. Frequencies refer to equations in the text.

to the magnetic field was checked by mapping the frequency shift vs. angle near the transverse and longitudinal orientations. It was found that the alignment was better than 1° causing an error of less than 0.1%. The Earth magnetic field rotated the magnetization vector from the horizontal plane by 1° for the measurements done at 27 G and by 2.5° for measurements at 11 G causing an error of less than 0.3% in the worst case. To check for the possibility of a polarization gradient across the cell, several EPR measurements were done along its axis. It was found that the changes in the EPR frequency shift along the length of the cell are on the order of 0.2% and monotonic from one end of the cell to the other. So they will not cause a error in the value of $\kappa_0$. They are probably due to a temperature gradient caused by the air inlet located near one end of the cell. We also checked the dependence of $\kappa_0$ on the magnitude of the holding magnetic field, the direction of circular polarization of the laser light, the magnitude of the $^3$He polarization (from 25 to 45%), the method of mounting the RTD's. In all cases we have not seen any effect at the level of 0.4%. We also studied the temperature dependence of $\kappa_0$ by making measurements at four different temperatures, from 110°C to 170°C. We get the following result:

$$\kappa_0 = 4.52 + 0.00934\,T\ (^\circ C) \tag{5.28}$$

The errors mostly come from the absolute temperature uncertainty (0.7%) and temperature asymmetry (0.6%). The total error of this $\kappa_0$ measurement is 1%. Our results are shown in Figure 5.11, where they are compared with previous measurements. As can be seen, our numbers are in good agreement with a measurement by Barton *et al.* [20], who used a similar experimental technique, but at a lower temperature. The temperature dependence has been measured previously in [19]. Their result for $\kappa_0$ has a relatively large absolute error, so we rescale it to Barton's number. The slope was extracted from measurements in the range 40 – 80°C, so its use at high temperatures is really an extrapolation. Nevertheless, the two slopes are in very good agreement, which implies that the temperature dependence of $\kappa_0$ is quite linear over the temperature range studied.

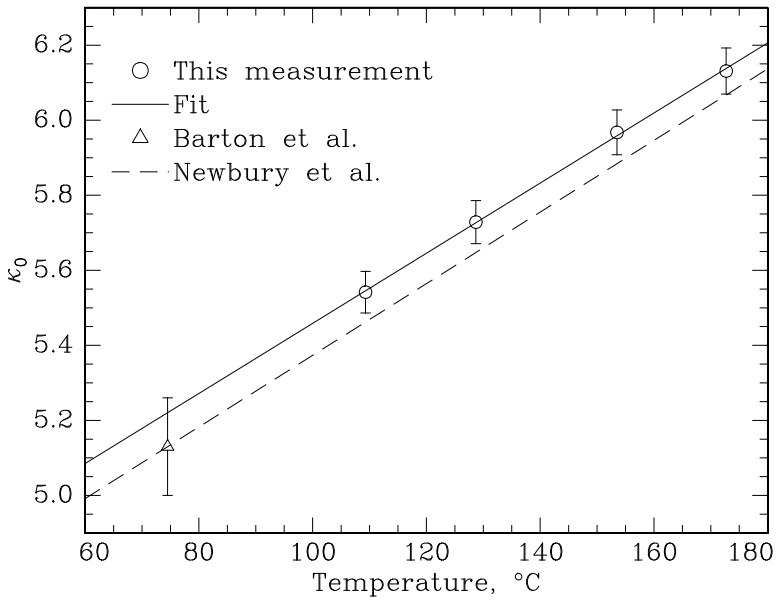


Figure 5.11: Comparison of several measurements of $\kappa_0$.

### 5.2.4 Polarization Gradient

The EPR frequency shift is a measure of the polarization in the pumping cell, while AFP measures it in the target cell. Since $^3$He is polarized in the pumping cell and diffuses down, there is a constant polarization gradient between the cells. The evolution of the polarization with time is governed by a set of differential equations that include spin exchange, spin relaxation and diffusion terms [24]. For diffusion in the

presence of a temperature gradient the flux is given by [25]:

$$G_i = -n(z)\,D(z)\left(\frac{dc_i}{dz} - \frac{k_T}{T}\frac{dT}{dz}\right), \quad i = 1,2 \tag{5.29}$$

where $c_i$ is the concentration of the $i$'s component in the mixture. Let $i = 1$ correspond to $^3$He atoms with the spin up and $i = 2$ to the atoms with the spin down. Since both types of atoms have the same mass, the thermal diffusion ratio $k_T$ vanishes [25]. We will assume that the flux is constant along the transfer tube, which neglects the volume of the transfer tube compared to the volume of the cell. We will further assume that the temperature changes linearly along the tube and that $D(T) = D(T_0)(T/T_0)^m$, where $m$ is a constant to be determined empirically. One can show that the rate of change of the polarization in the pumping and target cell due to diffusion is given by:

$$\frac{dP_T}{dt} = \frac{A_{Tr}D_T}{V_T L_{Tr}} K (P_P - P_T) \tag{5.30}$$

$$\frac{dP_P}{dt} = \frac{A_{Tr}D_T n_T}{V_P L_{Tr} n_P} K (P_T - P_P) \tag{5.31}$$

where $A_{Tr}$ and $L_{Tr}$ are the area and the length of the transfer tube, $D_T$ is the diffusion constant in the target cell and the dimensionless constant $K$ is given by:

$$K = \frac{(m-2)(T_T - T_P)T_T}{\left(\frac{T_T}{T_P}\right)^m T_P^2 - T_T^2} \tag{5.32}$$

We use the data on the diffusion constant of $^4$He and $^3$He from [26] to determine $D_T = 2.76$ cm$^2$/s at 80°C and 1 atm. and $m = 1.7$. We also use the fact that $D_T$ is inversely proportional to pressure. Combining (5.31) with the spin exchange and relaxation terms we get:

$$\frac{dP_P}{dt} = d_P (P_T - P_P) + \gamma_{SE} (P_{Rb} - P_P) - \Gamma_P P_P \tag{5.33}$$

$$\frac{dP_T}{dt} = d_T (P_P - P_T) - \Gamma_T P_T \tag{5.34}$$

where we defined the reduced diffusion constants $d_P$ and $d_T$ through equations (5.30, 5.31). $\gamma_{SE}$ is the Rb-$^3$He spin exchange rate per $^3$He atom, and $\Gamma_P$, $\Gamma_T$ are the spin relaxation rates which are allowed to be different for the two parts of the cell. The equations can be solved analytically, but it is easier to integrate them numerically on Mathematica.

We can check this model of the spin transfer by carefully studying the beginning of a spin-up when the diffusion effect is most pronounced. This was done for SMC after the run. Substituting appropriate dimensions we get for SMC $d_T = 0.95$ hrs$^{-1}$.

and $d_P = 1.56$ hrs$^{-1}$. Assuming $\Gamma_P = \Gamma_T = 1/50$ hrs. based on a spin-down, we fit the values of $\gamma_{SE}$ and $P_{Rb}$ to reproduce the long-term behavior of the spin-up data. It is also important to include the small contribution of the pumping cell to the AFP signal. We can now compare the spin-up data during the first hour with the predictions of the model. The result of the comparison is shown on Figure 5.12, and the agreement is quite satisfactory for our purposes. Now we can use this model to estimate the difference in polarization between the target and the pumping cell for Picard. Putting appropriate values for $d_T$ and $d_P$, and using $\Gamma_P = \Gamma_T = 1/70$ hrs, we reproduce the long-term spin-up data for $\gamma_{SE} = 1/9.2$ hrs. and $P_{Rb} = 73\%$. The difference between $P_P$ and $P_T$ can be approximated quite accurately by the following relationship:

$$P_P = P_T + 3.6\% - 0.0501 P_P \tag{5.35}$$

valid for $P_P > 15\%$. To estimate the error due to this correction we change various rates subject to two conditions: $P_{Rb} < 100\%$ and $\Gamma_{He} > \Gamma_D$ (equation 4.12), always adjusting the values of $\gamma_{SE}$ and $P_{Rb}$ to reproduce the observed spin-up data. In this fashion we determine that the error in the target cell polarization due to the gradient correction is 1.5%.

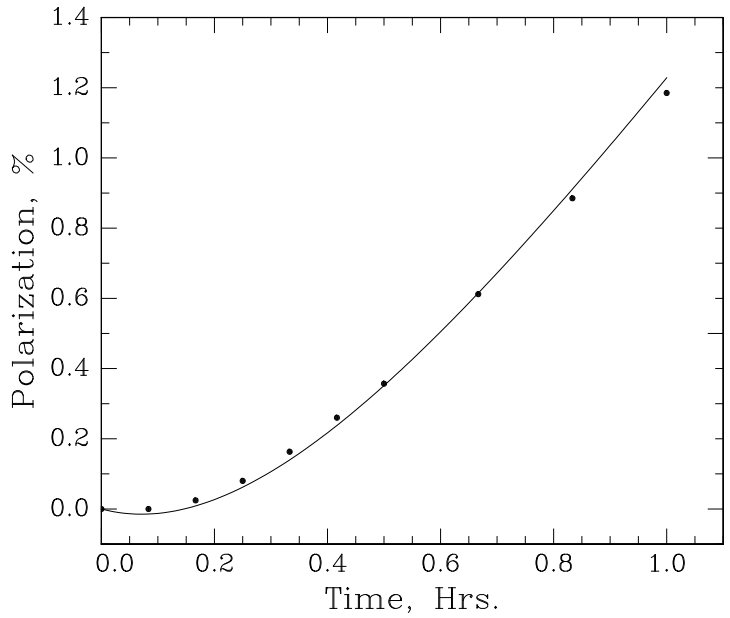


Figure 5.12: Polarization of SMC in the first hour of spin-up. The curve is a prediction of the diffusion model.

### 5.2.5 Temperature Distribution in the Pumping Cell

As described in Chapter 4 the temperature in the pumping cell is quite non-uniform. The frequency shift is proportional to $n_P \kappa_0 P_{He}$, and both $\kappa_0$ and the density depend on the temperature. Assuming that the polarization is constant in the pumping cell, we need to find the average value of $n_P \kappa_0$. Fortunately, $\kappa_0$ increases with temperature while $n_P$ decreases, so their product is not very sensitive to temperature. We will use the heat conduction model (4.34) to put a limit on the possible error from this source. Since we use the fluorescent light to detect the EPR signal, we need to calculate how much fluorescence comes from different parts of the cell. The fluorescence light is emitted with the same spectral profile as the absorbtion profile shown in Figure 4.10 [28]. The intensity of the fluorescence light propagating in the cell is attenuated according to the following equation:

$$I(x) = \frac{I_i}{\pi\Gamma} \int d\nu \sigma(\nu) e^{-\sigma(\nu) n x}, \quad \sigma(\nu) = \frac{\sigma_0 \Gamma^2}{(\nu - \nu_0)^2 + \Gamma^2} \tag{5.36}$$

where $\Gamma$ is the lorentzian half-width of the line, $n$ is the Rb number density, $I_i$ is the initial intensity of the light, and $\sigma_0 = c r_e f_2 / \Gamma$ ($f_2$ is the oscillator strength of the $D_2$ transition). Using a variable substitution $y = 2\Gamma^2 / \left((\nu - \nu_0)^2 + \Gamma^2\right)$ and a definite integral from [29], we get $I(x) = I_i e^{-\sigma_0 n x/2} I_0(\sigma_0 n x/2)$, where $I_0$ is the modified Bessel function. In the pumping cell typically $\sigma_0 n \approx 20$ cm$^{-1}$ and the Rb vapor is optically thick for unpolarized light. The function $I(x)$ drops very fast for small $x$, but for $x > 2$ mm it slows down and drops only as $1/\sqrt{x}$, as shown in Figure 5.13. So, even in optically thick vapor the fluorescence can penetrate quite far through the cell. The simple fact that we can see the laser beams in the pumping cell confirms this conclusion. For the temperature distribution we will use equation (4.34). We now weight the product of $n_P[T(r)] \kappa_0[T(r)]$ by the absorbtion function $I(x)$, where $x$ is the distance to the surface of the cell, to determine the average effective value of the product. Averaging over various paths through the cell we conclude that $\langle n_P[T(x)] \kappa_0[T(x)] \rangle$ is 0.5% higher than $\langle n_P \rangle \kappa_0[\langle T \rangle]$, where $\langle n_P \rangle$ is the average density of the pumping cell and $\langle T \rangle$ is the average temperature. In other words, by using the density and temperature from Table 4.11 we are making a error of only 0.5%. Since the temperature gradient is actually smaller than predicted by (4.34), we will not apply any correction, just assume a 0.5% error coming from this source.

### 5.2.6 The EPR Shift in the Cells

The pumping cell of the target has a cylindrical shape (see Figure 4.4). Therefore, the frequency shift has a contribution from the classical magnetic field created by $^3$He

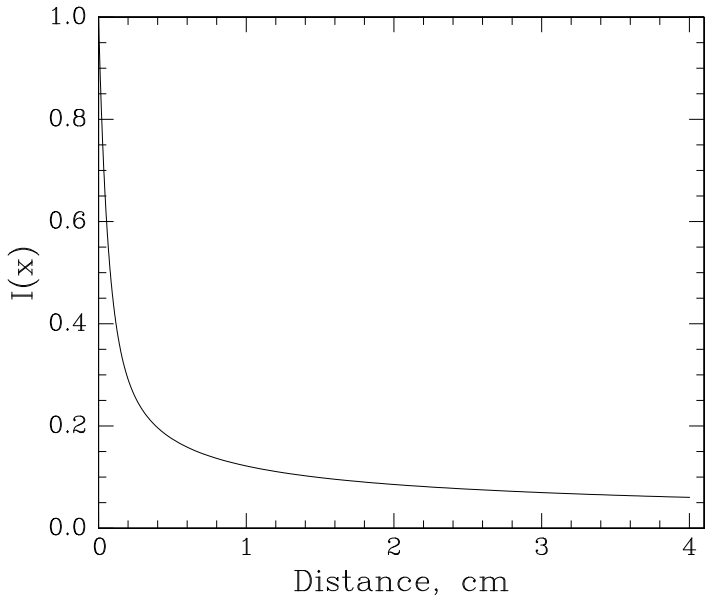


Figure 5.13: Fluorescence absorption function $I(x)$.

magnetization in addition to the shift given by equation (5.22). One can define

$$\kappa_{eff} = \kappa_0 + \frac{3}{8\pi} B_{He} \tag{5.37}$$

where $B_{He}$ is measured in units of the magnetization. The magnetic field of a uniformly magnetized pumping cell was calculated on Mathematica. It varied significantly across the cell. Therefore, we need to determine what region of the cell was sampled by the photodiode. The EPR photodiode was sensitive to a region 2 cm. in diameter in the rear portion of the cell. To evaluate the average depth that the photodiode was sampling, we used the absorbtion function (5.36). The intensity weighted average depth is 1.2 cm almost independent of temperature. The value of $B_{He}$ in the sampled region equals to $2.4 \pm 0.7$. It results in a 4.6% correction compared to a spherical cell and causes a 1.3% error.

We also need to know the values $F$ and $M$ of the state used in EPR detection to calculate $d\nu_{EPR}(F,M)/dB$. The direction of $^3$He spins was parallel to the holding field during the entire run. It means that the Rb spin was also parallel to the field and the spins were pumped into $F = 3$, $M = 3$ state. The RF frequency is tuned to $M = 3 \rightarrow 2$ transition which gives by far the strongest signal. It is separated from the next transition ($M = 2 \rightarrow 1$) by 45 kHz at 18 G while the full width of the EPR signal is only 13 kHz. (Two measurements were made at 9 G, where the separation is only 11 kHz, but the signal height of the $2 \rightarrow 1$ transition is about a

factor of 10 smaller, so it doesn't significantly affect the shape of the signal). Another way to check which transition was used for detection is to look at the absolute value of the EPR frequency. The magnetic field of the Helmholtz coils was calibrated by both $^3$He and proton NMR with an accuracy of 0.3%. Based on this calibration we can calculate the EPR frequency from equation (5.19). For the two measurements at 8.973 G and 18.324 G the results of the calculations agree with the data to 0.15%. If $M = -3$ state were pumped, the numbers would disagree by 2.6 %. Expanding equation (5.19) to second order in $\nu_{EPR}/\nu_{HF}$ we get:

$$\frac{d\nu_{EPR}(3,3)}{dB} = \frac{\mu_B g_e}{2I+1}\left(1 - 10\frac{\nu_{EPR}}{\nu_{HF}}\right) \tag{5.38}$$

Now we have all necessary numbers to convert the EPR frequency shift to $^3$He polarization.

### 5.2.7 Spin Exchange Effects

In this section we will discuss the effect of the $d^O\rho/dt$ term in equation (5.16). Although it does not depend explicitly on the $^3$He nuclear spin, it might affect the observed asymmetry indirectly through Rb-He spin exchange. The largest contribution to $d^O\rho/dt$ comes from the Rb-Rb spin exchange [15]:

$$\frac{d}{dt}\rho = \frac{1}{T_{Rb}}\left(4\alpha\left\langle\vec{S}\right\rangle - \vec{A}\right)\cdot\vec{S} + \frac{2iK_{Rb}}{T_{Rb}}\left[\left\langle\vec{S}\right\rangle\cdot\vec{S},\rho\right] \tag{5.39}$$

where $1/T_{Rb} = n_{Rb}\bar{v}\sigma_{Rb-Rb}$ is the spin exchange rate and $K_{Rb}$ is the frequency shift parameter. The real part of this expression affects the frequency shift only in the second order, i.e. $(\omega_0 T_{Rb})^{-2}$ [15]. Using $\sigma_{Rb-Rb} = 2\times10^{-14}$ cm$^2$ [30] we get at 170°C a correction on the order of $5\times10^{-5}$ or 200 Hz. The imaginary part of (5.39) contributes directly to the frequency shift. The shift parameter $K_{Rb}$ for Rb-Rb spin exchange is calculated by Kartoshkin [31]: $K_{Rb} = -0.14$. He also obtains $\sigma_{Rb-Rb} = 2.3\times10^{14}$ cm$^2$, reasonably close to the experimental result. Using his number for $K_{Rb}$, the shift due to the imaginary part is at most 3.7 kHz or 0.1% of the absolute frequency (assuming $\left\langle\vec{S}\right\rangle = 1/2$). The shift will affect the EPR measurements only if it changes when the $^3$He spins are flipped. This could happen due to the Rb-He spin exchange causing a change in the average value of the Rb polarization. To calculate how much the Rb polarization changes due to $^3$He spin flips we used a model of optical pumping based on the following equations:

$$P_{Rb}(z) = \frac{R_p(z) + \Gamma_{SE}P_{He}}{R_p(z) + \Gamma_{SD} + \Gamma_{SE}} \tag{5.40}$$

$$R_p(z) = \int \Phi(\nu, z)\,\sigma(\nu)\,d\nu \tag{5.41}$$

$$\frac{\partial \Phi(\nu, z)}{\partial z} = -n_{Rb}\sigma(\nu)\,\Phi(\nu, z)\,(1 - P_{Rb}(z)) \tag{5.42}$$

where $\Phi(\nu)$ is the laser photon flux per unit frequency, and $\Gamma_{SE} = n_{He}\bar{v}\sigma_{Rb-He}$. The numbers for the spin exchange cross-section were taken from [33, 34], for spin destruction rates from [32]. For the initial spectral distribution $\Phi(\nu, 0)$ we used a combination of two gaussians representing the diode and Ti-S laser profiles. $\sigma(\nu)$ was taken from pressure broadening measurements. We estimate that $R_p = 10^5$ s$^{-1}$, $\Gamma_{SE} = 24$ s$^{-1}$, and $\Gamma_{SD} = 734$ s$^{-1}$. Since $R_p \gg \Gamma_{SE}$, the effect of the $^3$He polarization reversal is not very large. However, it can affect the frequency shift in several ways, and we need to investigate it in more detail numerically.

A C program was used to solve the above set of integral-differential equations [35]. Since the spin exchange and destruction rates from different sources disagree by as much as a factor of 2, and other parameters (laser power, Rb number density, etc.) are also not very certain, we ran the model for many different combinations of parameters, considering a total of 1600 cases. Based on the results of the model the largest variation of the Rb polarization due to a $^3$He spin flip is 0.5%. From the form of equation (5.39) it can be seen that the false frequency shift is proportional to the Rb polarization [16]. Therefore, the EPR frequency asymmetry due to Rb-Rb spin exchange is at most 20 Hz or 0.1% of the frequency shift.

The other contribution to $d^O\rho/dt$ comes from the light shift [37]:

$$\frac{d}{dt}\rho = (-2\pi i\Delta\nu_{LS} - \gamma_{LS})\,\rho \tag{5.43}$$

where $\gamma_{LS}$ and $\Delta\nu_{LS}$ are the real and imaginary shift parameters proportional to the intensity of the light. Recent calculations and measurements at Princeton under similar conditions [36] showed that the light shift is about 1 kHz and has a dispersive pattern as a function of frequency (i.e. equals to zero when the laser is tuned exactly on resonance and reaches a maximum when it is detuned by about 2 nm). Since the light shift is proportional to the intensity of the light, it depends on $^3$He polarization through equation (5.42). The variations of intensity due to $^3$He flips are less than 1% based on the pumping model, so the asymmetry from this source is small.

The other possible source of the asymmetry comes from the changes in the laser intensity profile coupled to the magnetic field gradient. The EPR signal is approximately proportional to the difference in the intensity of the fluorescence with the resonant RF field turned on and off. The intensity of the fluorescence is proportional to the number of pumping photons absorbed per unit length as given by equation (5.42). To model the effect of the RF field we introduce an additional relaxation rate in equation (5.40). It can be seen from equation (5.42) that when the RF field is turned on, the amount of fluorescence coming from the front of the cell will increase, because $(1 - P_{Rb})$ will be larger. In the back of the cell the amount of the fluorescence

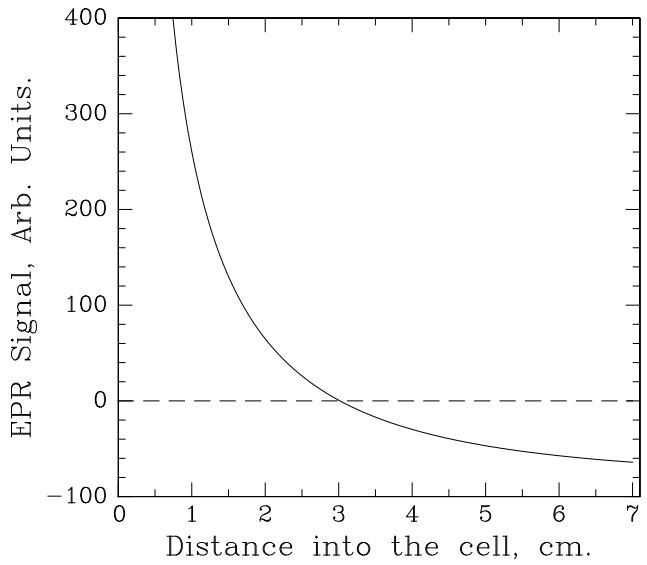


Figure 5.14: EPR signal vs. position in the cell according to the pumping model.

will become smaller because less light will penetrate through the cell. The dependence of the EPR signal on the position is shown on Figure 5.14, as calculated using the pumping model. The EPR signal can actually change sign in the middle of the cell. This effect was detected experimentally by observing the phase of the lock-in output. The phase of the signal coming from the front of the cell was opposite to the phase from the back of the cell. The exact position of the zero crossing is very sensitive to all parameters of the model. During initial setup it was determined that the best position for the photodiode was in the back of the cell, where the phase of the EPR signal was negative. However, the laser power was increased later and that moved the zero crossing further into the cell into the sampling region of the photodiode. As a result, the EPR signal taken at 170°C has a tail (see Figure 5.15) coming from the region of the cell with the opposite phase. This could potentially cause a big error, especially if the zero crossing is exactly in the center of the sampling region, making the EPR signal purely dispersive. Fortunately, we took data under several different conditions, varying the temperature and laser power (see Table 5.6). Based on the results of the pumping model for all 1600 possible variations of the parameters, we conclude that if for one of those conditions (i.e. combination of temperature and laser power) the zero crossing was in the sampling region, it could not have been in the sampling region for all other conditions. We can also estimate possible error in the case when the zero crossing is inside the sampling region by modelling the effect of the field gradient. We analyze the EPR signal shown in Figure 5.15, assuming a

Lorentzian line shape:

$$S(\nu) = \int_{z_1}^{z_2} \frac{h(z)\, w^2}{\left(w^2 + (\nu - \nu_0(z))^2\right)} dz \tag{5.44}$$

where $h(z) = h_0(z - z_0)$ is the height of the EPR signal vs. position with a zero crossing at $z_0$, and $\nu_0(z) = \nu_0 + (dB/dz)(d\nu/dB)\, z$ is the EPR frequency vs. position assuming a uniform gradient. $z_1$ and $z_2$ are the boundaries of the sampling region. Using this function to fit the data we get a gradient of 10 mG/cm, reasonable close to 3.6 mG/cm estimated from the AFP data. The width of the EPR signal can be calculated from the spin exchange cross-section by the following equation [15]:

$$w = \frac{2I(2I-1)}{6\pi(2I+1)^2 T_{Rb}} \tag{5.45}$$

Using the Rb-Rb spin exchange cross-section $\sigma_{Rb-Rb} = 2 \times 10^{-14}$ cm$^2$ [30] and $n_{Rb} = 2.73 \times 10^{14}$ cm$^{-3}$ at 170°C we get $w = 5.3$ kHz, while the fit gives 4.9 kHz, in surprisingly good agreement. Now we can calculate how much the position of the EPR peak changes when the $^3$He spins are reversed. Based on the pumping model the position of the zero crossing changes by no more than 1 mm. This causes a shift of the peak frequency by about 200 Hz or 0.5% of the total frequency shift. So, even if the EPR zero crossing is inside the sampling region, the false asymmetry is not too great.

Another possible correction we need to consider is the contribution to the frequency shift from the Van der Waals molecules. While equation (5.16) describes the frequency shift from the binary collisions, the Van der Waals molecules should be considered separately. In [18] a constant $\kappa_1$ is introduced to describe their contribution. The van der Waals molecules easily form for heavy noble gases, like Xe and Kr. They become less and less bound for lighter noble gases. Although there is no experimental evidence for $^3$HeRb Van der Waals molecules, their contribution was calculated based on interatomic potentials, giving [18]: $\kappa_1/\kappa_0 = 8 \times 10^{-6}$. Another way to put a limit on the contribution of the Van der Waals molecules is to use their very short lifetime at high pressure. We can use an expansion given in [37] for the frequency shift in the short lifetime limit:

$$\Delta\nu_{EPR} = \frac{\alpha\tau\langle K_z\rangle}{hT_w(2I+1)} + O\left(\frac{\alpha\tau}{\hbar}\right)^2 \tag{5.46}$$

where $\alpha = 8\pi g_e \mu_B \mu_{He} n_{He}/3K$, which is valid if the following conditions are satisfied: $\gamma N\tau/\hbar \ll 1$, $\alpha\tau/\hbar \ll 1$, and $\mu_B B\tau/\hbar \ll 1$, where $N\gamma$ is the strength of the spin-rotation interaction. To put an experimental limit on the contribution of the Van der Waals molecules we will use the lightest gas for which the data are available: Argon

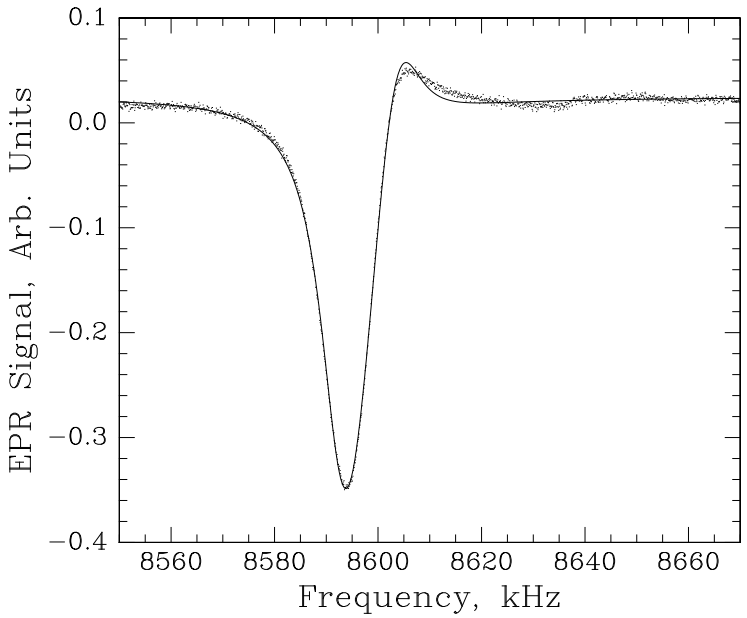


Figure 5.15: EPR signal detected with AM modulation of the RF field. The fit is based on the model described in the text.

[38]. The lifetime of the molecules is inversely proportional to pressure and at our pressures is $\tau = 8 \times 10^{-12}$ sec. $\langle \gamma N \rangle / \hbar = 2.1 \times 10^7$ sec from [39], so the first condition is satisfied. $\mu_B B \tau / \hbar = 1.0 \times 10^{-3}$, and $\alpha \tau / \hbar = 2.5 \times 10^{-6}$, so the other conditions are also satisfied and the second order term of the expansion, that would be non-linear in $\langle K_z \rangle$, is negligible.

### 5.2.8 EPR Results

Most EPR measurements were performed after the run on Picard. They were done under a variety of conditions (i.e. different laser power, temperature, magnetic field, polarization). Each measurement was preceded and followed by an AFP measurement. Since we did not make EPR measurements throughout the run, we can only use them as a calibration of the AFP system.

The $^3$He polarization can be found from the frequency shift by the following formula:

$$P_{He} = \frac{3}{8\pi} \frac{(2I+1)}{\mu_B \mu_{He} g_e \left[1 - 4I \left(\nu_{EPR}/\nu_{HF}\right)\right] \kappa_{eff} n_0 \left(n_P/n_0\right)} \Delta\nu_{EPR} - \Delta P_{PT} \qquad (5.47)$$

where $\kappa_{eff}$ is given by equation (5.37) and $\Delta P_{PT} = P_P - P_T$ is calculated from equation (5.35).

The list the EPR measurements done after the run on the cell Picard is shown in Table 5.6, along with the results of AFP measurements done at the same time. The ratio of the polarization measurements is presented graphically in Figure 5.16.

| # | $T_P$, °C | Laser Power | $\nu_{EPR}$ MHz | $\Delta\nu_{EPR}$ kHz | $\kappa_{eff}$ | $n_P/n_0$ | $\Delta P_{PT}$ % | $P_{EPR}$ | $P_{AFP}$ % | $\frac{P_{EPR}}{P_{AFP}}$ |
|---|---|---|---|---|---|---|---|---|---|---|
| 1 | 180 | Full | 4.159 | 18.98 | 6.49 | 0.833 | 1.8 | 33.7 | 36.3 | 0.928 |
| 2 | 180 | Full | 4.148 | 23.32 | 6.49 | 0.836 | 1.4 | 42.1 | 44.5 | 0.946 |
| 3 | 180 | Full | 8.445 | 22.46 | 6.49 | 0.836 | 1.5 | 41.0 | 42.7 | 0.960 |
| 4 | 170 | 1 LDA | 8.453 | 21.80 | 6.39 | 0.849 | 1.5 | 39.8 | 42.7 | 0.932 |
| 5 | 180 | Full | 8.444 | 21.74 | 6.49 | 0.837 | 1.5 | 39.6 | 41.7 | 0.950 |
| 6 | 160 | Full | 8.447 | 21.80 | 6.30 | 0.862 | 1.5 | 39.7 | 41.0 | 0.968 |
| 7 | 200 | Full | 8.472 | 22.71 | 6.67 | 0.818 | 1.5 | 41.3 | 45.2 | 0.914 |
| 8 | 180 | Full | 8.463 | 23.10 | 6.49 | 0.841 | 1.4 | 42.1 | 44.3 | 0.950 |
| 9 | 180 | Full | 8.603 | 15.35 | 6.49 | 0.836 | 2.1 | 26.9 | 28.8 | 0.934 |

Table 5.6: EPR Measurements.

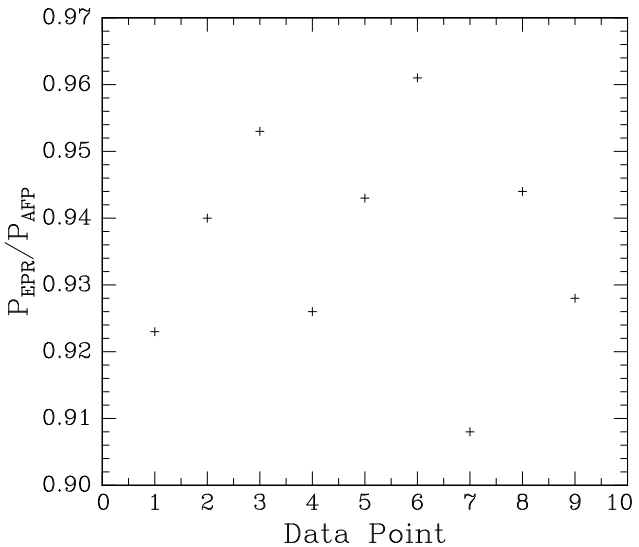


Figure 5.16: Comparison of the polarization measurements under different conditions.

The ratio of the polarization measurements is relatively stable for different operating conditions. There is one data point, however, whose quality is questionable. The measurement #7 was performed at 200°C (the temperature was raised up about 30 min. before the measurement). The Rb-He spin exchange rate in the pumping cell

was about 3.8 hrs. So, if the average Rb polarization dropped by, say, 20% because the lasers did not have enough power to polarize the Rb vapor at this temperature, the polarization in the pumping cell would drop by 2-3% in the time before the measurement. The polarization in the target cell did not follow since the diffusion time constant is about 0.7 hrs. This would explain a lower value of the polarization from the EPR method which measures $P$ in the pumping cell. Therefore, one might argue that this number should be disregarded. The average of all 9 measurements gives $P_{EPR}/P_{AFP} = 0.942 \pm 0.016$. If we drop point #7 we get $P_{EPR}/P_{AFP} = 0.946 \pm 0.013$. We will use the second number. The corrections due to the magnetic field shift and the polarization gradient can change within their error bars depending on the temperature and laser power. The variations seen in the data are less than the combined error due to the polarization gradient (1.5%), the magnetic field shift (1.3%) and various false asymmetries (0.7%).

The errors of the EPR measurements mostly come from $\kappa_0$ (1.0%), the polarization gradient (1.5%), magnetic field shift (1.3%), and the gas density (1.5%). Note that the error in gas density in the pumping cell is smaller than might be expected because the error in $n_P/n_0$ due to the temperature uncertainty is anticorrelated with the error in $\kappa_0$. We will also include the standard deviation of the data as an additional error (rather then divide it by the number of measurements) because it could be due to an effect other then those described above. So, the total error is 3.0%.

## 5.3 Comparison of Two Methods of Polarimetry

The results of the two polarimetry methods together with their error bars are shown in Figure 5.17 normalized to the calibration constant used for a preliminary result.

If we treat the errors as statistical the disagreement between the two polarimetry methods is $1.2\sigma$. The probability of this or bigger disagreement is 23%. Since our total error comes from many different sources, each on the order of 1-1.5%, the statistical approximation is quite good. Consider the following simple model. Suppose that the total error comes from ten independent sources each with a magnitude of 1.4% (this gives a total error of 4.4%, similar to our combined error of the two measurements). Assume that each source of the error will cause the final number to move by exactly 1.4% in either direction with equal probability. Assume that these changes are uncorrelated (since the errors come from totally different effects). We end up with the well-known binary distribution (e.g. coin toss). The resulting probability distribution of the final result together with a gaussian fit is shown in Figure 5.18. The statistical approximation is, in fact, quite reasonably. Since the results are not in disagreement, and there is no clear preference for either method (as quantified by their nearly identical error bars), we will average the two results. However, since the errors are mostly systematic and have some degree of arbitrariness, we will not use a

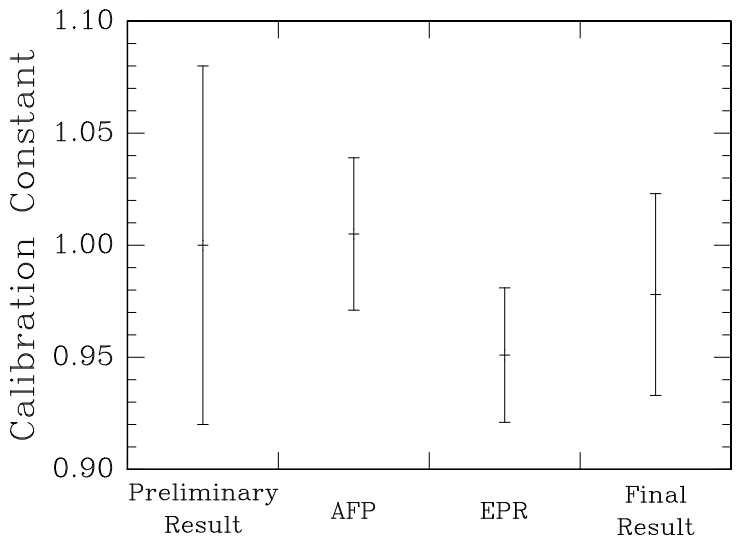


Figure 5.17: Polarization Calibration Constant (normalized to the Preliminary Result).

weighted average.

Estimating the error of the final result is more complicated. Naively, one should reduce it when averaging, which would give a error of 2.2%. This, however, disregards the possibility of an unidentified systematic error that could affect either of the methods. Therefore, when combining the two methods we will increase (rather then decrease) the total error. Different arguments could be used to estimate the size of the systematic error. One of the most conservative assumes that the entire difference comes from an unknown systematic effect in one of the methods. We want to include the possibility that the true answer is given by only one of the methods, the other being affected by a systematic error of unknown origin. Even if we reduced all known systematic errors to zero, the two numbers are not guaranteed to converge. In this case the probability distribution of the true calibration constant is a sum of the probability distributions of each method, as shown in Figure 5.19. The shape of the sum distribution is reasonably close to a gaussian. Therefore, we can parametrize the final error by the width of a gaussian which resembles the sum distribution. In this way we can identify the error with the width of the gaussian and it will have the most straight forward interpretation. Using a fit with a constraint on the total area, we obtain a gaussian with a width of 4.5%. This is the polarimetry error at the end of the run. We should add to this the error due to the drift of the coil sensitivity over the length of the run. Using the whole size of the drift, equal to 1.7%, as a error, we get the final polarization error of 4.8%. The final values of the calibration constants

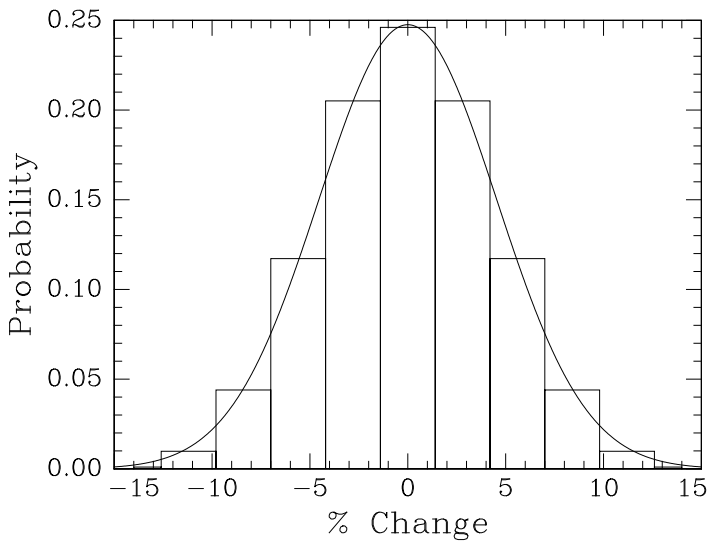


Figure 5.18: Simulation of the probability distribution based on 10 errors 1.4% each.

are shown in Table 5.7.

| Dave | Riker | Bob | SMC | Generals | Hermes | Prelims | Chance | Picard |
|---|---|---|---|---|---|---|---|---|
| 0.1552 | 0.1406 | 0.1560 | 0.1567 | 0.1436 | 0.1611 | 0.1456 | 0.1431 | 0.1313 |

Table 5.7: Final AFP Calibration Constants (%/mV)

## 5.4 Polarization Direction

The direction of the $^3$He polarization corresponding to an AFP signal of a particular sign was determined by a two step process. First, we determined the orientation of the polarization with respect to the magnetic field and then the orientation of the magnetic field relative to the electron beam. In each case we used several methods. To avoid masing during AFP $^3$He spins were always stored in high energy state. The direction of the polarization was reversed by rotating the holding field by 180°. This also resulted in the reversal of the AFP signal sign. Both the sign of the magnetic field and the sign of the AFP signal were recorded to tape. In the following discussion we will consider the positive polarization state.

We note that the AFP signal is positive for both $^3$He and water when the field is swept up through the resonance. On the way down the signals have opposite signs, but this is due to the fact that proton spins relax between the sweeps, while He spins do

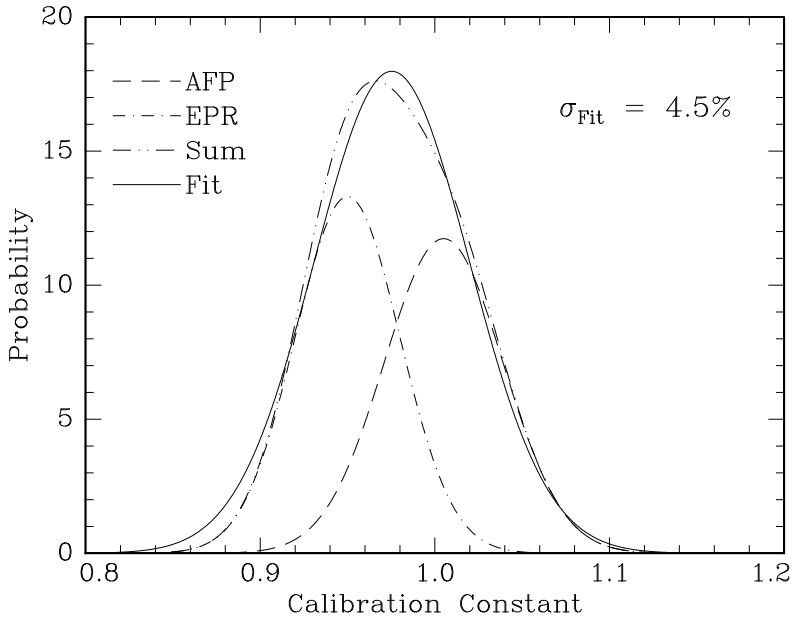


Figure 5.19: Probability distribution for the calibration constant compared with a gaussian.

not. The proton spins are polarized according to the Boltzman distribution, therefore they have to be in the low energy state. Since $\mathcal{H} = -\vec{M} \cdot \vec{B}$, the magnetization $M_p$ is parallel to $B$. The sign of the AFP signal depends on the sense of the magnetization precession, which is given by the Bloch equations [5]:

$$\frac{d\vec{M}}{dt} = \gamma \vec{M} \times \vec{H} \tag{5.48}$$

where $\gamma = \mu/\hbar$. Since protons have a positive magnetic moment and $^3$He has a negative moment we conclude that the magnetization of $^3$He is opposite to $B$. Finally, using $M_{He} = \mu_{He} K$, we determine that the $^3$He spin is parallel to $B$.

We note that the sign of the EPR shift is negative (see Figure 5.8). Since $\kappa_0$ is positive this implies that the magnetic field created by polarized $^3$He inside the cell is opposite to $B$. Again, we conclude that $M_{He}$ is opposite to $B$ and $K$ is parallel to $B$.

One can also determine the direction by looking for the occurrence of the masing effect. As was described in Chapter 4, masing can occur only if the spins are in the high energy state. If we believe that the polarization problems in SMC and Generals were due to masing, we conclude that the spins were stored in the high energy state. However, we can come to the same conclusion by noticing that no

masing was observed during AFP (where it would manifest itself as a large difference in the AFP signals for the up and down sweeps). For AFP we sweep the magnetic field up to 36 G, so the Larmor frequency of the spins passes through the pick-up coil resonance at 101 kHz. Since the coupling of the pick-up coils to the spin is much stronger on resonance (by a factor of 3500 compared with a holding field of 20G), one would expect that masing is very likely to occur there. To avoid this problem, the RF frequency is set below the coil resonance (in our case to 92 kHz) and the spins are stored in the high energy state. In this way, the direction of the polarization is reversed by AFP before the sweep reaches 101 kHz, and the spins pass through the coil resonance in the low energy state. If the spins are ever stored in the low energy state, they will end-up in the high state while passing through the resonance and lose their polarization due to masing. This effect was observed several times during the setup stages of the experiment. It was the reason that we reversed the polarization by a rather complicated field rotation, instead of a simple AFP. So, $^3$He is stored in the high energy state, which implies that its magnetic moment is opposite to the holding field, in agreement with the other two methods.

The direction of the magnetic field was also measured in several ways. It was determined using a compass, whose North direction shows the direction of the magnetic field. We also used a Flux-gate magnetometer and a Hall probe to measure the sign of the field. The Hall probe was calibrated against the spectrometer magnets. Finally, the direction of the field was determined from the direction of the coil winding and the electric current. All methods indicate that the field was pointing opposite to the direction of the electron beam. So, the $^3$He (and neutron) spin was pointing opposite to the electron momentum when the AFP signal was positive. The direction of the electron polarization was determined from the sign of the Møller asymmetry [40] as well as the direction of the circular polarization at the source. We could also determine the direction $^3$He polarization from the circular polarization of the optical pumping light. However, this method relies on the manufacturer's specification of the polarization direction for a circular analyzer (for example, a liquid crystal polarizer). Although this method agrees with the other, it cannot be trusted because there are two conflicting definitions of circular polarization in the optics manufacturing trade.

# Bibliography


[1] M.V. Romalis and T.B. Smith, E-154 Technical Note # 47, (1996).

[2] M.V. Romalis *et al.*, Proc. of 7th RCNP Workshop on Polarized $^3$He Beams and Gas Targets and their Applications, Japan, 1997.

[3] F. Bloch, A. Siegert, Phys. Rev. **57**, 522 (1940).

[4] G. D. Cates, D. J. White, T. R. Chien, S.R. Schaefer, W. Happer, Phys. Rev. A **38**, 5092 (1988).

[5] A. Abragam, *Principles of Nuclear Magnetizm*, (Oxford University Press 1961).

[6] S. Meiboom, Z. Luz, D. Gill, J. Chem. Phys. **27**, 1411 (1957).

[7] S. Meiboom, J. Chem. Phys. **34**, 375 (1961).

[8] R.E. Glick, K.C. Tewari, J. Chem. Phys. **44**, 546 (1966).

[9] J.H. Simpson, H.Y. Carr, Phys. Rev. **111**, 1201 (1956).

[10] G. Chiarotti, G. Cristiani, L. Giulotto, Nuovo Cimento **1**, 863 (1955).

[11] R. Hauser, G. Laukien, Z. Physik **153**, 394 (1959).

[12] B. Saam, PhD. thesis, Princeton University (1995).

[13] S. Meiboom, D. Gill, Rev. Scien. Instr. **29**, 688 (1958).

[14] J.K. Johnson (private communication).

[15] W. Happer, A.C. Tam, Phys. Rev. A **16**, 1877 (1977).

[16] L.C. Balling, R.J. Hanson, F.M. Pipkin, Phys. Rev. **133**, A607 (1964).

[17] G.K. Woodgate, *Elementary Atomic Structure*, (Oxford University Press, Oxford, 1989).

[18] S.R. Schaefer, G.D. Cates, T.R. Chien, D. Gonatas, W. Happer, T.G. Walker, Phys. Rev. A **39**, 5613 (1989).

[19] N.R. Newbury, A.S. Barton, P. Bogorad, G.D. Cates, M Gatzke, H. Mabuchi, B. Saam, Phys. Rev. A **48**, 558 (1993).

[20] A.S. Barton, N.R. Newbury, G.D. Cates, B. Driehuys, H. Middleton, B. Saam, Phys. Rev. A **49**, 2766 (1994).

[21] M.V. Romalis, Generals Project, Princeton University (1994).

[22] Bartington Instruments Ltd, Charlbury, Oxford OX7 3PQ, England, Tel. +44 608 810657.

[23] W. Farr, E.W. Otten, Appl. Phys. **3**, 367 (1974).

[24] T.E. Chupp, R.A. Loveman, A.K. Thompson, A.M. Bernstein, D.R. Tieger, Phys. Rev. C. **45**, 915 (1992).

[25] J.O. Hirschfelder, C.F. Curtiss, R.B. Bird, *Molecular Theory of Gases and Liquids*, (John Wiley 1954).

[26] J. Kestin, K. Knierim, E.A. Mason, B. Najafi, S. T. Ro, M. Waldman, J. Phys. Chem. Ref. Data **13**, 229 (1984).

[27] N.R. Newbury, A.S. Barton, G.D. Cates, W. Haper, H. Middleton, Phys. Rev. A **48**, 4411 (1993).

[28] Alan Corney, *Atomic and Laser Spectroscopy*, (Oxford Unversity Press 1977).

[29] I.S. Gradshteyn, I.M. Ryzhik, *Table of Integrals, Series, and Products*, (Academic Press 1980).

[30] J. Vanier, C. Audoin, *Quantum Physics of Atomic Frequency Standards*, (Bristol 1989).

[31] V.A. Kartoshkin, Opt. Spectr. **79**, 22 (1995).

[32] M.E. Wagshul, T.E. Chupp, Phys. Rev. A **49**, 3854, (1994)

[33] K.P. Coulter, PhD. thesis, Princeton University (1989).

[34] B. Larson, O. Häusser, P.P.J. Delheij, D.M. Whittal, D. Thiessen, Phys. Rev. A **44**, 3108 (1991).

[35] D. Walter, B. Driehuys (private communication).

[36] W.Happer, S. Appelt (private communication).

[37] W. Happer, E. Miron, S. Schaefer, D. Schreiber, W.A. van Wijngaarden, X. Zeng, Phys. Rev. A **29**, 3092 (1984).

[38] M. A. Bouchiat, J. Brossel, L.C. Pottier, J. Chem. Phys. **56**, 3703 (1972).

[39] M. A. Bouchiat, J. Brossel, P. Mora, L.Pottier, J. Phys. (Paris) 36, 1075 (1975).

[40] G. Mitchell, E-154 Collaboration meeting, June 1996.

# Chapter 6

# Results and QCD Analysis

## 6.1 Traditional Analysis

Our results for the neutron spin structure function $g_1^n$ and the virtual photon asymmetry $A_1^n$ are shown in Table 6.1 with their statistical and systematic errors. The systematic errors are comparable to the statistical errors in the lowest two $x$ bins (due to contamination by charge symmetric background) and are smaller at higher $x$. Before these data can be used for comparison with other experiments or tests of the sum rules, we need to calculate $g_1$ at a common $Q^2$. The raw data are in the range 1 GeV$^2$ $< Q^2 <$ 15 GeV$^2$ and the statistics weighted average $Q^2$ is about 5 GeV$^2$. This number is close to the average $Q^2$ of the SMC deuteron measurement and has been used in previous analyses of the spin structure functions [1]. Therefore, we evolve our data to 5 GeV.

Following traditional methods [1, 2], we assume that $A_1$ is independent of $Q^2$, and use the measured $Q^2$ dependence of the unpolarized structure function $F_1$ [3] to calculate $g_1$ at constant $Q^2$:

$$g_1\left(x, 5\,GeV^2\right) = g_1\left(x, Q^2\right)\frac{F_1\left(x, 5\,GeV^2\right)}{F_1\left(x, Q^2\right)} \tag{6.1}$$

As will be described in Section 6.3, a more sophisticated $Q^2$ evolution based on NLO QCD analysis does not significantly modify the results. Equation (6.1) is also consistent with our measured $Q^2$ dependence between the two spectrometers, however, this is not a very stringent test because of the small lever arm in $Q^2$.

Our results for $g_1^n(x)$ at $Q^2 = 5$ GeV$^2$ [4] are shown in Figures 6.1 and 6.2, where they are compared with previous SLAC and CERN results respectively, and the numbers are given in Table 6.2. Several observations can be made. The results of our experiment are in good agreement with all previously available data. This includes experiments done at SLAC with polarized gaseous $^3$He [2] and solid H/D targets [5],

| $\langle x \rangle$ | $\langle Q^2 \rangle$ (GeV$^2$) | $g_1^n \pm stat. \pm syst.$ | $A_1^n \pm stat. \pm syst.$ |
|---|---|---|---|
| 2.75° spectrometer | | | |
| 0.017 | 1.21 | $-0.351 \pm 0.115 \pm 0.104$ | $-0.058 \pm 0.019 \pm 0.017$ |
| 0.024 | 1.59 | $-0.374 \pm 0.071 \pm 0.062$ | $-0.080 \pm 0.015 \pm 0.014$ |
| 0.035 | 2.05 | $-0.290 \pm 0.061 \pm 0.037$ | $-0.078 \pm 0.018 \pm 0.011$ |
| 0.049 | 2.57 | $-0.212 \pm 0.041 \pm 0.021$ | $-0.089 \pm 0.016 \pm 0.010$ |
| 0.078 | 3.32 | $-0.119 \pm 0.031 \pm 0.013$ | $-0.078 \pm 0.019 \pm 0.009$ |
| 0.123 | 4.09 | $-0.075 \pm 0.030 \pm 0.009$ | $-0.089 \pm 0.031 \pm 0.011$ |
| 0.173 | 4.63 | $-0.070 \pm 0.033 \pm 0.009$ | $-0.100 \pm 0.053 \pm 0.014$ |
| 0.241 | 5.09 | $-0.053 \pm 0.028 \pm 0.007$ | $-0.078 \pm 0.077 \pm 0.018$ |
| 0.340 | 5.51 | $0.001 \pm 0.036 \pm 0.004$ | $-0.166 \pm 0.206 \pm 0.051$ |
| 0.423 | 5.82 | $0.027 \pm 0.059 \pm 0.007$ | $0.166 \pm 0.606 \pm 0.038$ |
| 5.5° spectrometer | | | |
| 0.057 | 4.03 | $0.224 \pm 0.285 \pm 0.035$ | $0.045 \pm 0.120 \pm 0.012$ |
| 0.084 | 5.47 | $-0.152 \pm 0.029 \pm 0.019$ | $-0.104 \pm 0.018 \pm 0.013$ |
| 0.123 | 7.23 | $-0.117 \pm 0.017 \pm 0.012$ | $-0.110 \pm 0.015 \pm 0.012$ |
| 0.172 | 8.94 | $-0.059 \pm 0.016 \pm 0.007$ | $-0.090 \pm 0.023 \pm 0.011$ |
| 0.242 | 10.71 | $-0.040 \pm 0.012 \pm 0.005$ | $-0.118 \pm 0.030 \pm 0.016$ |
| 0.342 | 12.55 | $-0.019 \pm 0.012 \pm 0.005$ | $-0.057 \pm 0.068 \pm 0.022$ |
| 0.442 | 13.83 | $-0.009 \pm 0.012 \pm 0.002$ | $-0.013 \pm 0.146 \pm 0.018$ |
| 0.564 | 15.00 | $0.003 \pm 0.008 \pm 0.001$ | $0.100 \pm 0.294 \pm 0.032$ |

Table 6.1: Results for the neutron spin structure function $g_1^n$ and the virtual photon asymmetry $A_1^n$

experiments at CERN using solid H/D targets [6], and at DESY with a polarized $^3$He internal target [9]. The experiments are also done under widely different kinematic conditions, with different sources of systematic errors, etc. Thus, the experimental measurements of the spin structure functions are quite reliable. In fact, history shows that all of polarized deep inelastic scattering experiments are in agreement with each other and have not suffered from unaccounted errors.

Second, our statistical errors are smaller by a factor of 3 or more than in any of the previous experiments. Our systematic errors are comparable to our statistical errors at low $x$ and are much smaller at higher $x$. The experiment also extends the precision measurements to lower $x$ than previous SLAC experiments. As we will see, this is critical for the extrapolation to low $x$ and the measurement of $\Gamma_1^n$. Although our data do not extend as far down in $x$ as the results of SMC, most fits of the low $x$ behavior of the spin structure function starting at $x = 0.1$ are dominated by our data because of higher statistical precision.

Third, our low $x$ data do not show any evidence for the onset of Regge behavior

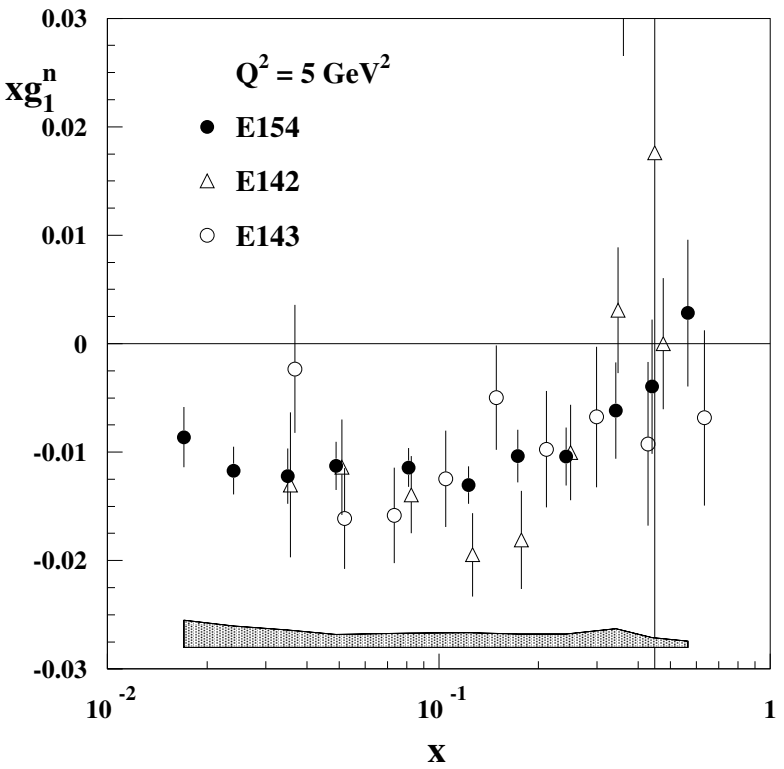


Figure 6.1: Our results for $g_1^n(x)$ compared with previous SLAC data. $xg_1$ is ploted on the vertical scale for better display.

| $x$ bin | $\langle x \rangle$ | $\langle Q^2 \rangle$ $GeV^2$ | $g_1^n \pm stat. \pm syst.$ $(Q^2 = 5\ GeV^2)$ |
|---|---|---|---|
| $0.014 - 0.02$ | 0.017 | 1.2 | $-0.497 \pm 0.163 \pm 0.148$ |
| $0.02 - 0.03$ | 0.024 | 1.6 | $-0.481 \pm 0.092 \pm 0.081$ |
| $0.03 - 0.04$ | 0.035 | 2.0 | $-0.345 \pm 0.073 \pm 0.046$ |
| $0.04 - 0.06$ | 0.049 | 2.6 | $-0.228 \pm 0.045 \pm 0.024$ |
| $0.06 - 0.10$ | 0.081 | 4.4 | $-0.139 \pm 0.022 \pm 0.016$ |
| $0.10 - 0.15$ | 0.123 | 6.6 | $-0.105 \pm 0.014 \pm 0.011$ |
| $0.15 - 0.20$ | 0.173 | 8.2 | $-0.060 \pm 0.014 \pm 0.007$ |
| $0.20 - 0.30$ | 0.242 | 9.8 | $-0.043 \pm 0.011 \pm 0.005$ |
| $0.30 - 0.40$ | 0.342 | 11.7 | $-0.018 \pm 0.013 \pm 0.005$ |
| $0.40 - 0.50$ | 0.441 | 13.3 | $-0.009 \pm 0.014 \pm 0.002$ |
| $0.50 - 0.70$ | 0.564 | 15.0 | $0.005 \pm 0.012 \pm 0.001$ |

Table 6.2: The results of our experiment for $g_1^n$ at $\langle Q^2 \rangle = 5$ GeV$^2$.

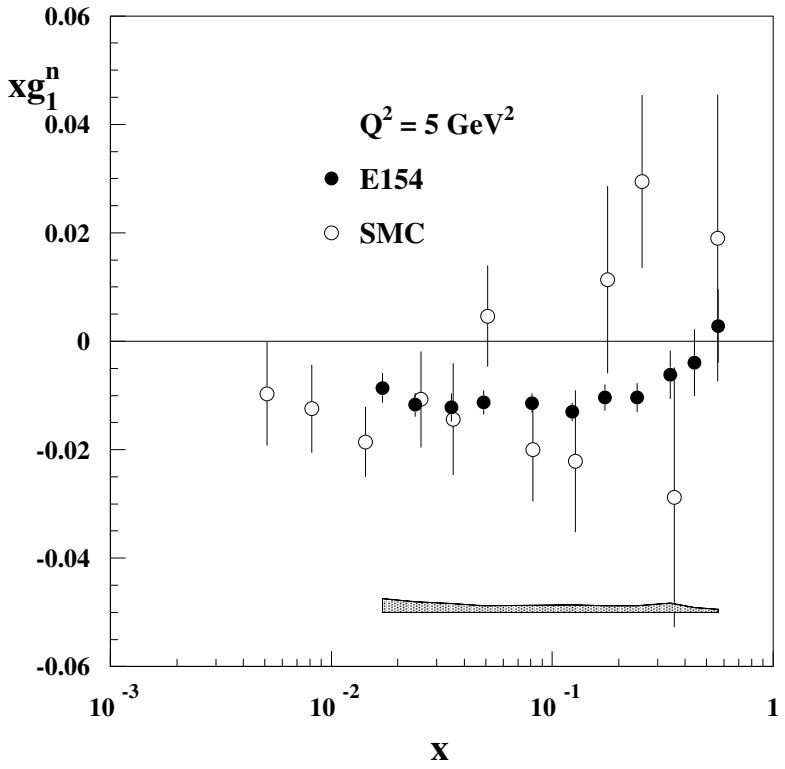


Figure 6.2: Our results for $g_1^n(x)$ compared with previous SMC data. $xg_1$ is ploted on the vertical scale for better display.

$g_1(x) \sim x^{(0-0.5)}$ in the measured range, in agreement with SMC results, see Figure 6.3. While in the past it was usually assumed that the Regge behavior sets in at $x \sim 0.03$ [5, 10], our data do not support this conclusion. While it may be true that Regge extrapolation is valid for SMC measurements starting at $x \sim 0.01$, there is no experimental evidence for it. In using Regge extrapolation experimenters in the past assigned a "conservative" error, for example, 100% of the extrapolated value of the integral [2, 5, 6]. However, as can be seen from our low $x$ data fitted to an unconstrained power law, such error estimates are dangerous. Figure 6.3 shows the low $x$ region of our data, as well as SMC data. Note that in this case $g_1$ itself is plotted, instead of $xg_1$, showing true divergence of the data. In Table 6.3 we give the parameters for several fits and the integral over the unmeasured region $\int_0^{0.0135} g_1^n(x)\,dx$ calculated from these parameters. For a power fit $g_1(x) \sim x^\alpha$, $\alpha = -0.92 \pm 0.16$. The value of the integral $\int_0^{0.0135} g_1^n(x)\,dx$ can range from $-0.14$ to infinity. In contrast, assuming a Regge fit with $\alpha = 0$ ( $g_1$ – const), we get for the extrapolation integral $-0.0055$. Clearly, a error equal to 100% of this value is inappropriate.

To test the sum rules, it is convenient to start the integral at $x = 1$ and integrate the data to the lowest $x$ point. Then one can attempt to extrapolate to $x = 0$. The

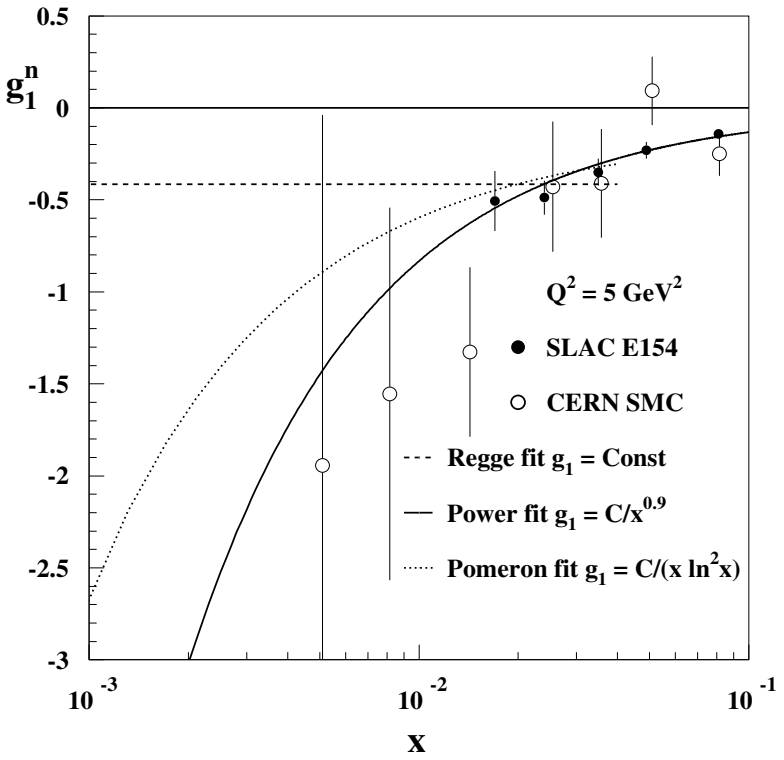


Figure 6.3: Several fits to the low $x$ region of our data.

| Fit | # p. | Parameters | $\int_0^{0.0135} dx\ g_1^n$ |
|---|---|---|---|
| $g_1^n = C$ | 3 | $C = -0.41 \pm 0.05 \pm 0.06$ | $-0.0055 \pm 0.0007 \pm 0.0008$ |
| $g_1^n = C/(x \ln^2 x)$ | 4 | $C = -0.125 \pm 0.014 \pm 0.016$ | $-0.0291 \pm 0.0032 \pm 0.0036$ |
| $g_1^n = Cx^{-\alpha}$ | 5 | $C = -0.014 \pm 0.007 \pm 0.004$<br>$\alpha = 0.92 \pm 0.16 \pm 0.09$ | $-0.14 \pm \infty \pm \infty$ |
| $g_1^n = Cx^{-\alpha}(1-x)^{\beta}$ | 11 | $C = -0.034 \pm 0.021 \pm 0.011$<br>$\alpha = 0.70 \pm 0.18 \pm 0.10$<br>$\beta = 3.2 \pm 1.6 \pm 0.7$ | $-0.031 \pm 0.022 \pm 0.013$ |

Table 6.3: Various low $x$ fits of the data and values of extrapolated integral.

results of such integration for the Ellis-Jaffe sum rule are shown in Figure 6.4 and for the Bjorken sum rule in Figure 6.5. It should be noted that the horizontal axis is logarithmic, and its zero is "infinitely" far away. It can be seen from Figure 6.4 that the Ellis-Jaffe sum rule is most likely violated. The integral already exceeds the prediction by $2\sigma$ and shows no sign of slowing down. Thus, the Ellis-Jaffe sum rule is violated in the neutron as well as in the proton [8, 6, 5].

For the test of the Bjorken sum rule we combine our neutron data with all available

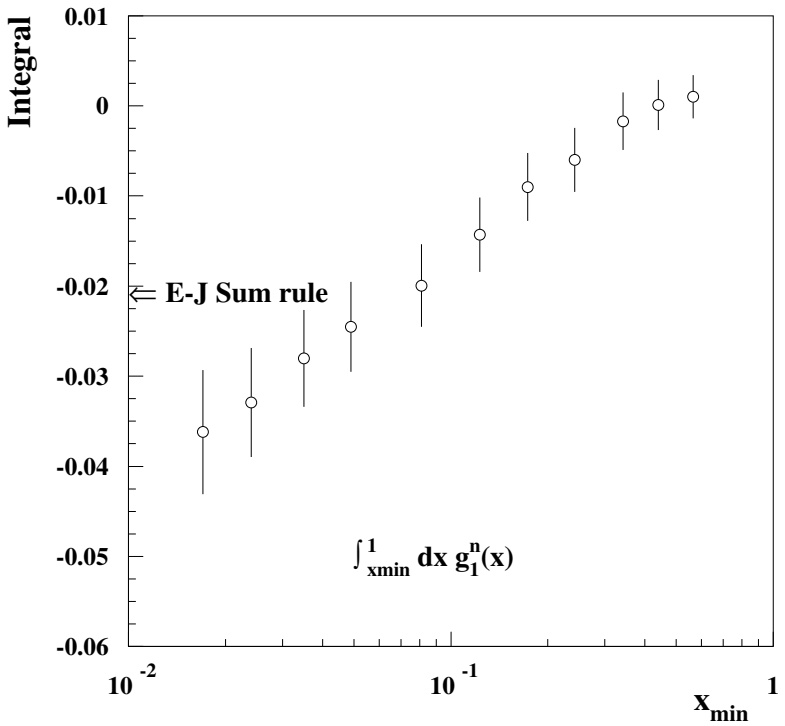


Figure 6.4: Integration of $g_1^n$ from 1 to $x$ compared with Ellis-Jaffe sum rule.

data on the proton (EMC, SMC, E143). As can be seen from Figure 6.5, the Bjorken sum rule is not violated by the data over the measured region. Its confirmation requires an extrapolation to $x = 0$ which should contribute about 12%. Fortunately, the difference $g_1^p(x) - g_1^n(x)$ is much less divergent than each structure function separately. Fitting the difference to a free power law gives: $g_1^p(x) - g_1^n(x) \sim x^{-(0.52\pm0.1)}$ and the low $x$ extrapolation gives $\int_0^{0.0135} (g_1^p - g_1^n)\, dx = 0.032 \pm 0.015$. The total integral is $\Gamma_1^p - \Gamma_1^n = 0.192 \pm 0.024$. An alternative extrapolation, based on Regge $g_1^p(x) - g_1^n(x) \sim const$ behavior gives $\Gamma_1^p - \Gamma_1^n = 0.170 \pm 0.012$. This is to be compared with the prediction of the Bjorken sum rule $\Gamma^{Bj} = 0.186 \pm 0.005$, which includes corrections up to $O(\alpha_s^3)$ [27]. Thus, both methods of extrapolation are consistent with the Bjorken sum rule and with each other. One can argue based on perturbative QCD that the two methods of extrapolation are extreme, and in reality $g_1$ diverges at low $x$ slower than any power of $x$, but faster than any power of $\log(x)$. Therefore, the test of the Bjorken sum rule is relatively robust against possible forms of low $x$ behavior, and our experiment confirms the sum rule.

Significantly more detailed information about the quark helicity distributions and other implications of our data can be obtained by considering their interpretation within QCD theory at Next-to-Leading order (NLO) level, which we turn to in the next section.

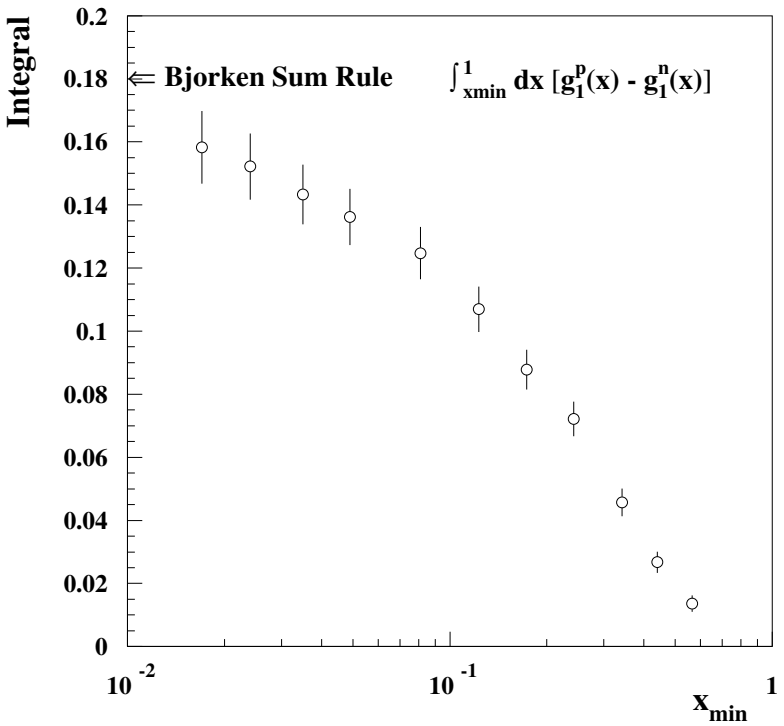


Figure 6.5: Integration of $g_1^p - g_1^n$ from 1 to $x$ compared with Bjorken sum rule.

## 6.2 The Interpretation of QPM within QCD

In our analysis of polarized DIS in Chapter 2 within the framework of the Quark Parton Model (QPM) we identified the integral of the quark helicity momentum distribution:

$$\Delta q = \int_0^1 \left( q^{\uparrow}(x) - q^{\downarrow}(x) + \bar{q}^{\uparrow}(x) - \bar{q}^{\downarrow}(x) \right) dx \tag{6.2}$$

with the matrix element of the quark helicity operator at zero $Q^2$:

$$\left\langle N \left| \bar{q}\gamma^{\mu}\gamma^5 q \right| N \right\rangle = 2\Delta q s^{\mu} \tag{6.3}$$

However, these two equations for quark helicity really apply to different quarks. In the first case, we are considering the quarks in the deep inelastic limit, where they are asymptotically free particles. In the second case, the relationship applies to constituent quarks present in the nucleon at rest. In the QPM these two types of quarks are not distinguished, because there is no $Q^2$ dependence and the quarks are not interacting. In QCD this is no longer true. The modifications due to QCD are three-fold. First, the Bjorken and Ellis-Jaffe sum rules receive calculable radiative corrections as a power series in $\alpha_s$. Second, the quark momentum distributions become dependent

on $Q^2$: $q(x) \to q(x, Q^2)$. Third, the interpretation of $\Delta q$ measured in deep inelastic scattering is modified.

There are at least two different approaches to the calculation of QCD corrections: one relying on Operator Product Expansion (OPE) and the other on perturbative calculations, also known as QCD improved Parton Model [11]. While the OPE method combined with the renormalization group equation is more widely used, greater insight can be obtained by following the perturbative approach. The two methods have been shown to be equivalent [11]. In the following discussion we will follow the perturbative treatment to illustrate the effects of QCD.

In calculating the QCD corrections to the parton model one extends the methods used in derivation of the parton model itself [12]. There, we defined the probabilities $q_i(x)$ of finding a quark inside a nucleon and then assumed that the scattering from different quarks is incoherent and that the cross-sections (instead of the amplitudes) can be added directly. Now we realize that because of QCD interactions the quark cross-section itself is modified from the simple Dirac form. To take this effect into account, we write the virtual photon cross-section in a more general form. Schematically, the process is shown in Figure 6.6. The nucleon with momentum $p$ contains a

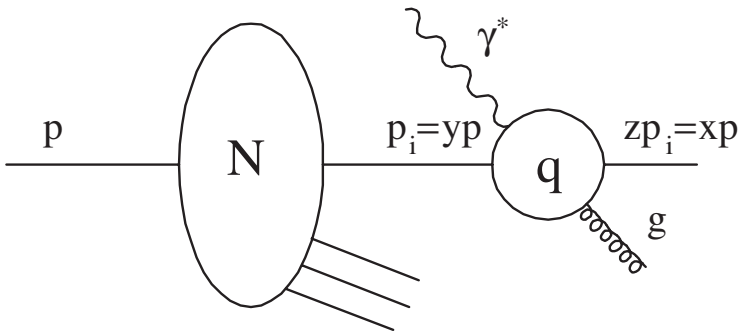


Figure 6.6: Embeding of the photon-quark cross-section into the photon-nucleon cross-section.

quark with momentum fraction $y$ which interacts with the photon and ends up with momentum fraction $x$. Because of possible gluon emission, $x$ is not necessarily equal to $y$. Thus, we can write:

$$F_1\left(x, Q^2\right) = \frac{1}{2}\sum_i e_i^2 \int_0^1 dz \int_0^1 dy q_i(y)\, \delta(x - zy)\, \sigma_{q\gamma}\left(z, Q^2\right) \tag{6.4}$$

where $\sigma_{q\gamma}(z, Q^2)$ is the (dimensionless) cross-section for quark-photon scattering normalized by appropriate kinematic factors. The other structure functions (including $g_1$ and $g_2$) can be written in similar form. Performing $z$ integration with the delta

function we get:

$$F_1\left(x,Q^2\right) = \frac{1}{2}\sum_i e_i^2 \int_0^1 \frac{dy}{y} q_i\left(y\right)\sigma_{\gamma q}\left(x/y,Q^2\right) \tag{6.5}$$

Several processes contribute to the quark-photon cross-section $\sigma_{\gamma q}\left(x/y,Q^2\right)$ [13], as shown schematically in Figure 6.7.

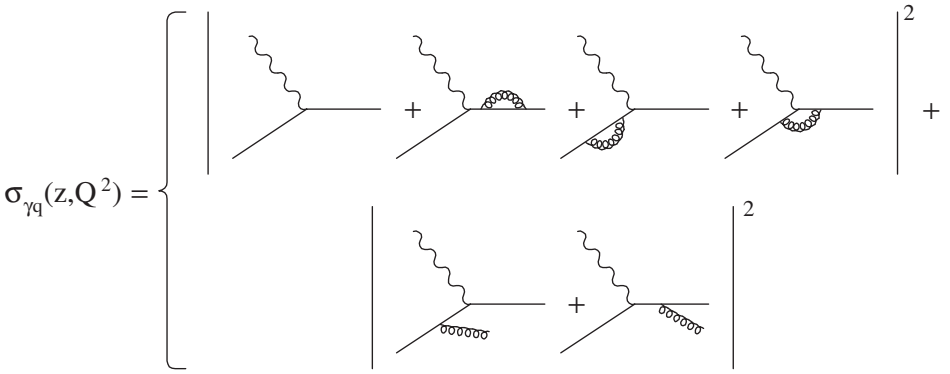


Figure 6.7: Contributions to $\sigma_{q\gamma}$ to order $\alpha_s$.

In calculating these diagrams we, as usual, encounter divergences. There are both infrared and ultra-violet divergences in the integrals over the internal lines and undetected final state particles. The ultraviolet divergences are dealt with by the usual process of UV regularization and renormalization [14], since QCD has been shown to be a renormalizable theory [15]. The most commonly used UV renormalization scheme is modified minimal subtraction [16], denoted $\overline{MS}$, which is based on dimensional regularization. In calculations of the cross-sections all UV divergent integrals should be renormalized in a consistent fashion. As long as this is done, the only other effect of UV divergences is the running of the coupling constant $\alpha_s$ with $Q^2$, which is governed by the renormalization group equations. From now on $\alpha_s$ will refer to $\alpha_s\left(Q^2\right)$ even if not stated explicitly. In the remainder of the discussion we will not concern ourselves with UV renormalization. All discussion about regularization and renormalization will refer only to infrared divergences. One does not have to choose the same scheme for UV and IR renormalization.

The infrared divergences can be divided in two types. One type is due to emission of soft and colinear gluons. The divergences cancel between the real gluon emission and the vertex correction diagrams shown in Figure 6.7 [17]. This is quite similar to the infrared divergences and their cancelation in QED, which were discussed in relation to the radiative corrections in Chapter 3. In addition, there are divergences which appear if we try to take the quark masses to zero. One method of infrared

regularization is to leave finite quark masses. Alternatively, we could set the masses to zero and use, for example, the dimensional regularization scheme to control divergent integrals. Other regularization schemes are also possible. In any scheme, we introduce a cut-off $\mu$, which has dimensions of mass, and in some schemes is associated directly with the mass or minimum momentum of the particles in the loop. In general, we get the following result:

$$\sigma_{\gamma q}\left(z,Q^2\right)=\delta\left(1-z\right)+\frac{\alpha_s}{2\pi}P_{qq}\left(z\right)\log\left(\frac{Q^2}{\mu^2}\right)+\frac{\alpha_s}{2\pi}C_{qq}\left(z\right) \tag{6.6}$$

where $P_{qq}\left(z\right)$ and $C_{qq}\left(z\right)$ are some functions, and $C_{qq}$ depends on the regularization scheme [13]. Clearly, this expression is dependent on the cut-off $\mu$ and diverges as $\mu\rightarrow 0$. Since we believe that the quark masses are small, and do not have a major effect on QCD interactions, this situation is unsatisfactory.

In addition, we calculated the cross-section only in first order perturbation, valid for $\alpha_s\ll 1$. Since the strong coupling constant is dependent on $Q^2$ and grows as $Q^2\rightarrow 0$, the results are invalid when the momentum transfer is comparable to or lower than the QCD interaction scale $\Lambda_s$. We need to separate the low energy non-perturbative behavior from the high energy perturbative behavior of QCD. One way of accomplishing this is to introduce a separation scale $\mu_f$ between the soft processes with $Q^2<\mu_f^2$ and the hard processes with $Q^2>\mu_f^2$ [18]. The non-perturbative, low $Q^2$ effects can be absorbed into the definition of the quark momentum distributions (QMDs). We can write:

$$F_1\left(x,Q^2\right) = \frac{1}{2}\sum_i e_i^2\int_0^1\frac{dy}{y}q_i^f\left(y,\mu_f^2\right)\sigma^f\left(x/y,Q^2,\mu_f^2\right) \tag{6.7}$$

$$q_i^f\left(x,\mu_f^2\right) = q_i\left(x\right)+\frac{\alpha_s}{2\pi}\log\left(\frac{\mu_f^2}{\mu^2}\right)\int_x^1\frac{dy}{y}q_i\left(y\right)P_{qq}\left(\frac{x}{y}\right) \tag{6.8}$$

$$\sigma^f\left(z,Q^2,\mu_f^2\right) = \left[\delta\left(1-z\right)+\frac{\alpha_s}{2\pi}P_{qq}\left(z\right)\log\left(\frac{Q^2}{\mu_f^2}\right)+\frac{\alpha_s}{2\pi}C_{qq}\left(z\right)\right] \tag{6.9}$$

which follows from equations (6.5) and (6.6) to first order in $\alpha_s$. This separation is known as *factorization*. $\mu_f$ is the factorization scale and $q_i^f\left(x,\mu_f^2,\mu^2\right)$ is the factorized QMD. The factorization scale $\mu_f$ is usually set to the $Q^2$ of the measurement: $\mu_f^2=Q^2$. In this case the QMD depends on $Q^2$:

$$q_i^f\left(x,Q^2\right)=q_i\left(y\right)+\frac{\alpha_s}{2\pi}P_{qq}\left(\frac{x}{y}\right)\log\left(\frac{Q^2}{\mu^2}\right) \tag{6.10}$$

while the factorized (hard scattering) cross-section $\sigma^f\left(z,Q^2,Q^2\right)=\sigma\left(z\right)$ is $Q^2$ independent. From equation (6.10) we obtain an integro-differential equation for $Q^2$

evolution of $q\left(x,Q^2\right)$ (we now drop the $f$ superscript):

$$\frac{dq\left(x,Q^2\right)}{d\log Q^2}=\frac{\alpha_s}{2\pi}\int_x^1\frac{dy}{y}q\left(y,Q^2\right)P_{qq}\left(\frac{x}{y}\right) \tag{6.11}$$

known as Dokshitzer-Gripov-Lipatov-Altareli-Parisi (DGLAP) [19] or simply Altarelli-Parisi equation. If we know $q\left(x,Q^2\right)$ at one $Q^2$ we can calculate (evolve) it to other values of $Q^2$. In addition, the factorization theorem states that the QMDs are independent of the process in which they are probed (i.e. DIS, Drell-Yan) while the hard scattering cross-sections $\sigma\left(z\right)$ are independent of the hadron being probed (i.e. proton, neutron, pion) [18].

Before proceeding any further, it is important to realize that there are several ambiguities in this decomposition. First, in calculating the cross-sections we introduced a cut-off $\mu$ using a *regularization* scheme. The function $C_{qq}$ is dependent on this choice. Sometimes this procedure is called *renormalization*, although technically this is not correct, since the quantities still depend on the cut-off and have not been made explicitly finite. Second, the factorization process is not unique. Finite terms can be moved between $q^f$ and $\sigma^f$. This ambiguity is known as the *factorization* scheme dependence. In practice, however, in each regularization scheme there is a most natural way to factorize hard and soft contributions. Therefore, the choice of the regularization and factorization schemes is related. The combination of regularization and factorization procedures makes all quantities finite and independent of quark masses. It can be properly called an infrared renormalization scheme. Finally, one does not have to choose $\mu_f^2=Q^2$, although it is a universal choice. Once the regularization and the factorization schemes are chosen, the expression for $C_{qq}$ can be uniquely calculated.

For polarized structure functions $g_1$ and $g_2$ the formalism is identical, with $q_i$ replaced by $\Delta q_i$. The function $P_{qq}$ is also identical for the polarized and unpolarized case, which explains why $g_1$ and $F_1$ evolve similarly with $Q^2$ and the asymmetry $A_1$ is approximately independent of $Q^2$. The relationship is only approximate because of the gluon contribution, which we will discuss next.

To order $\alpha_s$ we should also include the gluon diagram shown in Figure 6.8. Then the full expression for the spin structure function $g_1$ becomes:

$$\begin{aligned} g_1\left(x,Q^2\right) &= \frac{1}{2}\sum_i e_i^2\{\Delta q_i\left(x,Q^2\right)+\frac{\alpha_s}{2\pi}C_{qq}\left(x\right)\otimes\Delta q_i\left(x,Q^2\right) \\ &\quad +\frac{\alpha_s}{2\pi}C_{qg}\left(x\right)\otimes\Delta G\left(x,Q^2\right)\} \end{aligned} \tag{6.12}$$

were we have introduced convolution:

$$f\left(x\right)\otimes g\left(x\right)=\int\frac{dy}{y}f\left(\frac{x}{y}\right)g\left(y\right) \tag{6.13}$$

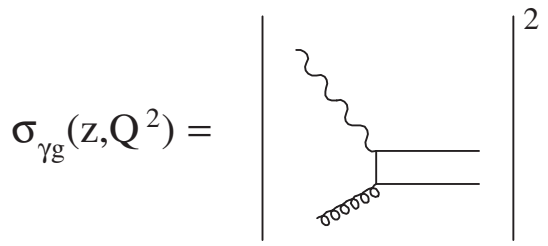


Figure 6.8: Gluon contribution to the photon-quark cross-section.

and $\Delta G\left(x,Q^2\right)=G^{\uparrow}\left(x,Q^2\right)-G^{\downarrow}\left(x,Q^2\right)$ is the gluon helicity distribution.

For the sum rules we are particularly interested in the gluon contribution to the integral of $g_1\left(x,Q^2\right)$:

$$\Gamma_1^{gl} = \frac{1}{2}\left(\sum_i e_i^2\right)\frac{\alpha_s}{2\pi}\int_0^1 dx\int_x^1\frac{dy}{y}C_{qg}\left(\frac{x}{y}\right)\Delta G\left(y,Q^2\right) \tag{6.14}$$

$$= \frac{1}{2}\left(\sum_i e_i^2\right)\frac{\alpha_s}{2\pi}\left[\int_0^1 dx\Delta G\left(x,Q^2\right)\right]\left[\int_0^1 dx C_{qg}\left(x\right)\right] \tag{6.15}$$

The last step follows from the properties of the convolution (6.13). Thus, we see that the gluon contribution to $\Gamma_1$ depends on the integral of $C_{qg}\left(x\right)$. As was mentioned before, the definition of $C_{qg}\left(x\right)$ depends on the renormalization scheme. In some schemes its integral is equal to zero, while in others its not. One may think that $\Gamma_1^{gl}$ is only a perturbation, because it is proportional to $\alpha_s$, and $\alpha_s$ goes as $1/\log\left(Q^2\right)$ in the deep inelastic limit $Q^2\to\infty$. However, the helicity carried by the gluons grows logarithmically with $Q^2$ [20]:

$$\lim_{Q^2\to\infty}\int_0^1\Delta G\left(x,Q^2\right)dx\to\log Q^2 \tag{6.16}$$

because of the axial anomaly, so $\alpha_s\left(Q^2\right)\Delta G\left(Q^2\right)$ is of order unity even at infinite $Q^2$.

Thus, we need to consider the gluon contribution in detail. The polarized cross-section, shown in Figure 6.8, is divergent, as usual. We will consider two regularization schemes which are particularly illustrative. In one scheme, we put a lower cut-off $p^2$ on the gluon momentum, which gives for $Q^2\gg -p^2$ [21]:

$$\sigma_{\gamma g}^{p}=\frac{\alpha_s}{2\pi}\left(2x-1\right)\left(\log\frac{Q^2}{-p^2}+\log\frac{1}{x^2}-2\right) \tag{6.17}$$

Alternatively, we can leave a finite quark mass $m$, in which case [22, 23]:

$$\sigma_{\gamma g}^{m}=\frac{\alpha_s}{2\pi}\left[\left(2x-1\right)\left(\log\frac{Q^2}{m^2}+\log\frac{1-x}{x}-1\right)+2\left(1-x\right)\right] \tag{6.18}$$

The cut-off dependent parts of the cross-section can be absorbed into the QMDs, while the finite terms give $C_{qg}$. For example, in the momentum regularization scheme by comparing with equation (6.6) we can read off:

$$P_{qg}^{p} = (2x-1) \tag{6.19}$$

$$C_{qg}^{p} = (2x-1)\left(\log\frac{1}{x^2}-2\right) \tag{6.20}$$

The integral of $C_{qg}$ is different in the two schemes:

$$\int_0^1 C_{qg}^{p}(x)\,dx = -1 \tag{6.21}$$

$$\int_0^1 C_{qg}^{m}(x)\,dx = 0 \tag{6.22}$$

Therefore, in the momentum regularization scheme

$$\Gamma_1 = \frac{1}{2}\sum e_i^2\left[\Delta q_i - \frac{\alpha_s}{2\pi}\Delta G\right] \tag{6.23}$$

and the gluon helicity appears in the integral of $g_1$, while in the mass regularization scheme:

$$\Gamma_1 = \frac{1}{2}\sum e_i^2 \Delta q_i \tag{6.24}$$

and the integral of $g_1$ does not depend on the gluon helicity.

One could argue that one or another of these schemes is unphysical[1]. In fact, for the polarized scattering structure functions there is no completely satisfactory choice of the regularization procedure. Because of the axial anomaly, the singlet axial current $J_5^{\mu} = \bar{q}\gamma^{\mu}\gamma^5 q$ is not conserved:

$$\partial_{\mu} J_5^{\mu} = \frac{\alpha_s}{\pi} N_f Tr\left[G_{\mu\nu}\tilde{G}^{\mu\nu}\right] \tag{6.25}$$

where $G_{\mu\nu}$ is the gluon field. As a result, when one chooses a regularization procedure either of the three things can happen [24]: the gauge invariance is lost, the chiral symmetry of QCD is broken, or the anomaly is not taken into account. For the gluon momentum regularization scheme the anomaly is not included because it cannot be obtained from the gluon equations of motion. The chiral symmetry is preserved, however. On the other hand, in the quark mass regularization scheme the chiral symmetry of QCD is broken.

On a more intuitive level (see Figure 6.9), by choosing a gluon momentum cut-off, we are including in the hard cross-section only processes which originated from

[1] In this case the momentum scheme [21] is questionable [23]. However, identical results can be obtained by another method [24].

a hard gluon. The gluon, therefore, is in perturbative realm of QCD and is weakly interacting. Its momentum distribution is well defined. The photon scatters from the virtual quark cloud of the gluon. Therefore, it is natural that gluon distribution contributes to $\Gamma_1$. In contrast, by using a quark mass cut-off, we are only considering the contribution of the quarks whose momentum $p^2 = m^2$ is large, without putting a cut on the gluons. In this case it is the quarks which are in the perturbative regime with a well defined momentum distribution. But the quark contribution is already included at the tree level. The fact that the quarks can originate from gluons is taken into account by allowing a contribution from the sea quarks. Therefore, no additional gluon contribution is required. These two interpretation are shown schematically in Figure 6.9.

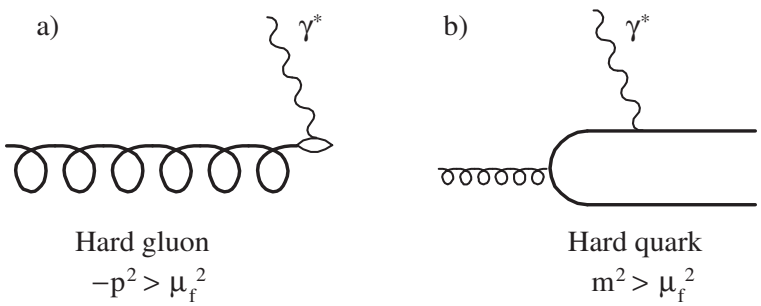


Figure 6.9: Hard scattering contribution: a) only from hard gluons, b) only from hard quarks.

For practical calculations it is more convenient to use different regularization schemes. One commonly used scheme is dimensional regularization, denoted $\overline{MS}$ by analogy with UV renormalization scheme. The results for $\Gamma_1$ and $\sigma_{\gamma g}$ obtained within this scheme are identical to our quark mass regularization scheme (to order $\alpha_s$ only). The chiral symmetry is broken in this scheme because of difficulty in defining $\gamma_5$ in $4 + \varepsilon$ dimensions. The other commonly used scheme is the Adler-Bardeen scheme, denoted AB, whose result for $\Gamma_1$ is identical to our gluon momentum cut-off scheme. The chiral symmetry is preserved in this scheme, but one cannot define gauge invariant operators for the quark helicity.

While the contribution of the gluons to the first moment of $g_1$ depends on the regularization scheme, there is always some contribution to $g_1(x)$ through $C_{qg}$ terms and to $Q^2$ evolution of quark densities through $P_{qg}$ terms. It is convenient to form particular linear combinations of the quark momentum distributions. In non-singlet combinations $\Delta u - \Delta d$ and $\Delta u + \Delta d - 2\Delta s$ the effect of the gluons always cancels, because gluons couple in the same way to all quarks. Or, to say it in different words, these combinations are proportional to the non-singlet axial current $J^{\mu}_{5NS} = \bar{q}\lambda^a\gamma^{\mu}\gamma^5 q$,

where $\lambda^a$ is an SU(3) matrix acting in flavor space. The non-singlet axial current does not get a contribution from the axial anomaly and is conserved. Only the singlet contribution $\Delta\Sigma = \Delta u + \Delta d + \Delta s$ is affected by the gluons. The $Q^2$ evolution of the non-singlet and singlet combinations is calculated separately:

$$\frac{d}{d\log Q^2}\Delta q_{NS}\left(x,Q^2\right) = \frac{\alpha_s\left(Q^2\right)}{2\pi}P_{qq}\otimes\Delta q_{NS} \tag{6.26}$$

$$\frac{d}{d\log Q^2}\begin{pmatrix}\Delta q_S\left(x,Q^2\right)\\ \Delta G\left(x,Q^2\right)\end{pmatrix} = \frac{\alpha_s\left(Q^2\right)}{2\pi}\begin{pmatrix}P_{qq} & P_{qg}\\ P_{gq} & P_{gg}\end{pmatrix}\otimes\begin{pmatrix}\Delta q_S\\ \Delta G\end{pmatrix} \tag{6.27}$$

Using the properties of the convolution (6.13) one can also write $Q^2$ evolution equations directly for first moments of $\Delta q_i$:

$$\frac{d}{d\log Q^2}\Delta q_{NS}\left(Q^2\right) = \frac{\alpha_s\left(Q^2\right)}{2\pi}\gamma_{qq}\left(1\right)\Delta q_{NS} \tag{6.28}$$

$$\frac{d}{d\log Q^2}\begin{pmatrix}\Delta\Sigma\left(Q^2\right)\\ \Delta G\left(x,Q^2\right)\end{pmatrix} = \frac{\alpha_s\left(Q^2\right)}{2\pi}\begin{pmatrix}\gamma_{qq}\left(1\right) & \gamma_{qg}\left(1\right)\\ \gamma_{gq}\left(1\right) & \gamma_{gg}\left(1\right)\end{pmatrix}\begin{pmatrix}\Delta\Sigma\\ \Delta G\end{pmatrix} \tag{6.29}$$

where $\gamma_{ij}\left(n\right) = \int_0^1 x^{n-1}P_{ij}\left(x\right)dx$ are called anomalous dimensions.

At this point it is appropriate to briefly describe the other method of QCD analysis based on Operator Product Expansion (OPE). In OPE the fundamental quantities are the moments of the structure functions:

$$f\left(n,Q^2\right) = \int_0^1 x^{n-1}f\left(x,Q^2\right)dx; \quad f = F_{1,2}, g_{1,2} \tag{6.30}$$

It can be shown that for inclusive deep inelastic scattering they are related to the forward matrix elements of local gauge-invariant operators of the form:

$$O_{qV}^{\mu_1\cdots\mu_n} = \bar{\psi}\gamma^{\mu_1}D^{\mu_2}\cdots D^{\mu_n}\psi \tag{6.31}$$

$$O_{qA}^{\mu_1\cdots\mu_n} = \bar{\psi}\gamma^{\mu_1}\gamma^5 D^{\mu_2}\cdots D^{\mu_n}\psi \tag{6.32}$$

$$O_{GV}^{\mu_1\cdots\mu_n} = G_a^{\mu_1}D^{\mu_2}\cdots D^{\mu_{n-1}}G_a^{\mu_n} \tag{6.33}$$

where $D^\mu$ is a covariant derivative. Using the renormalization group equation one can calculate the anomalous dimensions of the operators and their $Q^2$ evolution. Mellin transforms are used to convert back to the $x$ dependent spin structure functions.

From equations (6.17, 6.18) we see that $\gamma_{qg}\left(1\right) = 0$ in both renormalization schemes considered here. However, in the next order ($\alpha_s^2$) the $Q^2$ evolution is dependent on the renormalization scheme. It can be shown [25], that in the $\overline{MS}$ scheme:

$$\frac{d}{d\log\left(Q^2\right)}\begin{pmatrix}\Delta\Sigma_{\overline{MS}}\\ \Delta G'\end{pmatrix} = \left(\frac{\alpha_s}{2\pi}\right)^2\begin{pmatrix}-2N_f & 0\\ 2 & 0\end{pmatrix}\begin{pmatrix}\Delta\Sigma_{\overline{MS}}\\ \Delta G'\end{pmatrix} \tag{6.34}$$

where $\Delta G' \equiv (\alpha_s/2\pi)\,\Delta G$. So, in this scheme $\Delta\Sigma_{\overline{MS}}$ is not independent of $Q^2$ in second order of $\alpha_s$. On the other hand, in the Adler-Bardeen scheme:

$$\frac{d}{d\log(Q^2)}\begin{pmatrix}\Delta\Sigma_{AB}\\ \Delta G'\end{pmatrix} = \left(\frac{\alpha_s}{2\pi}\right)^2\begin{pmatrix}0 & 0\\ 2 & -2N_f\end{pmatrix}\begin{pmatrix}\Delta\Sigma_{AB}\\ \Delta G'\end{pmatrix} \tag{6.35}$$

and $\Delta\Sigma_{AB}$ is independent of $Q^2$. In fact, it can be shown that $\Delta\Sigma_{AB}$ is independent of $Q^2$ to all orders. This is because the singlet axial current is replaced by a *conserved* current of the form:

$$\tilde{J}_5^\mu = \bar{q}\gamma^\mu\gamma^5 q + N_f\frac{\alpha_s}{2\pi}\epsilon_{\mu\nu\rho\sigma}G_a^\nu D^\rho G_a^\sigma \tag{6.36}$$

$$\partial_\mu\tilde{J}_5^\mu = 0 \tag{6.37}$$

The second term is needed to cancel the contribution of the anomaly and can be interpreted as the gluon helicity operator.

To summarize, there are two commonly used renormalization schemes. In the $\overline{MS}$ scheme only quark helicities appear in the first moment of $g_1$:

$$\Gamma_1\left(Q^2\right) = \frac{1}{2}\sum e_i^2\Delta q_i\left(Q^2\right) \tag{6.38}$$

but the total quark helicity $\Delta\Sigma = \Delta u + \Delta d + \Delta s$ evolves with $Q^2$. Therefore, a value of $\Delta\Sigma$ obtained in DIS cannot be compared with static models of the nucleon. Also, the chiral symmetry is broken in $\overline{MS}$ because of the definition of $\gamma^5 = i\gamma^0\gamma^1\gamma^2\gamma^3$ in $4+\epsilon$ dimensions. In the Adler-Bardeen scheme the gluon helicity also appears in the expression for $\Gamma_1$:

$$\Gamma_1\left(Q^2\right) = \frac{1}{2}\sum e_i^2\left[\Delta q_i\left(Q^2\right) - \frac{\alpha_s}{2\pi}\Delta G\left(Q^2\right)\right] \tag{6.39}$$

but the total quark helicity $\Delta\Sigma$ is independent of $Q^2$ and the chiral symmetry is not broken.

The Bjorken sum rule involves a non-singlet combination $\Delta u - \Delta d$, so it is unaffected by the gluon contribution. In addition, because of the conservation of non-singlet axial current $J_{5NS}^\mu = \bar{q}\lambda^a\gamma^\mu\gamma^5 q$, it is also unaffected by the $Q^2$ evolution, i.e. $\int_0^1 P_{qq}^{NS}dx = 0$ to all orders in $\alpha_s$. The only QCD modification is due to the $C_{qq}$ term, which has a non-vanishing first moment $\int_0^1 C_{qq}(x)\,dx = -2$ [26], so we get:

$$\int_0^1 dx\,(g_1^p(x) - g_1^n(x)) = \frac{1}{2}(\Delta u - \Delta d)\left(1 + \frac{\alpha_s}{2\pi}(-2)\right) = \frac{1}{6}\frac{g_A}{g_V}\left(1 - \frac{\alpha_s}{\pi}\right) \tag{6.40}$$

using equation (6.12). It is easier to calculate the corrections using the techniques of OPE, and they have been calculated to order $\alpha_s^3$ [27]:

$$\Gamma^{p-n} = \frac{1}{6}\frac{g_A}{g_V}\left(1 - \frac{\alpha_s}{\pi} - 3.5833\left(\frac{\alpha_s}{\pi}\right)^2 - 20.215\left(\frac{\alpha_s}{\pi}\right)^3\right) \tag{6.41}$$

for three quark flavors.

## 6.3 Analysis of the Data within QCD

The analysis of the data within QCD proceeds through the following steps. First, one has to parametrize the helicity momentum distributions of the quarks and gluons. Many possible forms of the parametrization are possible, see for example [31]. In the range of $x$ where the data on $g_1$ exist, the exact form of the parametrization is not very critical, because several parameters are adjusted to fit the data. However, the form of the parametrization is critical for extrapolating to $x = 0$, since different functional forms fitted to the same data will give different results in the unmeasured region. In our analysis [30], we follow the anzatz of Glück *et al.* [29], who assume that the polarized momentum distributions are given by:

$$\Delta f = A_f \, x^{\alpha_f} f\left(x, Q^2\right) \tag{6.42}$$

where $f$ are the unpolarized momentum distributions. This parametrization has several advantages. For low $x$ the helicity momentum distributions behave as a power law and can be compared with Regge predictions. We also expect that $|A_f| \sim 1$, since at high $x$ the polarization of the quarks approaches unity. Thus, there are some theoretical expectations with which we can compare our results. But this is by no means a unique form of the parametrization.

The unpolarized momentum distributions are obtained from experimental data in [28]. They are separated into valence and sea distributions: $u\left(x\right) = u_V\left(x\right) + u_s\left(x\right)$ and similar for $d$ quarks. It is further assumed that $u_s\left(x\right) = \bar{u}_s\left(x\right) = d_s\left(x\right) = \bar{d}_s\left(x\right) = \lambda s\left(x\right) = \lambda \bar{s}\left(x\right)$, where $\lambda$ is an SU(3) symmetry breaking parameter, which can vary between zero and one. It is convenient to parametrize the sea distribution by $Q = (u_s + d_s)/2 + s/5$ which directly enters into the expression for $g_1$. In equation (6.42) $f$ is $u$, $d$, $Q$ or $G$ - the gluon momentum distribution. The unpolarized momentum distributions are given in Table 6.4. The parametrization is done at $Q_0^2 = 0.34$ GeV$^2$ and the momentum distributions are evolved up in $Q^2$ for comparison with DIS data at $Q^2 > 1$ GeV$^2$. In this way the positivity constraints are automatically satisfied. In addition, by evolving in $Q^2$ by a large amount, we are incorporating as much of perturbative QCD behavior as possible. It is also believed that the Regge behavior is more likely to be observed at very low $Q^2$ than at the $Q^2$ of measurement. As will be shown, our results for $g_1$ are relatively insensitive to the initial distributions. We cannot go any lower in $Q^2$ because $\alpha_s$ becomes too large and the NLO calculation is not sufficient.

A similar NLO analysis was recently performed by Altarelli *et al.* [31], including preliminary E-154 data released in the summer of 1996. They use several different functional parametrizations of the polarized momentum distributions, some similar to (6.42) and some different. They only work in the AB scheme. By comparing the results of their and our analysis we can estimate how the conclusions depend on different functional fits to the same data.

| | |
|---|---|
| $u_V(x,Q_0^2)$ | $0.988x^{-0.457}(1-x)^{3.380}(1+1.58x^{1/2}+2.58x+18.1x^{3/2})$ |
| $d_V(x,Q_0^2)$ | $0.182x^{-0.684}(1-x)^{4.113}(1+2.51x^{1/2}+25.0x+11.4x^{3/2})$ |
| $Q(x,Q_0^2)$ | $0.545x^{-0.70}(1-x)^{8.33}(1+2.65x)$ |
| $G(x,Q_0^2)$ | $26.2x^{0.9}(1-x)^{4.0}$ |

Table 6.4: Parametrization of the unpolarized momentum distributions.

With the unpolarized distributions and the parametrization (6.42) the polarized distributions are evolved in $Q^2$ using next-to-leading order evolution equations (6.26, 6.27). The splitting functions $P_{ij}$ have been calculated to next-to-leading order in [26]. The spin structure functions are calculated using equation (6.12). The hard scattering cross-sections are also given in [26]. We perform the calculations in moment space (6.30) and then convert to $x$ space by a Mellin transform. The calculations were performed in two renormalization/factorization schemes: $\overline{MS}$ and AB.

We used all available world data on the proton and neutron spin structure functions. The data were fit by adjusting 8 constants $A_f$ and $\alpha_f$ in equation (6.42). The errors of the fit were estimated by a Monte Carlo technique. Experimental data points were randomized within their statistical errors and the parameters of the fit were recalculated. In addition, all data points within a given experiment were moved by the systematic error, assuming that it was 100% correlated. We also assigned a theoretical error which came from several sources. The biggest contribution was from the uncertainty in the value of $\alpha_s$, which was determined from all available DIS data. To check the sensitivity to the parametrization functions, we used a different parametrization of unpolarized momentum distributions at $Q_0^2 = 1$ GeV$^2$ [32]. The SU(3) symmetry breaking parameter $\lambda$ was varied from 0 to 1.

The results for the fit parameters are shown in Table 6.5. The proton and neutron data together with the fits are shown in Figures 6.10 and 6.11. The results for physical quantities extracted from the fits are given in Table 6.6.

Several conclusions can be reached. The results for the scheme invariant quantities $\Delta q_3$, $\Delta q_8$ and $\Gamma_1$ are the same in the two schemes within theoretical uncertainties. For the Bjorken sum rule we get a world average[2] $\Gamma_1^{p-n} = 0.168 \pm 0.012$, while using only our results for the neutron we get $\Gamma_1^{p-n} = 0.172 \pm 0.013$. This is in agreement with the predicted value of $\Gamma_1^{Bj} = 0.186 \pm 0.005$. It is interesting to note that the NLO analysis gives a result very close to a naive Regge extrapolation. Thus, the Bjorken sum rule is verified with a precision of 8%.

For the neutron integral we get $\Gamma_1^n = -0.056 \pm 0.009$ (our data alone $\Gamma_1^n = -0.053 \pm 0.010$). Using the value of $a_8 = 0.579 \pm 0.025$ from a recent analysis by Close and Roberts [33], we get for the Ellis-Jaffe sum rule $\Gamma_1^n\,(EJ) = -0.021 \pm 0.004$. However, in calculating $a_8$ from the hyperon decay data, one has to apply a variety

[2] For definiteness we quote the numbers from the $\overline{MS}$ scheme.

| | $\overline{MS}$ | | | | AB | | | |
|---|---|---|---|---|---|---|---|---|
| | Value | Stat. | Syst. | Theory | Value | Stat. | Syst. | Theory |
| $A_u$ | 0.99 | $^{+0.08}_{-0.08}$ | $^{+0.04}_{-0.05}$ | $^{+0.97}_{-0.11}$ | 0.98 | $^{+0.07}_{-0.06}$ | $^{+0.05}_{-0.07}$ | $^{+0.96}_{-0.09}$ |
| $A_d$ | $-0.78$ | $^{+0.14}_{-0.20}$ | $^{+0.05}_{-0.05}$ | $^{+0.05}_{-1.28}$ | $-0.82$ | $^{+0.06}_{-0.11}$ | $^{+0.07}_{-0.06}$ | $^{+0.31}_{-1.21}$ |
| $A_Q$ | $-0.02$ | $^{+0.03}_{-0.06}$ | $^{+0.01}_{-0.02}$ | $^{+0.01}_{-0.35}$ | $-0.04$ | $^{+0.02}_{-0.05}$ | $^{+0.01}_{-0.03}$ | $^{+0.03}_{-0.06}$ |
| $A_G$ | 1.6 | $^{+1.1}_{-0.9}$ | $^{+0.6}_{-0.6}$ | $^{+0.2}_{-1.3}$ | 0.1 | $^{+1.0}_{-0.3}$ | $^{+0.5}_{-0.2}$ | $^{+0.1}_{-0.6}$ |
| $\alpha_u$ | 0.63 | $^{+0.06}_{-0.07}$ | $^{+0.04}_{-0.05}$ | $^{+0.36}_{-0.06}$ | 0.55 | $^{+0.08}_{-0.06}$ | $^{+0.03}_{-0.04}$ | $^{+0.56}_{-0.05}$ |
| $\alpha_d$ | 0.28 | $^{+0.15}_{-0.11}$ | $^{+0.05}_{-0.03}$ | $^{+0.75}_{-0.03}$ | 0.40 | $^{+0.20}_{-0.12}$ | $^{+0.07}_{-0.13}$ | $^{+0.53}_{-0.34}$ |
| $\alpha_Q$ | 0.04 | $^{+0.29}_{-0.03}$ | $^{+0.12}_{-0.03}$ | $^{+0.55}_{-0.01}$ | 0.00 | $^{+0.17}_{-0.00}$ | $^{+0.17}_{-0.00}$ | $^{+0.00}_{-0.00}$ |
| $\alpha_G$ | 0.8 | $^{+0.4}_{-0.5}$ | $^{+0.3}_{-0.3}$ | $^{+0.1}_{-0.6}$ | 0.0 | $^{+0.7}_{-0.0}$ | $^{+1.0}_{-0.0}$ | $^{+1.0}_{-0.0}$ |

Table 6.5: Parameters of the fits for polarized momentum distributions.

| | $\overline{MS}$ | | | | AB | | | |
|---|---|---|---|---|---|---|---|---|
| | Value | Stat. | Syst. | Theory | Value | Stat. | Syst. | Theory |
| $\Delta u_V$ | 0.69 | $^{+0.03}_{-0.02}$ | $^{+0.05}_{-0.04}$ | $^{+0.14}_{-0.01}$ | 0.74 | $^{+0.03}_{-0.02}$ | $^{+0.02}_{-0.03}$ | $^{+0.07}_{-0.01}$ |
| $\Delta d_V$ | $-0.40$ | $^{+0.03}_{-0.04}$ | $^{+0.03}_{-0.03}$ | $^{+0.07}_{-0.00}$ | $-0.33$ | $^{+0.03}_{-0.04}$ | $^{+0.03}_{-0.05}$ | $^{+0.01}_{-0.03}$ |
| $\Delta Q$ | $-0.02$ | $^{+0.01}_{-0.02}$ | $^{+0.01}_{-0.01}$ | $^{+0.00}_{-0.03}$ | $-0.03$ | $^{+0.02}_{-0.02}$ | $^{+0.01}_{-0.01}$ | $^{+0.01}_{-0.01}$ |
| $\Delta G$ | 1.8 | $^{+0.6}_{-0.7}$ | $^{+0.4}_{-0.5}$ | $^{+0.1}_{-0.6}$ | 0.4 | $^{+1.0}_{-0.7}$ | $^{+0.9}_{-0.6}$ | $^{+1.1}_{-0.1}$ |
| $\Delta q_3$ | 1.09 | $^{+0.03}_{-0.02}$ | $^{+0.05}_{-0.05}$ | $^{+0.06}_{-0.01}$ | 1.07 | $^{+0.03}_{-0.02}$ | $^{+0.06}_{-0.06}$ | $^{+0.10}_{-0.01}$ |
| $\Delta q_8$ | 0.30 | $^{+0.06}_{-0.05}$ | $^{+0.05}_{-0.05}$ | $^{+0.23}_{-0.01}$ | 0.42 | $^{+0.05}_{-0.08}$ | $^{+0.06}_{-0.06}$ | $^{+0.03}_{-0.01}$ |
| $\Delta q_0$ | 0.20 | $^{+0.05}_{-0.06}$ | $^{+0.04}_{-0.05}$ | $^{+0.01}_{-0.01}$ | 0.21 | $^{+0.05}_{-0.06}$ | $^{+0.06}_{-0.07}$ | $^{+0.05}_{-0.02}$ |
| $\Delta\Sigma$ | 0.20 | $^{+0.05}_{-0.06}$ | $^{+0.04}_{-0.05}$ | $^{+0.01}_{-0.01}$ | 0.25 | $^{+0.07}_{-0.07}$ | $^{+0.05}_{-0.05}$ | $^{+0.05}_{-0.02}$ |
| $\Gamma_1^p$ | 0.112 | $^{+0.006}_{-0.006}$ | $^{+0.008}_{-0.008}$ | $^{+0.009}_{-0.001}$ | 0.114 | $^{+0.005}_{-0.006}$ | $^{+0.008}_{-0.011}$ | $^{+0.001}_{-0.003}$ |
| $\Gamma_1^n$ | $-0.056$ | $^{+0.006}_{-0.007}$ | $^{+0.005}_{-0.006}$ | $^{+0.002}_{-0.001}$ | $-0.051$ | $^{+0.005}_{-0.007}$ | $^{+0.006}_{-0.007}$ | $^{+0.001}_{-0.012}$ |
| $\Gamma_1^d$ | 0.026 | $^{+0.005}_{-0.006}$ | $^{+0.005}_{-0.006}$ | $^{+0.005}_{-0.001}$ | 0.029 | $^{+0.005}_{-0.006}$ | $^{+0.006}_{-0.007}$ | $^{+0.001}_{-0.007}$ |
| $\Gamma_1^{p-n}$ | 0.168 | $^{+0.005}_{-0.004}$ | $^{+0.008}_{-0.007}$ | $^{+0.007}_{-0.001}$ | 0.165 | $^{+0.004}_{-0.004}$ | $^{+0.007}_{-0.009}$ | $^{+0.013}_{-0.001}$ |

Table 6.6: Physical quantities extracted from the fits.

of corrections which are not entirely unambiguous [34]. Depending on the analysis technique, $\Gamma_1^n(EJ)$ can have a error as large as 0.016 [2, 35]. The Ellis-Jaffe sum rule is violated by $3.5\sigma$ if we use the smaller error, or by $1.9\sigma$ with a larger error on $\Gamma_1^n(EJ)$.

One can also turn the analysis around, and assuming the validity of the Bjorken sum rule, perform a global fit of the polarized deep inelastic data to determine the value of $\alpha_s$. Such analysis was performed by Altarelli *et al* [31], who used our preliminary data. Their result is: $\alpha_s(M_Z) = 0.120^{+0.004\,+0.009}_{-0.005\,-0.006}$, where the first error is experimental and the second is theoretical. The total error is only twice larger than

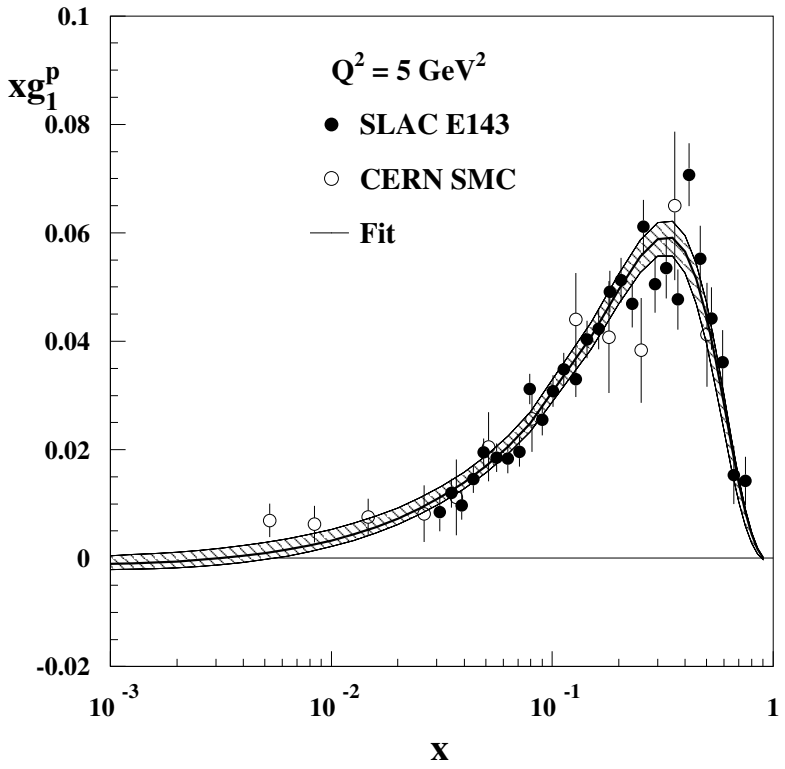


Figure 6.10: NLO fit to all available proton data.

the error on $\alpha_s$ determined from all unpolarized deep inelastic scattering data. Without our measurement the experimental error on $\alpha_s$ would have been larger by a factor of 2.

The question about the total amount of helicity carried by the quarks should be addressed with caution. The number that can be most closely associated with the interpretations of the naive parton model is $\Delta\Sigma_{AB}$ which is independent of $Q^2$ [22, 25]. Our result is $\Delta\Sigma_{AB} = 0.25 \pm 0.1$, very far from unity, which would be expected in the naive parton model based on SU(6). We emphasize, again, that because $\Delta\Sigma_{AB}$ is independent of $Q^2$, it can be identified with the spin fraction carried by the constituent quarks in a nucleon at rest, provided that the SU(3) and chiral symmetry breaking due to finite quark masses is small [31]. Of course, the SU(6) model is too naive. For example, in SU(6) $g_A/g_V = 5/3 = 1.66$, compared with experimental value of 1.26. However, using equation (2.33) we can calculate the polarization of the s quark from measured quantities without invoking any static model of the nucleon. The result is:

$$\Delta s = \frac{1}{3}\left(\Delta\Sigma_{AB} - a_8\right) = -0.11 \pm 0.035 \tag{6.43}$$

where we used $a_8 = 0.579 \pm 0.025$. It is $3\sigma$ away from zero. On the other hand, in the Adler-Bardeen renormalization scheme the chiral symmetry is preserved. Therefore,

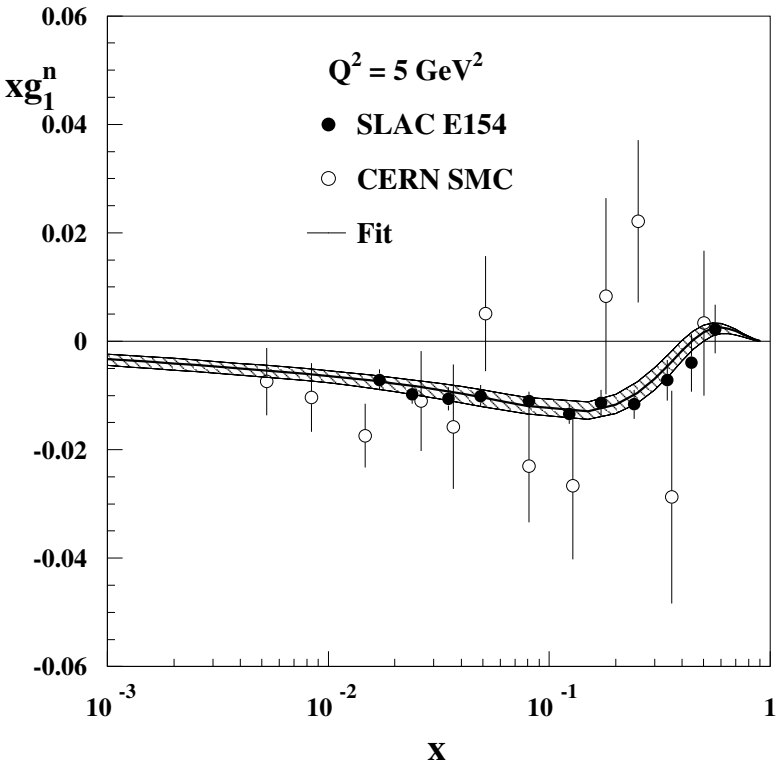


Figure 6.11: NLO fit to all available netron data.

helicity conservation at the gluon quark vertex (see Figure 6.9) should imply that $\Delta s \simeq 0$. So, our situation is reminiscent of the proton spin crisis.

At first, the EMC results were explained by noticing that the gluons make a contribution [22, 25, 24] to $\Gamma_1$, which, at that time, was not known. It was estimated that $\Delta G \sim 2.5$ is needed to reconcile $\Delta\Sigma$ with the naive parton model. Since $\Delta G \to +\infty$ for large $Q^2$ , such explanation seems quite reasonable. Several techniques for measuring the gluon helicity to confirm this explanation were proposed [36]. Alternatively, working in the $\overline{MS}$ scheme, one notices that $\Delta\Sigma_{\overline{MS}}$ depends on $Q^2$ and cannot be compared with static nucleon properties. In addition, in the $\overline{MS}$ scheme the chiral symmetry is broken, so there is no reason to expect $\Delta s \simeq 0$.

With new precision data on the spin structure functions it becomes possible to constrain the gluon contribution by studying the $Q^2$ dependence of the structure functions. Our result in the AB scheme $\Delta G = 0.4$ seems to indicate that the gluon helicity is smaller than expected, and the s quark polarization is $3\sigma$ away from zero. These conclusions, however, are not yet sufficiently robust. Altarelli *et al* [31] on the basis of similar analysis of similar data, obtain $\Delta\Sigma_{AB} = 0.45 \pm 0.09$ and $\Delta s = -0.04 \pm 0.03$, consistent with zero. The difference is presumably in the different functional form of the fits. Although our numbers are only $1.5\sigma$ apart, our conclusions

are opposite.

Another interesting conclusion can be drawn about the shape of the polarized momentum distributions. In our fits we used 8 adjustable parameters to calculate the polarized momentum distributions from the unpolarized distributions. However, as can be seen from Table 6.5, the errors for 6 of them: $A_Q$, $A_G$, $\alpha_u$, $\alpha_d$, $\alpha_Q$, and $\alpha_G$ are rather large. We can fix the low $x$ powers $\alpha_i$ using Regge behavior at $Q^2 = 0.34$ GeV$^2$ and ignore the gluon and sea quark contribution. In this case, there are only 2 free parameters, $A_u$ and $A_d$. Furthermore, we expect that the polarization of valence quarks goes to 1 as $x \to 1$ (see Chapter 2), in other words $|\Delta q_V(x)|/q_V(x) \to 1$ as $x \to 1$. This implies that $|A_u|$ and $|A_d|$ should be close to 1, which is indeed true (see Table 6.5). Thus, by using unpolarized momentum distributions at low $Q^2$ and some theoretical input about the low and high $x$ behavior, we can predict the spin structure functions with almost no free parameters. By evolving the momentum distributions using AP equations over a large range in $Q^2$, we essentially obtain a pQCD prediction for the spin structure functions which is insensitive to the initial distribution. The data for both the neutron and the proton can be reproduced within 2 $\sigma$ when we use only 2 adjustable parameters [30].

Finally, we can look at the $Q^2$ dependence of the asymmetry $A_1$ to check the scaling assumption, commonly used in the analysis of the spin structure functions. The comparison between the traditional evolution and evolution based on the AP equations is shown in Figure 6.12. As can be seen, the difference is noticeable, but is still smaller than the statistical errors of the experiment.

## 6.4 Conclusion and Outlook

Our experiment significantly improved the accuracy with which the neutron spin structure function is known. Perhaps the most surprising feature of our data is the apparent divergence of the neutron spin structure function at low $x$, in contradiction to the naive Regge behavior. This behavior requires us to analyze the data in the framework of NLO QCD to extract the information about the integral of $g_1^n$. On the basis of such analysis one can reach a number of conclusions:

- With our data, the Bjorken Sum rule is confirmed to an accuracy of 8%.
- The Ellis-Jaffe Sum rule is violated.
- If we adopt the AB renormalization scheme, in which the "proton spin crisis" is explained by a large gluon helicity contribution, we arrive at a contradiction again. Based on our analysis, the gluon contribution is only $\Delta G = 0.4$ and the total helicity carried by the quarks in the AB scheme is $\Delta\Sigma_{AB} = 0.25 \pm 0.1$, which implies that $\Delta s = -0.1 \pm 0.03$. This result is unexpected, since in the

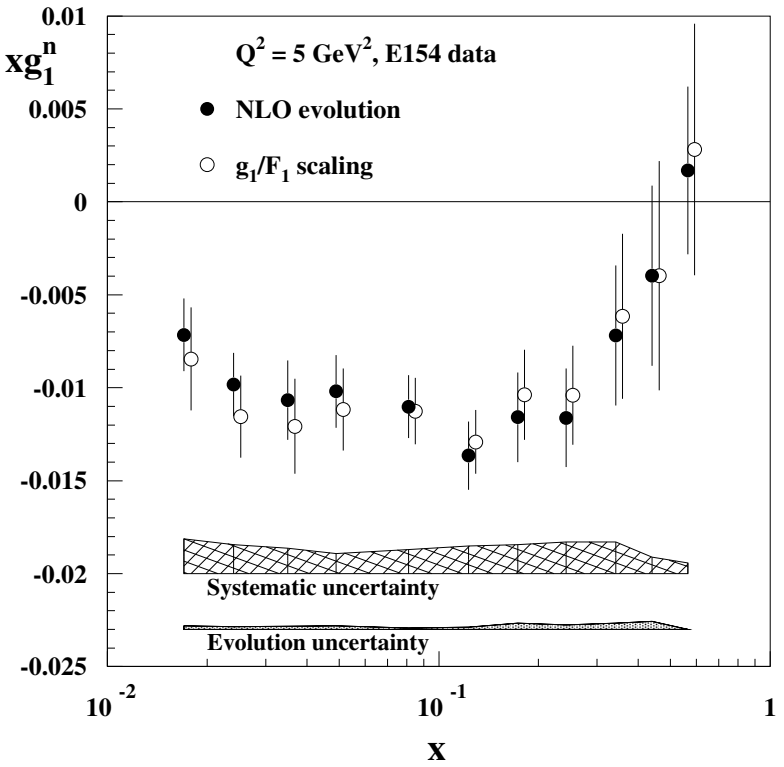


Figure 6.12: Traditional scaling and NLO $Q^2$ evolution.

AB scheme the chiral symmetry of QCD is preserved, and one expects that $\Delta s \simeq 0$. Therefore, it may be interpreted as a next generation proton (or, more appropriately, neutron) spin crisis. However, one should treat such conclusion with extreme caution. The extrapolation of $g_1$ to $x = 0$ contributes a significant amount to the first moments and is sensitive to the parametrization of the quark momentum distributions. The parametrization used in our analysis, while motivated by certain theoretical models, is not unique. A different analysis of the same data [31] gives $\Delta s$ which is only one sigma away from zero.

One of the main goals of our experiment was a precision measurement of the spin structure function at low $x$. We can now say that the low $x$ behavior is even more interesting than we thought, and one has to go to even lower $x$ to really understand it. This, undoubtedly, will be the goal of future experiments.

In the next year the results of E-155 will become available, giving a measurement of the proton spin structure function similar in accuracy to our neutron data. This will improve the precision with which one can do a global analysis of the polarized structure functions and test the Bjorken sum rule. E-155 will also measure the deuteron asymmetry and obtain the neutron structure function with comparable

accuracy. In the longer term, planning has started for an experiment at HERA which will use colliding polarized proton and electron beams to measure the proton spin structure function down to $x = 10^{-4}$. There is even a possibility of using a polarized $^3$He beam to obtain data on the neutron.

Our target represents a substantial improvement over previous polarized $^3$He targets, particularly in the dilution factor, the use of diode lasers, and the handling of systematic errors. However, some improvements are still possible, particularly in $^3$He polarization, by better optimization of the operating parameters. $^3$He targets polarized by spin exchange will continue to be widely used in nuclear physics experiments. Several experiments are planned at TJNAF [37]. A precision measurement of the neutron spin structure function at high $x$ will be able to test a prediction that $A_1 \to 1$ as $x \to 1$. A measurement at low $Q^2$ will observe a transition between the deep inelastic scattering and low energy behavior, establishing a connection between Bjorken and Gerasimov-Drell-Hearn sum rules. The electric form factor of the neutron will also be measured precisely.

And the searches for the Permanent Electric Dipole Moment will continue, aided by the efforts of the author.

# Bibliography


[1] B. Adeva *et al.* (the SMC Collaboration), Phys. Lett. B **320**, 400 (1994).

[2] P.L. Anthony *et al.* (the E-142 Collaboration), Phys. Rev. D **54**, 6620 (1996).

[3] M. Arneodo *et al.*, (the NMC Collaboration), Phys. Lett. B **364**, 107 (1995).

[4] K. Abe *et al* (the E-154 Collaboration), submitted to Phys. Rev. Lett.

[5] K. Abe *et al.* (the E-143 Collaboration), Phys. Rev. Lett. **74**, 346 (1995); Phys. Rev. Lett. **75**, 25 (1996).

[6] D. Adams *et al.* (the SMC Collaboration), Phys. Lett. B **329**, 399 (1994); Phys. Lett. B **357**, 248 (1995).

[7] B. Adeva *et al.* (the SMC Collaboration), Phys. Lett. B **302**, 533 (1993);

[8] J. Ashman *et al.* (the EMC Collaboration), Phys. Lett. **206**, 364 (1988).

[9] K. Ackerstaff *et al.* (the HERMES Collaboration), hep-ex/9703005 (1997).

[10] P.L. Anthony *et al.*, (the E142 Collaboration), Phys. Rev. Lett. **71**, 959 (1993).

[11] E. Reya, Phys. Rep. **69**, 195 (1981).

[12] F. Halzen and A. Martin, *Quarks and Leptons* (John Willey and So., New York, 1984).

[13] G. Altarelli, Phys. Rep. **81**, 1 (1982).

[14] T. Muta, *Foundations of Quantum Chromodymamics*, (World Scientific, Singapore, 1987).

[15] G. 't Hooft, Nucl. Phys. B **33**, 173 (1971).

[16] W.A. Bardeen, A.J. Buras, D.W. Duke, , and T. Muta, Phys. Rev. D **18**, 3998 (1978).

[17] T.D. Lee, *Particle Physics and Introduction to Field Theory*, (Harwood Academic, 1981).

[18] G. Sterman *et al.*, Rev. Mod. Phys. **67**, 157 (1995).

[19] V.N. Gribov and L.N. Lipatov, Sov. J. Nucl. Phys. **15**, 438 (1972); Yu. L. Dokshitzer, Sov. Phys. JETP **46**, 461 (1977); G. Altarelli and G. Parisi, Nucl. Phys. B **126**, 298 (1977).

[20] X.D. Ji and J. Tang, Phys. Rev. Lett. **76**, 740 (1996).

[21] R. D. Carlitz, J.C. Collins, and A.H. Mueller, Phys. Lett. B **214**, 229 (1988).

[22] G. Altarelli and G.G. Ross, Phys. Lett. B **212**, 391 (1988).

[23] G. T. Bodwin and J. Qiu, Phys. Rev. D **41**, 2755, (1990).

[24] H. Y. Cheng, Int. J. Mod. Phys. **11**, 5109 (1996).

[25] G. Altarelli and B. Lampe, Z. Phys. C **47**, 315 (1990).

[26] R. Mertig and W.L. van Neerven, Z. Phys. C **70**, 637 (1996); W. Vogelsang, Phys. Rev. D **54**, 2023 (1996).

[27] S. G. Gorishny and S.A. Larin, Phys. Lett. B **172**, 109 (1986); S.A. Larin and J.A.M. Vermasern, Phys. Lett. B **259**, 345 (1991).

[28] M. Glück, E. Reya, and A. Vogt, Z. Phys. C **67**, 433 (1995).

[29] M. Glück, E. Reya, M. Stratman, and W. Vogelsang, Phys. Rev. D **53**, 4775 (1996).

[30] K.Abe *et al*, (the E-154 Collaboration), submitted to Phys. Lett. B

[31] G. Altarelli, R. D. Ball, S. Forte, and G. Ridolfi, hep-ph/9701289

[32] A.D. Martin, R.G. Roberts, and W.J. Stirling, Phys. Lett. B **38**, 419 (1996).

[33] F.E. Close and R.G. Roberts, Phys. Lett. B **316**, 165 (1993).

[34] P.G. Ratcliffe, Phys. Lett. B **242**, 271 (1990).

[35] R.L. Jaffe and A. Manohar, Nucl. Phys. B **337**, 509 (1990).

[36] C. Bourrely, J. Ph. Guillet, and J. Soffer, Nucl. Phys. B **361**, 72 (1991).

[37] Z. Meziani, Proc. 7th RCNP Workshop on Polarized $^3$He Beams and Gas Targets, Kobe, Japan, (1997), to be published.

# Appendix A

# Shower Analysis

E154 Note #48

Yury Kolomensky, Mike Romalis
November 21, 1996

## Shower code for the "Caltech" analysis

This note describes the shower code used by the Caltech analysis group.

## A.1 Introduction

In this note, we describe the shower code used by the Caltech-based analysis. This code is one of the major parts of the raw analysis code that is different from the one used in the SLAC DST production. The shower counters provide electron identification via energy, $E/p$, and shower profile (shape, neural net) cuts. The cluster information is the basis for the tracking algorithm[1]; in addition, the shower position resolution directly affects momentum and angular resolution. The shower analysis meets certain challenges in the high rate environment of E154 due to the overlaps of the electron and pion clusters (Fig. A.1). Such overlaps create rate-dependent biases in energy and position reconstruction and calorimeter-based electron identification, and thus have a potential to alter experimental asymmetries. It is important to have an analysis algorithm that is robust in the high rate environment; it is also necessary to study and correct for any possible rate dependence.

The code benefited greatly from the experience with the existing SLAC code[2]. At the same time, it was an entirely new code written from scratch, so it provided an important cross-check of the existing algorithm. Besides, we improved the spatial and timing resolutions, and eliminated biases in the cluster position and energy reconstruction. Also, as an alternative to the neural network used in the SLAC analysis, we developed a particle ID method based on the information about the lateral

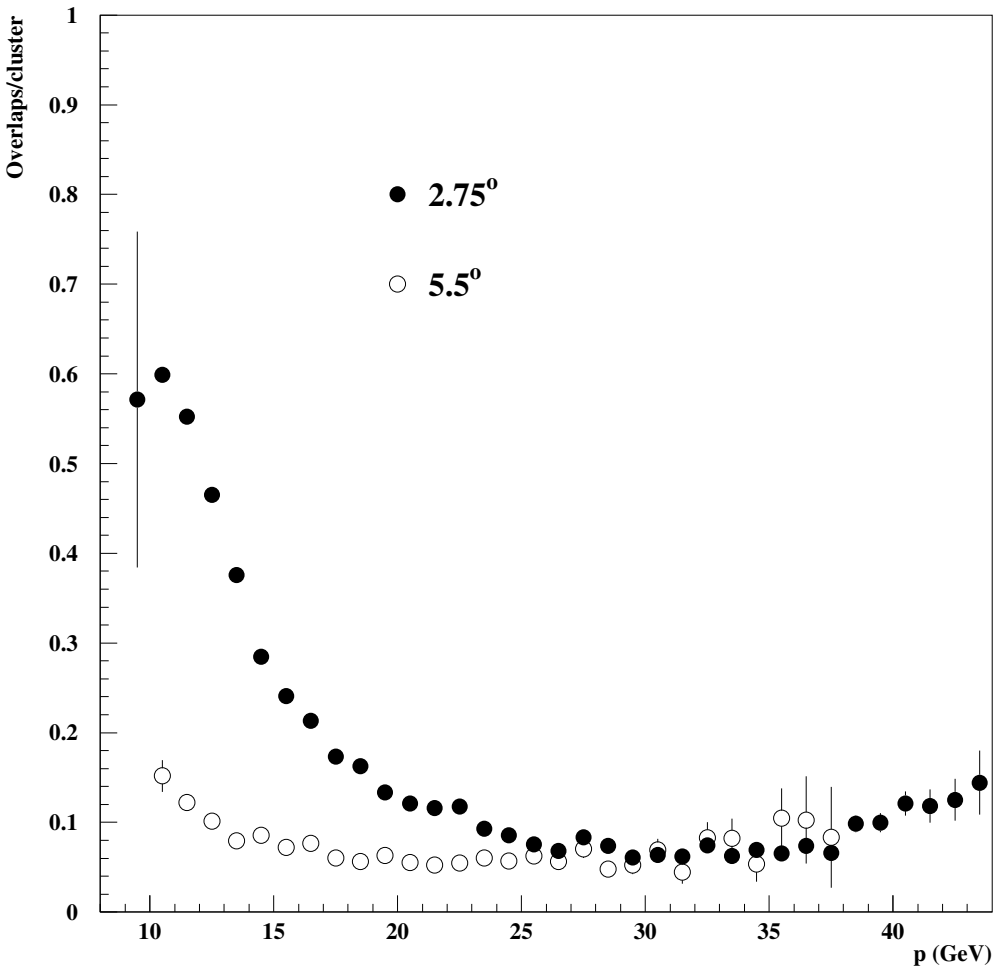


Figure A.1: Number of overlaps per electron cluster versus momentum of the electron in 2.75° (top) and 5.5° (bottom) spectrometers. A sharp rise at low momenta corresponds to increasing pion production rate.

shower profile (the "shape cut"). We will discuss the clustering algorithm and the shape analysis in the following pages.

In this note, we follow the definitions adopted in the SLAC shower code[2, 3]. An elementary *cell* is a signal induced by one particle in one block. Each cell is characterized by its *time* and *energy*. We record times of both leading (LE) and trailing edges (TE) of the photomultiplier pulses. Cell time is determined by its LE time. Cell energy is determined by the difference between TE and LE times as will be discussed below. Energies of all cells in one block always add up to the total energy deposited in that block in one spill. If a block does not have any TDC hits within one spill, we create one cell which carries full energy deposited in the block; the time of

such cell is undefined. A cell with a definite time is required to have a LE, but it does not always have a TE (misses of TE happen less than 1% of the time). A *cluster* is a collection of cells with common time that are grouped according to the set of rules to be discussed below.

## A.2 Clustering algorithm

### A.2.1 $5 \times 5$ clusters

Contrary to the standard SLAC analysis which employs the *cellular automaton*[4] technique, we have chosen a simpler and faster method sometimes referred to as "vector approach"[4]. As a first step, after the data from the TDCs and ADCs are copied into the local common blocks, we search the $10 \times 20$ shower array for the local energy maxima ("central blocks") that pass the following criteria:

1. There is at least 1 TDC hit in the central block;
2. The sum over 9 blocks around the central block

$$\sum_{3\times 3} E_i > E_{cut} = C_{cut} p_{\min}(row).$$

The first requirement ensures that the cluster candidate has timing information. Electrons energy deposition in the central block is always higher then the TDC threshold; the lack of a timing hit signals either a DAQ failure or an event affected by an overlap. Such clusters cannot be used in the further analysis. The second requirement provides a simple and effective pion rejection at the very early stage of the analysis. The value $p_{\min}(row)$ is determined by the lowest momentum of electrons that hit the particular block after passing through the spectrometer. This value is in principle different for every row (and is increasing from top to bottom of the calorimeter), in practice the value of 9 GeV was used for every block. The constant $C_{cut}$ was chosen to be 0.7, safely below any reasonable $E/p$ cut value[1]. Thus, most pions that deposit energy of less than 6.3 GeV are cut before the main clustering and tracking started, significantly reducing the precessing time.

Having found the central block, we share its energy among its cells. The cluster is started with the highest energy cell of the central block. We add to the cluster cells from the surrounding $5 \times 5$ matrix that

- among 8 blocks closest to the center and

[1]For the dedicated pion DST production, this value was lowered to 0.05.

1. Are in time with the central block, or
2. Have no TDC hits

- among the outer 16 blocks and

1. Are in time with the central block, or
2. Have no TDC hits and no other cluster nearby

The time window is set to be $|\Delta t| \leq 5$ nsec.

### A.2.2 Energy sharing

When two or more particles hit one block, energies are added in the ADC. To separate them, we use the correlation between the pulse height and the time difference between the leading (LE) and trailing edges (TE) of the pulse (Fig. A.2). For all pairs of leading and trailing edges (*cells*), we calculate the expected energy $e_i = f(t_i^{TE} - t_i^{LE})$ and error $\sigma_i$. We then minimize

$$\chi^2 = \sum_i \left( \frac{E_i - e_i}{\sigma_i} \right)^2 \tag{A.1}$$

with a constraint

$$\sum_i E_i = E_{tot} \tag{A.2}$$

where $E_{tot}$ is the full energy deposit in the block, and solve for cell energies $E_i$. The benefit of such an approach is obvious. For any TDC level, the dynamical range for the energy sharing is limited; from Fig. A.2 one can see that the meaningful information can only be extracted if the ratio of the pulse height to threshold $E/E_{thres} \leq 4$. Electron pulses are often much higher than that, especially for the low thresholds[2]. Pion pulses, on the contrary, are predominantly small. Thus, combining the pion and electron information reduces the error in electron energy determination. This is important to minimize the rate dependence associated with the $E/p$ cut.

### A.2.3 Cluster time and position

An energy-weighted average used by SLAC analysis

$$x = \frac{\sum_{blocks} x_i E_i}{\sum_{blocks} E_i} \tag{A.3}$$

[2]The values of the discriminator thresholds are summarized in Table A.1. Note the thresholds were set in mV, and the spread of thresholds in GeV corresponds to the spread of calibration constants.

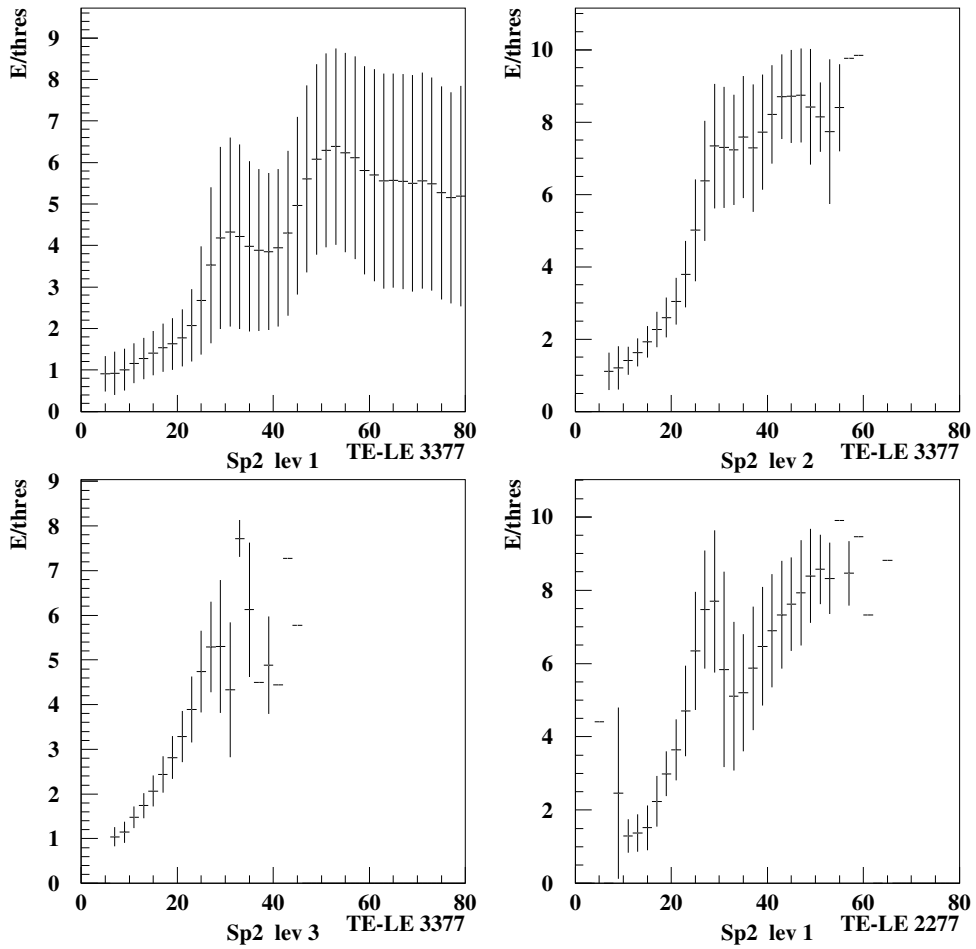


Figure A.2: The pulse height as a function of the difference between the leading and trailing edge times for different discriminator levels. The error bars represent the RMS of the distribution.

is known[5] to give a biased estimate of the cluster position due to the relatively coarse transverse segmentation of the calorimeter. It results in the bias towards the coordinate of the central block, as could be clearly seen in Fig. A.3 which shows the difference between the cluster and track positions for the SLAC code. The position bias is the strongest when electrons hit the boundary of the block ($x_{tr} - x_{sh} = \pm 32$ mm) and reaches 1 cm. Alternatively, we calculate the cluster position using the formula

$$x = A_x \left[2 - \exp(-c_x(r - b_x)) - \exp(-d_x(r - b_x))\right] \tag{A.4}$$

where $r = E_{side}/E_{c.b.}$ is the ratio of the energies in the side and central blocks. Coordinates determined by the blocks on either side of the central block are weighted

Table A.1: Range of discriminator thresholds

| Runs | Spec | mV | GeV | | |
|---|---|---|---|---|---|
| | | | min | max | average |
| 1304–2058 | 2.75° | 20 | 0.08 | 0.6 | 0.3 |
| | | 125 | 0.4 | 2.8 | 1.6 |
| | | 800 | 2.7 | 20.0 | 9.9 |
| | | 50 | 0.16 | 1.2 | 0.3 |
| 2059–2543 | 2.75° | 20 | 0.08 | 0.4 | 0.2 |
| | 2.75° | 125 | 0.4 | 1.9 | 1.12 |
| | 2.75° | 800 | 2.7 | 15.4 | 6.7 |
| | 2.75° | 50 | 0.15 | 1.16 | 0.4 |
| 2544–2902 | 2.75° | 20 | 0.09 | 0.23 | 0.15 |
| | 2.75° | 125 | 0.5 | 1.4 | 0.8 |
| | 2.75° | 800 | 2.8 | 8.0 | 4.7 |
| | 2.75° | 50 | 0.16 | 1.2 | 0.5 |
| 2902–3788 | 2.75° | 20 | 0.09 | 0.23 | 0.15 |
| | 2.75° | 125 | 0.5 | 1.4 | 0.8 |
| | 2.75° | 500 | 1.8 | 5.5 | 3.1 |
| | 2.75° | 50 | 0.16 | 1.2 | 0.5 |
| 1304–3788 | 5.5° | 50 | 0.0 | 0.8 | 0.4 |

Table A.2: Parameters of the Eq. (A.4).

| $A_x$ | $b_x$ | $c_x$ | $d_x$ |
|---|---|---|---|
| 17.1 | 0.031 | 3. | 31. |

by the uncertainties to calculate the cluster position. The parameters of the "double-spinup" function in (A.4), determined from the data (Fig. A.4), are listed in Table A.2.

The spatial resolution of the 2.75° and 5.5° shower counters is shown in Fig. A.5. The resolution in $x$ was determined to be 5.9 mm (2.75°) and 7.9 mm (5.5°), and in $y$ direction the resolution is 7.5 mm (2.75°) and 7.9 mm (5.5°). This is to be compared to $\sigma_x = 9.7$ mm and $\sigma_y = 9.3$ mm for the SLAC code (see Fig. A.3, top). The improvement in the position resolution results in a better angular and momentum resolution[1]. Note that the resolution was determined by comparing the coordinate of the shower cluster with the coordinate of the electron track at the $z$ position of the shower counter. The tracking spatial resolution without cluster constraints (i. e. for class 3 tracks used to determine the resolution) is expected to be $4 - 5$ mm at the shower counter[1], so the actual position resolution of the clustering might be even better than the numbers quoted above. The wings of the distribution are due to effects of accidental and correlated (delta rays) backgrounds in tracking. Fig. A.6

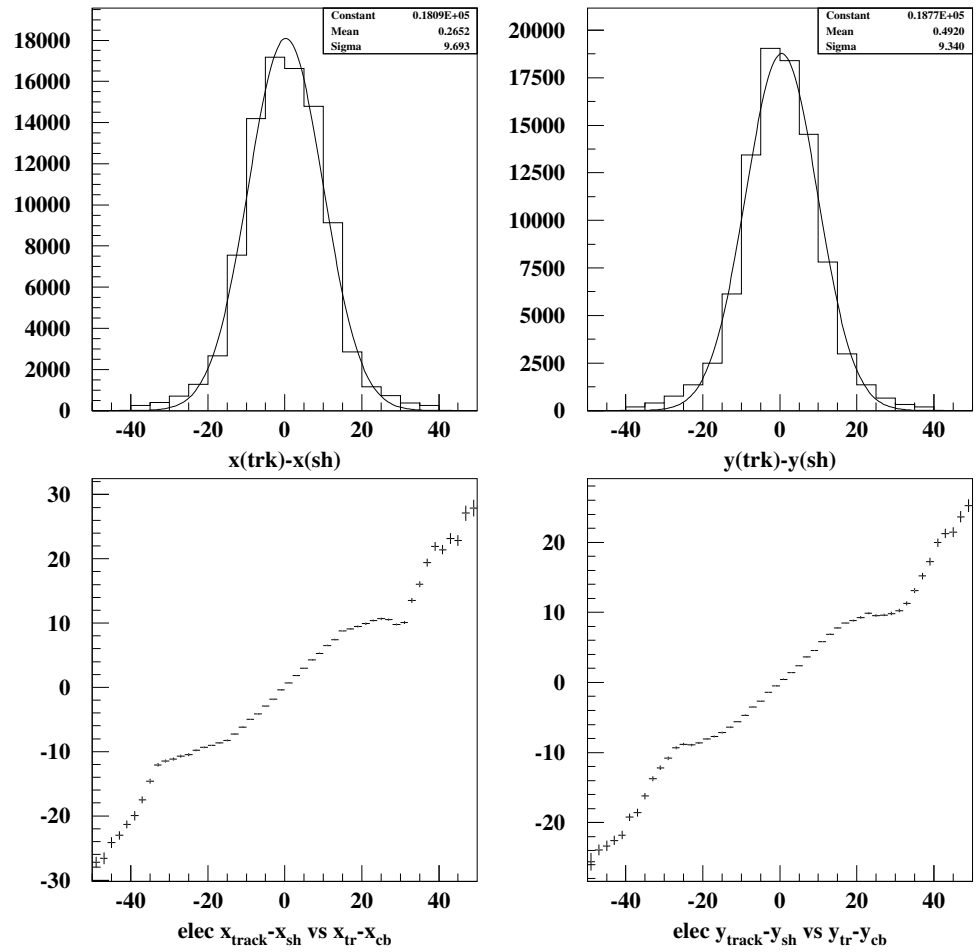


Figure A.3: Performance of the SLAC code. (top) Shower position resolution. (bottom) Cluster spatial offset versus the position of the track relative to the center of the central block. All numbers are in mm.

shows the distribution of the electron clusters in the calorimeter and the difference between the track position and the cluster position plotted versus the position of the track. Notice that there are no significant biases in either $x$ or $y$ direction (*c.f.* Fig. A.3, bottom).

The time of the cluster was determined by averaging TDC times of all blocks which energy deposit was at least 10% of the central block energy:

$$t = \frac{\sum_i t_i/\sigma^2(t_i)}{\sum_i 1/\sigma^2(t_i)} \tag{A.5}$$

where $\sigma(t_i)$ is the time uncertainty for each block. The energy cut minimized the timing jitter of the small pulses. Another potential problem with using blocks with

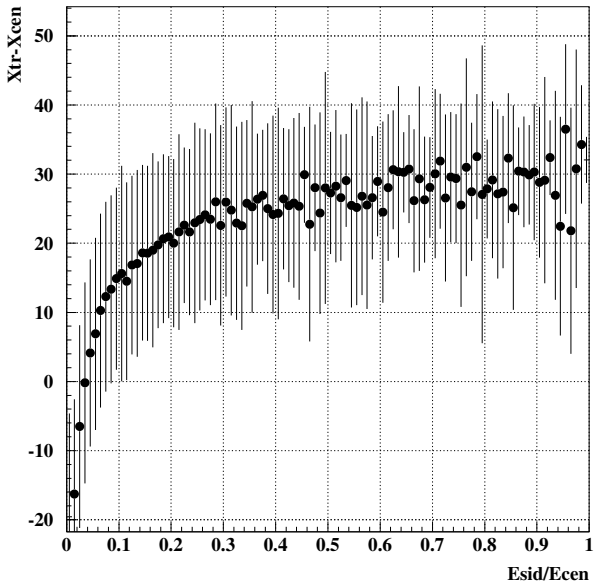


Figure A.4: Cluster position versus the ratio of energies in the side and central blocks. Error bars represent the RMS of the distribution.

small energy deposit is that they are usually on the tails of the shower and the effective $z$ position of the particles in the shower tail is significantly deeper than the core of the shower. The light from the shower tails reaches the phototube earlier than the light from the core (since the shower develops with the speed of light in the vacuum $c$ whereas the light propagation speed is $c/n$ with the index of refraction $n = 1.62$. The energy cut minimizes this effect so no correction is necessary.

The time resolution of both calorimeters is shown in Fig. A.7. With the technique described above we achieved the resolution of $\sim 0.7$ nsec (for electrons), compared to $\sim 0.9$ nsec for the SLAC code.

### A.2.4 Shower shape

The differences in electron and pion shapes are frequently used to separate the particles in the electromagnetic calorimeter. The standard measure of the shower cross section is the scaling variable referred to as the Moliére radius $R_m$[5]; for ASP(F2) lead glass used in our calorimeters $R_m \approx 5$ cm. For electromagnetic showers, 90% and 95% of the shower energy are contained in the cylinders with radii $R_m$ and $2R_m$ respectively. A simple approximation of the lateral shower profile is a one-exponential form[5]

$$A(R) = A(0)\exp(-R/R_0) \tag{A.6}$$

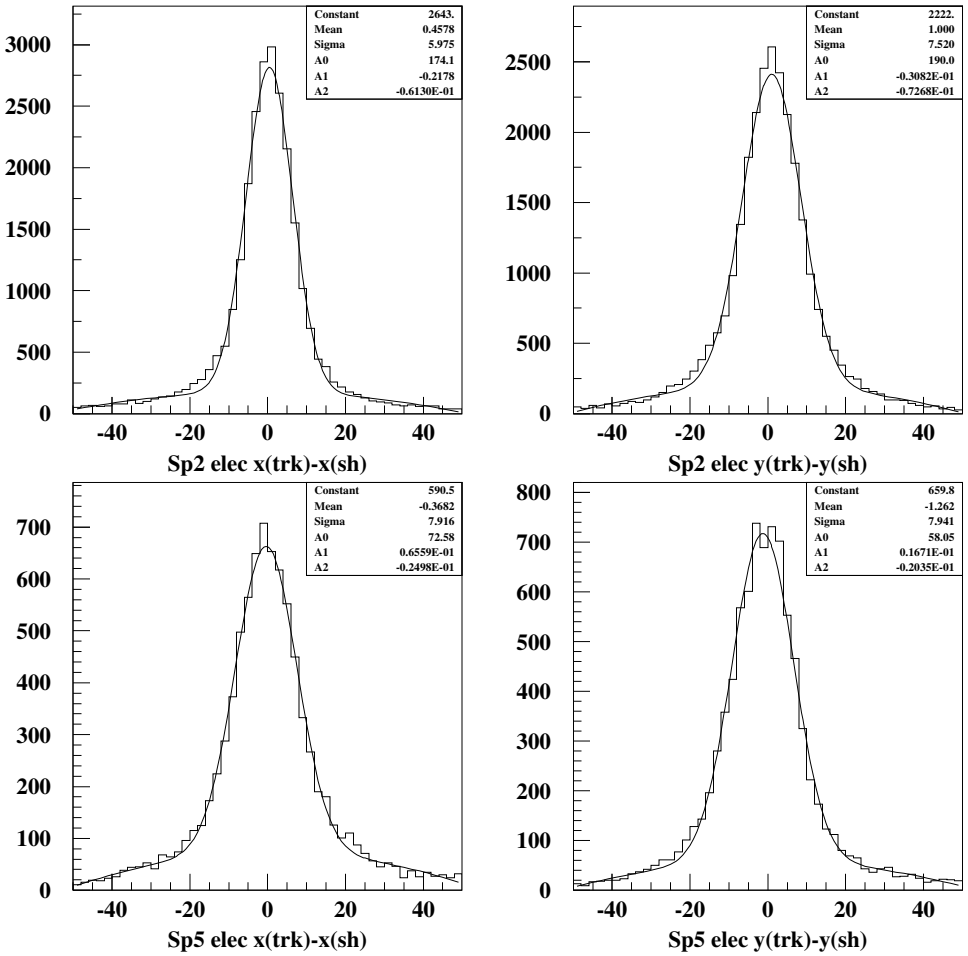


Figure A.5: The position resolution for electrons in 2.75° (top) and 5.5° (bottom) calorimeters. The fit is gaussian with quadratic background.

where $R$ is the transverse shower dimension and $R_0 = 0.25R_m$ is the damping constant. A more realistic model is a double-exponential shape[6]

$$A(R) = A_1 \exp(-R/R_1) + A_2 \exp(-R/R_2) \tag{A.7}$$

where the first exponent describes the narrow shower core, and the second corresponds to a longer tail of soft electrons and photons. For a finite calorimeter block of size $2s$, one can calculate the energy deposit from the shower centered at $(x_0, y_0)$:

$$E = E_0 \int_{-s}^{s} \int_{-s}^{s} dxdy \;\; a\left(\sqrt{(x-x_0)^2 + (y-y_0)^2}\right) \tag{A.8}$$

where $a(R)$ is a normalized shower profile of Equations (A.6) or (A.7) and $E_0$ is the total cluster energy. The resulting distribution is fitted to the following functional

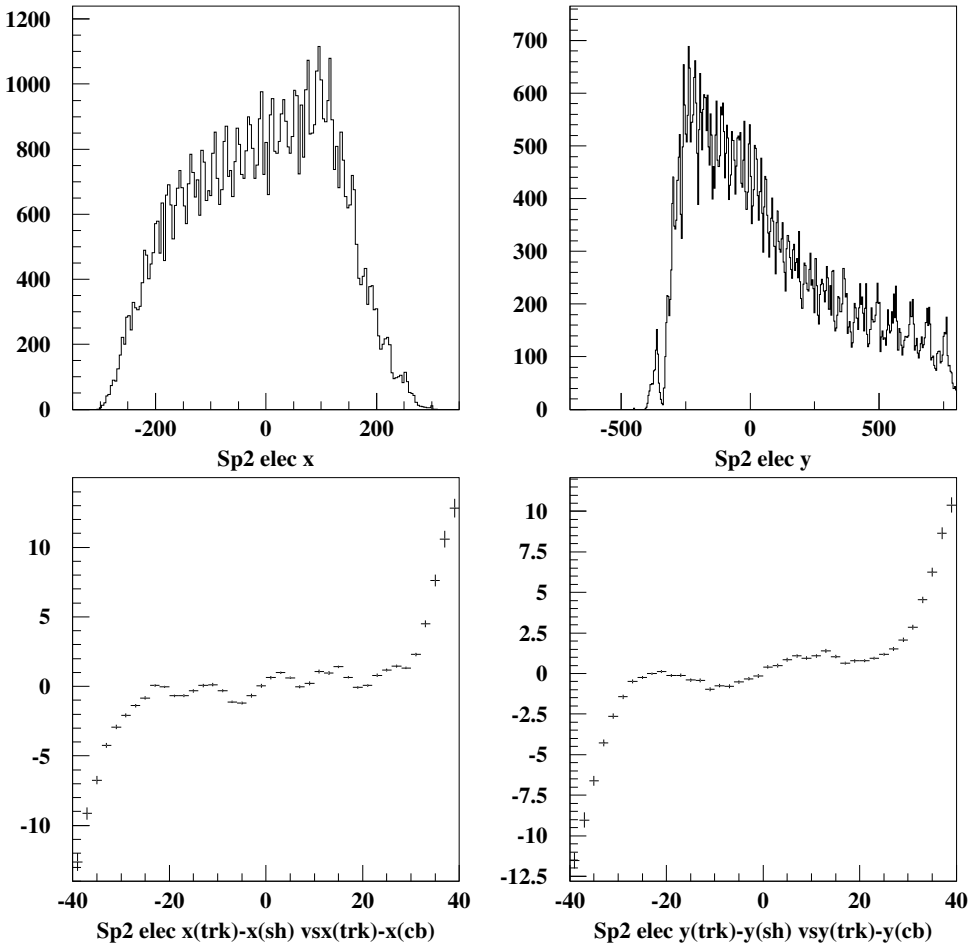


Figure A.6: (top) Cluster position distribution in the 2.75° shower counter for Caltech analysis. (bottom) The cluster spatial offset versus the position of the track relative to the center of the central block. The error bars are statistical.

form:

$$\frac{E}{E_0} = \mathcal{S}(x-x_0, y-y_0) = \begin{cases} h\,\{\,[1-\exp(-s/R_1)\cosh(d/R_1)]+ \\ \quad r[1-\exp(-s/R_2)\cosh(d/R_2)]\,\} & |d| \le s \\ h\,\{\,\sinh(s/R_1)\exp(-d/R_1)+ \\ \quad r\sinh(s/R_2)\exp(-d/R_2)\,\} & |d| > s\ , \end{cases} \tag{A.9}$$

where

$$d = (|x-x_0|^p + |y-y_0|^p)^{1/p}\,, \tag{A.10}$$

$(x, y)$ is the center of a given block and $(x_0, y_0)$ is the shower position. The electron shower profile is shown in Fig. A.8. The parameters of Eq. (A.9) are given

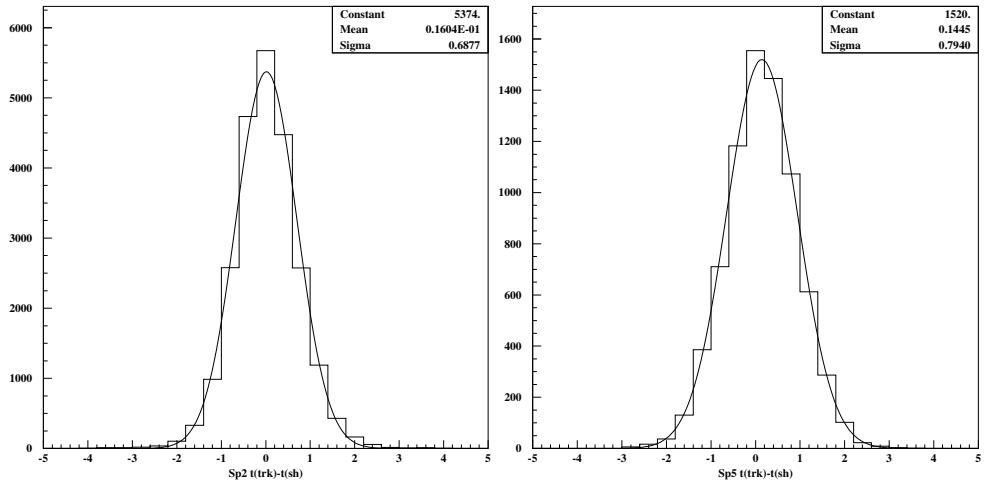


Figure A.7: Time resolution for electrons in 2.75° (left) and 5.5° (right) calorimeters. The fit is gaussian.

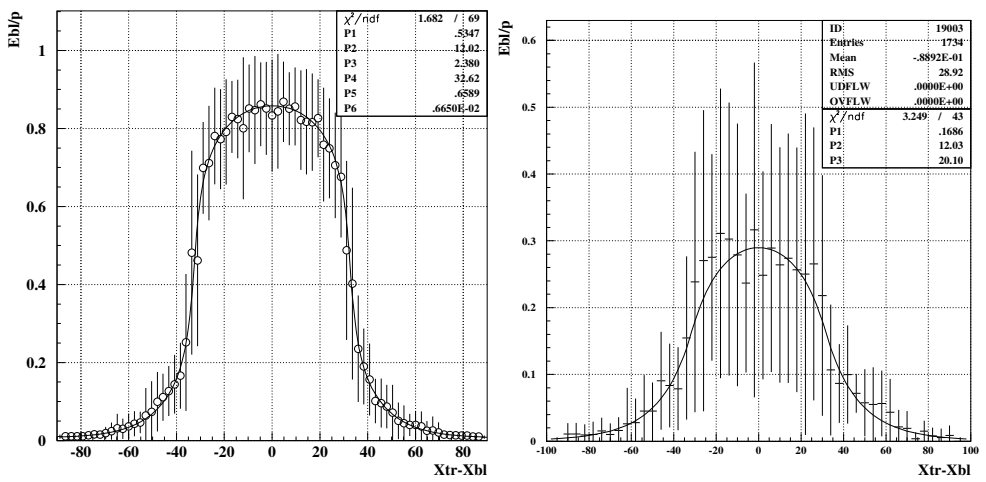


Figure A.8: (left) Electron shower shape; (right) Pion shower shape. Error bars represent the RMS of the distributions.

in Table A.3. The pion hadronic showers are wider on average (Fig. A.8), and the individual pion clusters are much less symmetric than the electron ones.

### A.2.5 Iterating the cluster shape

The energy sharing using the LE and TE information is not always perfect. First of all, it has a limited dynamic range. Pions with energy deposit below threshold are not detected by TDCs. Secondly, if electron energy deposit in one block is much

Table A.3: Parameters of the shower shape in Eq. (A.9).

| $s$ (mm) | $h$ | $r$ | $R_1$ (mm) | $R_2$ (mm) | $p$ |
|---|---|---|---|---|---|
| 34.0 | 0.872 | 0.3 | 4.0 | 19.0 | 2.9 |

bigger than the threshold, the time information is not reliable and leads to large errors in energy sharing. The latter fact is potentially more dangerous: if the energy of the cluster is underestimated due to energy sharing, the event may not pass the $E/p$ cut (typically, $E/p > 0.8$ cut is a part of electron definition). Another danger is the cluster position bias due to overlaps that translates into the error in momentum reconstruction. All these effects are rate-dependent and thus can bias the measured asymmetry.

In order to further reduce the rate-dependent effects in the cluster energy and position reconstruction, we developed an iterative procedure using the typical electron shape of Eq. (A.9)[3]. It works in two steps. First, we calculate the cluster position $(x_0, y_0)$ using Eq. (A.4) and the initial estimate of the cluster energy

$$E^{(0)} = \frac{E_c}{\mathcal{S}(x_c - x_0, y_c - y_0)} \tag{A.11}$$

where $E_c$ and $(x_c, y_c)$ are the energy and position of the central cell. We then calculate

$$\chi^2 = \sum_i \left( \frac{E_i^{(0)} - E^{(0)} \mathcal{S}(x_i - x_0, y_i - y_0) - E_{back}}{\sigma_i} \right)^2 \tag{A.12}$$

where the sum is over all cell in the cluster. Here $E_i^{(0)}$ is the initial energy of each cell determined as described in Section A.2.2. $E_{back} = 50$ MeV is the average background noise, and $\sigma_i$ is the uncertainty of the block energy given by

$$\sigma_i^2 = a^2 + \left( bE_i + c\sqrt{E_i} \right)^2 + \sigma_{share}^2 \tag{A.13}$$

where $\sigma_{share}$ is the uncertainty in energy sharing. A fit to the data yields $a = 0.15$ GeV, $b = 0$, and $c = 0.2$.

Minimizing $\chi^2$, we find a new estimate of energy $E = E^{(1)}$ and position $(x_0, y_0)^{(1)}$ (we linearize the problem by treating $\Delta x = x_0^{(1)} - x_0^{(0)}$ as perturbation). The energies of each cell $E_i$ are allowed to vary within their uncertainties. The cell is "frozen" (i. e. its energy is fixed) if change in its energy exceeds the uncertainty. The $\chi^2$ minimization is repeated with new cell energies $E_i^{(1)}$. The iterations converge if one of the following conditions is met:

[3]It is not used for special pion DST production.

- Cluster position does not change
- All cells are frozen
- Number of iterations exceeds 10

The convergence is typically achieved in 1–2 iterations. Cluster position $(x_0^{(n)}, y_0^{(n)})$ and its uncertainty are copied to the output common block and used in tracking.

After a track has been associated with the cluster, the electron coordinates at the shower counter are determined quite accurately. We can now fix the cluster position $(x_0, y_0)$ in Eq. (A.12) to be the track position at the shower counter, and minimize shape residuals varying only cluster energy $E$.

### A.2.6 Energy measurement

Three energy variables and corresponding uncertainties are reported by the shower code and are written to DSTs:

- $\boldsymbol{E_9}$: Sum of cells in $3 \times 3$ matrix around the central block.
- $\boldsymbol{E_4}$: Sum of four most energetic blocks in the cluster (the central block, the most energetic blocks in $x$ and $y$ directions, and 1 diagonal block). The sum is scaled by a factor of 1.05 to normalize it to $E_9$.
- $\boldsymbol{E_1}$: energy determined in iterative process (after tracking).

The ratios $E_1/E_9$ and $E_4/E_9$ and their momentum dependence are shown in Eq. (A.9). $E_9$ is a basic energy definition and is used for shower calibration. The advantage of $E_4$ and $E_1$ over $E_9$ is reduced sensitivity to overlaps. $E_4$ samples smaller number of blocks than $E_9$ and therefore the pileup probability for $E_4$ is lower. The drawback is that $E_4$ is an approximation that is reasonably good up to energies of $\sim 30$ GeV. At higher energies, the shower broadens and energy deposit into other blocks of the $3 \times 3$ matrix becomes increasingly important. This is evident from Fig. A.9: the ratio $E_4/E_9$ deviates significantly from 1 starting at $p \sim 30$ GeV. The iterated energy $E_1$ does not exhibit such a behavior (Fig. A.9).

Fig. A.10 shows the ratio $E/p$ for electrons in both spectrometers. Left plots correspond to $E_9$ energy, and right plots are for $E_1$ energy. The energy resolution is comparable to that of SLAC code. In Fig. A.11 we show the ratio $E_1/p$ in the 2.75° calorimeter for four special cases: clusters with no overlaps (top left), clusters with an overlap in any of the blocks (top right), clusters in overlaps in the central block (bottom left), and clusters with the central block on the edge of the calorimeter. No significant degradation of energy resolution and no significant bias is observed for either case. Fig. A.12 shows the same plots for the low $x$ (2.75° spectrometer, $9 < p < 12$ GeV). Again, energy determination is reasonably stable.

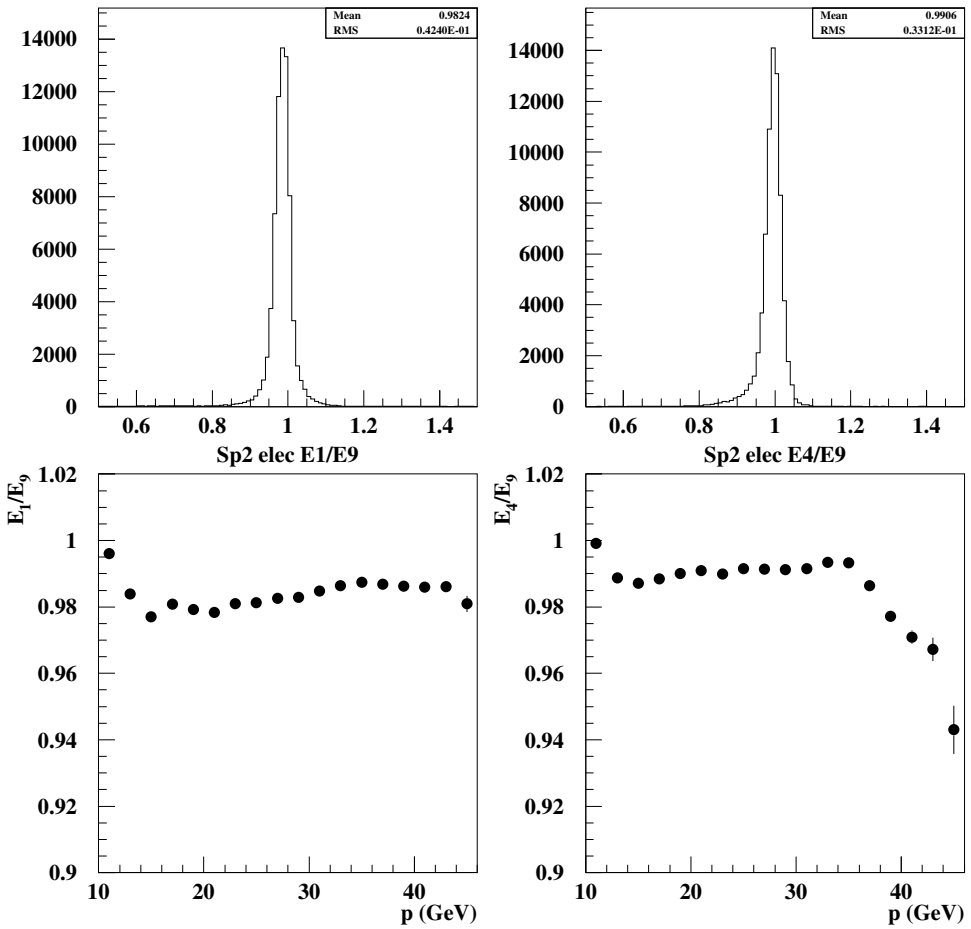


Figure A.9: Ratios of energies $E_1/E_9$ (top,left) and $E_4/E_9$ (top,right) and their momentum dependence (bottom).

## A.3 Shape cut

The difference between pion and electron shapes (Fig. A.8) can be used to separate electrons from pions using only shower counter information. SLAC analysis uses the algorithm based on a multi-layered neural network[4, 7]. A set of input parameters (discriminating variables), e. g. energy deposited in each cluster block, cluster position, etc., combined in a non-linear fashion, identifies the event. Due to its non-linear nature, the properties of the network highly depend on the environment (rate, pion to electron ratio, etc.) and the event sample on which the network is "trained" (i. e. the way the relative weights of the input parameters are determined). Thus, the neural network efficiency is potentially rate dependent[7, 8], especially at low momentum where the rate of pion-electron overlaps is high. The overall efficiency is about 90%

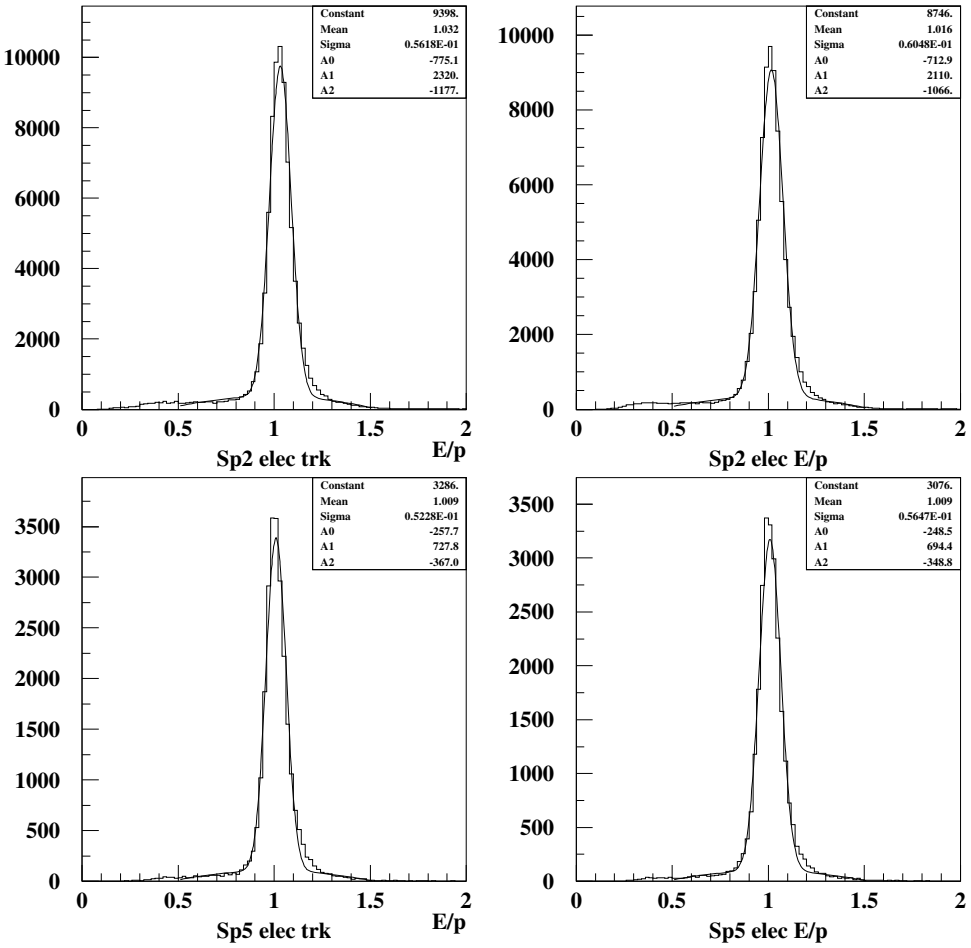


Figure A.10: Ratios $E_9/p$ (left) and $E_1/p$ (right) for electrons in 2.75° (top) and 5.5° (bottom) spectrometers. The fit is gaussian with quadratic background.

at low $x$[7], and increases with momentum.

We discriminate between electron and pion showers by calculating the deviation from the electron shower shape $\chi$

$$\chi = \frac{1}{E_4}\sqrt{\sum_i \left(E_i - E_4 \mathcal{S}(x_i - x_0, y_i - y_0) - E_{back}\right)^2} \tag{A.14}$$

where the summation is over all cluster blocks, except for four most energetic ones used in the definition of $E_4$. The electrons are identified by the requirement $\chi \leq 0.045$. The distribution of variable $\chi$ for electrons and pions is shown in Fig. A.13. The electron and pion efficiencies are shown in Fig. A.14. The electrons were selected by requiring a track with cherenkov pulses in both tanks higher than 4.5 photoelectrons and a good match with the shower cluster. The pions were defined as class 2 (no

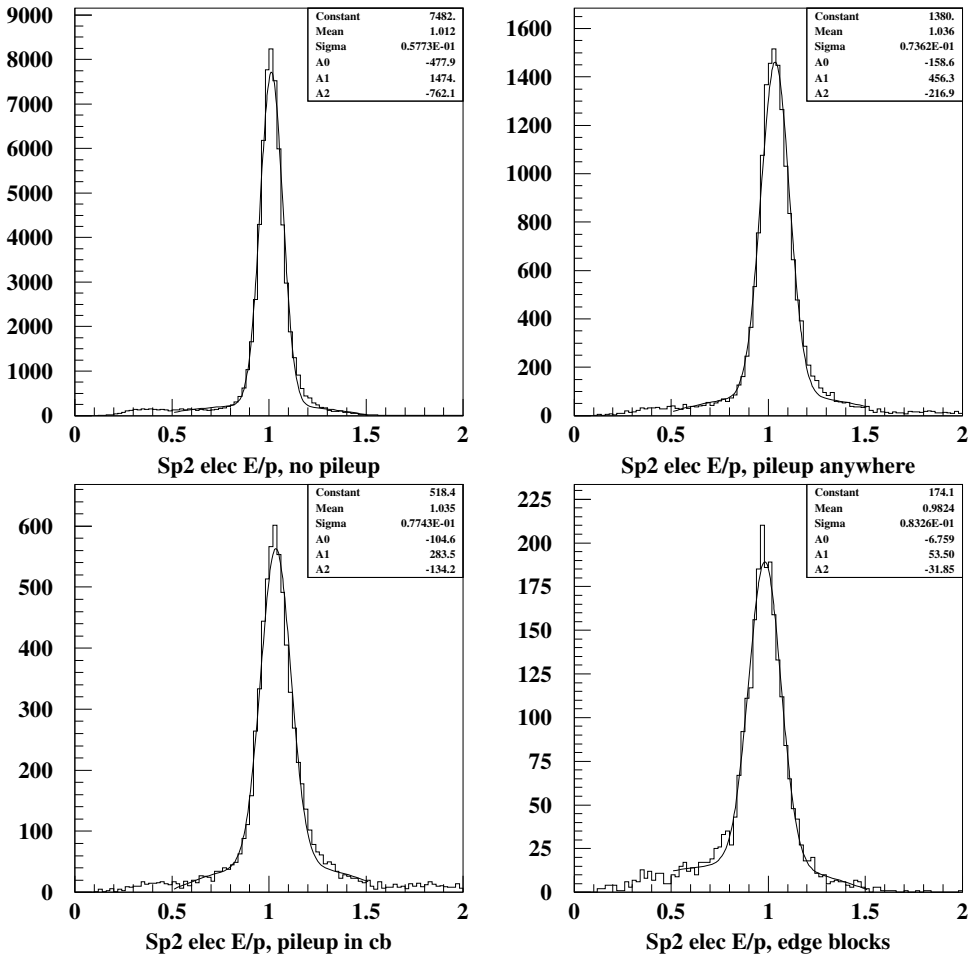


Figure A.11: Ratios $E_1/p$ for electron clusters in 2.75° counter with (top left) no overlaps, (top right) overlaps in any of the cluster blocks, (bottom left) overlaps in central block, (bottom right) clusters with the central block on the edge of the calorimeter.

cherenkov signals and a good match with a shower cluster) tracks. Open circles in Fig. A.14 show the efficiencies for the electron and pion samples that included additional cut $E/p > 0.8$.

Several observations can be made. First, the pion rejection power of the $\chi$ cut is about 10:1. However, for the pions that have $E/p > 0.8$, it is at best 2:1, comparable to the SLAC neural network performance under the same conditions[7]. The reason is that pions usually deposit large amount of energy if they undergo a charge exchange $\pi^- p \to \pi^0 n$. $\pi^0$ decays instantly into two photons and develops an electromagnetic shower; such a cluster is almost indistinguishable from an electron cluster. Since the shape or neural net cut is optional and is usually applied in *addition* to the $E/p$ cut,

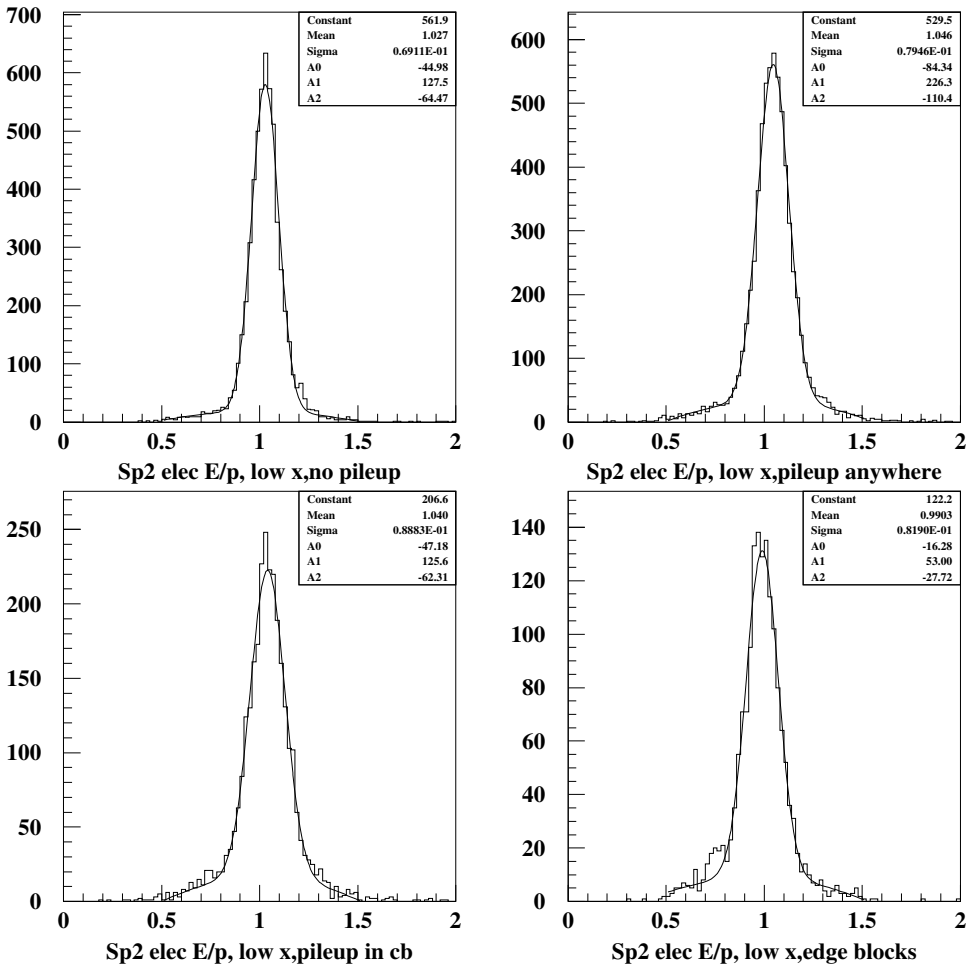


Figure A.12: Same as Fig. A.11 for electrons with $9 < p < 12$ GeV.

it is the later rejection power that is relevant for the background analysis.

Electron efficiency ranges from 92% to 95% at low $x$ (depending on the run), and slowly increases with momentum. It is comparable, if not slightly higher, than the neural network efficiency[7]. The variations with the run conditions are smaller than quoted for the SLAC code[7] that implies smaller rate dependence[4]. The reason for a sharp drop at about 30 GeV is use of variable $E_4$ in Eq. (A.14). As was shown above (Fig. A.9), it deviates significantly from the true cluster energy starting at about 30 GeV, and the shape function $E_4\mathcal{S}(x_i - x_0, y_i - y_0)$ systematically underestimates true cell energy. The situation is improved, indeed, if other energy variables, $E_1$ or $E_9$ are used in Eq. (A.14) (Fig. A.15). This effect was discovered too late to be applied to

[4]The rate dependence of the overall shower efficiency, including the shape cut, was studied by Piotr Zyla[10] and was found to be small.

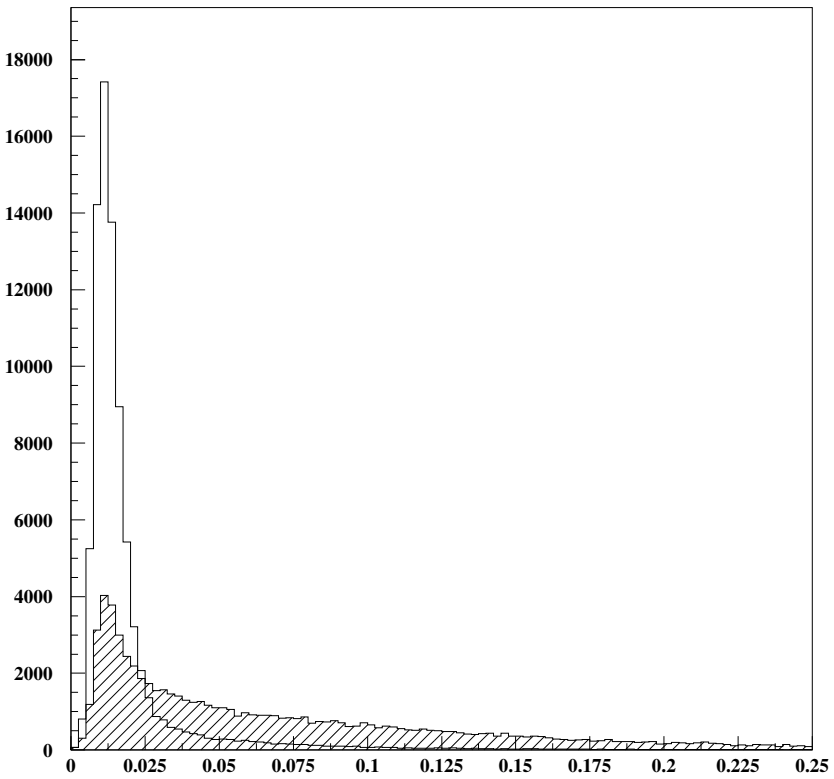


Figure A.13: Distribution of the shower shape variable $\chi$ for electrons (open) and pions (hatched).

the DST production code. Instead, we turn off the shape cut for $p > 30$ GeV where pion contamination is negligible[9].

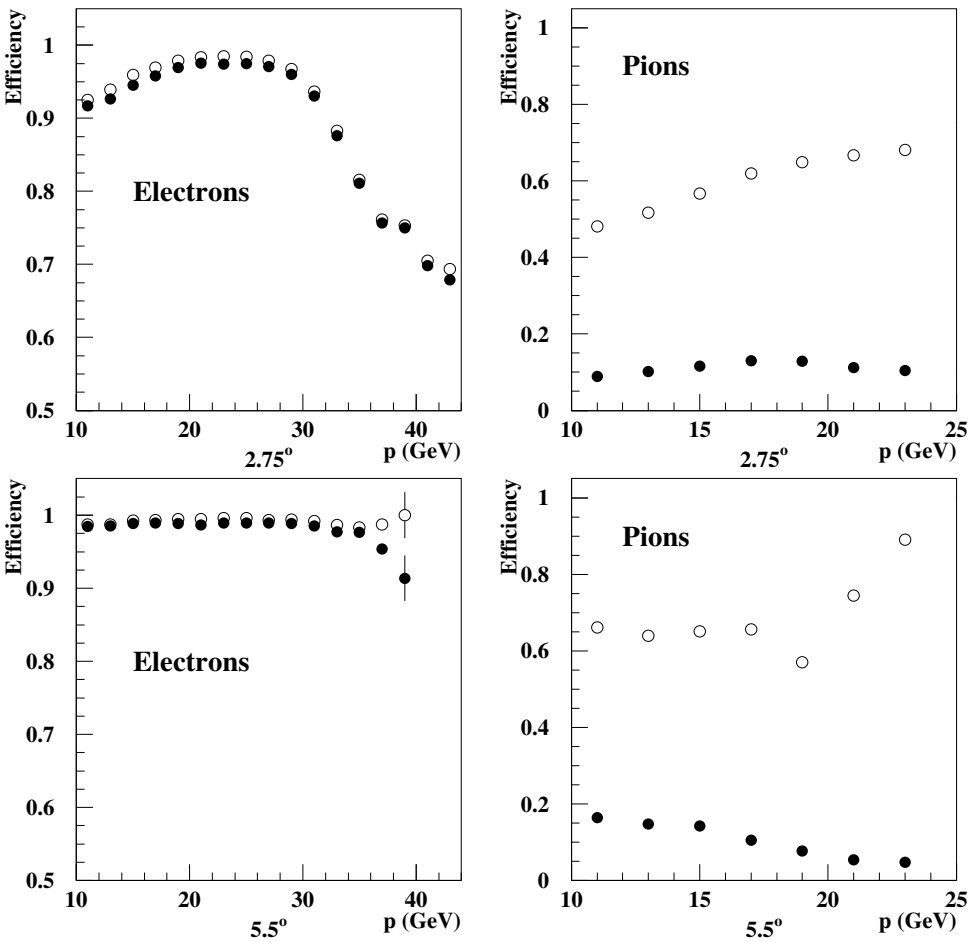


Figure A.14: Efficiencies of the shape cut for electrons (left) and pions(right) for 2.75° (top) and 5.5° (bottom) shower counters. A sample of electrons and pions is formed using the tracking and cherenkov information as described in the text (closed circles). Open circles show efficiencies for the samples that included $E/p > 0.8$ cut.

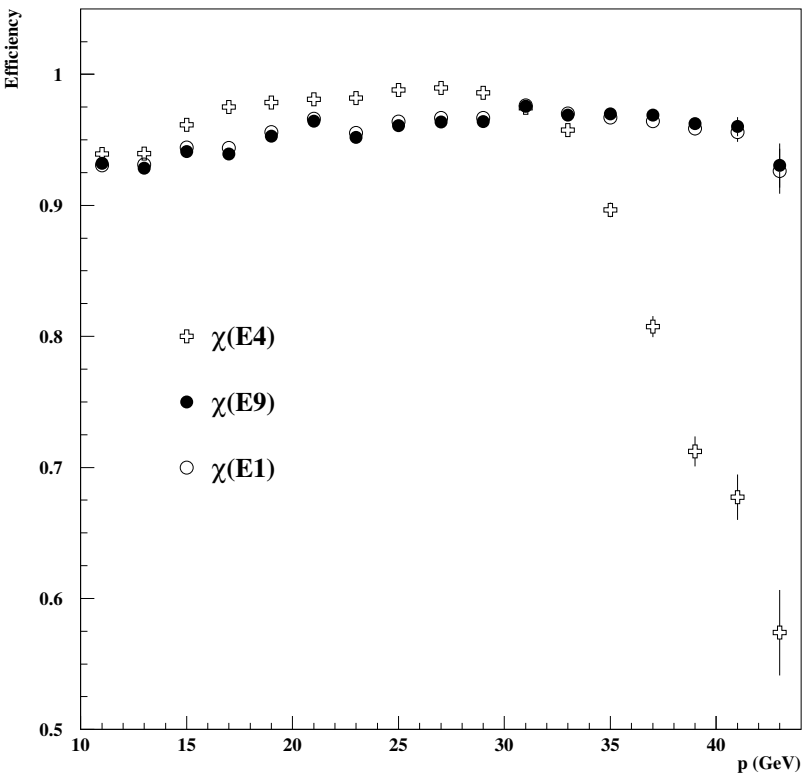


Figure A.15: Efficiency of the shape cut with different energy variables. Energy used in Eq. (A.14) is $E_4$ (crosses), $E_1$ (open circles), $E_9$ (closed circles). Note that the drop in efficiency disappears for $E_1$ and $E_9$.

# Bibliography


[1] Yu. Kolomensky, E154 technical note #53 (1996).

[2] S. Incerti, E154 technical note # 30 (1996).

[3] S. Incerti and Y. Terrien, E154 technical note # 22 (1995).

[4] V. Breton, H. Fonvieille, P. Grenier, C. Guicheney, J. Jousset, Y. Roblin, F. Tamin, Nucl. Instr. Meth. A **362**, 478 (1995).

[5] N. V. Rabin, Inst. Exp. Tech. **35**, 1, (1992).

[6] Yu. Bushnin *et al.*, Nucl. Intr. Meth. **106**, 493, (1973);
G. A. Akopdjanov *et al.*, Nucl. Instr. Meth. **140**, 441 (1977);
F. Bianchi *et al.*, Nucl. Instr. Meth. A **279**, 473 (1989);

[7] S. Incerti, E154 technical note # 31 (1996).

[8] D. Kawall, Ph. D. thesis, Stanford University (1995).

[9] Yu. Kolomensky and F. Sabatié, E154 technical note # 44 (1996).

[10] P. Zyla, E154 collaboration meeting, May 1996.

# Appendix B

# Pressure Broadening

## Pressure broadening of Rb $D_1$ and $D_2$ lines by $^3$He, $^4$He, $N_2$, and Xe: line cores and near wings*

M.V. Romalis, E. Miron†, G.D. Cates
Physics Department, Princeton University, Princeton, NJ 08544

We studied the line shape of Rb $D_1$ and $D_2$ resonance lines in the presence 1 to 10 amg. of several foreign gases: $^3$He, $^4$He, $N_2$, and Xe. We found that the line cores are well describe by an asymmetric line shape for a Van der Waals interatomic potential. The width and shift of the lines is proportional to the density of the foreign gas with high degree of accuracy, while the asymmetry is independent of the density. The constants of proportionality for pressure broadening and shift were measured with much higher accuracy than in previous experiments. We also studied the density dependence of the transition oscillator strength.

## B.1 Introduction.

The study of pressure broadening of atomic resonance lines by collisions with neutral atoms has a long history starting with work of Michelson [1], who observed that the line width increases with pressure in a roughly linear fashion. Early theoretical work by Lorentz [2] and Weisskorf [3] predicted a lorentzian shape for the line core, treating the broadening as an interruption of the radiation wave train by collisions with gas atoms. This approach is called the impact approximation. Later work by Lindholm [4] and Anderson [5] also predicted the shift of the line center and a dispersion-like

*To be submitted to Phys. Rev. A.
†Permanent Address: NRCN, P.O. Box 9001, Beer Sheva 84910, Isreal.

asymmetry of the line core. The experimental measurements of the line cores are reviewed by Chen and Takeo [6], Lewis [7], Allard and Kielkorf [8]. The widths and shifts of the alkali metals spectral lines in the presence of noble and other chemically inert gases have been studied very extensively, with perturber gas pressures up to several tens of atmospheres. The accuracy of most measurements, however, is only about 10-20%.

Another important feature of the pressure broadening is the formation of satellite lines. This effect is most easily explained in the framework of the quasi-static approach, first developed by Kuhn [9]. It relates the line intensity to the dependence of the energy difference between the atomic levels involved in the transition on the distance between the colliding atoms. An extremum in the energy difference results in the formation of a satellite line. The quasi-static formalism can be applied most successfully to the far wings of the atomic lines. In a series of papers Gallagher and co-workers used the measurements of the far wing profiles to extract the interatomic potentials for a number of alkali metal-noble gas pairs [10].

A unified quantum-mechanical theory for the line core and wings was developed by Szudy and Baylis using the Franck-Condon treatment [11]. It also predicted a specific lineshape for the line core and the satellite lines for a given interatomic potential. For the line core, the lowest order correction to the lorentzian line shape is a dispersion-like asymmetry. The first quantitative observation of the asymmetry was reported by Walkup et al. [12] for Na resonance lines in the presence of about 10 torr. of several noble gases. Higher order corrections can also be calculated. The calculation was done for a van-der-Waals potential [13]. A recent review by Szudy and Baylis [14] summarizes the quantitative experimental and theoretical results on the line shape for the cores and far wings of spectral lines, including satellite lines.

Here we present a measurement of line cores and near wings of Rb $D_1$ and $D_2$ lines in the presence of $^3$He, $^4$He, $N_2$ and Xe. Our measurements are done for perturber gas densities ranging from 1 to 10 amg. Compared with previously available data, our results on line widths, shifts and asymmetry are much more accurate. We also report on the first quantitative study of the spectral line cores exhibiting deviations from the lorentzian line shape beyond the first order dispersion asymmetry. Our measurements are in good agreement with calculations by Walkup *et al.* [13] for a van-der-Waals potential. We also present measurements of the pressure dependence of the $D_1$ and $D_2$ oscillator strengths.

One of the initial motivations for this work was an accurate determination of pressure broadening and shift density coefficients, which can be used to measure gas pressure in experiments using optical pumping. The technique of Rb optical pumping and spin exchange [15, 16] finds many applications. $^3$He polarized using this technique is used in measurements of the neutron spin structure functions [17, 18], tests of fundamental symmetries [19], neutron polarizes and analyzers [20], and magnetic

resonance imaging (MRI) of the lungs [21]. $^{129}$Xe polarized by Rb-Xe spin exchange is used in MRI [22], surface studies [23], cross-polarization experiments [24] and other applications. $N_2$ and sometimes $^4$He [25] are added to aid in the process of optical pumping. In some of these applications it is important to know accurately the pressure of the gas in the optical pumping cell. For example, in a recent precision measurement of the neutron spin structure function $g_1^n$ at SLAC [18], the $^3$He pressure in the target cells was determined with an accuracy of 1% by measuring the broadening and shift of Rb $D_1$ and $D_2$ lines using the results of this paper as a calibration. Also, the knowledge of pressure broadening and oscillator strength can be used to determine the Rb number density and for modelling of the optical pumping process. These technique were used in several experiments [26, 27]. The choice of the gases used for this study, while motivated by the optical pumping experiments, provides a good sampling of noble (He is least polarizable, Xe is most polarizable) and diatomic ($N_2$) gases.

In section B.2 we describe our experiment, which uses a laser absorption method to measure the line profile. Section B.3 describes our analysis technique, which is based on the classical limit of the unified Franck-Condon theory [11] for a van-der Waals interatomic potential [13]. In section B.4 we present our results for the line width, shift, asymmetry and oscillator strength.

## B.2 Experimental Technique.

In this experiment we used laser absorption spectroscopy. We measured the transmission of a laser beam through a cell filled with Rb vapor and the perturber gas as the frequency of the laser was scanned through the resonance. This technique is free from optical attenuation effects, which can cause distortions of the line core in measurements based on detection of the fluorescence light. It also allows simple measurements of the oscillator strength, provided that the Rb number density is known. The schematic of the experiment is shown in Figure B.1. We used a single frequency Ti:Sapphire ring laser (Coherent 899-29) to scan across the absorption lines. The laser linewidth of about 500 kHz and wavelength jitter of about 100 MHz were much smaller than the width of the pressure broadened lines, so no instrumental corrections were needed. The absolute wavelength was measured by a build-in wavemeter with an accuracy of 0.5 GHz, sufficient for shift measurements. The power of the laser was attenuated to a few mW/cm$^2$ by two reflections from uncoated glass to avoid saturating the atomic line. For this intensity the product of the optical excitation rate times the atomic lifetime $I\sigma\tau$ was always less than $3 \times 10^{-4}$. The laser beam was chopped at a frequency of 340 Hz. The incident and transmitted intensities were measured using silicon photodiodes. The signals were detected with lock-in amplifiers

referenced to the chopper and digitized by a computer. The same computer also controlled the wavelength scan. Fluctuations in the incident light intensity were canceled by dividing the transmitted intensity by the incident intensity. We also recorded the fluorescence coming from the cell. It was not used in the analysis of the line core because of significant optical attenuation, but was used to check the transmission measurements in the far wings. To ensure the linearity of the photo-diodes and the absence of line saturation, we also performed measurements with the light intensity attenuated by a factor of 1000, to a few $\mu$W/cm$^2$. No changes in the line shape were observed.

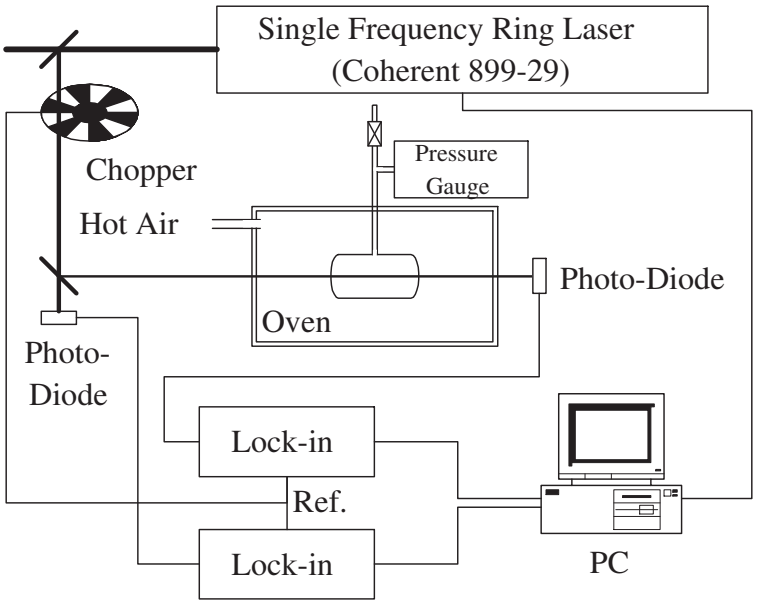


Figure B.1: Experimental Setup. The laser intensity is attenuated by reflection from two optical blanks. The computer controlled the wavelength scan and stored the lock-in amplifier signals.

The cell used for the measurements was a simple cylinder 7.15 cm long. It was placed in a large oven heated by flowing hot air. The temperature was measured with an RTD sensor and controlled by an analog Omega controller. We also measured the temperature with an accurate mercury thermometer. The air flow rate was stabilized using a pressure regulator. The temperature in the oven was stable to 0.1°C with time and varied by less than 1°C across the cell. For most measurements the temperature was 80°C corresponding to Rb number density $[Rb] = 1.4\times10^{12}$ cm$^{-3}$, so the optical thickness varied between 0.3 and 0.005, depending on the density of the gas. Some measurements with $^4$He were also done at 100°C and 60°C.

The signal to noise ratio was limited by two factors. The laser intensity fluctuations, which are on the order of 5-10%, were not perfectly canceled by taking the ratio of the incident to transmitted intensity. In addition, because the coherence length of the laser is very long, the glass windows of the cell and the oven can act as etalons, resulting in oscillations of the transmitted intensity. This effect was reduced by expanding the laser beam. The signal to noise ratio is the worst for the highest density, because the optical thickness is small and the maximum absorption is only 30%. At low density, on the other hand, the absorption is very strong, and the line shape can be distorted by the finite dynamic range of the A/D board. The temperature and the length of the cell were chosen to find the best compromise between these two limitations.

The cell, made out of Pyrex, was initially baked under high vacuum and a small amount of Rb was distilled into the cell. It was then filled with about 10 amg. of the gas. About 8-12 measurements were performed with densities ranging from 10 to 1.5 amg. After each measurement some of the gas was released from the cell. When the pressure in the cell approached atmospheric pressure, the measurements were stopped. The cell was attached to the vacuum system, evacuated and filled with the next gas.

## B.3 Data Analysis

The collision-broadened line profile is usually expressed in terms of the Fourier transform of the dipole autocorrelation function $g(\tau)$ [5, 11]:

$$I(\omega) \propto \frac{1}{2\pi} \int_{-\infty}^{\infty} d\tau \, e^{-i(\omega-\omega_0)\tau - ng(\tau)} \tag{B.1}$$

where $g(\tau)$ is given in the classical approximation by:

$$g(\tau) = \left\langle 1 - e^{i\int_0^\tau dt\omega(R(t))} \right\rangle \tag{B.2}$$

and $n$ is the density of the foreign gas perturbers. Here $\omega(R) = (V_e(R) - V_g(R))/\hbar$, where $V_g(R)$ and $V_e(R)$ are the interatomic potentials for the ground and excited state respectively. $R(t)$ describes the path of the perturbing atom in the center of mass frame during the collision. For straight trajectories $R(t) = \sqrt{b^2 + v^2t^2}$. The average $\langle ... \rangle$ is over the impact parameter $b$ and thermal velocity $v$.

Equation (B.1) can be simplified for low perturber density by performing two integrations by parts and expanding the exponent in powers of $n$ [14, 29, 30]. The low density approximation is justified if the time between collisions is much longer than the duration of the collisions. This condition is satisfied for most of our data.

The specific limits of applicability will be discussed later. With this approximation we get [14]:

$$I(\xi) \propto \frac{\Gamma(\xi)}{\xi^2 + (\gamma/2)^2} \tag{B.3}$$

where $\xi = \omega - \omega_0 - \Delta$. Here $\gamma$ is the full width and $\Delta$ is the shift of the lorentzian line core. They are defined in terms of $g(\tau)$ by: $\gamma/2 - i\Delta = ng'(\infty)$, which predicts a linear dependence of the width and shift on the gas density.

The dependence of $\Gamma$ on the detuning $\xi$ is responsible for deviations from the lorentzian shape. In terms of the autocorrelation function $g(\tau)$ it is given by [14]:

$$\Gamma(\xi) = \int_{-\infty}^{\infty} d\tau e^{-i(\omega-\omega_0-\Delta)\tau} g''(\tau) \tag{B.4}$$

To calculate $\Gamma(\xi)$ one needs to assume a specific shape for the difference potential $\omega(R)$. The calculation for a van der Waals potential $\omega(R) = (V_e(R) - V_g(R))/\hbar = -C_6/R^6$ has been done by Walker *et al.* [13] and will be used in our analysis. They convert equation (B.4) to the following form [30, 29]:

$$\Gamma(\xi) = n\left\langle v \int_0^{\infty} 2\pi b db \left| \int_{-\infty}^{\infty} dt \omega(R(t)) \exp\left[ i\left( \xi t - \int_{-\infty}^{t} \omega(R(t'))\, dt' \right) \right] \right|^2 \right\rangle \tag{B.5}$$

assuming straight classical trajectories for $R(t)$. The results of their calculation are parametrized in the following fashion:

$$\Gamma(\xi) = n v_{th} 8\pi R_{th}^2 I(\xi T_d) \tag{B.6}$$

where $T_d = C_6^{1/5} v_{th}^{-6/5}$ is the duration of the collision, $R_{th} = T_d v_{th}$ is the effective radius of the collisions, and $v_{th} = \sqrt{2kT/\mu}$ is the most probable thermal velocity in the center of mass frame. $I(x)$ is a dimensionless function of a dimensionless parameter $x = \xi T_d$ that contains all numerical information. If $C_6$ is positive (the excited state is more attractive than the ground state), then $x < 0$ corresponds to the quasi-static wing and $x < 0$ to the anti-static wing. The low density approximation, used in derivation of equation (B.3), can be quantitatively expressed as $T_d\gamma \ll 1$, since the time between collisions is on the order of $1/\gamma$.

The results of the calculation for $I(x)$ are plotted in Figure B.2. The calculation is done numerically for $-2.4 < x < 2.4$ with an accuracy better than 1%, except near $x = 2.4$, where the error is $\leq 5\%$ [13]. For $x < -2.4$ the quasi-static result $I(x) = \pi/6\sqrt{x}$ is sufficiently accurate. For the anti-static wing $x > 2.4$ one can use the result of an asymptotic expansion $I(x) = 0.8464\sqrt{x}\exp\left(-2.1341\, x^{5/9}\right)$ derived in [28]. We use a polynomial to interpolate between the calculated points and smoothly match to the asymptotic functions. Near $x = 0$, $I(x)$ is well approximated by a linear function

$I(x) = 0.3380 - 0.2245\,x$. It shows that the first order correction to the lorentzian profile is a dispersion term. This observation has been confirmed experimentally [12]. By making measurements at higher pressures (but still low enough for the low density approximation to be valid), we can observe the non-linear behavior of $I(x)$. We can also check the prediction of the theory that the asymmetry, parametrized by the collision time $T_d$, should be independent of the pressure.

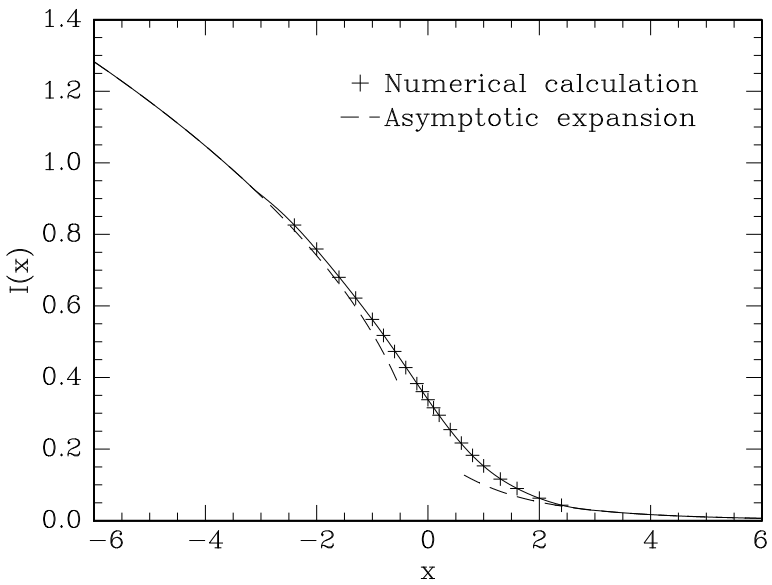


Figure B.2: Function I(x) calculated by Walkup *et al.* [13] for a van der Waals potential.

The intensity transmitted through the cell $I_T$ is given by:

$$I_T = I_0 \exp\left(-\left[Rb\right]\sigma\left(\nu\right)L\right) \tag{B.7}$$

where $I_0$ is the incident intensity and $L$ is the length of the cell. To extract the line profile from our data we plot $S(\nu) = \ln\left(G_T I_T / G_0 I_0\right) = -\left[Rb\right]\sigma\left(\nu\right)L + \ln\left(G_T/G_0\right)$, where $G_T$ and $G_0$ are the gains of circuits used to detect the transmitted and incident intensity respectively. These data are fitted to the following equation:

$$S(\nu) = \frac{AI\left(2\pi T_d\left(\nu - \nu_c\right)\right)}{\left(\nu - \nu_c\right)^2 + \left(\gamma/2\right)^2} + B \tag{B.8}$$

where the constants $A, B, T_d, \nu_c$, and $\gamma$ are allowed to vary to minimize the $\chi^2$ of the fit. The constant $B$ absorbs the values of the signal gain and does not carry

any physical information. To correct for the ground state hyperfine splitting, we fit to the sum of four functions (two for each $^{85}$Rb and $^{87}$Rb) in the form (B.8) with appropriate weights and shifts. This results in a very small correction. We ignore much smaller hyperfine splitting of the excited state. We also ignore Doppler broadening, which gives a negligible contribution to our width. The asymmetry due to collision correlations [31] is also negligible.

Also of interest is $\int \sigma(\nu)\, d\nu = \pi r_0 c f$, where $r_0 = 2.82 \times 10^{-13}$cm. is the classical electron radius and $f$ is the transition oscillator strength. This gives us a relationship between the oscillator strength and the Rb number density. If we assume that the Rb number density is given by the equilibrium vapor pressure, we can measure the oscillator strength and study its dependence on the gas density.

We note that for a pure van der Waals potential the width, shift and asymmetry can be calculated for a given value of $C_6$ [4]:

$$\begin{aligned} \gamma &= 17.0 n v_{th}^{3/5} C_6^{2/5} \\ \Delta &= 0.182\gamma \\ T_d &= C_6^{1/5} v_{th}^{-6/5} \end{aligned} \tag{B.9}$$

However, these equations are not in good agreement with experimental data. Therefore, we vary all constants independently. Then we can compare our results with values predicted by equations (B.9) using $C_6$ determined from measurements of atomic polarizability [32].

## B.4 Results and Discussion.

### B.4.1 $^3$He and $^4$He data.

The $D_1$ absorption cross-section for several pressures of $^3$He is shown in Figure B.3. The cross-section is fitted to equation (B.8). Because the value of the asymmetry is quite small, the results of the fit based on the Walkup function $I(x)$ are indistinguishable from the fits using only a first order approximation, which gives a dispersion-like asymmetry:

$$S(\nu) = \frac{A\left(1 + 0.664\ 2\pi T_d\ (\nu - \nu_c)\right)}{(\nu - \nu_c)^2 + (\gamma/2)^2} + B \tag{B.10}$$

For example, for the largest value of $T_d$ ($D_1$ line for $^4$He) detuning of 500 GHz corresponds to $x = 1$, the point where $I(x)$ just starts to deviate from the linear behavior. The dispersion form of the asymmetry can be derived without reference to a particular interatomic potential [33]. Our data agree very well with equation (B.8) for all densities studied. Small oscillations in the data for the highest density are due to the windows of the cell acting as etalons.

| | $^4$He | | $^3$He | | Temp. Depen. |
|---|---|---|---|---|---|
| | This Work | Previous Results | This Work | Previous Results | |
| $D_1$ full width, GHz/amg. | 18.0±0.2 | 16.6±3 [34] 17.6 [35] | 18.7±0.3 | 19.9±0.4 [37] | $T^{0.05\pm0.05}$ |
| $D_1$ line shift, GHz/amg. | 4.3±0.1 | 8.0 [36] 5.2 [35] | 5.64±0.15 | 5.78±0.2 [37] | $T^{1.1\pm0.1}$ |
| $D_1$ asymmetry, $T_d$, $10^{-13}$s | $-3.5 \pm 0.1$ | | $-1.9 \pm 0.1$ | | |
| $D_2$ full width, GHz/amg. | 18.1±0.2 | 17.4±3 [34] 19.4 [35] | 20.8±0.2 | | $T^{0.53\pm0.06}$ |
| $D_2$ line shift, GHz/amg. | 0.46±0.06 | 0.77 [34] 1.8 [35] | 0.68±0.05 | | $T^{1.6\pm0.4}$ |
| $D_2$ asymmetry, $T_d$, $10^{-13}$s | $-0.44 \pm 0.1$ | | $-0.73 \pm 0.1$ | | |

Table B.1: Broadening and shift coefficients, asymmetry parameters and temperature dependence for $^3$He and $^4$He. Negative value of $T_d$ implies that $C_6 < 0$.

The dependence of the line width and shift on the gas density is shown in Figure B.4. As predicted by the theory at low densities the dependence is quite linear. In all cases the offset of a linear fit is consistent with zero within error bars. The broadening and shift density coefficients are summarized in Table B.1. We also found that the asymmetry is independent of the density. Because the asymmetry is quite small, the best fit value of the asymmetry is strongly correlated with the fit value of the line center. Therefore, in addition to fitting each pressure scan individually, we also fitted them simultaneously with a common value of $T_d$. When the number of adjustable constants is reduced from 5 per scan to about 4.1 (10 data sets are analyzed with a common value of $T_d$), the value of $\chi^2$ increases by only 1-2%. This confirms that the asymmetry is independent of density.

The low density approximation used in the analysis requires that $T_d\gamma \ll 1$. To check the validity of this approximation we calculate the critical density $n_c$ for which $T_d\gamma = 1$. The most stringent constraint comes from the $D_1$ line in $^4$He, which gives $n_c = 25$ amg. Thus, the condition is satisfied, although not by a large margin. To check if the broadening and shift are slightly non-linear due to the breakdown of the low density approximation we fit the lowest four data points independently. The broadening and shift coefficients change by less than 1 sigma indicated in Table B.1. Therefore, we conclude that the low density approximation remains valid for $n/n_c$ approaching unity.

We have also studied the temperature dependence of the pressure broadening and

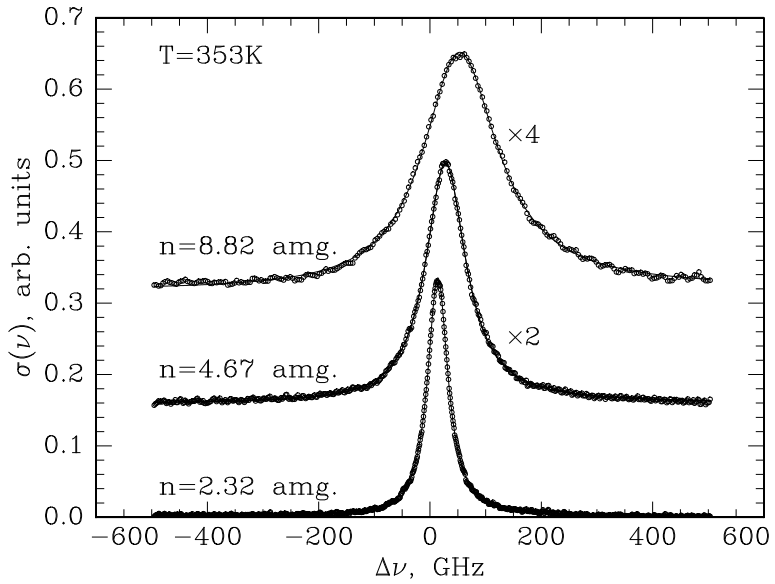


Figure B.3: Absorption cross-section for Rb $D_1$ line in the presence of 3 different densities of $^3$He. The solid lines are fits to equation (B.8). The curves have arbitrary offset and are scaled for better display.

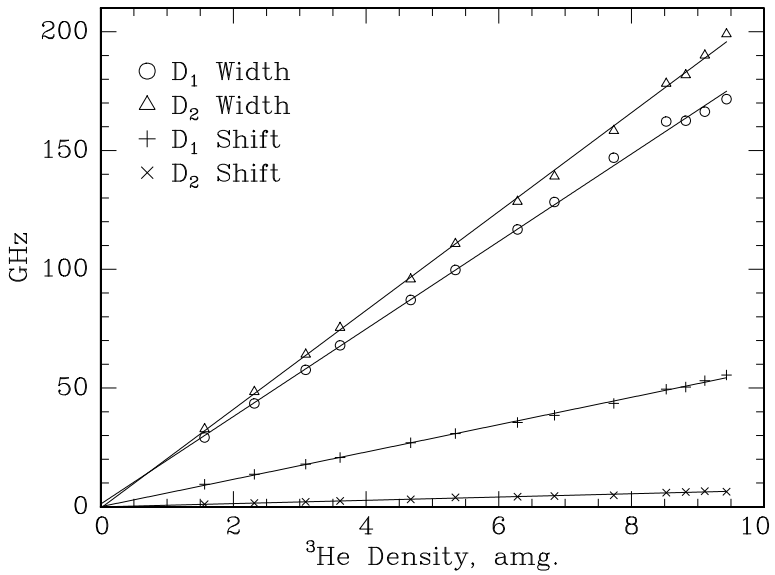


Figure B.4: The dependence of the shift and width of Rb $D_1$ and $D_2$ lines on the density of $^3$He.

shift. The temperature dependence can come from two effects. The average velocity of the collisions depends on temperature through $v_{th} = \sqrt{2kT/\mu}$. In addition, the probability of finding a He atom a distance $R$ from the Rb atom is proportional to $\exp\left(-V_g\left(R\right)/kT\right)$. However, if one assumes straight path trajectories for $R\left(t\right)$ in equation (B.2), this factor is neglected. Such approximation is justified, because typical values of $V_g\left(R\right)$ for the line core correspond to about 5 K, much lower than the temperature of the atoms. Thus, the factor $\exp\left(-V_g\left(R\right)/kT\right)$ is very close to unity. If all temperature dependence is due to the average velocity, then the data for $^3$He are equivalent to the $^4$He data taken at a temperature higher by a factor of $\mu_4/\mu_3 = 1.312$. Figure B.5 shows the line widths and shifts for $^4$He measured at 60, 80 and 100°C, as well as the data for $^3$He taken at 80°C and converted to effective $^4$He temperature of 463 K. As can be seen, the scaling between the temperature and reduced mass is reasonably well satisfied within error bars. The temperature dependence is very different for the four quantities studied. This is to be contrasted with predictions based on the van der Waals $R^{-6}$ interaction which give $T^{0.3}$ dependence for all four quantities [4]. We fit the temperature dependence to a power law $T^n$, with the results for $n$ shown in Table B.1.

This temperature dependence is used to convert previous measurements of the $^4$He and $^3$He width and shift density coefficients to our temperature. In general, our results are in agreement with previous measurements, although in some cases it is difficult to judge the agreement quantitatively because the authors do not quote a error for their data. There is only one measurement ($^3$He $D_1$ width and shift) with an accuracy comparable to ours [37]. Although the results for the shift are in good agreement, the width measurements disagree. This may be due to the fact that in [37] the authors use a different functional form to describe the line asymmetry and do not correct for the instrumental broadening of 18 GHz.

We can compare our results with predictions based on the van der Waals interaction using equations (B.9). The line center is shifted to the blue and $T_d < 0$, which implies that the interatomic difference potential is repulsive (i.e. $C_6 < 0$). On the other hand, the long range van der Waals interactions are always attractive, and larger for the excited state than for the ground state, so one expects $C_6 = C_e - C_g > 0$, as can be seen in Mahan's numbers derived from atomic polarizability [32]. However, because of low polarizability of He, the Rb-He van der Waals interactions are very weak and at shorter distances are overwhelmed by core repulsion [38]. Apparently, the line shift and asymmetry are dominated by the repulsive core interactions. The anomalously small value of the shift and asymmetry for the $D_2$ line is most likely due to cancelation of the effect of van der Waals attraction and core repulsion.

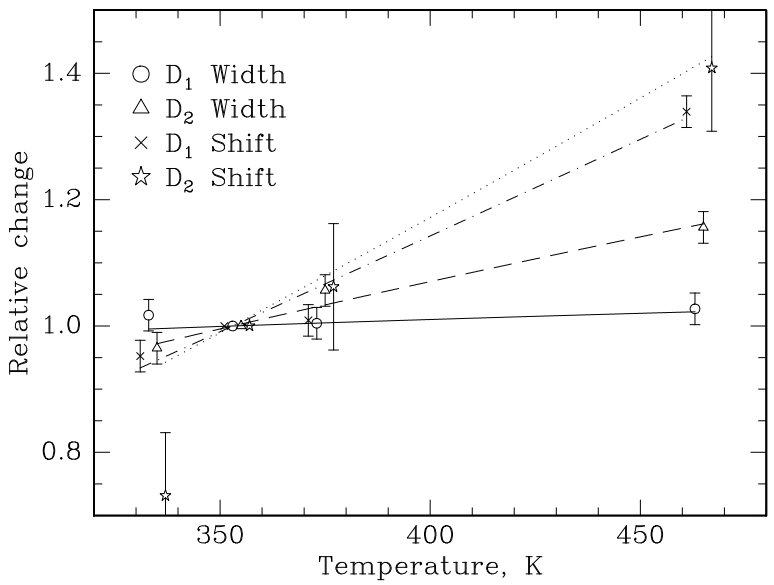


Figure B.5: Temperature dependence of the line width and shift. Relative change normalized to 353 K is plotted. The data points are shifted slightly in temperature for clarity. The lowest 3 points are for $^4$He, while the highest point is for $^3$He scaled as described in the text.

### B.4.2 $N_2$ and Xe data.

$N_2$ and Xe are heavier than He and have a smaller thermal velocity. In addition, they are more polarizable and, therefore, have a stronger van der Waals interaction with Rb. As a result, the duration of the collisions $T_d = C_6^{1/5} v_{th}^{-6/5}$ is longer and the low density approximation is not satisfied for all densities studied. Figure B.6 shows the absorption cross-section for $N_2$ at two different densities. For $N_2$ the critical density corresponding to $T_d\gamma = 1$ is equal to $n_c = 5.5$ amg. As can be seen from Figure B.6, the line shape at low density ($n = 2.66$ amg.) is described very well by equation (B.8), while at $n = 7.43$ amg. it shows small systematic deviations. Figure B.7 shows the values of the line shift and width as a function of $N_2$ density. As before, we find that the asymmetry is independent of density. To determine the pressure broadening and shift rates we fit only the lowest 3 data points with $n < 4$ amg. For higher density the widths deviate slightly from the linear behavior, while the shift remains quite linear. Table B.2 summarizes our results for the pressure broadening and shift coefficients and the asymmetry. To our knowledge, no previous measurements for Rb-$N_2$ broadening exist. Because $N_2$ is diatomic, it has a large radiationless quenching and mixing cross-sections, unlike the noble gases. It results in the reduction of the Rb excited state

lifetime and contributes to broadening. Using the values of the cross-sections from [39], we calculate that inelastic processes contribute 3.3 GHz/amg. width to the $D_1$ line and 3.0 GHz/amg. to the $D_2$ line.

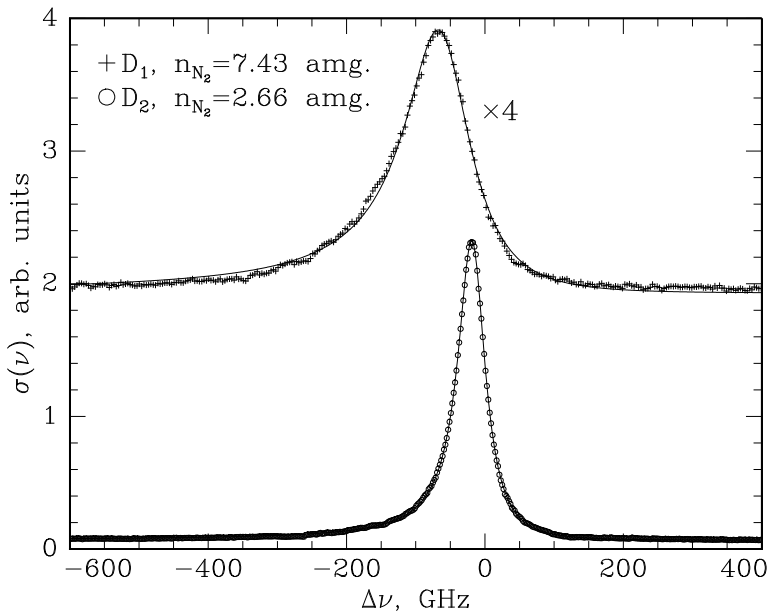


Figure B.6: Pressure broadening by $N_2$ with a fit to function (B.8).

Figure B.8 shows the absorption cross-section for Xe with a fit to equation (B.8). The critical density for Xe is $n_c = 2.3$ amg. The lineshape agrees very well with the data. The broadening and shift coefficients, given in Table B.2, are calculated from the data with $n < 2$ amg. The collision time $T_d$ is independent on pressure within our error bars. Our numbers for the width agree well with the results of Ottinger et al. [34], while our shift rate is substantially smaller. However, they define the shift as the position of the line center at the half-height, which is affected by the asymmetry of the line. Table B.2 also shows results predicted by equations (B.9) for a van der Waals potential. We used $C_6 = 6.86 \times 10^{-58}$ erg cm$^6$ for the $D_1$ line and $C_6 = 7.26 \times 10^{-58}$ erg cm$^6$ for the $D_2$ line from [32]. The agreement with experiment is reasonably good, especially for the collision time $T_d$, which characterizes the line asymmetry.

Because the asymmetry is larger than for He, higher order corrections to the lineshape become important for Xe and $N_2$. For Xe, $2\pi T_d\,(\nu - \nu_c) = 1$ for detuning of 45 GHz, while for $N_2$ this happens at 100 GHz. To evaluate the importance of the higher order effects, we tried to fit the data using only a linear approximation

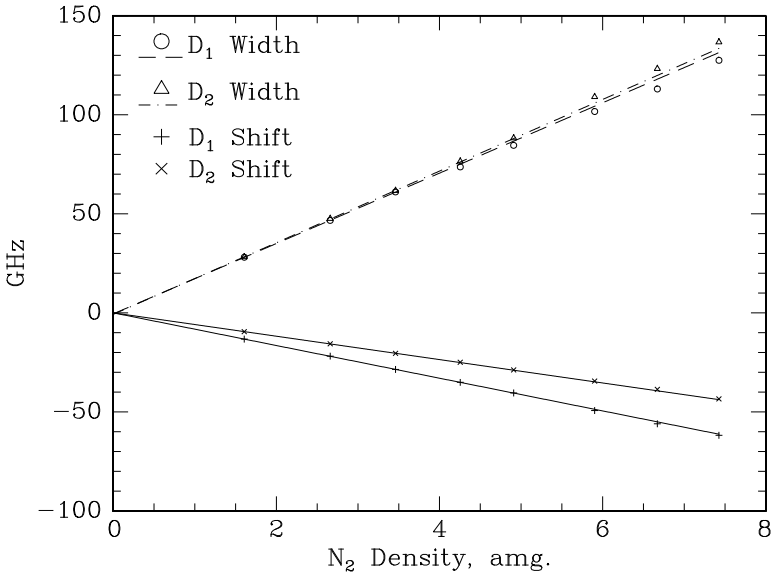


Figure B.7: Broadening and shift as a function of $N_2$ density. The straight lines are fits to the lowest 3 data points, where the low density approximation is valid.

(B.10). For both Xe and $N_2$ it resulted in the increase of the $\chi^2$ by a factor of 2-3. It is difficult to get a more significant confirmation of the higher order effects in (B.8). For the higher order effects to be important, one would like to have $T_d\gamma \sim 1$. However, this is exactly the place where the low density approximation starts to break down.

Equation (B.8) uses only one parameter ($T_d$) to characterize the asymmetry of the line. It is independent of the gas density, has a clear physical interpretation and is in agreement with calculations. For comparison, we also tried to fit the data with several other functions which use two parameters to characterize the shape of the asymmetry that are free to vary with density. Nevertheless, we could not find a simple function which would consistently give $\chi^2$ better than or comparable with the results of equation (B.8). Therefore, we conclude that the function $I(x)$ calculated for a van der Waals potential in [13] is very successful in describing the shape of the line core, including corrections beyond the first order dispersion asymmetry.

For Xe data with $n > 3$ amg. the line shape becomes significantly distorted by formation of a satellite line. Figures B.9 and B.10 show several absorption cross-sections measured at densities ranging from 4.87 to 9.31 amg. The peak cross-section of the line core goes down as $1/n$ with density, while the peak cross-section of the satellite is proportional to $n$. Therefore, the relative size of the satellite line grows as $n^2$.

In quasi-static theory of line shapes the appearance of the satellite is associated

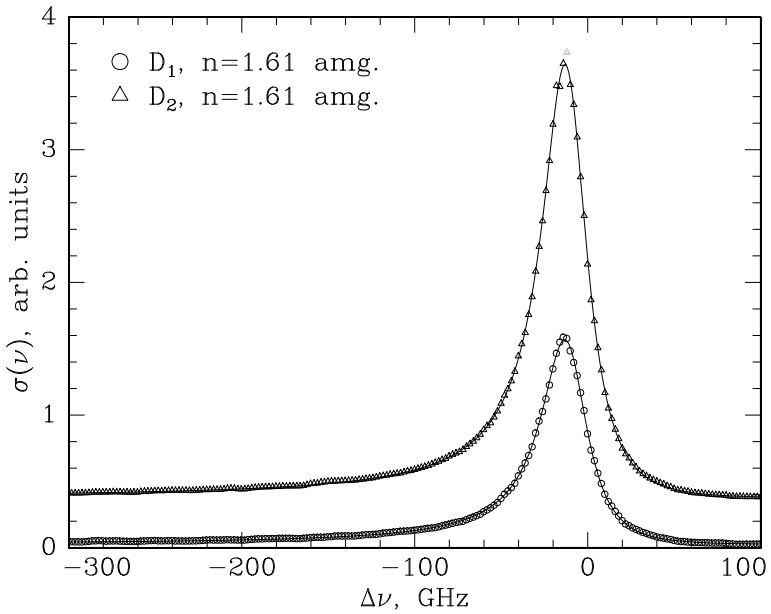


Figure B.8: Pressure broadening by Xe with fits using function (B.8).

| | $N_2$ | Xe | | |
|---|---|---|---|---|
| | This Work | This Work | Previous Results | Van der Waals |
| $D_1$ full width, GHz/amg. | 17.8±0.3 | 18.9±0.5 | 19.2±2[34]<br>14.2[40] | 15.9 |
| $D_1$ line shift, GHz/amg. | $-8.25 \pm 0.15$ | $-5.05 \pm 0.3$ | 6.95±0.7[34]<br>6.5[36] | −5.76 |
| $D_1$ asymmetry, $T_d$, $10^{-13}$s. | $16 \pm 2$ | $35 \pm 2$ | | 34 |
| $D_2$ full width, GHz/amg. | 18.1±0.3 | 19.2±0.5 | 19.5[34]<br>14.2[40] | 16.3 |
| $D_2$ line shift, GHz/amg. | $-5.9 \pm 0.1$ | $-5.15 \pm 0.3$ | $-8.34 \pm 0.6$[34] | −5.92 |
| $D_2$ asymmetry, $T_d$, $10^{-13}$s. | $12 \pm 1$ | $35 \pm 2$ | | 34 |

Table B.2: Broadening and shift coefficients and asymmetry for $N_2$ and Xe.

with an extremum in the interatomic difference potential $\Delta V(R) = V_e(R) - V_g(R)$. If $d\Delta V(R_s)/dR_s = 0$, then a satellite line should appear at detuning $\nu_s = \Delta V(R_s)/h$. If the difference potential can be approximated by a parabola near the extremum, one can derive a characteristic line shape for the satellite [11]. However, we were not able to fit the data to such a line shape. We believe that for Xe-Rb the satellite is due to two extrema, one minimum and one maximum, located very close to each other. The Rb-Xe interatomic potential for the $D_1$ line is shown in Figure B.11 [41]. The difference potential has a minimum of 1544 GHz at $R = 5.77$Å and a maximum of 2042 GHz at $R = 7.06$ Å, while we observed the satellite at about 700 GHz. However, the shape of the interatomic difference potential near the extrema is very sensitive to the shape of $V_e(R)$ and $V_g(R)$. The values of the maximum and minimum of the difference potential can probably be moved to 700 GHz by adjustments of the parameters which are consistent with other data from which the interatomic potentials where determined. Therefore the position of the satellite can be used in combination with other data to determine more accurately the interatomic potentials. Once the interatomic potentials are determined, the shape of the satellite line can be used as a good test case to compare against the predictions of the unified satellite line shape theory [11].

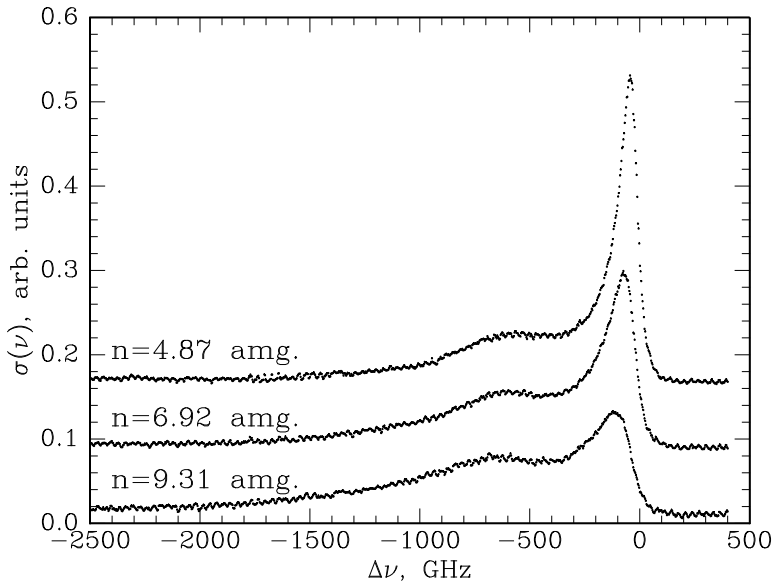


Figure B.9: Rb $D_1$ absorption cross-section in the presence of high density Xe.

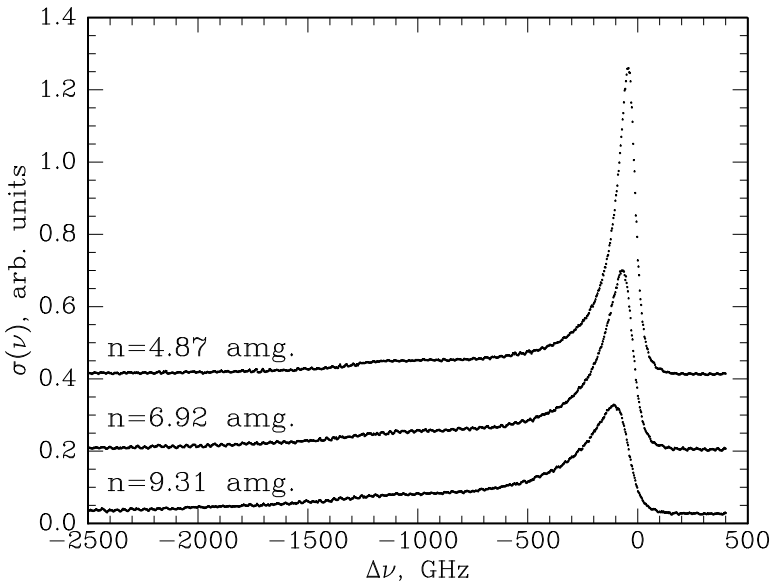


Figure B.10: Rb $D_2$ absorption cross-section in the presence of high density Xe.

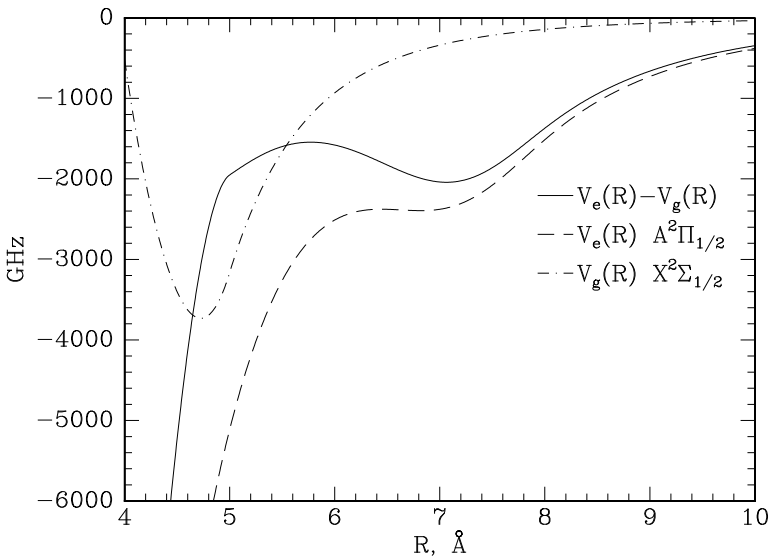


Figure B.11: Rb-Xe interatomic potentials for the ground state and the $P_{1/2}$ state [41].

### B.4.3 Oscillator Strength.

By integrating the absorption cross-section over the wavelength we can also get information on the oscillator strengths of the $D_1$ and $D_2$ transitions and their pressure dependence. It requires the knowledge of the Rb number density, which we can only determine from the vapor pressure curves. The cell was kept at 80°C for a period of several days prior to each set of measurements, and the temperature was very uniform across the cell. So, it is reasonable to assume that the Rb vapor pressure should be close to equilibrium. To calculate Rb number density we use the data from CRC Handbook of Chemistry and Physics [42], which have a quoted accuracy of 5%:

$$[Rb] = 10^{26.178-4040/T}/T \tag{B.11}$$

At 353 K it gives density 7% higher than more commonly used Killian formula [43]. However, Killian does not quote a error for his data.

Our results for the oscillator strength are shown in Figure B.12. The area is calculated from the parameters of the fit. This takes into account the area under the wings outside our measured range, which is on the order of several percent. It should be accurate for He because the low density approximation is satisfied for all of our data and the lineshape agrees with data quite well. In addition, there are no significant satellite lines for He [34]. For $N_2$ our fits do not work very well at high pressures, so the numbers should be treated with caution. However, as can be seen in Figure 12, the results for $N_2$ are similar to $^3$He and $^4$He. The uncertainty in the temperature of the cell is 0.5°C, corresponding to a density error of 4%. The error in the length of the cell is 2%, and the error in the determination of the area under the absorption curve for $^3$He and $^4$He is 3%. The total error for our values of $f$ is 7%, including the uncertainty in the vapor pressure curve.

We parametrize the density dependence of the oscillator strength by $f(n) = f\,(1 + a\,n)$. Because of the uncertainty in the estimation of the area for $N_2$ based on the fit, only $^3$He and $^4$He data are used for quantitative analysis. We find that the oscillator strength of the $D_1$ line is independent of pressure within our sensitivity: $|a_1| < 0.003$ amg$^{-1}$ ($1\sigma$), while the $D_2$ oscillator strength decreases with pressure: $a_2 = -0.019 \pm 0.003$ amg$^{-1}$ (the results for $^3$He and $^4$He are the same within errors). Our results for the oscillator strengths at zero pressure $f_1 = 0.33 \pm 0.02$ and $f_2 = 0.66 \pm 0.05$ are in very good agreement with commonly accepted values $f_1 = 0.322$ and $f_2 = 0.675$ [44]. We can compare our numbers with measurements by Chen [35], who studied the Rb oscillator strengths for $^4$He densities up to 45 amg using a technique similar to ours. He found $a_1 = -0.017$ amg$^{-1}$ and $a_2 = -0.019$ amg$^{-1}$. While the results for the $D_2$ line are in agreement, the pressure dependence of the $D_1$ oscillator strength is different from our result.

Since the sum rule $\sum f_i = 1$ is almost saturated by the $D_1$ and $D_2$ transitions: $f_1 + f_2 = 0.997$, their oscillator strength should decrease with density as the intensity of the

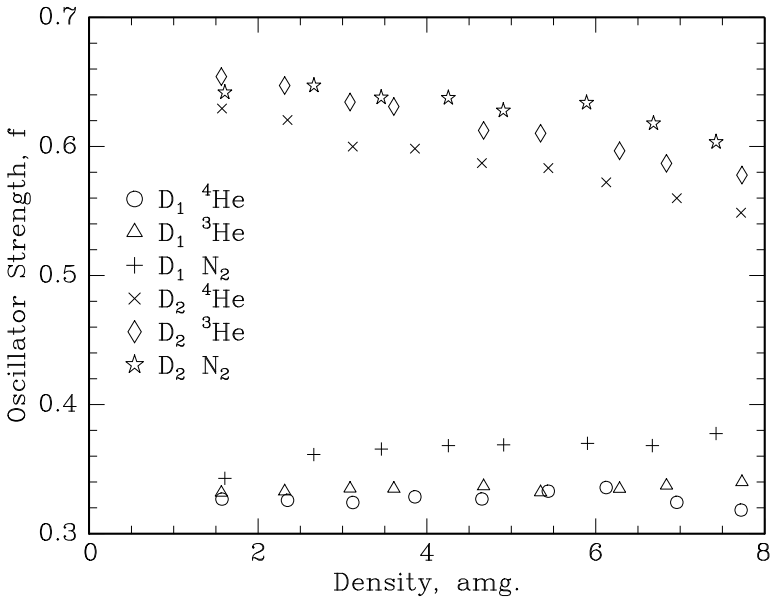


Figure B.12: Oscillator strength determined from the integral of the absorption cross-section as a function of the foreign gas density.

forbidden transitions increases. The density dependence of the oscillator strengths for forbidden transitions was studied in more details for Cs than for Rb [46, 47, 48]. The density dependence of the $D_1$ and $D_2$ transitions in Cs was also studied in detail [45]. It was found that the ratio of the $D_1$ to $D_2$ oscillator strength for Cs remains constant as the density is increased. This would imply that $a_1 = a_2$ in agreement with Chen's Rb measurements [35]. On the other hand, it is difficult to imagine how our slope for the $D_1$ oscillator strength could be more negative. If there is a significant area in the satellites which is not included in our integral, it can only result in the reduction of the apparent oscillator strength at higher densities. If the vapor pressure of Rb is reduced by the presence of He [49], it will also result in the apparent reduction of the oscillator strength with pressure. When the gas was released from the cell, some of the Rb vapor was released as well, reducing the Rb number density. This effect could result in the apparent reduction of the oscillator strength at low density. The vapor pressure will come back to equilibrium with a time scale given by the diffusion from the walls to the center of the cell, which was 6-30 sec. Each scan took about 5 min. and we alternated between first scanning the $D_1$ line followed by the $D_2$ line and vise versa after each release of the gas. Therefore, if this systematic effect was significant, it should have resulted in a systematic difference between odd and even points in our measurement, which was not observed.

## B.5 Conclusion

We have reported on a study of the line cores and near wings of the Rb $D_1$ and $D_2$ lines in the presence of 1-10 amg. of $^4$He, $^3$He, Xe, and $N_2$. The measurements were performed using laser absorption spectroscopy, which is free from systematic effects that can cause distortions of the lineshape. Unlike many earlier measurements, we extracted the values for the line width, shift and asymmetry by fitting the entire lineshape to a theoretically well-motivated functional form. As a result, our parameters are measured in an unambiguous fashion without mutual correlation and can be directly related to physical quantities. The accuracy of our data is in most cases significantly higher than in previous measurements. We have also confirmed with high degree of accuracy that the line width and shift increase linearly with density until the time between collisions becomes comparable to the duration of the collisions.

We also studied the temperature dependence of the line width and shift for $^3$He and $^4$He, and confirmed a scaling relationship between the temperature and reduced mass. Our lineshape data agree very well with calculations for a van der Waals potential made by Walkup et al. [13]. By making measurements at densities comparable to the critical density, we have confirmed not only the first order dispersion correction to the lorentzian lineshape, but also higher order corrections. We have also obtained data for the Rb-Xe lineshape at high Xe density exhibiting strong satellite lines, which can be used with other available data for accurate calculations of the interatomic potentials. We have measured oscillator strength of Rb resonance lines as a function of the foreign gas density and observed a reduction of the oscillator strength for the $D_2$ line with density, but not for the $D_1$ line. Our data provide important tests of the pressure broadening theory and also will be useful in applications of optical pumping.

We would like to thank Prof. William Happer for stimulating discussions. MVR would like to acknowledge support from Elizabeth Procter Fellowship. This work was supported by DOE contract DE-FG02-90ER40557.

# Bibliography


[1] A.A. Michelson, Astrophys. J. **2**, 251 (1895).

[2] H.A. Lorentz, K. Acad. Wet. (Amsterdam) **8**, 591 (1906).

[3] V. Weisskorf, Z. Phys. **77**, 398 (1932).

[4] E. Lindholm, Ark. Fys. A **32**, No. 17, 1 (1945).

[5] P.W. Anderson and J.D. Talman, Bell System Technical Publication No. 3117, (1956).

[6] S. Chen and M. Takeo, Rev. Mod. Phys. **29**, 20 (1957).

[7] E.L. Lewis, Phys. Rep. **58**, 1 (1980).

[8] N. Allard and J. Kielkorf, Rev. Mod. Phys. **54**, 1103 (1982).

[9] H.G. Kuhn, Philos. Mag. **18**, 987 (1934).

[10] R. Scheps, C. Ottinger, G. York, and A. Gallagher, J. Chem. Phys. **63**, 2581 (1975).

[11] J. Szudy and W.E. Baylis, J. Quant. Spectrosc. Radiat. Transfer **15**, 641 (1975).

[12] R.E. Walkup, A. Spielfiedel, and D.E. Pritchard, Phys. Rev. Lett. **45**, 986 (1980).

[13] R. Walkup, B. Stewart, and D.E. Pritchard, Phys. Rev. A **29**, 169 (1984).

[14] J. Szudy and W.E. Baylis, Phys. Rep. **266,** 127 (1996).

[15] M.A. Bouchiat, T.R. Carver, and C.M. Varnum, Phys. Rev. Lett. **5**, 373 (1960).

[16] W. Happer, E. Miron, S. Schaefer, D. Schreiber, W.A. van Wijngaarden, and X. Zeng, Phys. Rev. A **29**, 3092 (1984).

[17] P.L. Anthony *et al.*, Phys. Rev. Lett. **71**, 959 (1993).

[18] K. Abe *et al.*, Submitted to Phys. Rev. Lett.

[19] R.E. Stoner, M.A. Rosenberry, J.T. Wright, T.E. Chupp, E.R. Oteiza, and R.L. Walsworth, Phys. Rev. Lett. 77, 3971 (1996).

[20] G.L. Greene, A.K. Thompson, M.S. Dewey, Nucl. Instr. Meth. A **356**, 177 (1995).

[21] H. Middleton *et al*, Mag. Res. in Med. **33**, 271 (1995).

[22] M.S. Albert, G.D. Cates, B. Driehuys, W. Happer, C.S. Springer Jr., B. Saam, and A. Wishnia, Nature 370, 199 (1994)

[23] B. Driehuys, G.D. Cates, W. Happer, H. Mabuchi, B. Saam, M.S. Albert, and A. Wishnia, Phys. Lett. A **184**, 88 (1993)

[24] G. Navon, Y.-Q. Song, T. Rõõm, S. Appelt, R.E. Taylor, and A. Pines, Science **271**, 1848 (1996).

[25] B. Driehuys, G.D. Cates, E. Miron, K. Sauer, D.K. Walter, and W. Happer, Appl. Phys. Lett. **69**, 1668 (1996).

[26] P. Bogorad *et al.*, to be published in Nucl. Instr. and Meth.

[27] S. Appelt, A. Baranga, A. Young, and W. Happer, to be published.

[28] R.E. Walkup, Phys. Rev. A **25**, 596 (1982).

[29] V. I. Kogan and V. S. Lisitsa, J. Quant. Spectrosc. Radiat. Transfer **12**, 881 (1972).

[30] V.V. Yakimets, Zh. Eksp. Teor. Fiz. **51**, 1469 (1966) [Sov. Phys.-JETP **24**, 990 (1967)].

[31] I. Shannon, M. Harris, D.R. McHugh, and E.L. Lewis, J. Phys. B **19**, 1409 (1986).

[32] G. D. Mahan, J. Chem. Phys. **50**, 2755 (1969).

[33] J. Szudy and W.E. Baylis, J. Quant. Spectrosc. Radiat. Transfer **17**, 681 (1977).

[34] C. Ottinger, R. Scheps, G.W. York, and A. Gallagher, Phys. Rev. A **11**, 1815 (1975).

[35] S. Y. Chen, Phys. Rev. **58**, 1051 (1940).

[36] V. V. Gershun, V. Khutorschikov, and N.N. Yakobson, Opt. Spektrosk. **31**, 866 (1971) [Opt. Spectrosc. **31,** 470 (1971)].

[37] B. Larson, O. Häusser, P.P.J. Delheij, D.M. Whittal, and D. Thiessen, Phys. Rev. A, **44** (1991).

[38] J. Pascale, Phys. Rev. A **28**, 632 (1983).

[39] E. S. Hrycyshyn and L. Krause, Can. Jour. Phys. **48**, 2761 (1970).

[40] M. Takeo and S.Y. Chen, J. Quant. Spectrosc. Radiat. Transfer **4**, 471 (1964).

[41] R. J. Bieniek, Phys. Rev. A **15**, 1513 (1977).

[42] *CRC Handbook of Chemistry and Physics*, 74th Ed., p. 4-124 (1993).

[43] T. J. Killian, Phys. Rev. **27**, 578 (1926).

[44] *Atomic, Molecular, and Optical Physics Handbook*, ed. G. Drake, (1996).

[45] D. E. Gilbert and S. Y. Chen, Phys. Rev. **188**, 40 (1969).

[46] G. Moe, A.C. Tam, and W. Happer, Phys. Rev. A **14**, 349 (1976).

[47] B. Sayer, M. Ferray, and J. Lozingot, J. Phys. B **12**, 227 (1979).

[48] B. Sayer, M. Ferray, J.P. Visticot, and J. Lozingot, J. Phys. B **13**, 177 (1980).

[49] G. Wannier, *Statistical Physics*, p. 372 (Dover Publications, New York, 1987).

# List of Figures


2.1 Kinematic variables used in deep inelastic scattering. . . . . 5
2.2 Helicity preserving spin scattering process. . . . . 14
2.3 Kinematic factors $D$ and $\eta$ for the 2.75° spectrometer. . . . . 16
2.4 World data on the proton spin structure function $g_1^p$. . . . . 20
2.5 World data on the neutron spin structure function $g_1^n$. . . . . 21

3.1 The energy level diagram for strained GaAs crystal. . . . . 26
3.2 The layered structure of the strained GaAs cathode. . . . . 27
3.3 Negative electron affinity created by Cs-F film. . . . . 27
3.4 The polarization of the electron beam vs. run number. . . . . 32
3.5 Layout of the E-154 spectrometers. . . . . 33
3.6 The kinematic coverage of the E-154 spectrometers. . . . . 34
3.7 The $E/p$ ratio for electrons and pions. . . . . 38
3.8 The transverse profile of the electron shower in our calorimeter . . . . 42
3.9 Electron selection by a series of cuts. . . . . 44
3.10 Contribution to the unpolarized inelastic tail vs. $x$ and $Q^2$. . . . . 53
3.11 Contribution to the polarized inelastic tail vs. $x$ and $Q^2$. . . . . 54
3.12 Contribution to the unpolarized quasi-elastic tail vs. $Q^2$. . . . . 55
3.13 Contribution to the unpolarized elastic tail vs. $Q^2$. . . . . 55
3.14 The unpolarized Born cross-section and tails in the 2.75° spectrometer. 56
3.15 The polarized tails in the 2.75° spectrometer. . . . . 57
3.16 Uncorrected asymmetry $A_{||}$ for $^3$He and the radiative corrections. . . 58

4.1 Optical pumping by circularly polarized light. . . . . 65
4.2 Ground state energy levels for $^{85}$Rb. . . . . 65
4.3 The schematic of the inverted window design. . . . . 71
4.4 Dimensions of the target cell Picard, mm. . . . . 73
4.5 X-ray spectrum from $^{55}$Fe source recorded by a Germanium detector . 77
4.6 Absorption of X-rays in windows as a function of their thickness. . . . 79
4.7 Setup for interferometric thickness measurements. . . . . 79
4.8 Reflection coefficient as a function of the laser frequency. . . . . 80
4.9 Comparison of the mechanical and optical measurements of the window thicknesses. . . . . 81

4.10 Rb $D_1$ absorption cross-section for several $^3$He densities. . . . . 85
4.11 The width and shift of Rb resonance lines as a function of $^3$He density. 87
4.12 The overall setup of the $^3$He target. . . . . 89
4.13 Approximate positions of the RTDs mounted on the target cell. . . . 92
4.14 Target temperatures of 3 cells compared with the heat conduction model. 94
4.15 The $^3$He spectrum compared with calculated cross-sections. . . . . 98
4.16 The event spectrum from an empty glass cell . . . . . 99
4.17 The event spectrum for a polarized $^3$He target "Picard". . . . . 99
4.18 Radiative corrections to the dilution factor. . . . . 100
4.19 Two methods of calculating the dilution factor. . . . . 101
4.20 Target polarization during the run. . . . . 102
4.21 Spin-up of target cell Picard during the run. . . . . 103
4.22 Total charge accumulated by cells before failure. . . . . 104
4.23 Polarization of cell "SMC" during the run. . . . . 105
4.24 Polarization of cell "Generals" during the run. . . . . 106
4.25 Tests done with SMC after the run. . . . . 107
4.26 Simulation of the polarization based on the masing model. . . . . 112

5.1 NMR equipment setup. . . . . 121
5.2 $^3$He AFP signal with a lorentzian fit. . . . . 122
5.3 An average of 50 water signals with a fit based on the Bloch equations. 128
5.4 Average residual of the water signal as a percentage of the peak height. 129
5.5 The frequency of the EPR transitions as a function of the magnetic field. 136
5.6 Equipment setup for EPR detection. . . . . 137
5.7 The circuit diagram of the proportional-integral feedback and the mixer. 139
5.8 EPR polarization measurement for the target cell Picard. . . . . 140
5.9 Experimantal arrangement for $\kappa_0$ measurements. . . . . 141
5.10 The $\kappa_0$ measurement sequence. . . . . 144
5.11 Comparison of several measurements of $\kappa_0$. . . . . 145
5.12 Polarization of SMC in the first hour of spin-up. . . . . 147
5.13 Fluorescence absorption function $I(x)$. . . . . 149
5.14 EPR signal vs. position in the cell according to the pumping model. . 152
5.15 EPR signal detected with AM modulation of the RF field. . . . . 154
5.16 Comparison of the polarization measurements under different conditions. 155
5.17 Polarization Calibration Constant. . . . . 157
5.18 Simulation of the probability distribution based on 10 errors 1.4% each. 158
5.19 Probability distribution for the calibration constant. . . . . 159

6.1 Our results for $g_1^n(x)$ compared with previous SLAC data. . . . . 166
6.2 Our results for $g_1^n(x)$ compared with previous SMC data. . . . . 167
6.3 Several fits to the low $x$ region of our data. . . . . 168

6.4 Integration of $g_1^n$ from 1 to $x$ compared with Ellis-Jaffe sum rule. . . 169
6.5 Integration of $g_1^p - g_1^n$ from 1 to $x$ compared with Bjorken sum rule. 170
6.6 Embeding of the photon-quark cross-section into the photon-nucleon cross-section. . . . . 171
6.7 Contributions to $\sigma_{q\gamma}$ to order $\alpha_s$. . . . . 172
6.8 Gluon contribution to the photon-quark cross-section. . . . . 175
6.9 Hard scattering gluon and quark contribution. . . . . 177
6.10 NLO fit to all available proton data. . . . . 183
6.11 NLO fit to all available netron data. . . . . 184
6.12 Traditional scaling and NLO $Q^2$ evolution. . . . . 186

A.1 Number of overlaps per electron cluster versus momentum. . . . . 192
A.2 The pulse height as a function of the difference between the LE and TE. 195
A.3 Performance of the SLAC code: shower position resolution and bias. . 197
A.4 Cluster position versus the ratio of energies in the side and central blocks. 198
A.5 The position resolution for the electrons . . . . . 199
A.6 Position biases. . . . . 200
A.7 Time resolution for the electrons. . . . . 201
A.8 Electron and pion shower shapes. . . . . 201
A.9 Ratios of energies $E_1/E_9$ and $E_4/E_9$ and their momentum dependence. 204
A.10 Ratios $E_9/p$ and $E_1/p$ for electrons. . . . . 205
A.11 Ratios $E_1/p$ for electron clusters in 2.75° counter with overlaps. . . . 206
A.12 Same as Fig. A.11 for electrons with $9 < p < 12$ GeV. . . . . 207
A.13 Distribution of the shower shape variable $\chi$ for electrons and pions. . 208
A.14 Efficiencies of the shape cut for electrons and pions. . . . . 209
A.15 Efficiency of the shape cut with different energy variables. . . . . 210

B.1 Experimental setup for pressure broadening measurements. . . . . 216
B.2 Function I(x) calculated by Walkup *et al.* [13] for a van der Waals potential. . . . . 219
B.3 Absorption cross-section for Rb $D_1$ line in the presence of 3 different densities of $^3$He. . . . . 222
B.4 The dependence of the shift and width of Rb $D_1$ and $D_2$ lines on the density of $^3$He. . . . . 222
B.5 Temperature dependence of the line width and shift. . . . . 224
B.6 Pressure broadening by $N_2$ with a fit to function (B.8). . . . . 225
B.7 Broadening and shift as a function of $N_2$ density. . . . . 226
B.8 Pressure broadening by Xe with fits using function (B.8). . . . . 227
B.9 Rb $D_1$ absorption cross-section in the presence of high density Xe. . . 228
B.10 Rb $D_2$ absorption cross-section in the presence of high density Xe. . . 229
B.11 Rb-Xe interatomic potentials for the ground state and the $P_{1/2}$ state. 229

B.12 Oscillator strength as a function of the foreign gas density. . . . . 231

# List of Tables


3.1 Parameters of the Cherenkov detectors . . . . . 36
3.2 The radiative corrections to $A_{||}^{^3He}$ and their effect on the errors. . . . 59

4.1 Cell Dimensions in mm. . . . . 74
4.2 Cell lengths, lifetimes and densities of $N_2$ gas. . . . . 75
4.3 Wall Thickness, mm. (c - caliper, l -laser) . . . . . 76
4.4 X-rays emitted by the $^{55}$Fe source. . . . . 77
4.5 Window thicknesses. . . . . 82
4.6 Cell Volumes in cm$^3$. . . . . 83
4.7 Individual volumes of cell chambers. . . . . 83
4.8 Specific broadening and shift of Rb resonance lines in the presence of $^3$He. . . . . 86
4.9 $^3$He densities in amagats. . . . . 88
4.10 RTD Corrections. . . . . 91
4.11 Cell Temperatures and relative densities. . . . . 96
4.12 Chemical composition of Corning 1729 glass by weight. . . . . 97
4.13 Cell usage during the run. . . . . 103

5.1 AFP Parameters. . . . . 122
5.2 Coil Flux $F$ in units of cm$^2$. . . . . 125
5.3 Water Calibration Error Table. . . . . 133
5.4 Water Calibration Constants, %/mV . . . . . 134
5.5 Parameters for EPR frequency shift measurements. . . . . 138
5.6 EPR Measurements. . . . . 155
5.7 Final AFP Calibration Constants (%/mV) . . . . . 158

6.1 Results for the neutron spin structure function $g_1^n$ and the virtual photon asymmetry $A_1^n$ . . . . . 165
6.2 The results of our experiment for $g_1^n$ at $\langle Q^2 \rangle = 5$ GeV$^2$. . . . . 166
6.3 Various low $x$ fits of the data and values of extrapolated integral. . . 168
6.4 Parametrization of the unpolarized momentum distributions. . . . . 181
6.5 Parameters of the fits for polarized momentum distributions. . . . . 182
6.6 Physical quantities extracted from the fits. . . . . 182

A.1 Range of discriminator thresholds . . . . . 196
A.2 Parameters of the Eq. (A.4). . . . . 196
A.3 Parameters of the shower shape in Eq. (A.9). . . . . 202

B.1 Broadening and shift coefficients, asymmetry parameters and temperature dependence for $^3$He and $^4$He. . . . . 221
B.2 Broadening and shift coefficients and asymmetry for $N_2$ and Xe. . . . 227